UNIVERSITY OF SOUTHAMPTON

FACULTY OF ENGINEERING AND THE ENVIRONMENT
National Centre for Advanced Tribology at Southampton

Surface Texturing for Hydrodynamic Bearings

by

Daniel Gropper

Thesis for the degree of Doctor of Philosophy

January 2019

UNIVERSITY OF SOUTHAMPTON

ABSTRACT

FACULTY OF ENGINEERING AND THE ENVIRONMENT
National Centre for Advanced Tribology at Southampton

Doctor of Philosophy

SURFACE TEXTURING FOR HYDRODYNAMIC BEARINGS

by Daniel Gropper

In the present thesis the concept of surface texturing, i.e. the intentional introduction of surface features, is investigated as a means of enhancing the tribological performance of hydrodynamic bearings. An in-depth literature review is conducted, outlining the research effort worldwide, analysing the current understandings on how textures can improve the bearing performance, discussing recommended texture geometries and providing a comparative summary of state of the art modelling techniques to study textured surfaces under hydrodynamic conditions. Based on the findings of this literature review, a fast and robust numerical model is developed that allows to study and mathematically optimize texture patterns for tilting pad thrust bearings under a wide range of conditions. The model is based on a non-uniform finite volume discretization of the Reynolds partial differential equation and includes a mass-conserving cavitation algorithm. Meshes are adaptive and film discontinuities are directly incorporated in the discrete equations to improve accuracy and computational speed. A Gauss-Seidel method with successive relaxation is used to solve the discrete system. A novel bearing equilibrium solver is developed, based on a strategic combination of the Newton-Raphson method, Broyden's method with Sherman-Morrison formula and a continuation approach with fourth-order Runge-Kutta technique, where results from the equivalent untextured bearing are used to speed up the computation. Thermal effects are considered through an effective temperature method, while considering the hot-oil-carry-over effect. The model takes advantage of multiple processor cores and allows the execution of arbitrary parametric studies as well as the optimization of texture designs by incorporating an interior-point algorithm. The model is validated by comparison with literature and applied to optimize surface textures for tilting pad thrust bearings under various conditions. Moreover, experiments are carried out on a purposely developed thrust bearing test rig to study the influence of surface texturing on the performance of tilting pad thrust bearings and validate the developed numerical model.

Contents

List of Figures

List of Tables

Nomenclature

Latin symbols

A	Control volume face dimension (m or rad)
A_c	Contact area (m^2)
A_{cell}	Texture cell area (m^2)
$A_{texture}$	Texture area (m^2)
$A_{textured}$	Textured area (m^2)
a	Discretization coefficient (m.s or kg/s), coefficient for temperature viscosity relationship, texture cell dimension (m)
B	Relative textured portion, Bernoulli coefficient (Pa or kg/s)
b	Texture cell dimension (m), discretization coefficient for MNUFVD method (m.s)
c	Clearance (m), speed of sound in oil at 20°C (m/s)
c_d	Damping coefficient
c_p	Lubricant specific heat (J/kg/K)
D	Diameter (m), damping intensity
d_f	Discontinuity coefficient
e	Eccentricity (m), solver tolerance value
$\boldsymbol{F}(\boldsymbol{x})$	Error function for bearing equilibrium
f	Linear interpolation factor
$f(\boldsymbol{x})$	Objective function for optimization
f_t	Offset factor for Jacobian matrix
$\boldsymbol{G}(\Lambda, \boldsymbol{x})$	Homotopy
g	Switch function of Elrod cavitation algorithm

$H_r = S + 1$	Texture height ratio
h	Local film thickness (m)
h_p	Film thickness at pivot position (m)
$h_{texture}$	Texture depth (m)
ii	Total number of nodes in r direction
J	Film thickness jump coefficient (kg/s)
jj	Total number of nodes in θ direction
$K = \frac{h_{in}}{h_{out}} - 1$	Convergence ratio
k_{con}	Convection parameter
l	Texture dimension in flow direction (m or rad), Texture arc length at mid radius (m)
M_x	Moment of force about the x axis (Nm)
M_y	Moment of force about the y axis (Nm)
m	Coefficient for temperature viscosity relationship
N	Total number of textures, number of steps for continuation method
n	Coefficient for temperature viscosity relationship
n_{pad}	Number of pads
n_r	Number of textures in r direction
n_θ	Number of textures in θ direction
p	Local pressure (Pa)
Q	Volumetric flow rate (m^3/s)
q	Mass flow rate (kg/s)
R_B	Bush radius (m)
Re	Reynolds number
R_J	Journal radius (m)
r	Radial coordinate (m)
r_{cell}	Cell dimension in r direction (m)
r_{cop}	Radial coordinate of the centre of pressure (m)
r_p	Radial pivot position (m)
r_{pad}	Pad radius (m)
$r_{texture}$	Texture dimension in r direction (m)

$r_{textured}$	Dimension of the textured area in r direction (m)
$S = h_{texture}/h_{min}$	Relative texture depth
T	Temperature (°C)
T_f	Friction torque (Nm)
$T_{\circ K}$	Temperature (K)
t	Time (s)
U	Average fluid velocity (m/s)
$\boldsymbol{u}$	Velocity vector (m/s)
u	Velocity in sliding direction (m/s)
v	Velocity in y direction (m/s)
V	Volume (m^3)
W	Load carrying capacity (N)
W_0	Applied load (N)
W_{res}	Reaction force from pressure field normal to pad surface (N)
w	Velocity in z direction (m/s)
w_0	Applied specific load (MPa)
X_c	Contact dimension in x direction (m)
X_{cell}	Cell dimension in x direction (m)
$X_{textured}$	Dimension of textured area in x direction (m)
$\boldsymbol{x}$	Film thickness vector, texture design vector
x	Cartesian coordinate (m)
Y_c	Contact dimension in y direction (m)
Y_{cell}	Cell dimension in y direction (m)
$Y_{textured}$	Dimension of textured area in y direction (m)
y	Cartesian coordinate (m)
z	Cartesian coordinate (m), specific acoustic impedance (rayl)

Greek symbols

α	Relative texture extent in x or θ direction
α_r	Pitch angle (rad)

α_θ	Roll angle (rad)
β	Relative texture extent in y or r direction, lubricant bulk modulus (Pa)
Γ	Interfacial diffusion coefficient (m.s)
Δ_1, Δ_2	Indicators for the validity of the Reynolds equation
ΔT	Average temperature rise (°C)
δr	Distance between pivot and centre of pressure in r direction (m)
δW	Difference between applied load and load carrying capacity (N)
$\delta\theta$	Distance between pivot and centre of pressure in θ direction (rad)
$\widetilde{\delta\theta}$	Circumferential size of additionally added control volume (rad)
ε	Eccentricity ratio, solver residual
ε_o	First order optimality
η	Lubricant dynamic viscosity (Pa.s)
Θ	Fractional film content
θ	Circumferential coordinate (rad)
θ_c	Contact dimension in θ direction (rad)
θ_{cell}	Cell dimension in θ direction (rad)
θ_{cop}	Circumferential coordinate of the centre of pressure (rad)
θ_p	Circumferential pivot position (rad)
θ_{pad}	Pad angle (rad)
$\theta_{texture}$	Texture dimension in θ direction (rad)
$\theta_{textured}$	Dimension of the textured area in θ direction (rad)
Λ	Homotopy parameter
$\lambda = \frac{h_{texture}}{l}$	Texture aspect ratio
ν_{cSt}	Lubricant kinematic viscosity (cSt)
ξ	Pressure drop coefficient
Π	Dissipated energy/ power loss (W)
ρ	Lubricant density (kg/m^3)
ρ_r	Texture density in r direction
ρ_{ref}	Reference density (kg/m^3)

$\rho_{texture}$	Texture density
ρ_θ	Texture density in θ direction
σ	Surface rms roughness (m), standard deviation
τ	Shear stress (Pa)
φ	Attitude angle (rad)
ϕ_s	P&C method shear flow factor
ϕ_x	P&C method pressure flow factor for x direction
ϕ_y	P&C method pressure flow factor for y direction
ω	Rotational speed (rad/s)
ω_p	Relaxation parameter for pressure
ω_Θ	Relaxation parameter for fractional film content

Other symbols

$\boldsymbol{\mathcal{D}}^0$	Cavitation subdomain
$\boldsymbol{\mathcal{D}}^+$	Pressure subdomain
$\boldsymbol{\mathcal{F}}$	Computational domain
$\boldsymbol{\mathcal{J}}$	Jacobian matrix

Subscripts and Superscripts

$+$	Quantity just downstream of a discontinuity
$-$	Quantity just upstream of a discontinuity
bp	Bypass
cav	Cavitation
eff	Effective
i	Inner, node index in r direction
in	Inlet
j	Node index in θ direction
k	Iteration
lb	Lower bound
max	Maximum
min	Minimum

n	Newton
o	Outer, optimization
opt	Optimum
out	Outlet
P	Quantity at current node
ref	Reference value
ri	Inner radius
ro	Outer radius
sup	Supply
t	Temperature
ub	Upper bound
W, E, S, N	Quantity at west, east, south, north node
w, e, s, n	Quantity at west, east, south, north control volume face

Abbreviations

ADI	Alternating Direction Implicit
CAD	Computer-Aided-Design
CFD	Computational Fluid Dynamics
COF	Coefficient Of Friction
CPU	Central Processing Unit
CV	Control Volume
DOF	Degrees Of Freedom
EHL	Elasto-Hydrodynamic Lubrication
FBNS	Fischer-Burmeister-Newton-Schur
FCM	Finite Cell Method
FDM	Finite Difference Method
FEM	Finite Element Method
FSI	Fluid Structure Interaction
FVM	Finite Volume Method
GA-SQP	Genetic Algorithm – Sequential Quadratic Programming hybrid method

ISO	International Organization for Standardization
JFO	Jacobsson-Floberg-Olsson
LCP	Linear Complementarity Problem
LU	Lower Upper
MNUFVD	Modified Non-Uniform Finite Volume Discretization
NC	Not Converged
NS	Navier-Stokes
NUFVD	Non-Uniform Finite Volume Discretization
NUFVD+A	Non-Uniform Finite Volume Discretization with Additional points
P&C	Patir & Cheng flow factor method
PDE	Partial Differential Equation
SAI	Specific Acoustic Impedance
SEM	Spectral Element Method
SiC	Silicon Carbide
SIMPLE	Semi-Implicit Method for Pressure Linked Equations
SOR	Successive Over Relaxation
SQP	Sequential Quadratic Programming
TEHD	Thermo-Elasto-Hydrodynamic
THD	Thermo-Hydrodynamic
TPT	Tilting Pad Texturing
VG	Viscosity Grade

Declaration of Authorship

I, Daniel Gropper, declare that this thesis *Surface Texturing for Hydrodynamic Bearings* and the work presented in it are my own and has been generated by me as the result of my own original research.

I confirm that:

- This work was done wholly or mainly while in candidature for a research degree at this University;
- Where any part of this thesis has previously been submitted for a degree or any other qualification at this University or any other institution, this has been clearly stated;
- Where I have consulted the published work of others, this is always clearly attributed;
- Where I have quoted from the work of others, the source is always given. With the exception of such quotations, this thesis is entirely my own work;
- I have acknowledged all main sources of help;
- Where the thesis is based on work done by myself jointly with others, I have made clear exactly what was done by others and what I have contributed myself;
- Either none of this work has been published before submission, or parts of this work have been published as:

Journal Articles (peer reviewed)

1. Gropper D, Wang L, Harvey TJ. Hydrodynamic lubrication of textured surfaces: A review of modeling techniques and key findings. Tribology International. 2016;94:509-29.
2. Gropper D, Harvey TJ, Wang L. A numerical model for design and optimization of surface textures for tilting pad thrust bearings. Tribology International. 2018;119:190-207.
3. Gropper D, Harvey TJ, Wang L. Numerical analysis and optimization of surface textures for a tilting pad thrust bearing. Tribology International. 2018;124:134-44.

Conference Papers

4. Gropper D, Wang L, Harvey TJ. Journal and thrust bearings with textured surfaces: A review of modelling techniques. 14th EDF/Pprime Workshop, FUTUROSCOPE. 2015. Poitiers, France.
5. Gropper D, Wang L, Harvey TJ, Meck K-D, Gviniashvili V. Influence of surface texturing on the performance of tilting pad thrust bearings. 71st STLE Annual Meeting and Exhibition. 2016. Las Vegas, USA.
6. Gropper D, Wang L, Harvey TJ, Meck K-D, Ricchiuto F. Numerical optimization of surface textures for tilting pad thrust bearings. 72nd STLE Annual Meeting and Exhibition. 2017. Atlanta, USA.

Conference Posters

7. Gropper D, Wang L, Harvey TJ. Journal and thrust bearings with textured surfaces: A review of modelling techniques. 14th EDF/Pprime Workshop, FUTUROSCOPE. 2015. Poitiers, France.
8. Gropper D, Wang L, Harvey TJ, Meck K-D, Gviniashvili V. Influence of surface texturing on the performance of tilting pad thrust bearings. 71st STLE Annual Meeting and Exhibition. 2016. Las Vegas, USA.
9. Gropper D, Wang L, Harvey TJ, Meck K-D, Ricchiuto F. Numerical optimization of surface textures for tilting pad thrust bearings. 72nd STLE Annual Meeting and Exhibition. 2017. Atlanta, USA.

Signed: _____

Date: 2nd January 2019

Acknowledgements

The work presented in this thesis was carried out during my time at the national Centre for Advanced Tribology at Southampton (nCATS), Faculty of Engineering and the Environment at the University of Southampton, UK.

I would like to express my gratitude towards my supervisors, **Prof Ling Wang** and **Dr Terry J Harvey**, for their continuous guidance and support throughout my studies. I would also like to thank **Prof Robert J K Wood** and **Dr Georges Limbert** for acting as internal examiners as well as **Prof Michel Fillon** from the University of Poitiers, France for agreeing to be my external examiner.

The bearing test rig used in this work was developed and manufactured by the industrial sponsor of this project: John Crane UK Ltd. The experimental work was conducted at their laboratories in Slough, UK. In this context, I want to thank **Dr Fabio Ricchiuto** for carrying out the experiments. His patience, great interest in this work and help during countless technical discussions contributed significantly to the experimental part of this work. I want to also thank **Klaus-Dieter Meck** and **Eckhard Schüler** for their helpfulness and contribution through numerous suggestions as well as **Dr Duc Nhin-Ha** and **Dr Vladimir Gviniashvili** for designing the bearing test rig.

I would also like to acknowledge the financial support from the Engineering and Physical Sciences Research Council (EPSRC) via grant EP/M50662X/1 and John Crane UK Ltd. I also acknowledge the Institution of Mechanical Engineers (IMechE) for awarding me a conference grant, which allowed me to travel to Las Vegas, USA and present my work at the 71st STLE Annual Meeting and Exhibition.

I would also like to thank **Dr Christos I. Papadopoulos** from the National Technical University of Athens for providing the data used for validation in this work.

I thank all my friends and colleagues from the faculty for innumerable helpful discussions and feedback in various matters. In particular, I would like to thank **Dr Simon Watson**, **Dr Timothy Kamps**, **Dr Pawee Kucita**, **Dr Maria Fabiola Leyva-Mendivil** and **Dr Alex Richardson**.

Finally, I want to express my deepest gratitude towards my family and my girlfriend for their continuous support and encouragement during this time.

Chapter 1

Introduction

Inspired by nature, surface texturing has become a promising way of enhancing the performance of tribological contacts found in various engineering applications. One of the most popular applications of surface texturing are hydrodynamic bearings, where the aim is an improvement of durability, safety and efficiency. Surface textures have an influence on the pressure development in the lubricant and this way are capable of improving the bearing's performance characteristics. Surface textures may also have the ability to trap wear particles and act as a lubricant reservoirs, potentially decreasing friction during mixed lubrication and prolonging bearing lifetime. However, no experimental evidence of these effects is available. This work is focussed on facilitating the design of optimized surface textures in order to increase the still limited number of successful industrial applications. This chapter provides information regarding the research background, aim and objectives of this project.

1.1 Research background

Using textured surfaces for contact performance enhancement is not a new concept. For example, special surface structures can increase adhesion, enabling some amphibians, such as tree frogs, to safely walk on wet surfaces [1] or reduce aerodynamic drag, making the movement of sharks more efficient [2] (Figure 1.1). The dimpled surface of a golf ball also highly reduces drag and allows it to fly up to four times as far as compared to a golf ball having a smooth surface [3].

Surface textures also have an influence on the tribological performance of lubricated contacts. In 1966, Hamilton *et al.* [4] found that micro irregularities on the surfaces of rotary-shaft seals were capable of producing hydrodynamic pressure and hence, created a load carrying capacity. They directly observed cavitation at the diverging

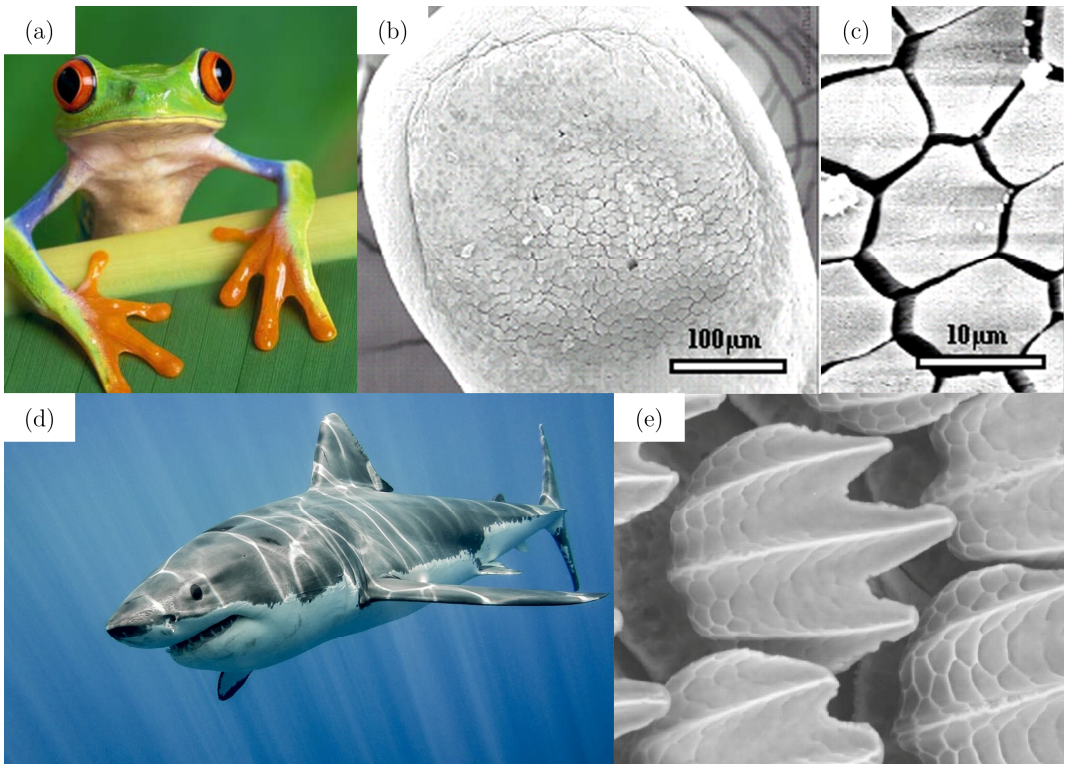

Figure 1.1 (a) Tree frog (adapted from [5]), (b)–(c) scanning electron microscopy (SEM) images of a tree frog toe pad [6], (d) great white shark [7], (e) SEM image of the skin of a bonnethead shark [8].

part of asperities by using a transparent rotor and proposed that local cavitation was the responsible mechanism for the observed load support. Anno *et al.* [9, 10] investigated this theory some years later and concluded that the introduction of micro-asperities was an efficient method for lubricating mechanical face seals and parallel rotating thrust bearings. One of the first successful commercial applications of surface texturing, however, was that of cylinder liners of combustion engines [11]. The micro-grooves on the liner surface produced by the honing process are able to retain oil and trap wear debris in the contact and thus increase lifetime. In the following three decades, rather little attention on textured surfaces was paid, with only a handful papers being published.

The research on surface texturing gained a new momentum in 1996, when Etsion's group published one of their first papers on surface texturing [12]. They used the incompressible, two-dimensional Reynolds equation together with the Half-Sommerfeld cavitation boundary condition to mathematically investigate mechanical seals with hemispherical dimples on one of the mating surfaces. They concluded that an increase in load carrying capacity was obtained due to local cavitation and that a proper selection of texture size and density was crucial. They conducted field tests to compare the performance of non-textured seals with textured ones and showed that texturing could increase seal lifetime threefold [13]. Since then, due to the promising results obtained by Etsion and co-workers, hundreds of theoretical and experimental studies have been conducted worldwide in order to improve the

performance of tribological contacts. A wide range of applications have been explored, including thrust bearings, journal bearings, cylinder liners, piston rings, concentrated contacts, mechanical seals, magnetic storage devices, piston pins and drill bits. One of the most popular application of surface texturing are hydrodynamic bearings, where textures are introduced to increase the minimum film thickness, decrease friction and temperature and reduce wear.

Although a large number of publications exist and promising results have been obtained, the industrial application of surface texturing remains a major challenge. This is mainly due to the dependency of the optimum texture design (size, shape and distribution) on the type of contact and the operating conditions. If designed wrong, textures may provide unreasonable performance enhancement or even become detrimental [14, 15]. Hence, a proper texture design is crucial and the profitability and effectiveness of surface texturing need to be assessed for a given application and range of operating conditions. However, finding the best texture design is very challenging due to the large number of parameters involved and the complexity in the patterns. Experimental trial and error approaches are time consuming and costly and do not allow an efficient design of surface textures. This has led to the development of numerous numerical models. However, the complexity of the governing equations, their numerical solution and the lack of standard methods have led to conflicting conclusions. Results are often limited to a certain application or certain operating conditions due to the high computation times involved. The significant influence of film discontinuities on the numerical accuracy is often not accounted for, leading to erroneous results. Also, many theoretical studies make use of non-mass-conserving cavitation boundary conditions, which have been shown to result in a considerable over-estimation of the benefits of surface textures [16]. In conclusion, a successful application of surface texturing relies to a great degree on fast and robust numerical models that allow an accurate evaluation of the impact of surface texturing on the performance of hydrodynamic bearings under a wide range of conditions.

This work is focussed on tilting pad thrust bearings, an application of surface texturing that has hardly been given any attention. The schematic of a tilting pad thrust bearing is shown in Figure 1.2. This type of bearing was developed independently by A.G.M. Michell and Albert Kingsbury at the beginning of the 20th century. Under operation, the thrust pads form a converging wedge that builds up pressure in the lubricant that balances the applied load. Fixed geometry thrust pad bearings have a fixed pad inclination, i.e. the convergence ratio depends on the encountered operating condition. In tilting pad thrust bearings the pads can freely tilt and adjust the film thickness, keeping the convergence ratio constant, i.e. the convergence only depends on the position of the pivot, making it possible to determine a convergence ratio by design. As friction and load carrying capacity depend significantly on the convergence ratio, this offers a great advantage. Tilting

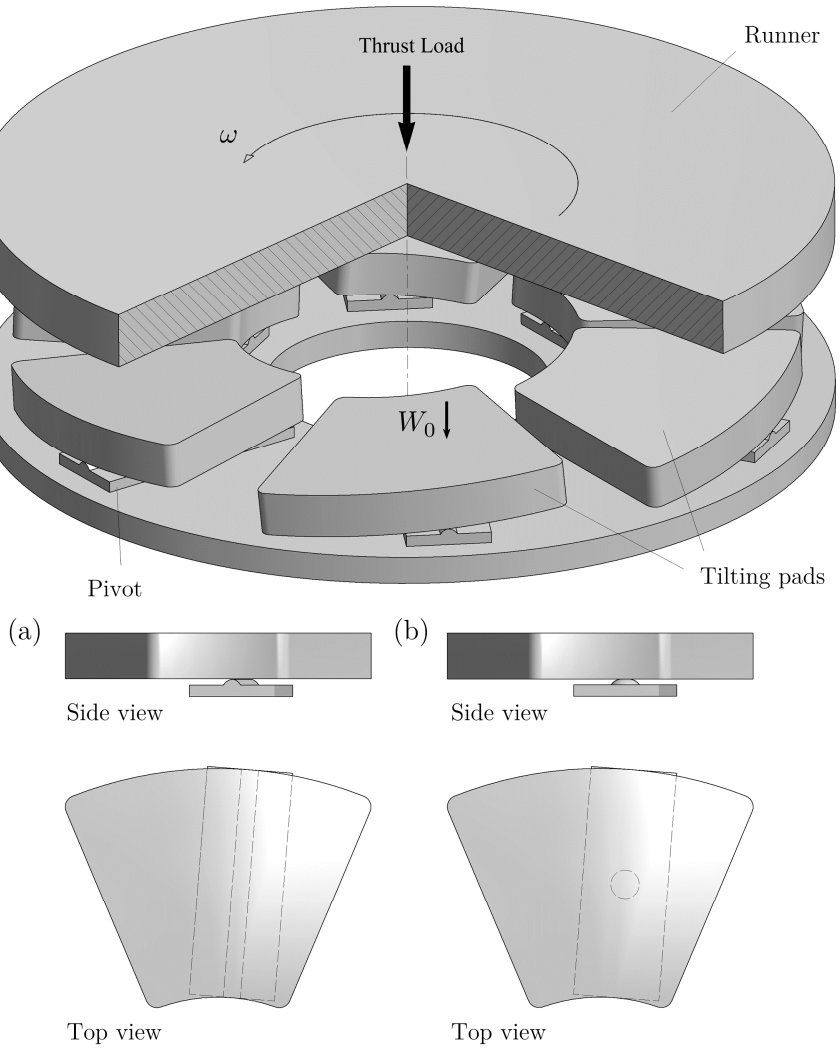

Figure 1.2 Tilting pad thrust bearing with (a) Michell offset line pivot and (b) Kingsbury offset point pivot (adapted from [17]).

pad bearings are predominantly used in heavy-duty rotating machinery, such as turbines, pumps and compressors. A failure of one of these bearings often results in high costs. Therefore, improving the durability through surface texturing is of high interest. Surface texturing may also be capable of reducing the energy loss caused by tilting pad thrust bearings, making many industrial processes more efficient.

One of the only studies on textured tilting pad bearings was published in 2017 by Zouzoulas and Papadopoulos [18]. They compared the hydrodynamic performance of a conventional point-pivoted tilting pad thrust bearing with a pocketed, grooved and dimpled design using commercial CFD software. The results showed that minimum film thickness, friction torque and maximum temperature can be improved but a proper texture design is crucial. Texturing was shown to be capable of increasing the minimum film thickness by up to 24% and reducing the maximum temperature by up to 7°C. Although a parametric study was presented, results were limited due to the high computation times encountered. Further research is needed to understand the complex relationship between texture geometries and bearing performance,

particularly the impact of surface texturing on the equilibrium position on the pads and the dependency of optimum texturing parameters on the operating conditions.

1.2 Aim and objectives

One of the key challenges in applying surface texturing industrially is the design of proper texture patterns due to the large number of parameters and the dependency of the optimum texture geometry on the application and operating conditions. Easing the design of surface textures is thus an essential step towards successful industrial applications of this technology. The aim of this work is to facilitate the design of surface textures for hydrodynamic bearings, in particular tilting pad thrust bearings, as this is the core product of this project's industrial sponsor. However, the developed theoretical model is easily adaptable to other types of hydrodynamic bearings.

The main objectives of this project are given in the following:

- **Conduct an in-depth study on the state of the art** Completion of an in-depth literature review on surface texturing for hydrodynamic bearings and modelling techniques for textured contacts under hydrodynamic lubrication conditions. Review texture design recommendations provided in literature and assess the key issues that are responsible for the still very limited number of successful industrial applications.
- **Develop an accurate, fast and robust numerical model** Development of an accurate, fast and robust numerical framework that allows to efficiently evaluate the performance of textured bearings under a wide range of conditions. The model should be capable of performing arbitrary parametric studies and mathematically optimizing texture patterns for best bearing performance. For accurate results, the model should include a mass-conserving cavitation algorithm and consider thermal effects. To allow the use of the model in an industrial setting, a texture optimization should be executable on a normal desktop computer within an hour.
- **Validation of the numerical model** Validate the developed mathematical model by detailed comparison with published data. In addition, conduct experiments on conventional and textured tilting pad thrust bearings under various load and speed conditions for further validation.
- **Analyse the applicability of surface texturing for tilting pad thrust bearings** Apply the developed model to study the impact of surface texturing on the main performance characteristics of tilting pad thrust bearings under various operating conditions. Numerically optimize texture patterns and investigate possible performance improvements and assess the industrial

applicability of surface texturing for this application.

1.3 Scope of the thesis

This thesis is divided into 8 chapters, outlined in the following:

Chapter 2 provides an in-depth literature review on surface texturing for various types of hydrodynamic bearings. The research effort worldwide is outlined and current understandings on how surface textures are capable of improving the performance of hydrodynamically lubricated contacts are analysed. Optimum texturing parameters as proposed in literature are discussed for various applications, followed by a comprehensive review on available modelling techniques.

Chapter 3 provides details of the proposed mathematical model to study and optimize textured tilting pad thrust bearings. The considered bearing and texture geometries are discussed and the applied mass-conserving formulation of the Reynolds equation is introduced, followed by the mathematical description of the bearing equilibrium and thermal effects. The utilized formulation to optimize texture patterns is presented in the last section of this chapter.

Chapter 4 explains the numerical solution of the proposed mathematical model with regards to the fluid solver, equilibrium solver, temperature solver and optimization solver. Three finite volume discretization schemes as well as the utilized mass-conserving cavitation algorithm are introduced, followed by a presentation of the three applied nonlinear root finding techniques to solve the bearing equilibrium problem. Detailed descriptions of the temperature solver and the optimization algorithm are given at the end of this chapter.

Chapter 5 In this chapter, the numerical model is improved in terms of accuracy, stability and computational speed by comparing the implemented discretization methods, equilibrium and temperature solver strategies as well as numerical solution techniques. In the second part of this chapter, the model is validated by comparison with published data.

Chapter 6 In this chapter, the developed numerical model is applied to study the influence of surface texturing on the performance of a tilting pad thrust bearing. Texture depth, circumferential and radial extent are numerically optimized to improve three bearing performance characteristics: minimum film thickness, friction torque and maximum temperature. Results are discussed for various operating conditions and texturing recommendations are provided.

Chapter 7 This chapter is devoted to the experimental part of this work. The utilized bearing test rig as well as the analysed tilting pad thrust bearing and its

instrumentation are presented. After introducing the test methodology, experimental results are presented to compare the performance of a conventional bearing with a textured bearing. The experimental results are then compared to the predictions of the numerical model.

Chapter 8 concludes the work presented in this thesis and outlines possible future work to further advance the knowledge around surface texturing for hydrodynamic bearings.

The contents of chapter 2 have been published as "Hydrodynamic lubrication of textured surfaces: A review of modeling techniques and key findings". Tribology International. 2016;94:509-29.

The contents of chapters 3, 4 and 5 have been published as "A numerical model for design and optimization of surface textures for tilting pad thrust bearings". Tribology International. 2018;119:190-207.

The contents of chapter 6 have been published as "Numerical analysis and optimization of surface textures for a tilting pad thrust bearing". Tribology International. 2018;124:134-44.

Chapter 2

Literature Review

This chapter outlines the worldwide research effort on surface texturing for hydrodynamically lubricated contacts and summarizes the key findings. The current understandings on how artificial textures can enhance the performance are discussed, followed by an in-depth review on optimum texture designs as proposed in literature for different bearing applications. Modelling techniques for fluid flow, cavitation and micro-hydrodynamic effects as well as discretization and numerical methods are reviewed and conclusions are drawn with regards to this work. Although this work is focussed predominantly on tilting pad thrust bearings, this review includes other bearing-like applications as well to offer an exhaustive overview.

2.1 Background

2.1.1 Literature survey

Hundreds of studies on the influence of textured surfaces on tribological performance of lubricated contacts have been published since 1966. The vast majority has been published over the last two decades (Figure 2.1 (a)). In an extensive literature survey, the author found hundreds of publications that are concerned with textured surfaces, published between 1966 and 2015. Interestingly, more than 50% of the studies are purely theoretical, based on different forms of the Reynolds equation, Navier-Stokes equations or Stokes equations (Figure 2.1 (b)). Models in the early years were based on the steady-state, two-dimensional Reynolds equation, applying non-mass-conserving cavitation boundary conditions and neglecting changes in viscosity, density and temperature. Also, surface deformations and the effect of surface roughness were not considered. Examples of more basic models can be found in

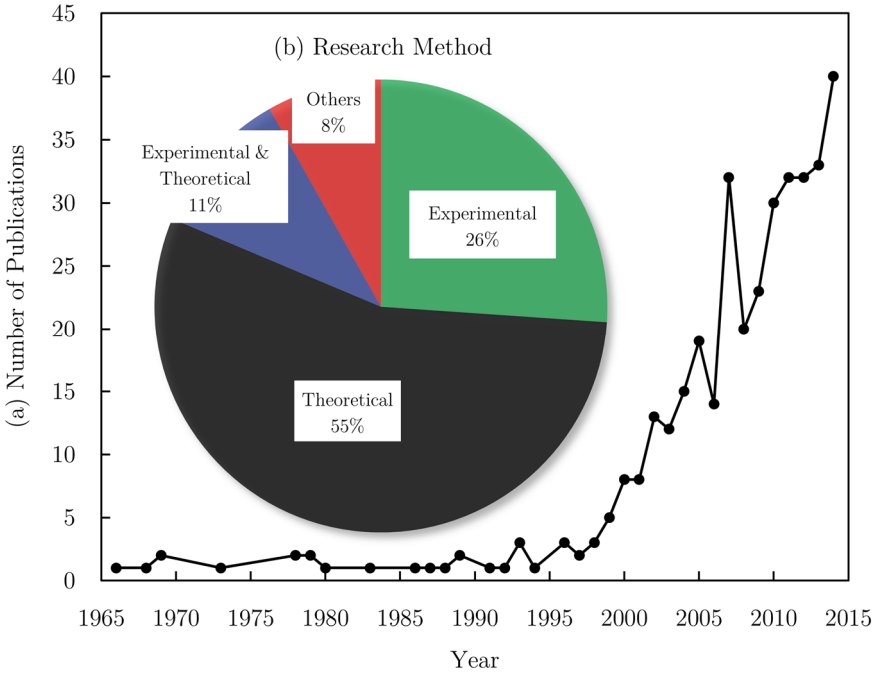

Figure 2.1 Worldwide research effort on surface texturing over the last 50 years: (a) number of publications per year and (b) research method.

[19-23] for journal bearings, in [12, 24, 25] for mechanical seals, in [26, 27] for thrust bearings and in [28, 29] for cylinder liners.

The development of more efficient algorithms and solution techniques combined with the increase in computational power available have led to much more sophisticated models, especially over the last 10 years. Papadopoulos *et al.* [30], for example, used commercial computational fluid dynamics (CFD) software to solve the Navier-Stokes and energy equations to study the effect of rectangular dimples on the performance of partially textured sector-pad thrust bearings. Kango *et al.* [31] investigated textured journal bearings using a generalized Reynolds equation. Their model is capable of describing viscous heat dissipation and non-Newtonian lubricant behaviour and incorporates a mass-conserving cavitation algorithm based on the Jakobsson-Floberg-Olsson (JFO) boundary conditions. Han *et al.* [32] used a modified averaged Reynolds equation to study the effect of misalignment and shaft axial motion on the performance of journal bearings with rough surfaces under transient and mixed lubrication conditions.

Less than a third of all publications were based on experimental approaches only, of which the most commonly used are pin-on-disc [33-38] and ball-on-disc [39] setups as well as reciprocating sliding tests [40]. Some studies, however, were conducted on real components. Examples include journal bearings [41, 42], thrust bearings [43-45] and seals [46-48]. About 11%, corresponding to 41 references in the author's survey, describe both, experimental and theoretical investigations. The remaining 8% of publications analysed are, for example, reviews [13, 49-54], publications on manufacturing techniques [55-57] and classification/characterization of textured

surfaces [58]. Further results of the survey are given in respective sections.

A large number of researchers have contributed to today's knowledge around surface texturing, however, the still very limited number of successful industrial applications emphasizes the difficulties and challenges that are still encountered in this field. The following sections are thus intended to give the reader a brief overview of the key findings, common conclusions and some guidelines on texture design given in literature so far.

2.1.2 Definition of surface texturing

Surface texturing is the intentional introduction of well-defined surface features (discrete dimples, grooves) on surfaces. An example of a partially textured parallel thrust pad bearing can be seen in Figure 2.2. In contrast to textures, surface roughness is generally considered random and not well characterized. However, some of the functions of textures described below can also be related to rough surfaces. For example, the valley between two adjacent asperities can be interpreted as a dimple.

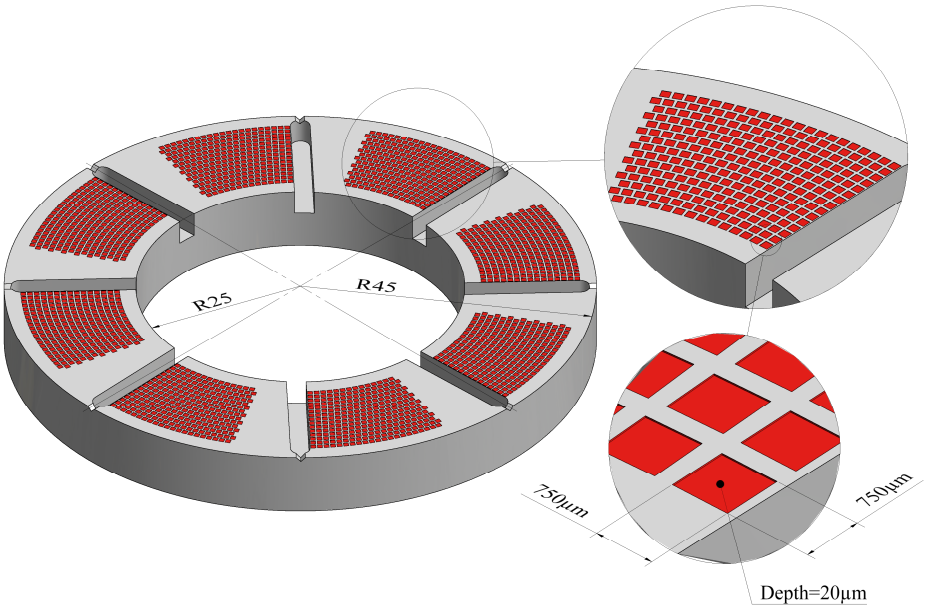

Figure 2.2 Partially textured parallel thrust pad bearing with rectangular dimples (adapted from [59]).

2.1.3 Functions of surface textures

Surface textures may act as lubricant reservoirs [4, 60], providing lubricant to the contact in cases of starved lubrication, and entrap wear debris [61-63], minimizing third-body abrasion. Although the aforementioned effects are often described in

literature, consistent results do not exist and further research in this direction is needed. A textured surface also has an overall lower contact area, which can lead to a reduction of stiction [64]. The aforementioned mechanisms can reduce wear and thus increase durability. The most dominant effect, however, as well as the only one captured by theoretical models, is the creation of an additional hydrodynamic lift that can lead to a certain increase in load carrying capacity of the contact in cases of mixed and hydrodynamic lubrication. This can also lead to an expansion of the range of hydrodynamic lubrication [65]. Although this phenomenon of load support is not yet fully understood, some commonly accepted explanations exist.

One of the earliest explanations was the occurrence of local cavitation [4, 13, 24, 66], which can lead to an asymmetric pressure distribution over a single texture, as negative pressures caused the divergent part of a texture are limited by the lubricant's cavitation pressure (Figure 2.3 (a) and (b)).

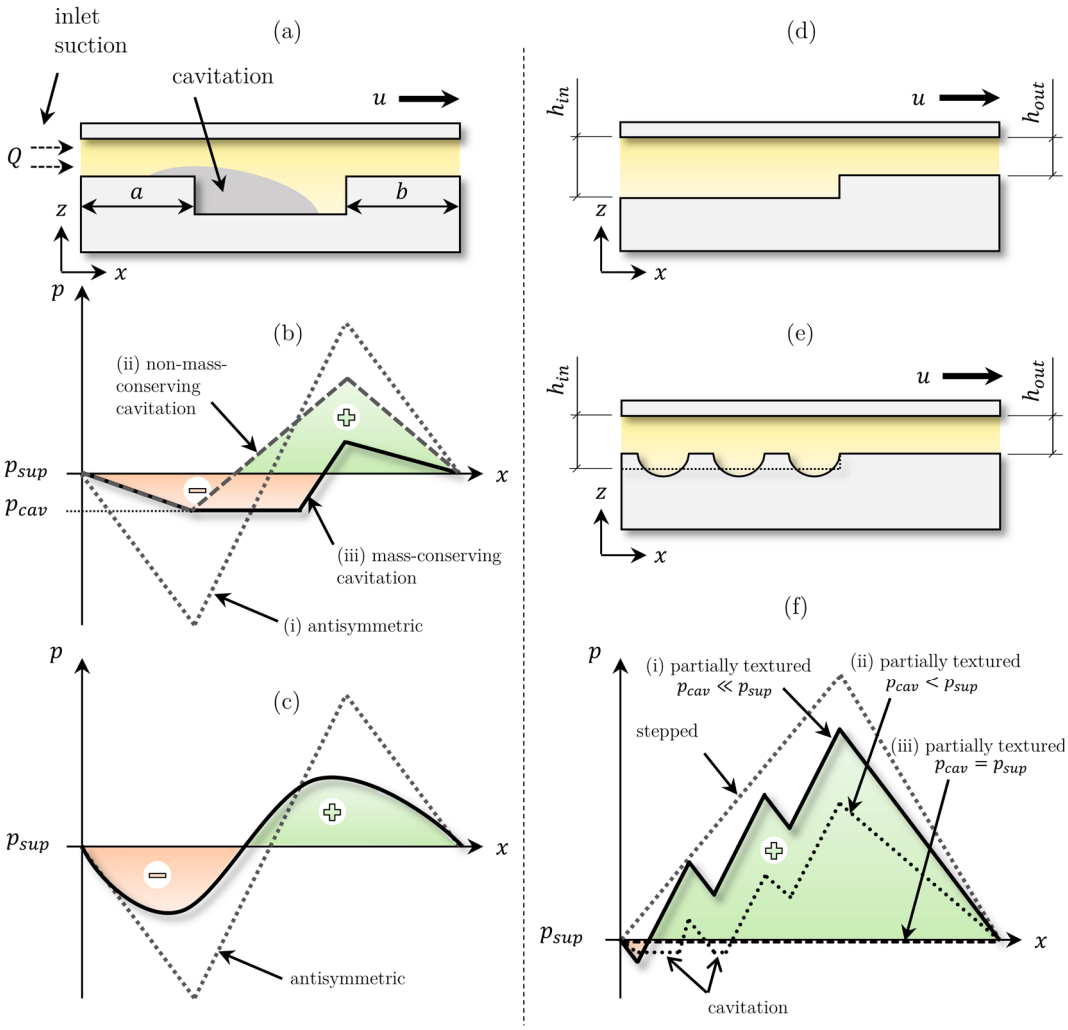

Figure 2.3 (a) Single texture cell, (b) typical pressure distribution over a single texture with cavitation, (c) typical pressure distribution over a single texture with inertia effects, (d) stepped slider, (e) partially textured slider and (f) typical pressure distributions over a stepped and partially textured slider.

The occurrence of cavitation inside individual dimples was also shown experimentally by Qiu and Khonsari [45, 67] and Zhang and Meng [68], using high speed cameras. Figure 2.3 (b) illustrates typical pressure distributions over a single, cell-centred texture for three different cases:

- Cavitation does not occur ($p_{cav} \ll p_{sup}$).
- Predicted by a non-mass-conserving cavitation algorithm for $p_{cav} < p_{sup}$.
- Predicted by a mass-conserving cavitation algorithm for $p_{cav} < p_{sup}$.

Note, however, that load is only generated in certain cases, as the positive pressures are also influenced. In some cases the load support may even become negative, depending on the shape of the asymmetric pressure distribution. Additionally, lift can only be generated when the cavitation pressure is inferior to the supply pressure, as this will provide the necessary pressure gradient to ensure a sufficient lubricant supply (*inlet suction* [69, 70], Figure 2.3 (a)). If cavitation and supply pressure are equal this pressure gradient does not occur, leading to starvation in the dimple, hence, no pressure can build up. If the supply pressure is much higher than the cavitation pressure, cavitation will not occur at all. In this case the pressure distribution over a single texture is antisymmetric and no lift can be generated either.

The promising results concerning cell centred dimples published in early papers (e.g. [26]) were caused by the implementation of non-mass-conserving cavitation boundary conditions. The pressure distribution over a single cell-centred dimple obtained with a non-mass-conserving cavitation algorithm falsely predicts a high load support as compared to the solution of the same problem with a mass-conserving treatment of cavitation, as first discussed by Ausas *et al.* [16] in 2007 (Figure 2.3 (b)). Another way to obtain load carrying capacity is to shift the texture towards the inlet, i.e. $a < b$ in Figure 2.3 (a). This will always (even if cavitation does not occur at all) lead to a load carrying capacity as long as $p_{cav} < p_{sup}$. However, this configuration should be interpreted as *partial texturing*, where lift is generated in a more traditional geometrical way, as discussed below.

Ultimately, today's understanding is that, despite the fact that local cavitation effects obviously have a significant influence on the pressure distribution and thus load capacity, they can only in certain cases lead to additional load support in individual, cell-centred textures, i.e. fully textured contacts. The crucial factor here is the p_{cav}/p_{sup} ratio. Tønder [71, 72] suggested that the introduction of roughness at the inlet of a parallel sliding bearing provides a step-like configuration similar to a Rayleigh step bearing. It was also found that more lubricant is available in the pressure build-up zone as the roughness at the inlet could prevent leakage.

Another explanation for a *disturbed* pressure distribution over a single texture and thus in certain cases load carrying capacity are inertia-related effects (Figure 2.3 (c)),

which were first studied by Arghir *et al.* [73]. As simplified models based on the Reynolds equation or Stokes equations do not consider inertia effects, they solved the full Navier-Stokes equations for different macro-roughness cells and showed that inertia effects could provide a load carrying capacity for flows with higher Reynolds numbers. Note, however, that the considered dimple geometries had very large aspect ratios (λ) that are quite different from the ones typically studied in lubrication theory, leading to pronounced inertia effects. Subsequently, Sahlin *et al.* [74] further investigated inertia effects in single texture configurations using CFD and reported that the effects of inertia were the dominant mechanism for pressure build-up. In their study a maximum load carrying capacity could be achieved with a dimple depth close to the depth at which a vortex, i.e. flow recirculation within the dimple, appears. Completely contrary results were presented by Dobrica and Fillon in [75]. They studied the validity of the Reynolds equation for two-dimensional textured parallel slider configurations and concluded that inertia in general has a negative effect on the load carrying capacity. De Kraker *et al.* [76] stressed that inertia can cause an increase or a reduction of the load carrying capacity, depending on the local flow conditions. More CFD investigations were carried out by Cupillard and co-workers for textured sliders [77-79] and journal bearings [80, 81]. In [79] they also pointed out that inertia does not necessarily have positive effects on the load carrying capacity. In fact, positive influences were only observed up to a critical texture depth value, similar to the results by Sahlin *et al.* [74].

Another effect was described by Fowell *et al.* [70] and Olver *et al.* [69], as *inlet suction*, as mentioned above. They argued that the sub-ambient pressure caused by the diverging part of a single texture has the ability to *suck* more lubricant into the contact zone, hence increasing maximum pressure and load carrying capacity.

Yagi and Sugimura [82] suggested a mechanism called *balancing wedge action*. They studied the equilibrium of moment on a centrally pivoted pad bearing and concluded that the incorporation of a texture could disturb this balance, rotating the pad and thus increasing the convergence ratio. Hence, pressure and load carrying capacity could be generated by the resulting wedge action.

Etsion's group found that partial texturing can improve the tribological performance by a so-called *collective dimple effect*, similar to the concept proposed by Tønder [71, 72]. They showed that the textured inlet has a larger average film thickness than the non-textured outlet and therefore a partially textured contact behaves similarly to a Rayleigh step bearing (Figure 2.3 (d) – (f)). Note that the concept of partial texturing is a rather conventional way to create load support, as the hydrodynamic effects are caused solely by geometrically approximating a step or pocket. However, partial texturing might still have other advantages as compared to traditional stepped or pocketed contacts, e.g. act as lubricant reservoirs or trap wear debris. Figure 2.3 (f) shows typical pressure distributions over a stepped and partially textured slider. The

pressure distribution over a partially textured slider is illustrated for three cases:

- Cavitation does not occur ($p_{cav} \ll p_{sup}$).
- Cavitation occurs in the first two dimples ($p_{cav} < p_{sup}$).
- Cavitation occurs in all dimples ($p_{cav} = p_{sup}$).

As long as $p_{cav} < p_{sup}$, significant pressure can build up, leading to a certain load support similar but inferior to the one encountered in stepped or pocketed contacts, even if cavitation does not occur at all. Therefore, cavitation cannot and should not be named as the responsible load support mechanism. Etsion's group demonstrated the potential of partial texturing for mechanical seals [83], thrust bearings [26, 43], journal bearings [22] and piston rings [84-86]. Partial texturing is generally considered more efficient than full texturing and often the only way to reasonably improve the tribological contact performance.

It is noteworthy that the aforementioned load-support mechanisms are complex phenomena that may occur simultaneously. Moreover, the influence and magnitude of cavitation and inertia highly depend on the operating conditions and the type of contact. Hence, today's knowledge is that both phenomena may either improve or harm the overall contact performance, depending on the specific application.

2.2 Texture design

2.2.1 Texturing parameters

A slider bearing with circular/rectangular dimples is shown in Figure 2.4 to illustrate the parameters commonly used to describe textured contacts. However, the parameters can easily be related to other textured components (Figure 2.5, Figure 2.7 and Figure 2.8).

An individual texture can be characterized by its three-dimensional shape (base shape and internal structure/bottom profile), size (base dimensions and depth) and in case of an asymmetric texture its orientation with respect to the direction of sliding. Another parameter that arises is the texture aspect ratio, which is defined as $\lambda = h_{texture}/l$, with $h_{texture}$ and l being the texture's maximum depth and dimension in sliding direction respectively. In cases of circular textures l represents the texture's diameter. Although generally used in literature, this parameter does not capture the texture's base shape nor its internal structure.

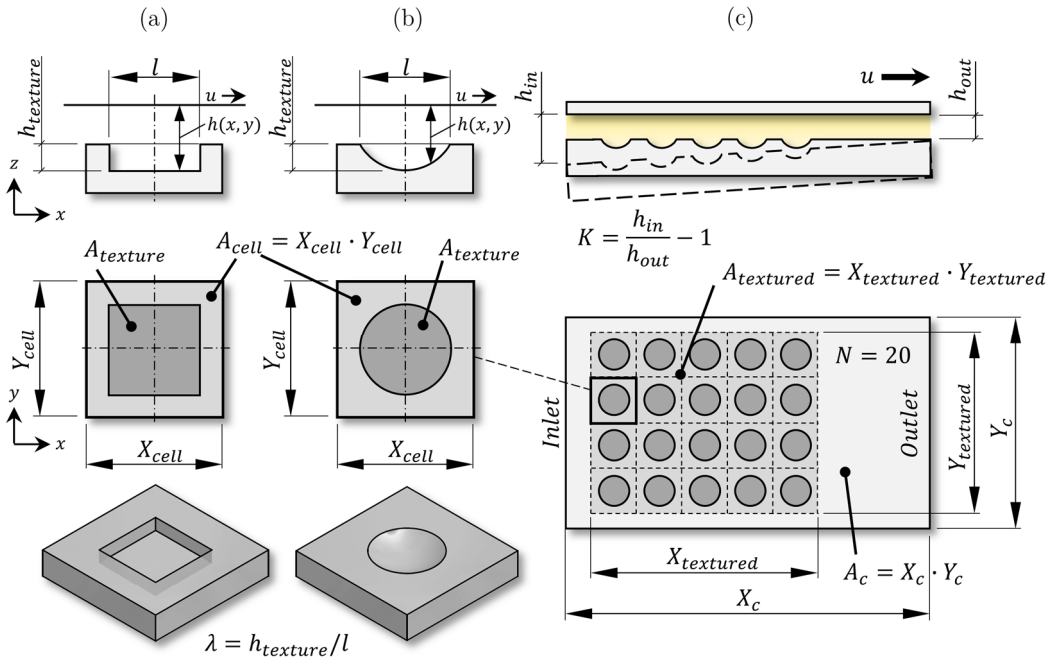

Figure 2.4 Texturing parameters for parallel/convergent slider bearings: (a) Cuboid dimple with texture cell, (b) Spherical dimple with texture cell and (c) parallel/convergent slider bearing.

On a global scale a textured contact can be further described by its relative textured portion $B = A_{textured}/A_c = \alpha\beta$ and its relative texture extends in x and y direction, given as $\alpha = X_{textured}/X_c$ and $\beta = Y_{textured}/Y_c$ respectively. To allow a consistent use of these parameters in this work, the relative texture extends are defined as $\alpha = \theta_{textured}/\theta_c$ and $\beta = r_{textured}/r_c$ in circumferential and radial direction respectively, whenever polar coordinates are applied. The texture density ($\rho_{texture} = A_{texture}/A_{cell}$ for uniformly distributed textures or in general $\rho_{texture} = NA_{texture}/A_{textured}$, where N is the total number of textures) and the relative dimple depth $S = h_{texture}/h_{min}$ complete the parameters. Please note that in some literature a height ratio $H_r = (h_{texture} + h_{min})/h_{min} = S + 1$ rather than a relative dimple depth is used.

Although understandably all these parameters affect the overall contact performance, it is well accepted that dimple aspect ratio, texture density, relative dimple depth and for partial texturing, i.e. $A_{textured} \neq A_c$, the relative texture extends are the ones having the most pronounced influence and are thus the most important design parameters for textured contacts. Therefore most studies have been contributed to finding optimal values for these parameters.

2.2.2 Key findings for parallel contacts

2.2.2.1 Seals and parallel rotating thrust bearings

For the application of texturing in seals or seal-like structures, such as parallel rotating thrust bearings, the relative texture extend in circumferential direction $\alpha = \theta_{textured}/\theta_c$ is meaningless, because these contacts are obviously always fully textured in this direction, thus $\alpha = 1$ (Figure 2.5). Partial texturing in radial direction, however, can lead to high performance improvements for seals, as will be shown below.

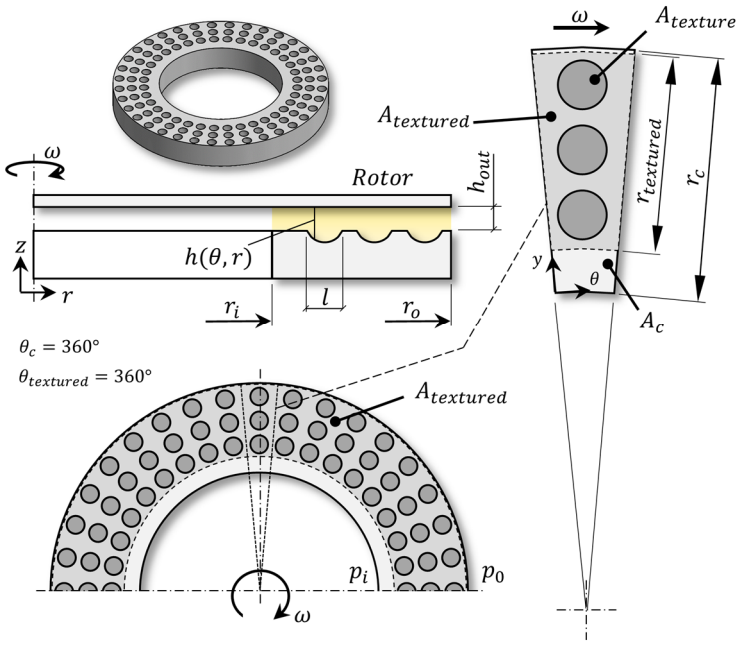

Figure 2.5 Texturing parameters for seals and parallel rotating thrust bearings.

The pioneering work on textured mechanical seals has been carried out by Etsion and co-workers. They conducted a series of theoretical parametric studies and experiments on face seals with dimples in the form of spherical caps ($5 \leq l \leq 200$ µm and $0 \leq \lambda \leq 0.5$) and found that textures can significantly improve seal performance and durability in terms of load carrying capacity, wear resistance, friction and face temperature [12, 24, 47, 83]. They recommended a texture density of 20% and stressed that the dimple depth over diameter ratio λ can be optimized for given operating conditions and that this is the most important parameter. In [83] a seal was partially textured on the high pressure side, reassembling a virtual step in radial direction. An optimal value for the relative texture extend in radial direction was given in the range of $0.55 \leq \beta \leq 0.65$ in terms of average pressure. The experimental comparison of a partially textured seal with a smooth one showed a significant reduction in friction torque.

A mechanical gas seal, partially textured with elliptical dimples, was numerically investigated by Bai *et al.* [87]. They reported an open force improvement of 20% and demonstrated the importance of dimple orientation with respect to the direction of sliding. Meng *et al.* [88] applied a finite element method (FEM) with a mass-conserving cavitation algorithm to numerically investigate the influence of full texturing on a seal's flow rate and load carrying capacity. In their study texturing could not always increase the seal's load capacity, however, dimples were shown to be a feasible method to control seal leakage.

Ma *et al.* [89] highlighted the complex relation between the optimum texture density and the operating conditions using a mass-conserving numerical approach based on the Reynolds equation. Wang *et al.* [90] performed a multi-objective optimization of texture shapes for mechanical face seals and recommended v-shaped dimples in terms of load capacity and leakage.

Brunetière and Tournerie [91] studied fully textured seals under mixed lubrication by solving the isothermal Reynolds equation together with a deterministic asperity contact model to incorporate roughness effects and a mass-conserving cavitation algorithm. In their investigation texturing was found to be incapable of generating any load carrying capacity whenever roughness effects of the untextured surface portions between textures were not considered. One the other hand, when roughness was accounted for, untextured and textured seals showed significantly better friction characteristics than smooth seals in both, mixed and hydrodynamic regime. These results stand in high contrast to previous findings for fully textured seals. The reason for this is the numerical treatment of cavitation: whereas many previous studies applied non-mass-conserving cavitation boundary conditions (Half-Sommerfeld or Reynolds) or did not consider cavitation at all, Brunetière and Tournerie used a mass-conserving approach based on the JFO boundary conditions, which correctly describes film rupture and reformation [92].

In fact, Ausas *et al.* [16] have shown that a non-mass-conserving treatment of cavitation highly overestimates the predicted load carrying capacity of dimpled surfaces and that therefore a mass-conserving implementation of cavitation is crucial in the field of surface texturing.

Following this new insight Qiu and Khonsari [67] further studied the effect of cavitation on fully textured rotating thrust bearings. In addition to experimentally observing local cavitation inside individual textures, they confirmed that a non-mass-conserving treatment of cavitation leads to a significant overestimation of load carrying capacity. It was concluded that for fully textured contacts load carrying capacity caused solely by cavitation is very limited. In a subsequent study by the same authors [45], a series of stainless steel rings (heat-treated 17-4 PH) were fully laser textured and experimentally evaluated. Samples with circular and elliptical dimples having different sizes ($200 \leq l \leq 2000$ µm), depths ($46 \leq h_{texture} \leq 60$ µm)

and densities ($15 \leq \rho_{texture} \leq 58.6\%$) were considered. It was experimentally observed that at low speeds no cavitation occurs in the dimples, at increasing speeds gaseous cavitation and at high speeds vapour cavitation. Thus, cavitation pressure and therefore ultimately load carrying capacity is highly affected by the operational speed. Unlike the untextured specimens, which only showed minor scratches, the textured samples showed significant surface damage after conducting the aforementioned experiments. However, their coefficient of friction (COF) was considerably lower during all tests performed. It was further found that for a given dimple depth over diameter ratio λ, a higher texture density leads to higher friction reduction and for a given density an optimal value for λ exists.

In a later study Qiu and Khonsari [93] applied an averaged Reynolds equation to parametrically study fully textured thrust bearings considering roughness effects. It was shown that surface roughness has a positive but limited influence on bearing performance. They also found that optimal values for λ and $\rho_{texture}$ exist and that the cavitation pressure is crucial, which agrees well with findings in [24], [94] and [45]. However, optimal texture parameters were found to highly depend on sliding speed and cavitation pressure.

Wang *et al.* [94] used reactive ion etching to produce circular dimples on SiC thrust bearings and in a series of experiments investigated the effect of different dimple sizes, depths and densities ($50 \leq l \leq 650$ µm, $2 \leq h_{texture} \leq 16.6$ µm and $0 \leq \rho_{texture} \leq 22.5\%$) on the load carrying capacity under water lubrication. All specimens in their study were fully textured. They illustrated the effect of texture density and depth over diameter ratio in a *load carrying capacity map* and stressed that both of these parameters can be optimized for given operating conditions. Optimal performance was achieved with the specimen having texturing parameters of $l = 350$ µm, $h_{texture} = 3.2$ µm and $\rho_{texture} = 5\%$. In a following study by the same group [95], the authors conducted further experiments with water lubricated SiC bearings having no textures, single-sized textures and mixed-sized textures. Interestingly, the rings having both, small and large dimples, showed the best performance, increasing load carrying capacity threefold when compared to the untextured specimen.

Zhang *et al.* [38] conducted pin-on-disc experiments with Babbitt alloy discs under mixed lubrication having circular dimples ($500 \leq l \leq 950$ µm, $h_{texture} = 10$ µm and $8.6 \leq \rho_{texture} \leq 13.9\%$) and stated that the lowest texture density studied (8.6%) gave the highest friction reduction.

In a paper by Wang *et al.* [96], the authors reviewed published studies on the optimal texture density for fully textured contacts. They stressed that optimal texture densities stated in literature are usually much higher when predicted by theoretical methods than those obtained by experiments, as material properties are not accounted for. The authors recommended that texture densities should be in the

range of $5\% \leq \rho_{texture} \leq 13\%$ for oil lubricated metal components. Furthermore, a texture density exceeding 20% should be avoided to limit stress concentration effects.

Sharma and Yadav [97] showed numerically that partial texturing of thrust bearings is capable of reducing the frictional power loss by up to 20%.

Another recent numerical study was conducted by Shi *et al.* [98] on gas seals having different texture and groove patterns. It was concluded that both, grooves and discrete dimples are capable of enhancing seal load carrying capacity, especially for small clearances. Optimal texturing parameters were shown to depend on the chosen texture geometry.

The key findings for textured seals and seal-like contacts, such as parallel rotating thrust bearings, can be summarized as follows:

- Full texturing may improve performance in terms of friction and load carrying capacity under certain conditions, however, reported performance improvements are usually very limited. Nevertheless, full texturing can be a feasible method to control seal leakage.
- Optimal values for λ and $\rho_{texture}$ for full texturing exist, but highly depend on operating conditions. Optimal densities given in literature are quite low and in a range between 5 and 20%.
- Roughness seems to have a positive but limited influence on the performance.
- A mass-conserving treatment of cavitation is crucial. Moreover, the ratio of cavitation over supply pressure (p_{cav}/p_{sup}) is an essential performance parameter.
- Partial texturing of seals in radial direction can lead to significant performance improvements by reassembling a virtual step. Optimal values for texture density, relative texture depth, texture aspect ratio and relative texture extend may be the ones most closely approximating an optimal step, as this seems to be the case for parallel slider bearings and parallel thrust pad bearings. However, studies in this direction are limited.

2.2.2.2 Parallel slider bearings and parallel thrust pad bearings

Parallel slider bearings and parallel thrust pad bearings are shown in Figure 2.4 and Figure 2.7 respectively. Especially for this type of contacts, texturing – in particular partial texturing – has shown to be highly beneficial and a reasonable way to improve contact performance.

One of the first studies on textured parallel slider bearings was conducted by Brizmer

et al. [26] in 2003. They numerically investigated bearing performance applying the two-dimensional Reynolds equation and found that whereas full texturing cannot provide a satisfying load support, partially textured contacts are capable of generating significant load carrying capacities. Parameters mostly affecting load capacity were found to be texture density, relative texture depth, relative texture extend and the bearing width to length ratio Y_c/X_c. Best performance enhancement was achieved with a relative texture extend in x direction of 65%, a maximum possible texture density and a relative dimple depth of 1.25. The relative texture extend in y direction was not investigated and kept constant at $\beta = 100\%$. Their findings were experimentally validated in a later study by the same group [43] by comparing non-textured and partially textured water lubricated parallel thrust pad bearings. The partial texturing resulted in a threefold increase in clearance and a friction reduction of 50%.

Following this study Rahmani and co-workers [99] attempted to find optimal texturing parameters with an analytical approach, applying the one-dimensional Reynolds equation for infinitely long parallel sliders having textures with flat bottom profiles. They stated optimal values for the relative texture depth in the range between 0.5 and 0.57 in terms of load capacity and friction force. It was further shown that a minimum number of textures results in best performance, which implicitly stands for a maximum texture density. In a more generalized optimization study by the same group [100], infinitely long parallel sliders with different texture bottom shapes were analysed. Three different bottom profiles were considered: R, T2 and T1 (Figure 2.9). The optimal value for the relative texture depth was found to be $S = 0.58$ for the flat textures (R) in terms of both, load carrying capacity and COF. For the other profiles, T2 and T1, values were found to be $S = 1.17$ and $S = 1.2$ for maximum load carrying capacity and minimum COF respectively. In general, the performance of the flat textures (R) was reported to be superior. In a more recent study [101], they confirmed previous findings.

Another analytical investigation on infinitely long parallel sliders was performed by Pascovici *et al.* [102]. They found optimal values for S and α to be in the ranges of $0.5 - 0.9$ and $50 - 62\%$ respectively, agreeing well with previous findings.

One of the first parametric numerical investigations on finite sliders was conducted by Dobrica *et al.* [14] in 2010, applying a two-dimensional mass-conserving form of the Reynolds equation. They demonstrated that fully textured parallel sliders can only generate load carrying capacities when the inlet is textured, i.e. textures are shifted towards the inlet in each cell, as shown for a partially textured contact in Figure 2.6, but the effect was minimal.

Note that texturing the inlet results in a larger inlet film thickness, which also means a higher oil supply rate is necessary. The question whether the term *full texturing* is still appropriate when the inlet is textured is debatable. On the other hand, partially

textured parallel sliders were shown to be capable of creating substantial hydrodynamic lift, especially when the supply pressure is higher than the cavitation pressure ($p_{sup} > p_{cav}$) and textures are placed at the inlet. Furthermore, it was found that the texture density cannot be optimized for partially textured sliders, because load carrying capacity always increases with density, resulting in an optimum density of 100%. However, a density of 100% actually results in a stepped slider and the term *texture* becomes questionable. In practise, that means that the optimal texture density is the maximum achievable, limited by the fact that high densities may lead to stress concentration, weakening the surface.

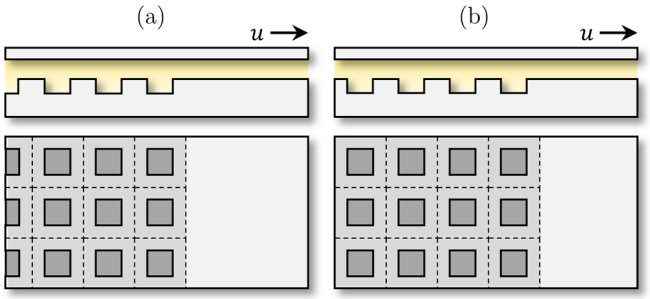

Figure 2.6 (a) Partial texturing with shifted dimples and (b) Partial texturing with cell centred dimples.

Guzek *et al.* published unified computational approaches to optimize texturing parameters for both, two-dimensional [103] and three-dimensional [104] parallel slider bearings. Their results agreed well with findings of previous exhaustive analytical and numerical studies. For example, they also showed that increasing the texture density always leads to better performance and that shifting the textures towards the inlet is highly beneficial. Therefore the value for the texture density was set to 80% in their study. Optimal values for the relative texture depth were found to be $0.68 \leq S \leq 0.9$ for rectangular dimples and $0.97 \leq S \leq 1.21$ for elliptical dimples in terms of load carrying capacity. In terms of friction reduction optimal values were $0.76 \leq S \leq 0.81$ and $1.19 \leq S \leq 1.28$ for rectangular and elliptical dimples respectively. The higher values obtained for elliptical dimples were explained by the fact that, as the volume of cuboid dimples is higher than that of ellipsoidal ones, cuboid dimples closer approximate a stepped bearing. This also confirms the results obtained by Rahmani [100]. The relative texture extend in x direction was recommended to be 60% and in the range of $60 - 70\%$ for load carrying capacity enhancement and friction reduction respectively, for both shapes.

Very recently Gherca *et al.* [105] published another numerical parametric study on three-dimensional textured parallel slider bearings. Whereas most results were quite similar to studies conducted by other researchers, they obtained much smaller optimal values for the relative texture extend in x direction ($20 \leq \alpha \leq 40\%$ and $\beta = 100\%$). They also ran some simulations in transient flow conditions, i.e. the moving surface was textured rather than the stationary one. Yet, the large computational

power required limited the investigations to only a few geometric configurations. The results showed that texturing the moving surface instead of the stationary one may lead to a certain pressure build-up at the inlet, due to squeeze effects. However, texturing only the stationary surface was shown to be much more efficient. Interestingly, when both surfaces were textured, an additional performance improvement was obtained.

Malik and Kakoty [106] presented another parametric study on textured parallel sliders, however, their results are questionable as they used a non-mass-conserving cavitation algorithm. They concluded that for slider ratios of $Y_c/X_c = 2$ full texturing is preferable and for smaller ratios partial texturing is preferable. Marian *et al.* [107] performed a thermo-hydrodynamic (THD) analysis of parallel thrust pad bearings with pads having rectangular dimples ($h_{texture} = 9$ µm, $\lambda = 0.045$ and $\rho_{texture} = 25\%$) and found optimal relative texture extends of $\alpha = 50\%$ and $90\% \leq \beta \leq 100\%$ in terms of load carrying capacity maximization. These values are comparable to the ones obtained by other researchers.

A partially textured parallel eight-pad bearing (cuboid dimples, $l = 750$ µm, $h_{texture} = 20$ µm, $\alpha = 64\%$, $\beta = 75\%$ and $\rho_{texture} = 56\%$) was investigated by Charitopoulos *et al.* [108], solving the incompressible Navier-Stokes equations and considering thermal effects as well as elastic deformation. They stressed that oil heating significantly decreases the load carrying capacity of textured pad bearings, however, this is also the case for untextured bearings. A comparison of the relative influence of oil heating on the load carrying capacity between untextured and textured bearings was not conducted. The same group also presented a CFD study to optimize automotive turbocharger thrust pad bearings [109]. They presented a pocketed design that was able to increase the minimum film thickness by 40%, while also decreasing the power loss by 12% in comparison to a reference design. The pocketed design was shown to be able to also decrease the maximum temperature by up to 16°C. In contrast to other research, a parametric study revealed that the optimum pocket depth should be about five times the value of film thickness.

Henry and co-workers [44] experimentally compared smooth parallel thrust pad bearings with partially textured ones having rectangular dimples ($h_{texture} = 20$ µm, $\lambda = 0.04$, $\alpha = 70\%$ and $\beta = 75\%$). At low loads texturing was able to reduce friction by up to 32% while at higher loads texturing was uninfluential or even detrimental. They also stated the importance of the position of the first row of textures relative to the pad inlet and that higher texture densities are preferable in terms of load carrying capacity, confirming previous findings by Dobrica *et al.* [14] and Guzek *et al.* [104]. In a later study [110], they experimentally investigated the performance of untextured parallel, tapered, pocketed and partially textured thrust pad bearings during start-up. It was found that the pocketed pads result in best performance, potentially reducing wear by minimizing the friction torque encountered during start-

up.

Fouflias *et al.* [111] applied CFD to study four different bearing designs: open pocket, closed pocket, tapered-land and partially textured with rectangular dimples. Their results revealed that the textured bearing ($h_{texture} = 20$ µm, $\lambda = 0.027$ and $\rho_{texture} = 56\%$) performs reasonable only at low and moderate rotational speeds. At high speeds its load carrying capacity is considerably lower compared to the other bearings, however, its friction torque is lowest in this case, because it shows the lowest values for minimum film thickness. The same group also published a numerical optimization study on a curved pocket thrust pad bearing [112]. The in optimized curved pocket design was able to reduce friction by 21% and increase load carrying capacity by 16% as compared to a bearing with rectangular pockets.

In a recent CFD study, Papadopoulos *et al.* [30] proposed optimal relative texture extends for partially textured pad bearings having rectangular dimples ($h_{texture} =$ 20 µm, $\lambda = 0.027$ and $\rho_{texture} = 56\%$). In their study highest load carrying capacity was obtained by texturing 2/3 and 3/4 of the pad length and width respectively. Exact values for relative texture extents were given as $\alpha = 62\%$ and $75 \leq \beta \leq 85\%$. Furthermore, a relative dimple depth close to 1 was recommended, agreeing very well with findings from other researchers.

The key findings for parallel sliders and parallel thrust pad bearings can be summarized as follows:

- Full texturing can have detrimental or mild beneficial effects on the bearing performance, depending on operating conditions and cavitation phenomena. Beneficial effects have only been reported for certain cases, e.g. when the inlet is textured, and are very limited.
- Partial texturing on the other hand is capable of generating significant load support and reducing friction. Texturing the inlet is an efficient way to further increase load carrying capacity, as the higher inlet film thickness ensures sufficient lubricant supply for the first portion on the slider.
- The key to obtain best slider/pad performance seems to be to as closely as possible approximate an optimal step bearing. Optimal values obtained by different researchers are summarized in Table 2.1. For the step-bearing listed in the table, the relative texture extend in x direction and the relative dimple depth stand for the relative inlet length and the relative step height ($(h_1 - h_0)/h_0$) respectively (Figure 2.3 (d)). The best approximation can be achieved with rectangular textures having a flat bottom profile and a maximum possible texture density. Note, however, that a too high density may lead to stress concentration and thus increased wear or failure. The relative dimple depth should be just under 1 for rectangular dimples and slightly higher for other shapes.

Table 2.1 Optimal texturing parameters given in selected literature for partially textured parallel sliders/pads.

Author	Ref.	Y_c/X_c	α	β	S	$\rho_{texture}$
Brizmer *et al.*	[26]	1	60%	-	1.25	max
Rahmani *et al.*	[100]	∞	54…57%	-	0.58	max
Pascovici *et al.*	[102]	∞	50…62%	-	0.5…0.9	max
Dobrica *et al.*	[14]	1	-	100%	-	max
Guzek *et al.*	[104]	1	60…70%	-	0.68…0.9	max
Gherca *et al.*	[105]	0.6	20…40%	100%	-	max
Marian *et al.*	[107]	≈ 1	50%	90…100%	1	-
Papadopoulos *et al.*	[30]	≈ 0.8	62%	75…85%	≈ 1	max
Lord Rayleigh	[113]	∞	72%	-	0.87	100%

- Studies are generally limited to unidirectional sliding conditions. More research needed regarding bidirectional conditions.
- Cavitation phenomena play an important role and influence contact performance. Particularly, an appropriate value of p_{cav} and the ratio of cavitation pressure over supply pressure is crucial [114]. Furthermore, cavitation should be taken into account in a mass-conserving way, when performing numerical simulations [16].
- Optimal texturing parameters are generally independent of speed and viscosity. However, changes in this values may result in the occurrence of cavitation, which can ultimately change optimal texturing parameters.

2.2.3 Key findings for non-parallel contacts

The more complex case of non-parallel applications, e.g. convergent sliding contacts or journal bearings, is less explored than the one of parallel contacts. In fact, the author's literature survey revealed that about twice as many studies focused on parallel contacts. In the following the key findings for convergent contacts as well as journal bearings are reviewed.

2.2.3.1 Convergent contacts

Convergent contacts, such as plane inclined slider bearings (Figure 2.4) or tapered-land/tilting pad thrust bearings (Figure 2.7), are characterized by an overall wedge effect that in many cases overshadows any potential benefits from texturing. However, at low convergence ratios, K, textures may improve performance slightly,

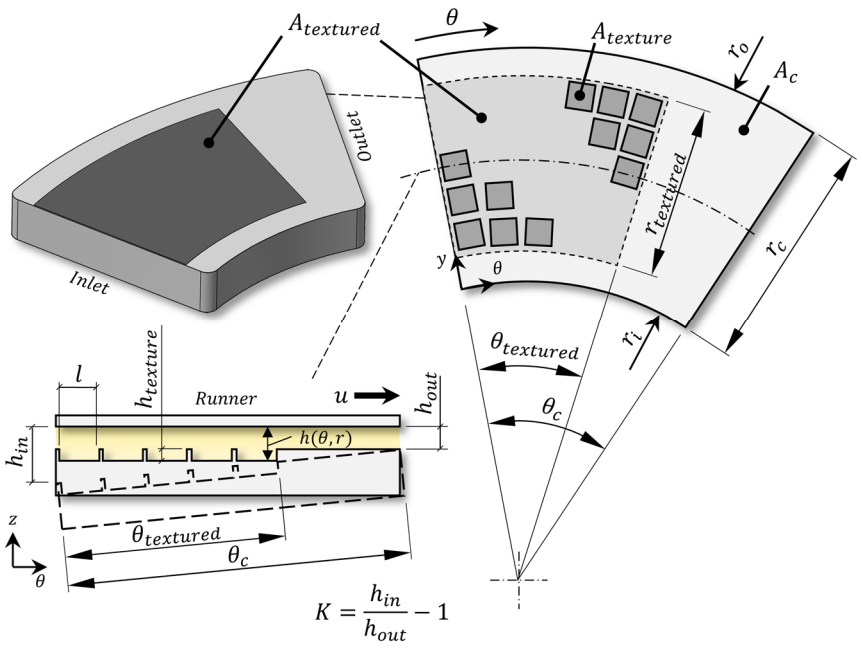

Figure 2.7 Texturing parameters for parallel and convergent thrust pad bearings.

if designed correctly.

Cupillard *et al.* [78] studied infinitely long slider bearings having convergence ratios of 0.1, 0.2, 1 and 2 and relative texture depths of 0.1, 0.33 and 0.75 by solving the Navier-Stokes equations with a finite volume method, without considering cavitation. For all these twelve cases considered, three dimples were placed close to the slider inlet. The results showed that with respect to load carrying capacity, texturing was more efficient at lower values of K. Moreover, it was found that optimal values for S highly depended on the convergence ratio. The authors further pointed out that flow recirculation may occur in deep dimples or close to the inlet at high convergence ratios, reducing load carrying capacity. The consideration of thermal effects in a later study [115] led to similar results.

The parametric investigation of Dobrica *et al.* [14] showed comparable results. It was shown that both, the gain of additional load carrying capacity and the reduction of friction decrease with an increase of convergence ratio, being best for $K = 0$, which is the parallel case. It was further demonstrated that full texturing of convergent sliders is detrimental and partial texturing can lead to a small performance improvement. They also conducted a parametric optimization study to find optimal values (S, α and β) for convergence ratios in the range of $0.066 \leq K \leq 4$. The texture density was set to $\rho_{texture} = 30\%$, as it was shown that increasing the density always leads to a better performance. This is also the case for partially textured parallel sliders, as discussed in the previous sections. The results revealed a high dependency of optimal values on the convergence ratio, except for the relative texture extend β, which remained 70% for a wide range of convergence ratios and reached a maximum

of 100% for $K = 0$. Optimal values for S and α were found to be in the ranges of $0.4 \leq S \leq 0.8$ and $0.4 \leq \alpha \leq 0.95$ respectively. The authors also proposed an additional performance enhancement by utilizing a trapezoidal shape for the textured region $A_{textured}$, similar to the concept of Aker's optimum finite Rayleigh step [113]. However, improvements were rather small.

Tønder [116, 117] investigated fully textured pivoted plane bearings, applying the averaged Reynolds equation proposed by Patir and Cheng [118] and concluded that under certain conditions full texturing may improve friction, damping or stiffness, but in general full texturing is inefficient. However, these conclusions are very limited, as cavitation was not taken into account and only full texturing was considered.

Recently, Papadopoulos *et al.* [119] performed an optimization study applying genetic algorithms coupled with CFD to study optimal texturing parameters for three-dimensional inclined slider bearings having grooves perpendicular to the direction of sliding. The previous findings (maximum texture density always leads to best performance and texturing efficiency decreases with an increase in convergence ratio) could be confirmed in their study. They also demonstrated that optimal values for S and α highly depend on the slider's width to length ratio Y_c/X_c and convergence ratio, further confirming the findings in [14, 78]. Equations providing optimal values of S and α for given Y_c/X_c and K were provided. Optimal partial texturing could improve load carrying capacity by up to 7.5% for low convergent sliders compared to the untextured configuration and pressure build-up was possible even for slightly divergent sliders. In a following study [120] the dynamic characteristics of optimal textured sliders were investigated. It was found that partially textured convergent sliders show improved stiffness but lower damping levels.

Fowell *et al.* [15] applied the Buckingham-PI theory to fully describe two-dimensional convergent slider bearings with just nine non-dimensional parameters. The importance and possible interactions of these parameters were then investigated in a parametric study. Their findings agree very well with those reported by other researchers and are not repeated here. However, their results revealed the complex interaction of different parameters. For example, it was observed that the sudden event of cavitation tends to disturb the otherwise continuous interaction between parameters, leading to complex but predictable relationships.

Aggarwal and Pandey [121] numerically investigated grooved fixed inclined thrust pad bearings having different bottom profiles. They stated that highest improvements are realizable at low convergence ratios and that the best performance is achieved with a flat bottom profile.

One of the only studies on the influence of texturing on the performance of tilting pad thrust bearings was published by Zouzoulas and Papadopoulos [18]. Discrete

dimples, circumferential grooves, radial grooves and a pocket were compared to a bearing with untreated pads using CFD while considering thermal effects in the fluid domain and the solid domains. All texture patterns had a constant depth of $h_{texture} = 30$ µm. Almost no impact on the bearing performance was caused by applying textures in form of radial grooves. Although a slight decrease in maximum fluid temperature was achieved, minimum film thickness was reduced and friction torque increased for most operating conditions. The pad having a texture pattern with discrete dimples performed slightly better, increasing film thickness by up to 6%. Friction torque was moderately increased and maximum fluid temperature a bit reduced, however, the impact was minimal. Both, the pad having a pocket and the pad with textures in form of circumferential grooves had similar impact and could significantly enhance bearing performance. Best improvements were achieved for the pocketed bearing. In this case minimum film thickness could be increased by 24% and friction torque reduced by 12%. However, this highly beneficial impacts were only obtained at certain operating conditions. The impact and effectiveness of texturing was shown to be highly dependent on load and speed.

The following summarizes the key findings for convergent contacts:

- At convergence ratios close to 0, the summary given above for parallel sliders holds true.
- Full texturing of convergent contacts is detrimental and partial texturing can lead to mild performance improvements, however, only at low convergence ratios ($K < 1$). At larger convergence ratios the influence of texturing diminishes completely.
- Optimal texturing parameters (α, β and S) highly depend on the convergence ratio and the slider's/pad's width to length ratio. Best performance is always achieved with a maximum possible texture density, i.e. the best configuration is actually a stepped/pocketed slider, as is the case for parallel contacts. As optimal values vary with K, textures designed for low convergence ratios may cause a performance degradation when used at high convergent ratios [14, 15].
- Generally, cavitation effects are important, causing sudden changes on the performance and optimal texturing parameters. At higher values of K cavitation does not occur or is only present at small portions of the contact area, as the overall wedge effect builds up sufficient pressure to prevent pressures below p_{cav}, as also shown by Brajdic-Mitidieri *et al.* [122].

2.2.3.2 Journal bearings

As the film thickness of a journal bearing in circumferential direction represents a converging-diverging gap (Figure 2.8), this application is probably the most challenging scenario in terms of surface texturing. The aforementioned may be responsible for the still limited number of publications on textured journal bearings. Another limitation is the large discretization effort encountered in the study of textured journal bearings. For example, in order to achieve an overall resolution of 5 µm for a journal bearing with a diameter of 100 mm and a width of 40 mm, one would need a mesh containing about 500 million points.

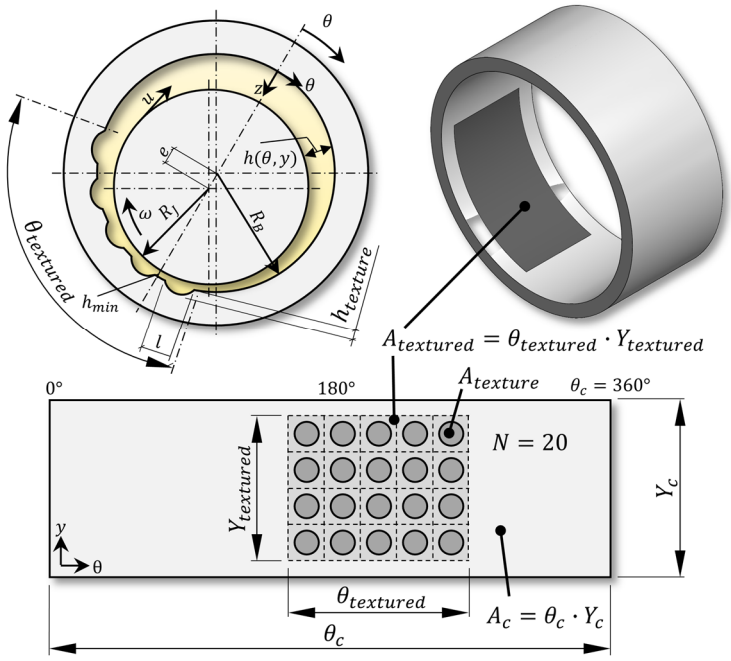

Figure 2.8 Texturing parameters for journal bearings.

One of the first studies on textured journal bearings was conducted by Tala-Ighil *et al.* [19] in 2007. They solved the two-dimensional Reynolds equation with a finite difference method, applying the Reynolds cavitation boundary condition to investigate the effect of spherical dimples on the bearing performance. It was shown that, depending on the dimple parameters (size, depth, density and distribution), texturing can have an either positive or negative influence on the main bearing characteristics (film thickness, load carrying capacity, axial flow rate and frictional torque) and thus, a proper texture design is crucial. In a later study by the same group [20], a journal bearing with cylindrical dimples ($h_{texture} = 15$ µm, $l = 2$ mm and $\lambda = 0.0075$) was further investigated by means of numerical simulation, focusing on the effect of texture distribution. For this purpose 25 cases with the same textures but different texture distributions were simulated, including full texturing, partial texturing and a partial texturing of multiple zones of the bearing surface. They concluded that full texturing is ineffective, leading to a degradation in performance

and that partial texturing including the texturing of multiple zones can be beneficial. Best performance was achieved when the area under the declining part of the pressure field was textured, although the improvements were minimal.

Ausas *et al.* [16] numerically investigated fully textured journal bearings with rectangular dimples with different texture depths. They reported a slight increase in minimum film thickness and friction torque due to texturing. It was furthermore shown that in the study of journal bearings, a mass-conserving treatment of cavitation is crucial, as the Reynolds cavitation model largely underestimates the cavitated area.

Cupillard *et al.* [80, 81] simulated partially textured journal bearings using CFD and argued that deep textures ($S > 1$) should be located in the maximum pressure zone and shallow textures ($S \leq 1$) in the maximum film zone for high and low eccentricity ratios respectively. They also observed a high dependence of optimal texturing values on the operating conditions and that the effect of texturing seems to be significantly higher at low eccentricities.

Brizmer and Kligerman [22] performed a non-dimensional parametric study on textured journal bearings. Their results showed that full texturing is inefficient and partial texturing can improve load capacity and attitude angle, however, reasonable improvement could only be observed at low eccentricity ratios, confirming the results obtained by Cupillard *et al.* [80, 81]. Their results also showed a high dependency of optimal dimple depth and relative texture extend in circumferential direction on the bearing's eccentricity ratio.

Recently, Kango *et al.* [31, 123] applied the Reynolds equation together with a mass-conserving cavitation algorithm to study journal bearings having spherical dimples or longitudinal/ transversal grooves. Temperature effects were considered by solving the energy equation simultaneously. It was found that partially texturing the convergent part of the bearing increases load carrying capacity compared to smooth and fully textured bearings. They further observed that texturing reduces the average temperature and that the performance improvement is more dominant at low eccentricity ratios, further confirming previous research in [22, 80, 81].

Lu and Khonsari [42] experimentally investigated fully and partially textured journal bearings with different dimple shapes and sizes ranging from $l = 2$ to 4 mm. Under mixed lubrication the fully textured bearing showed better performance than the partially textured one. They further stated that a careful design of texture size, shape and depth is crucial. Another experimental study was conducted by Dadouche *et al.* [41]. Four journal bearings were textured with equal spherical dimples ($h_{texture} =$ 60 µm and $l = 1$ mm) but different texture densities and compared to an untextured bearing. The results revealed that texturing affects the dynamic bearing coefficients (stiffness and damping) and results in a slightly higher bearing temperature (increase

of 6 to 8°C).

Lin *et al.* [124] utilized a fluid structure interaction (FSI) approach to study textured journal bearings under transient conditions. They concluded that texturing is capable of affecting the eccentricity ratio and stated that textures should be placed in the pressure build-up area for positive effects.

Matele and Pandey [125] studied the dynamic characteristics of fully and partially textured journal bearings considering different dimple geometries (circular and rectangular) and texture locations. It was found that the angular location of the textures is of key importance with regards to stability and that textured bearings provide better stability than conventional bearings. Gu *et al.* [126] presented a mixed lubrication model and investigated axially grooved journal bearings. They concluded that for friction reduction the grooves should be placed at the inlet of the pressurized zone at low eccentricity ratios and downstream of the pressurized zone for high eccentricity ratios.

Gui and Meng [127] numerically analysed the performance of journal bearings having spherical dimples and bumps considering elastic deformation. They stated that whereas dimples should be placed at the pressure build up portion of the bearing, bumps should be placed at the pressure falling portion. Dimples were recommended for high load carrying capacities and bumps for high friction reduction effects. Meng *et al.* [128] also investigated the effect of compound dimples consisting of a cuboid upper part and additional spherical cap shape dimple using a FSI method. Interestingly, the compound dimples were able to provide superior performance in terms of load carrying capacity and friction torque as compared to normal cuboid dimples.

Yamada *et al.* [129] conducted a numerical and experimental study on the static characteristics of fully textured journal bearings with rectangular dimples. They concluded that the load carrying capacity was decreased through texturing. In a later study [130] they also analysed the dynamic characteristics of textured journal bearings and concluded that although stiffness is reduced by texturing the running stability is improved.

Zhang *et al.* [131] used the Reynolds equation and genetic algorithms to optimize the shape of the textured area of partially textured journal bearings having circular dimples where the converging part of the film was textured. A semi-elliptical shape of the textured area was found to be best in terms of friction and load capacity.

The findings with regards to journal bearings are summarized below:

- Full texturing is generally reported to be detrimental, however, conflicting results have been obtained.
- Partial texturing can have beneficial effects, however, performance

improvements have not been spectacular. The efficiency of texturing decreases with an increase in eccentricity ratio. This is similar to the case of convergent contacts, where a high convergence ratio overshadows the effects of texturing.

- In numerical simulations, cavitation effects should be treated in a mass-conserving way to avoid errors in the predicted performance.
- Optimal texturing parameters highly depend on operating conditions and eccentricity ratio. Furthermore, a poor texture design can have detrimental effects.
- The angular location of the textured area appears to be a key parameter, however, conflicting results regarding the location have been reported and more research in this direction is needed.

2.2.4 Texture shape and internal structure

The two most commonly investigated dimple shapes are circular dimples with a curved bottom profile (spherical caps, Figure 2.4 (b)) and rectangular dimples with a flat bottom profile (cuboids, Figure 2.4 (a)). However, today's manufacturing techniques, e.g. laser surface texturing (LST) as the most commonly used one, are capable of producing all kinds of complex three-dimensional texture shapes (up-to-date reviews on different manufacturing techniques are given in [55] and [57]). Textures with different bottom profiles and base shapes are shown in Figure 2.9 and Figure 2.10 respectively, for example. A number of publications were devoted to study the effect of different texture shapes and internal structures on the performance of textured contacts.

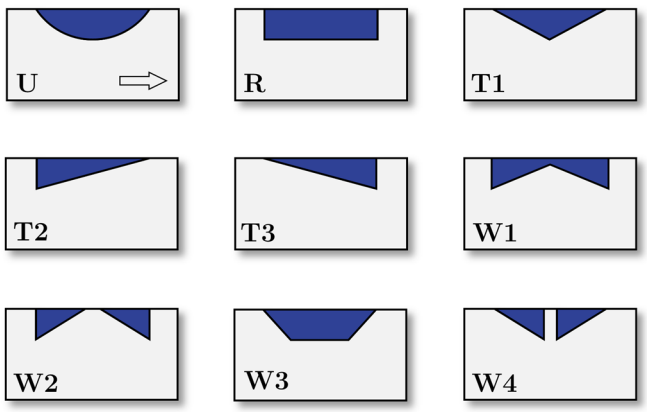

Figure 2.9 Textures with different bottom profiles (adapted from [132]).

Costa and Hutchings [40] experimentally investigated the influence of different geometries of surface textures on the hydrodynamic performance of sliding contacts.

They performed a number of reciprocating sliding tests between stationary cylinders and fully textured sample plates with either grooves, circular or chevron-like dimples at different orientations, depths, densities and aspect ratios. A clear impact of texturing on the film thickness was observed. It was found that an optimal density exists for texturing with circular dimples and that out of all textures investigated ($\lambda \approx 0.1$), the one having a density of 11% resulted in the highest film thickness. Such an optimum was not observed for textures in the form of grooves, however, tests were limited to a maximum density of 15%. The authors further stated that an optimal value for λ exists. In terms of texture orientation, chevrons pointing along the sliding direction were found to be most effective. This was explained by the restriction and direction of flow within a texture towards the high pressure side.

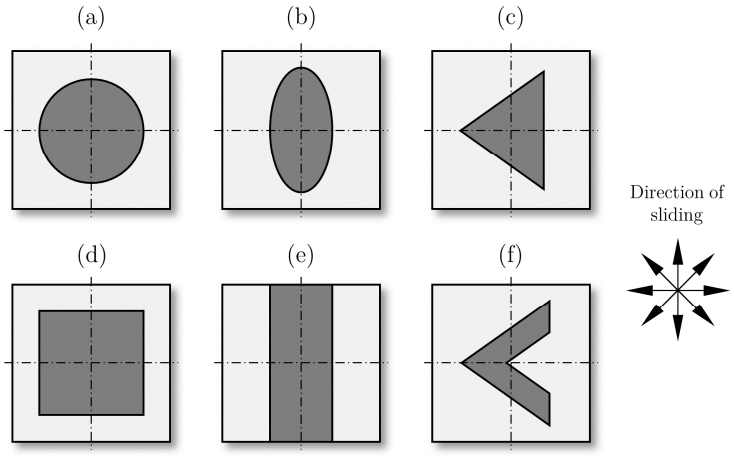

Figure 2.10 Selection of different texture base shapes: (a) circular, (b) elliptical, (c) triangular, (d) rectangular, (e) groove and (f) chevron-like.

Yu *et al.* [133] studied the effect of different dimple shapes (circular, triangular and elliptical) and orientations on the pressure distribution. They simulated single texture cells applying the Reynolds equation with a non-mass-conserving treatment of cavitation (Reynolds) and periodic boundary conditions and concluded that the shape and orientation of dimples have a significant influence on the load carrying capacity. The best results were obtained with elliptical dimples having the major axis perpendicular to the direction of sliding. In their study all geometries had the same texture area $A_{texture}$, texture density and texture depth, which limits their conclusions, as individual shapes should be optimized before comparing them with each other, as stated by Etsion in [134]. In a later study by the same group [135], reciprocating sliding tests were carried out to further investigate the effect of dimple shape on the pressure generation. Circular, rectangular and elliptical dimples with different depths and densities were analysed and compared. It was found that individual shapes can be optimized for best performance and that elliptical dimples with the major axis perpendicular to the direction of sliding always showed the highest friction reduction under different load and speed conditions.

Qiu *et al.* [136] used the compressible form of the Reynolds equation to simulate the

performance of gas-lubricated parallel slider bearings fully textured with six different dimple shapes (spherical, ellipsoidal, circular, elliptical, triangular and chevron-shaped). They optimized each shape individually before comparing them with each other and found that the ellipsoidal texture performed best in terms of load carrying capacity. They also stated that the base shape of the texture determines the optimal texture density whereas the optimal aspect ratio is defined by the dimple's internal structure. In a more recent paper [137], the authors also stressed that ellipsoidal dimples not only provide the minimum coefficient of friction, but also lead to highest bearing stiffness. Optimal texture density for this shape was found to be 35% and resulted in a 24.5% lower COF when compared to optimized circular textures. They further stressed that there exists an optimal geometry for every shape, however, this geometry is different depending on what the texture was optimized for: load carrying capacity maximization, friction reduction or stiffness maximization.

In a recent study, Shen and Khonsari [138] presented a numerical texture shape optimization approach based on the sequential quadratic programming (SQP) algorithm. They investigated fully textured parallel slider bearings and presented optimal dimple shapes for unidirectional sliding (chevron-like shapes with flat fronts) and bidirectional sliding (pairs of trapezoid-like shapes). They also compared the performance of these optimized shapes with textures having ordinary geometries (circle, ellipse, square, hexagon and diamond) and concluded that after optimization symmetric textures provide a higher load carrying capacity at a texture density of 30%, independently of operating conditions and cavitation pressure. However, at lower densities this superiority diminished. As they used a mass-conserving cavitation algorithm to simulate the regular shapes and a non-mass-conserving cavitation algorithm for the numerically optimized shapes, this comparison is questionable, as these different treatments of cavitation may lead to significantly different results [16].

The effect of different texture bottom profiles was explored in detail by Nanbu *et al.* [132] for concentrated conformal contacts applying an elasto-hydrodynamic lubrication (EHL) model (Figure 2.9). They found that textures with bottom profiles containing micro-wedges or micro-steps were able to further increase film thicknesses. Opposing results regarding the internal structure of textures were obtained by Shen and Khonsari in a recent paper [139]. They numerically and experimentally investigated the effect of circular dimples with different bottom profiles on the performance of parallel rotating discs and found that the flat profile yields the highest load carrying capacity.

Uddin and Liu [140] presented a numerical study based on the Reynolds equation on fully textured parallel sliding contacts. They compared circular, elliptical, triangular and chevron-like dimples and concluded that the triangular shaped dimples result in best friction performance. They also proposed a star-like shape that outperformed the other shapes, however, Reynolds boundary conditions were used to describe

cavitation, limiting their conclusions.

Using a genetic algorithm Zhang *et al.* [141] optimized the texture shape for parallel sliding contacts and concluded that bullet and fish shaped textures provide best performance. Another optimization was performed by Shen and Khonsari [142] for seal-like contacts. Highest load carrying capacities and lowest friction were achieved by chevron-like dimples. Wang *et al.* [143] numerically optimized the bottom profile for a parallel rotating thrust bearing using a genetic algorithm – sequential quadratic programming hybrid (GA-SQP) method.

The internal structure is also affected by the manufacturing technique itself. It is understandable that the real feature geometry may differ from the optimal and smooth shape usually considered in theoretical studies. Thus, in a study by Qiu and Raeymaekers [144] the effect of internal dimple-roughness was investigated. It was found that random Gaussian roughness inside a texture has a negligible impact on load carrying capacity, friction and flow rate. Charitopoulos *et al.* [145] further investigated manufacturing errors of grooves in thrust bearings using CFD. Deviations in texture shape, size and macroscopic errors, i.e. form errors of the contacting surfaces, were studied. It was found that in most cases these errors enhance load carrying capacity and improve friction characteristics.

Regarding texture shapes and internal structures it can be concluded that:

- Individual texture shapes can be optimized for given operating conditions.
- Asymmetric textures, e.g. ellipses and chevrons, seem to be the preferable option in terms of load carrying capacity enhancement and friction reduction, as they outperform the commonly used circular textures.
- An additional tuning of texture performance may be achieved by a careful selection of bottom profiles containing micro-steps, micro-wedges or both.
- Please note that the aforementioned findings are generally only valid for fully textured contacts. Partially textured contacts are an exception, as the best approximation of an optimal stepped or pocketed bearing always seems to be preferable, i.e. rectangular dimples with a flat bottom profile (cuboids) and maximum texture density.

Ultimately, universal guidelines on texture selection are impossible to give. Textures need to be carefully designed for a given type of contact and operating conditions. This further underlines the need for accurate and robust models that allow the evaluation of texture designs prior to being manufactured. The following is thus intended to provide a comparative summary of state of the art modelling techniques.

2.3 Modelling techniques

Results of the author's literature survey on modelling techniques used to analyse textured and/or rough surfaces are presented in Figure 2.11. It can clearly be seen that the most common approach is the solution of the Reynolds differential equation with purpose-developed codes, usually with an easy implementable finite difference method, however, it will be shown here that this is not necessarily the best choice. Moreover, source codes are rarely provided, which has led to a variety of different models and conflicting conclusions. This section is intended to provide a comparative overview of different available techniques to analyse textured and rough surfaces under hydrodynamic conditions.

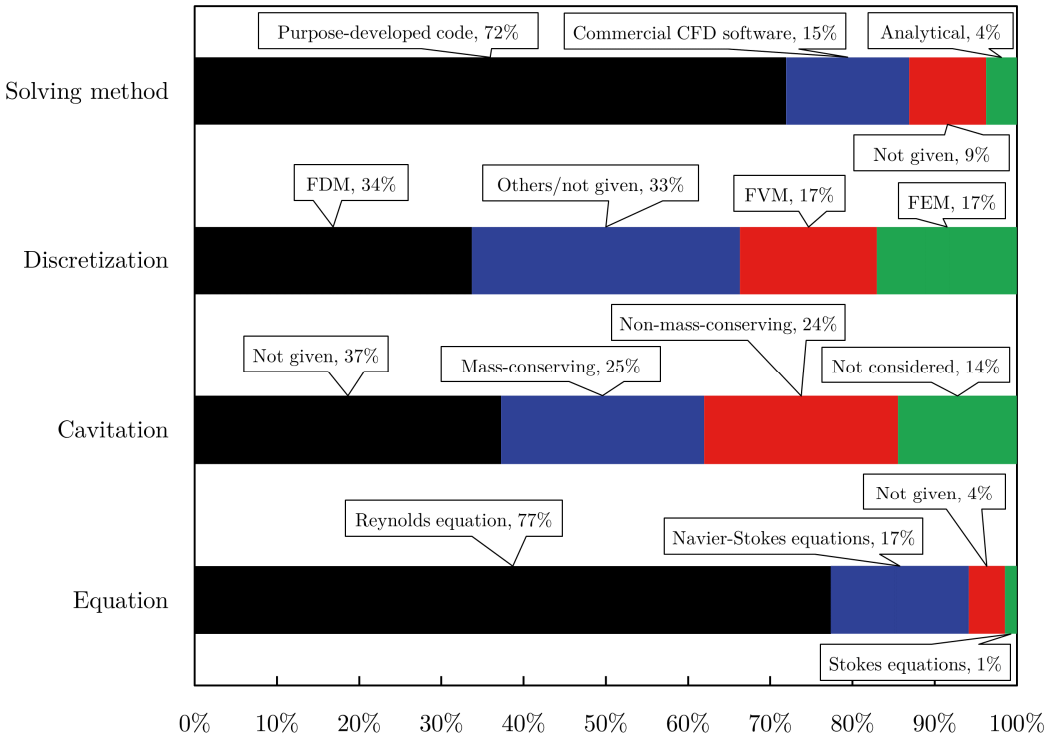

Figure 2.11 Results of the literature survey on theoretical models for textured and rough surfaces.

2.3.1 Fluid mechanics

The motion of fluid is generally governed by the conservation equations for mass (Continuity equation) and momentum (Navier-Stokes equations). If gravitational and other external body forces are neglected and the flow is assumed to be Newtonian, steady and incompressible, the Continuity and Navier-Stokes equations in vector form can be written respectively:

$$\nabla \cdot \boldsymbol{u} = 0 \tag{2.1}$$

$$\rho(\boldsymbol{u} \cdot \nabla)\boldsymbol{u} = -\nabla p + \nabla \cdot (\eta \nabla \boldsymbol{u}) \tag{2.2}$$

$\boldsymbol{u}$ is the velocity vector with the velocities u, v and w in x, y and z direction respectively, ρ the lubricant density, η the dynamic viscosity and p the pressure. The Stokes system of equations is formed by neglecting the convective inertia term (left-hand-side of equation (2.2)). Commonly used in lubrication theory is the classical Reynolds equation, derived by Osborne Reynolds in 1886 [146]. This partial differential equation can be derived from the Navier-Stokes equations by neglecting inertia effects, body forces and assuming that the pressure gradient in film thickness direction is zero. Furthermore, all velocity gradients in x and y direction as well as $\partial w/\partial z$ are assumed to be zero. For a laminar and transient flow of an incompressible, isothermal and isoviscous lubricant, the Reynolds equation can be written as:

$$\frac{\partial}{\partial x}\left(h^3 \frac{dp}{dx}\right) + \frac{\partial}{\partial y}\left(h^3 \frac{dp}{dy}\right) = 6\eta u \frac{\partial h}{\partial x} + 12\eta \frac{\partial h}{\partial t} \tag{2.3}$$

where h is the film thickness, p the pressure, η the dynamic viscosity and u the velocity in sliding direction. Since, in most cases, no analytical solutions for any of these equations exist, a numerical solution is necessary. Whereas the Navier-Stokes or Stokes equations are usually solved with commercial CFD software or the *SIMPLE* algorithm, solutions of the Reynolds equation are generally obtained with purpose-developed codes.

The main advantage of the Navier-Stokes (NS) model lies in the more accurate and complete description of the flow, especially the ability to describe inertia effects and three-dimensional flow. On the other hand, the solution of the NS system of equations is much more time consuming. In particular, for simulations under transient conditions, parametric studies or whenever surface roughness or small textures are considered, a solution of the NS equations becomes impracticable. Thus, NS equations are often solved for small contact areas [78, 79, 147] or individual dimple configurations [73, 74, 148] to investigate texture lift-off phenomena in detail. However, some studies have been conducted for textured journal bearings [80, 81] and thrust pad bearings [119, 120, 149]. Recently, CFD studies on thrust pad bearings were also extended to incorporate thermal effects by solving the Energy equation for both, the fluid and the solid domain [30, 108, 111].

One of the reasons for the popularity of the Reynolds equation is the lower computational effort required, as compared to the Navier-Stokes equations. Yet, due to the assumptions made during its derivation, the Reynolds equation is not capable of describing three-dimensional flow phenomena (e.g. recirculation inside textures) nor inertia related effects, which may lead to inaccurate results. The question whether the Reynolds equation or the Stokes equations are applicable for the study

of textured surfaces has thus been the subject of numerous studies [74, 150-152]. In 2009, Dobrica and Fillon [75] conducted an in-depth investigation on the validity of the Reynolds and Stokes models for textured slider contacts and demonstrated that the validity depends on two parameters: the Reynolds number (Re) and the texture aspect ratio (λ). It was shown that the Reynolds equation remains applicable as long as shallow dimples and flows with low Reynolds numbers are simulated. Deep textures may lead to recirculation, so that the Stokes system was recommended. For flows with high Reynolds numbers and whenever deep textures are studied, inertia and recirculation effects have a dominant influence on the pressure distribution and the full Navier-Stokes equations should be applied. They also showed that the applicability of the Reynolds equation can be largely improved by introducing correcting pressure terms to account for inertia based on the Bernoulli equation.

In summary, no consistent recommendation for the governing system of equations can be given. The choice depends on the specific application, operating conditions and texture configurations investigated. Despite the computational power available today, the Reynolds equation remains the more attractive choice in most cases, especially for more complex simulations involving, for example, transient conditions, rough surfaces or mixed lubrication. Whenever the Reynolds or Stokes equations are used, the validity should be evaluated for the application and range of operating conditions investigated. Please note that, since the Navier-Stokes equations are generally solved by commercial CFD software, the following sections are focused on methods based on the Reynolds equation.

2.3.2 Cavitation

In diverging areas of lubricated contacts, the increase in film thickness results in a reduction of pressure. As the continuity equation demands a full film at all times, the Reynolds equation predicts negative (sub-ambient) pressures to ensure mass conservation in these areas. Negative pressures, however, are physically impossible as lubricants are not capable of withstanding high tensile stresses. In reality, whenever the pressure drops below the saturation pressure of dissolved gases (gaseous cavitation) or below the vapour pressure of the lubricant (vapour cavitation), a two-phase flow of liquid lubricant and dissolved gas in form of bubbles or streamers forms. This phenomenon is called cavitation and needs to be considered in the study of lubricated contacts having diverging areas. In the study of textured or rough surfaces cavitation may occur not only globally in divergent contact areas, but also locally inside of individual dimples or in-between asperities (micro-cavitation) (Figure 2.12).

As rupture and reformation of the lubricant film may occur multiple times, a mass-conservative treatment of cavitation has been shown to be crucial for accurate performance predictions [16, 67]. A number of different mass-conserving cavitation

algorithms have been proposed over the past 40 years. Developed algorithms are generally based on the well-accepted and experimentally validated JFO cavitation boundary conditions proposed by Jakobsson and Floberg [153] and Olsson [154] and many have been successfully implemented for the study of textured surfaces.

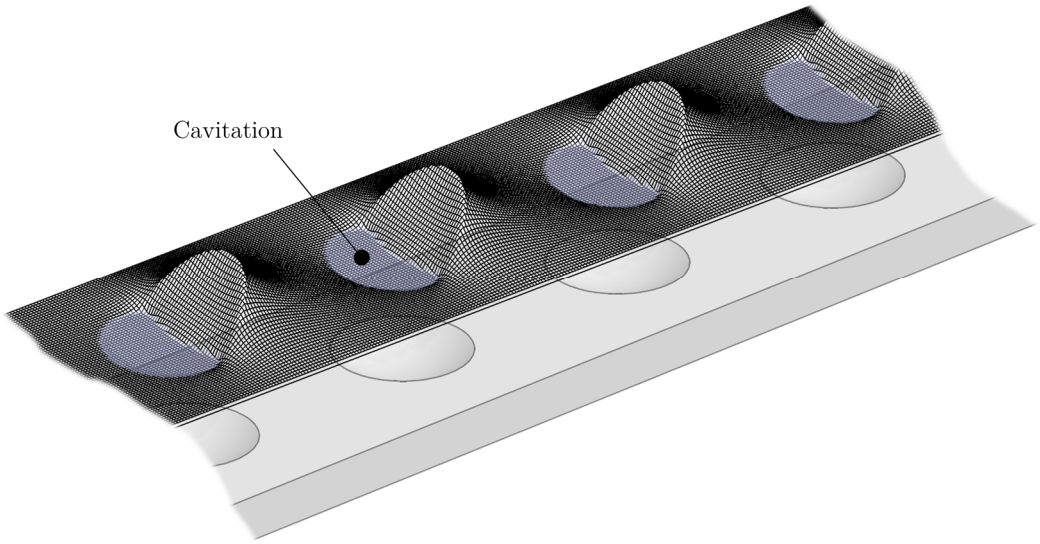

Figure 2.12 Exemplary pressure distribution over a fully textured parallel slider with dimples in the form of spherical caps as predicted by the Reynolds equation and a mass-conserving cavitation algorithm for $p_{cav} < p_{sup}$.

A first efficient cavitation algorithm that implicitly incorporates the JFO boundary conditions was developed by Elrod [155] and Elrod and Adams [156] in 1974. This algorithm is based on a finite difference method (FDM) and iteratively divides the solution domain in a full film and cavitated region with the help of a switch function (g), defined as

$$g = \begin{cases} 0 & \Theta < 1 \\ \\ 1 & \Theta \geq 1 \end{cases} \tag{2.4}$$

which also terminates the pressure terms in cavitated areas, allowing the use of a single equation throughout the domain and ensuring pure Couette flow in cavitated areas. Furthermore, a density ratio $\Theta = \rho/\rho_{ref}$ was introduced, which can also be interpreted as a fractional film content [155]. The flow in cavitated areas was treated as a two-phase flow of lubricant and vapour/gas with homogeneous density and in full film areas as a compressible flow with constant bulk modulus. The resulting modified Reynolds equation can be written as follows:

$$\frac{\partial}{\partial x}\left[\beta h^3 g(\Theta)\left(\frac{d\Theta}{dx}\right)\right] + \frac{\partial}{\partial y}\left[\beta h^3 g(\Theta)\left(\frac{d\Theta}{dy}\right)\right] = 6\eta u \frac{\partial \Theta h}{\partial x} \tag{2.5}$$

where

$$\beta = \rho \frac{\partial p}{\partial \rho} \tag{2.6}$$

is the bulk modulus. Although the Elrod algorithm has been successfully applied in lubrication theory, the elliptic-hyperbolic character of this equation combined with the sudden changes in the switch function can lead to instability and may cause convergence problems [157]. Therefore, many improvements to the Elrod algorithm (also called $p-\theta$ algorithm) have been proposed hereafter.

In 1986, Brewe [158] applied the $p-\theta$ model to study dynamically loaded journal bearings. As the Elrod algorithm requires and iterative solution, he used an alternating direction implicit (ADI) method and in a later study together with Woods [159] Multigrid techniques to increase convergence speed. Vijayaraghavan and Keith [160, 161] modified the Elrod algorithm some years later by using different finite difference schemes for the two flow regions, which improved its numerical stability. Their model was applied, for example, for textured thrust bearings by Qiu and Khonsari [67], using a Multigrid method with an iterative Gauss-Seidel relaxation scheme based on FDM. In a later study by the same authors [93], the algorithm was applied together with the Patir and Cheng (P&C) flow factor method to study roughness effects inside textures.

In 1991, Kumar and Booker [162, 163] proposed an algorithm for transient conditions optimized for FEM. Their algorithm was recently successfully applied by XIE *et al.* [164] for textured surfaces considering roughness effects. Other models based on FEM were developed by, for example, Shi and Paranjpe [165] and Hajjam and Bonneau [166]. The model of [166] was recently applied for the study of textured parallel sliders under steady and transient conditions by Gherca *et al.* [105].

Another cavitation algorithm was developed by Payvar and Salant in 1992 [167]. Based on the $p-\theta$ theory, they developed a finite difference version of the algorithm with optimized numerical stability. Their model was adapted for mixed lubrication by Wang *et al.* in 2003 [168], applying the P&C flow factor method and a rough surface contact model to study misalignment effects in coupled journal-thrust bearings. Harp and Salant [169] made use of the Payvar-Salant algorithm to develop a universal Reynolds equation that allows a simultaneous calculation of macro and micro-cavitation in rough journal bearings. The Payvar-Salant algorithm was also successfully applied for the study of lip seals under mixed lubrication [170], textured thrust bearings [68] and textured rough seals [91]. Recently, Xiong and Wang [171] performed a detailed analysis of the numerical finite volume implementation of this model, in particular regarding different finite difference schemes and solvers.

In 2007, Sahlin *et al.* [172] proposed an iterative algorithm based on a FDM that incorporates a switch function, similar to the concept of Elrod. However, rather than using an explicit relation between pressure and density based on the bulk modulus,

their model allows an arbitrary treatment of compressibility. Fesanghary and Khonsari [157] proposed another improvement to the Elrod algorithm. They used a continuous switch function (g) instead of the conventional binary one and reported significant improvements in numerical stability and convergence speed.

Ausas *et al.* [16] proposed a finite volume based version of the $p-\theta$ model for incompressible fluids. The arising nonlinear system of equations was solved with an iterative Gauss-Seidel method with successive over-relaxation. In 2009, the same group published a transient version of their cavitation algorithm and applied it for dynamically loaded journal bearings and squeeze flows [173]. It is noteworthy that their source code is publicly available on the internet. Their algorithm was applied, for example, in the numerical texture-optimization study by Guzek *et al.* [104], considering thermal effects by simultaneously solving the Energy equation, and for piston ring/cylinder liner contacts by Spencer *et al.* [174] in 2011.

Recently, Giacopini *et al.* [175] took advantage of the mathematical concept of complementarity used in the study of free boundary problems. After reformulating and discretizing the Reynolds equation through FEM, they constructed a linear complementarity problem (LCP) for which well-developed solution techniques exist that result in a converged solution within a finite number of steps. Bertocchi *et al.* [176] extended this model to include compressibility, piezoviscosity and non-Newtonian fluid behaviour. The model was applied recently by Medina *et al.* [177] to study textured bearings under transient reciprocating conditions.

To evaluate the stability and convergence characteristics of some of today's most sophisticated cavitation models, Woloszynski *et al.* [177] compared required iterations and computation times of the algorithms proposed by Ausas *et al.* [173], Bertocchi *et al.*[176] and Fesanghary and Khonsari [157] with their own algorithm based on a LCP formulation, called Fischer-Burmeister-Newton-Schur (FBNS). In their paper from 2015, fully textured parallel sliders having different numbers of dimples and different mesh densities were considered. The results showed that the proposed FBNS model is significantly faster (two orders of magnitude) than the other algorithms. The algorithm developed by Bertocchi *et al.* only converged within reasonable time when very coarse grids were used. The algorithms by Ausas and Fesanghary/Khonsari both always converged, the latter being about twice as fast on average. The truly impressive superiority of their algorithm was further demonstrated for textured contacts under transient conditions.

Another modification to the Elrod algorithm was proposed by Miraskari *et al.* [178] in 2017 based on a direct solution of the linear system. It was shown that the modification improves both robustness and convergence speed of the standard Elrod algorithm.

A variety of solutions to the complex task of solving the discrete system and

determining priori unknown cavitation zones within the solution domain have been proposed. Algorithms were optimized for different discretization methods, modified for improved stability or enhanced computational efficiency and incorporated in the study of rough surfaces, mixed lubrication, transient flow and thermo-hydrodynamic lubrication. However, no easily implementable standard method exists and numerical details or source codes are rarely provided, hence, the often time-consuming implementation remains with the individual researcher. This inevitable leads to slightly different algorithms and makes comparison and validation challenging. The question of which algorithm should be applied depends on the specific problem investigated. Especially for the simulation of transient conditions or whenever very fine meshes are required, more computational efficient algorithms (e.g. [179]) may become necessary, despite the increased implementation effort.

2.3.3 Micro-hydrodynamic

Another issue in the simulation of textured surfaces is the large difference in scale between the global contact dimensions and local surface properties, such as textures or roughness (Figure 2.13). Generally, two different approaches exist to consider these local changes in film thickness in the numerical solution: direct/deterministic methods and indirect/stochastic methods.

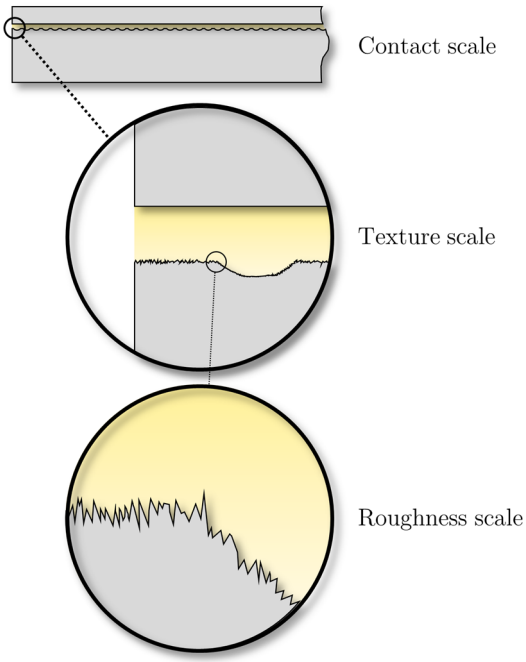

Figure 2.13 Different scales of a textured contact.

In the direct method the mesh is chosen fine enough to capture the surface topography up to the micro/nano scale, i.e. roughness and/or textures are directly included in the film thickness equation. This may work for medium-sized and large

textures, however, if textures are very small or one wants to consider the effect of surface roughness, a direct method becomes nearly impossible due to the fine meshes needed and the related high computation time encountered. Only for very small domains, e.g. Hertzian contacts, this method becomes applicable. The EHL contact model by Hu and Zhu [180, 181], for example, was used to deterministically investigate differently engineered surfaces, including dimpled ones, by Epstein *et al.* [182], Wang and Zhu [183] and Wang *et al.* [184]. Brunetière and Tournerie [91] were able to deterministically investigate fully textured seals while considering roughness by reducing the solution domain with the help of periodic boundary conditions. Other proposed deterministic models include those by Shi and Salant [170] and Jiang *et al.* [185].

Despite the advantages in accuracy, a direct method can rarely be applied, which has led to the development of numerous indirect/stochastic methods. All these methods include some kind of averaging and can be divided into two groups: flow factor methods and homogenization methods.

In flow factor methods the influence of local changes in film thickness on the pressure distribution is incorporated in the pressure and shear flow terms of the Reynolds equation by a number of correction factors, so-called *flow factors*. One of the earliest and most popular methods is the P&C flow factor method, developed in 1978 by Patir and Cheng [118, 186]. The steady-state form of the P&C averaged Reynolds equation can be written as:

$$\frac{\partial}{\partial x}\left(\phi_x h^3 \frac{dp}{dx}\right) + \frac{\partial}{\partial y}\left(\phi_y h^3 \frac{dp}{dy}\right) = 6\eta u \frac{\partial h}{\partial x} + 6u\sigma \frac{\partial \phi_s}{\partial x} \tag{2.7}$$

where ϕ_x and ϕ_y are pressure flow factors, ϕ_s is the shear flow factor and σ the surface rms roughness. Pressure flow factors are generally obtained through numerical experiments performed on a local scale, i.e. a small representative contact area, and ϕ_s was given in [186]. Despite numerous proposed improvements and modifications (see e.g. Elrod [187], Tripp [188], Wu and Zheng [189], Harp and Salant [169], Rocke and Salant [190] or Wilson and Marsault [191]), the classic P&C method is still the most commonly used flow factor technique in the study of textured/rough surfaces and was applied, for example, in the study of journal bearings with axial grooves by Chan *et al.* [192], dimpled contacts by XIE [164] and textured bearings by Tønder [116, 117].

Especially for the study of textured contacts, de Kraker *et al.* [76, 193] developed a *texture averaged Reynolds equation*. Similar to the P&C theory, so-called *texture flow factors* were introduced to modify the Reynolds equation on the global domain. Unlike in Patir and Cheng's method, flow factors were obtained by local flow simulations based on the Navier-Stokes equations rather than the Reynolds equation in order to account for inertia and recirculation effects and depend on the operating

conditions. In 2006, Dobrica *et al.* [194] compared the results obtained by the P&C flow factor model with a deterministic model for a partial arc journal bearing. It was found that, in general, the P&C model showed a good agreement with the deterministic results in terms of pressure and film thickness, although values for friction torque and attitude angle showed deviations.

The other type of indirect method is based on the mathematical concept of homogenization, used for partial differential equations (PDEs) with oscillating coefficients. Similar to the aforementioned flow factor techniques, multiple scales are used and local effects are averaged and then incorporated in the global, smooth Reynolds equation. The due to surface roughness or textures oscillating film thickness equation is homogenized, resulting in a so-called *homogenized Reynolds equation*. This method was originally proposed by Elrod [195] in 1973 and has been further studied by many authors [194, 196-207].

For example, Bayada *et al.* [199] proposed a homogenized Reynolds equation that incorporates mass-conserving cavitation based on the JFO boundary conditions and Sahlin *et al.* [205, 206] developed a mixed lubrication model that allows the simulation of measured surface topography. Another interesting concept based on homogenization was applied by Almqvist *et al.* [207], called *reiterated homogenization*. They studied the combined effect of surface roughness and texturing by dividing the problem in three scales rather than two: a roughness scale, a texture scale and the global contact scale. Both, the oscillations of the roughness and texture scale were homogenized and incorporated in the global, smooth Reynolds equation. Since the study of rough textured surfaces involves three scales, one could also treat the texture scale deterministically and the roughness scale with a homogenization or flow factor method, resulting in a *semi-deterministic* approach, as performed by Spencer *et al.* [174] for textured cylinder liners and by Qiu and Khonsari [93] for seal-like structures. Rom and Mueller [208] proposed a reduced basis method to improve the computational speed of the homogenization. For the case of a textured journal bearing having a large number of cuboid textures, a speedup of up to 65 as compared to directly solving the Reynolds equation was demonstrated.

It has been shown that, compared to classic flow factor methods, the concept of homogenization leads to more accurate results whenever arbitrary roughness is encountered, i.e. the patterns do not show any symmetries [205-207]. Hence, for cases with arbitrary roughness patterns the homogenization techniques is recommended. Generally, it should be noted that local flow information is lost whenever stochastic methods are used, hence, a deterministic method is always preferable, particularly for textures, as local cavitation has an important influence on the contact performance. Also, partially textured contacts would require locally different flow-factors. The same holds true for surface roughness, however, a deterministic treatment is, despite the available computational power today, not usually applicable

and therefore some kind of averaging technique needs to be performed.

2.3.4 Spatial discretization and numerical methods

In most cases, the Reynolds equation requires a numerical solution, i.e. a discretization of the solution domain and a subsequent solution of the arising systems of algebraic equations. Generally, mathematics provides methods for the solution of this type of equation and the reader is referred to respective literature. However, some issues arise particularly in the study of textured surfaces and are briefly discussed here.

The Reynolds equation is an elliptic second order PDE, however, whenever mass-conserving cavitation is considered, the equation becomes hyperbolic in cavitated areas, forming a highly nonlinear mixed type PDE. Most discretization methods are applicable for this kind of equation and many have been successfully applied in the field of surface texturing (e.g. see: finite difference method (FDM) [67, 134, 157, 209, 210], finite volume method (FVM) [14, 104, 171, 209-211], finite element method (FEM) [166, 175, 209, 210], finite cell method (FCM) [212] and spectral element method (SEM) [209, 210]). Pei *et al.* [213] presented a further developed SEM for the efficient simulation of lubrication problems with rough surfaces and Profito *et al.* [214] proposed a general element-based finite volume method that combines the advantages of both methods.

One of the differences between these methods is their capability of handling discontinuous coefficients. As surface textures in the form of dimples or grooves are discontinuities in the film thickness equation by nature, special care should be taken regarding discretization and meshing. For methods based on finite elements this issue is less pronounced, since the element edges can be made coincide with the discontinuities [105, 215, 216]. For FDM and FVM, on the other hand, discontinuities may cause large approximation errors, especially in cavitated areas, since the hyperbolic type of the Reynolds equation does not allow the use of central finite difference schemes. Thus, whenever the discretization is based on finite differences, a special treatment of discontinuities is generally required, such as local mesh refinement [217] or special finite approximation schemes [215, 218].

Also, the accuracy and convergence speed of the solution may differ, depending on the discretization method chosen. Woloszynski *et al.* compared the accuracy of four different discretization methods (FDM, FVM, FEM, SEM) for one-dimensional [209] and two-dimensional [179] textured slider bearings. It should be noted here that, since cavitation was not considered in their study, the problem considered was purely elliptic. The number of mesh points required in order to achieve a predetermined accuracy was evaluated for each method and compared. SEM was shown to require

the smallest number of nodes, 28 and 72 times fewer than the other methods for the one-dimensional and two-dimensional case respectively, resulting in a significantly higher convergence speed. Both, FVM and FEM were stated to be the best compromise between accuracy and ease of implementation. FDM required the highest number of nodes and was not recommended. Nevertheless, due to the ease in implementation, FDM is the most popular discretization method used in the study of textured surfaces (Figure 2.11), despite its inaccuracy and inability to handle complex geometries.

The generally fine meshes required to accurately describe surface textures and the complexity of the Reynolds equation especially related to cavitation phenomena require fast and robust solvers. The choice of the numerical solver obviously depends on the numerical details of the model and the particular system of equations encountered after discretization. For example, a number of cavitation algorithms are iterative by design and therefore require iterative solvers. Very popular in the study of surface textures are Gauss-Seidel methods, often implemented with successive relaxation (see e.g. [14, 16, 19, 157, 179]) to improve convergence speed. Other successfully applied iterative schemes include alternating direction implicit (ADI) methods [190] and for nonlinear systems Newton-Raphson [219, 220] methods. Cavitation algorithms based on LCP can take advantage of pivoting algorithms [175-177, 179, 221], for example, Lemke's algorithm [222]. Also, in order to further increase convergence speed, Multigrid methods [67, 93, 138, 139] have been applied and algorithms were modified to take advantage of multicore processing [32, 192].

2.4 Limitations of this review

This review is focused on findings regarding texturing for typical bearing applications under hydrodynamic conditions. Texture design choices may differ for counterformal contacts or other lubrication regimes. For research on surface texturing for concentrated contacts the reader is referred to a recently published review article by Sudeep *et al.* [52] and for studies concerning different lubrication regimes the reader may be interested in references [33, 34, 36, 65].

The review on modelling techniques presented in this chapter is focused on methods based on the Reynolds equation and is limited to hydrodynamic lubrication, cavitation and micro-hydrodynamic effects. If the reader is interested in the simulation of mixed lubrication or elasto-hydrodynamic modelling, references [54, 223-225] may be interesting. Furthermore, it is well known that thermal effects and elastic deformation play a crucial role in hydrodynamic lubrication, particularly in bearings, and these effects should be included in the numerical simulation for accurate performance predictions. Also, whenever the Reynolds equation is applied,

additional models to describe turbulent flow may become necessary for certain applications. However, these effects were not considered *texture-specific*, and have thus not been included in this review. Temperature effects have been included in the theoretical study of textured surfaces based on the Reynolds equation by a simultaneous solution of the Energy equation. The interested reader is referred to references [31, 104, 107, 123].

2.5 Summary

Surface texturing has been shown to be capable of enhancing the tribological contact performance for a wide range of applications. One of the main issues is the dependency of optimal texturing parameters on the type of contact and, in particular, the operating conditions. Furthermore, complex phenomena, such as cavitation and inertia related effects, have been shown to highly affect texture performance.

A lot of research has thus been aimed at finding optimal texturing parameters for best performance enhancement. Although some general guidelines exist, it has become clear that in most cases textures need to be designed for a specific application and given operating conditions. Especially for convergent film geometries or journal bearings, for which optimal parameters have been shown to significantly depend on the convergence ratio or the eccentricity, the chosen texture design will always be a compromise, adapted for the range of operating conditions encountered. For some scenarios texturing may even be found to be detrimental or provide unreasonable improvements; this means that the profitability and effectiveness of surface texturing need to be assessed for a given application.

Numerical models allow the evaluation of texture designs prior to being manufactured and can avoid time consuming experimental trial and error approaches. However, the numerical simulation of textured surfaces still involves major challenges:

- A mass-conserving treatment of cavitation has been shown to be crucial, however, the arising elliptic-hyperbolic system with initially unknown locations of cavitation areas provides difficulties and can lead to numerical instability.
- Surface textures are discontinuities in film thickness by nature. To avoid large discretization errors, a special treatment of film discontinuities is required (e.g. local mesh refinements or special discretization schemes).
- The large difference in contact and texture dimensions often results in very fine meshes and therefore impractical computation times. Especially when roughness is considered, averaging techniques need to be applied, which lead

to the loss of local flow information.

- The assumptions made by using the Reynolds equation may be violated, depending on the Reynolds number and texture dimensions. Hence, the applicability of the Reynolds equation is limited.
- Parametric and optimization studies are crucial for an effective texture design, demanding numerical solvers with high numerical stability and computational speed.

Although a number of numerical models have been proposed, no model complies with all of the above points. Many studies are limited to certain operating conditions due to high computation times, make use of non-mass-conserving cavitation algorithms or do not account for discontinuities. To allow an effective texture design and make a step towards successful industrial applications of surface texturing, a numerical model is required that complies with all of the above requirements. The development of such a model was one of the objectives of this work. The developed numerical model is introduced in the following chapters.

Chapter 3

Mathematical Model

As discussed in the previous chapter, a successful application of surface texturing relies to a great degree on fast and robust numerical models that allow an accurate evaluation of the impact of surface texturing on the performance of hydrodynamic bearings under a wide range of conditions. Based on the findings of the literature review, a mathematical model was developed specifically for the analysis and optimization of surface textures for tilting pad thrust bearings. The mathematical framework is presented in this chapter.

The model is based on the two-dimensional Reynolds equation and incorporates a mass-conserving cavitation algorithm. Thermal effects are described through an effective temperature method while taking into account the hot-oil-carry-over effect encountered in thrust pad bearings. The optimization of texture patterns is made possible by formulating multidimensional constrained optimization problems.

3.1 Geometry and film thickness

3.1.1 Bearing geometry

To mathematically describe the film thickness distribution of a tilting pad thrust bearing, a polar coordinate system is used, where the radial coordinate (r) has its origin at the bearing centre and the angular coordinate (θ) has its origin at the pad inlet (Figure 3.1). Under the assumption that no misalignment is occurring, it is common practice to model only one of the sector shaped pads and subsequently extrapolate the results to obtain the overall bearing performance. The pads are supported at a pivot, allowing them to freely tilt and self-adjust the film thickness

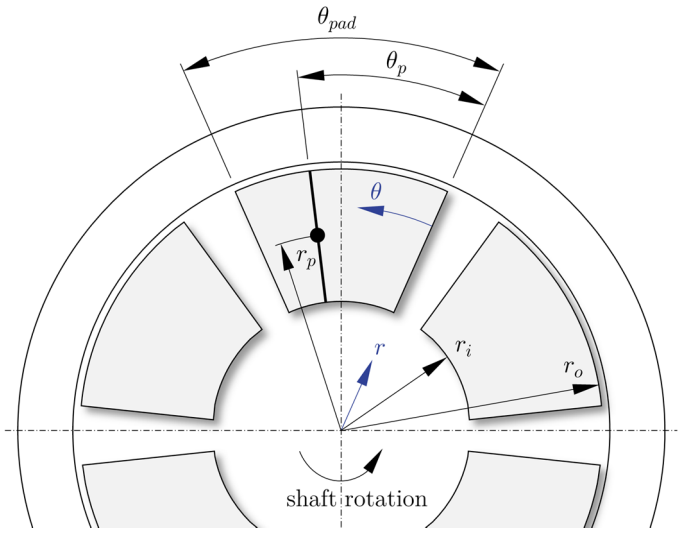

Figure 3.1 Tilting pad thrust bearing with coordinate system.

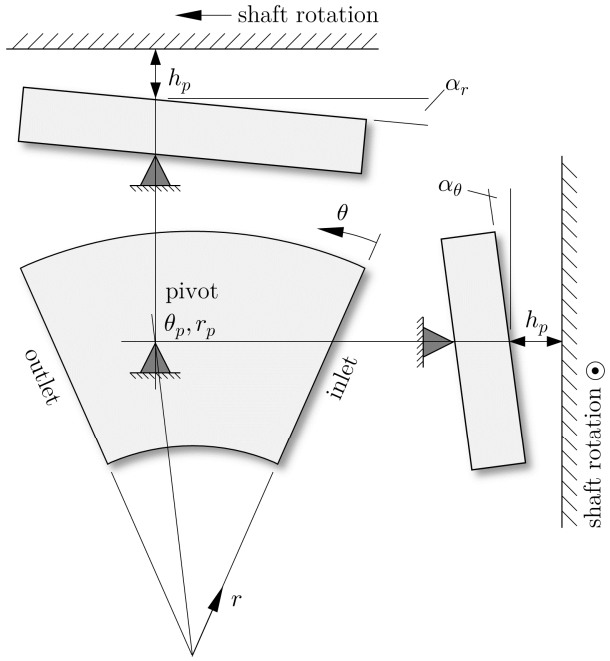

Figure 3.2 Film thickness of a thrust pad with spherical pivot.

in order to balance the applied load (Figure 3.2). Pads with line pivot (Michell type bearings) can only tilt about a certain radial line, called pitch, and given by the pitch angle α_r. Pads with point pivot (Kingsbury type bearings) can also tilt about a certain tangential line, called roll, and given by the roll angle α_θ. The film thickness directly above the pivot location is defined as h_p and the coordinates of the pivot as θ_p and r_p. These parameters allow to express the film thickness distribution for point pivoted pads as

$$h(\theta, r) = h_p + r\sin(\theta_p - \theta)\sin\alpha_r + \left[r_p - r\cos(\theta_p - \theta)\right]\sin\alpha_\theta \tag{3.1}$$

For pads with line pivot, α_θ equals 0, and the equation simplifies to

$$h(\theta, r) = h_p + r\sin(\theta_p - \theta)\sin\alpha_r \tag{3.2}$$

Making use of the so-called *Michell bearing approximation*, which assumes that the film thickness does not vary along the radius, equation (3.2) can be further simplified to give

$$h(\theta, r) = h_p + (\theta_p - \theta)\tan\alpha_r \tag{3.3}$$

However, it has been shown that this geometrical approximation overestimates the predicted load carrying capacity [226], hence, equations (3.1) and (3.2) are used in this work to describe the film thickness distribution.

3.1.2 Texture geometry

In the present work, only partial texturing is considered, as it is well known that partial texturing is recommended for parallel and moderately converging contacts under hydrodynamic conditions. Moreover, although a large variety of texture shapes and internal structures have been proposed, textures with maximum volume result in best performance. Therefore, only partially textured pads and angular sector shaped textures with flat bottom profile in form of discrete textures or grooves are considered here (Figure 3.3).

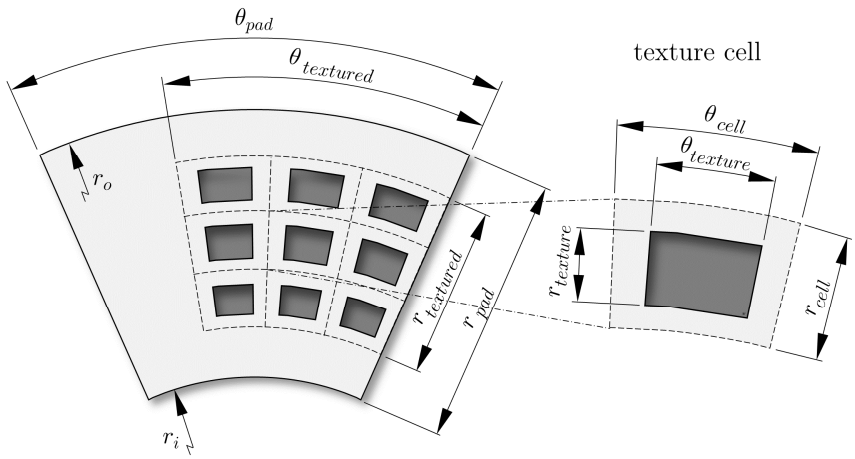

Figure 3.3 Thrust pad with a 3 x 3 texture pattern.

A particular texture design is initially defined by the relative texture extent in circumferential and radial direction:

$$\alpha = \frac{\theta_{textured}}{\theta_{pad}} \qquad \beta = \frac{r_{textured}}{r_{pad}} \tag{3.4}$$

The textured area is then sub-divided into so-called *texture cells*, according to the specified number of textures in circumferential (n_θ) and radial direction (n_r). Individual textures are then placed at the centre of each texture cell, where the size

of the textures is specified by the texture density in circumferential and radial direction:

$$\rho_\theta = \frac{\theta_{texture}}{\theta_{cell}} \qquad \rho_r = \frac{r_{texture}}{r_{cell}} \tag{3.5}$$

where the overall, area-specific texture density can be evaluated as

$$\rho_{texture} = \rho_\theta \cdot \rho_r \tag{3.6}$$

The texture depth is considered uniform and defined as $h_{texture}$. To consider surface textures in the film thickness equation, the film thickness is initially evaluated for an equivalent untextured pad. Thereafter, $h_{texture}$ is simply added numerically wherever textures are located. Whenever the inlet is textured, the first row of textures is simply elongated towards the pad inlet (Figure 2.6). Although this methodology obviously falsifies the numerical value of the texture density, deviations are generally negligibly small.

The proposed method of defining texture patterns allows to easily generate a variety of textured, grooved and pocketed pads (Figure 3.4).

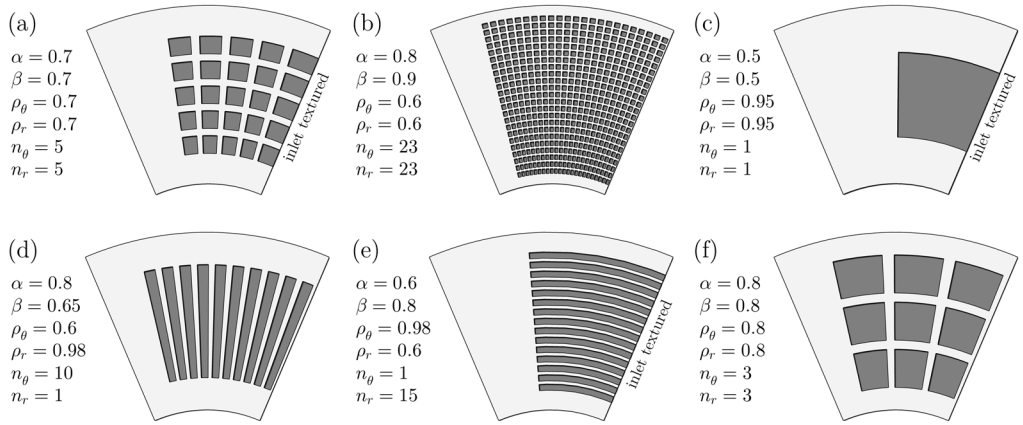

Figure 3.4 Exemplary texture designs: (a) 5 x 5 textures, (b) 23 x 23 textures, (c) pocket, (d) 10 radial grooves, (e) 15 circumferential grooves and (f) 3 x 3 textures.

3.2 Fluid mechanics

3.2.1 Reynolds equation

The steady-state and incompressible form of the Reynolds differential equation is utilized to compute the pressure distribution over the sector-shaped thrust pads. In polar coordinates, the equation can be written as follows:

$$\frac{\partial}{\partial r}\left(r\frac{\rho h^3}{\eta}\frac{\partial p}{\partial r}\right)+\frac{1}{r}\frac{\partial}{\partial \theta}\left(\frac{\rho h^3}{\eta}\frac{\partial p}{\partial \theta}\right)=6\omega r\frac{\partial(\rho h)}{\partial \theta} \tag{3.7}$$

where p is the local pressure, ρ the lubricant density, η the lubricant dynamic viscosity and ω the rotational speed of the runner. Equation (3.7) is an elliptic inhomogeneous partial differential equation. Therefore, a numerical solution with appropriate boundary conditions is necessary.

The question, whether the assumptions made during the derivation of the Reynolds equation from the Navier-Stokes equations are violated for the case of textured surfaces, cannot be answered generally. Dobrica and Fillon [75] showed that the validity of the Reynolds equation depends on both the texture aspect ratio (λ) and the Reynolds number (Re). It was shown that the Reynolds equation is applicable for most practical applications of surface texturing. They evaluated the validity of the Reynolds equation in textured parallel sliders of infinite width and introduced two indicators: Δ_1, which is the average absolute variation in the local pressure and Δ_2, which is the variation in the predicted integral of the positive components of the pressure profiles, i.e. the load carrying capacity (Figure 3.5).

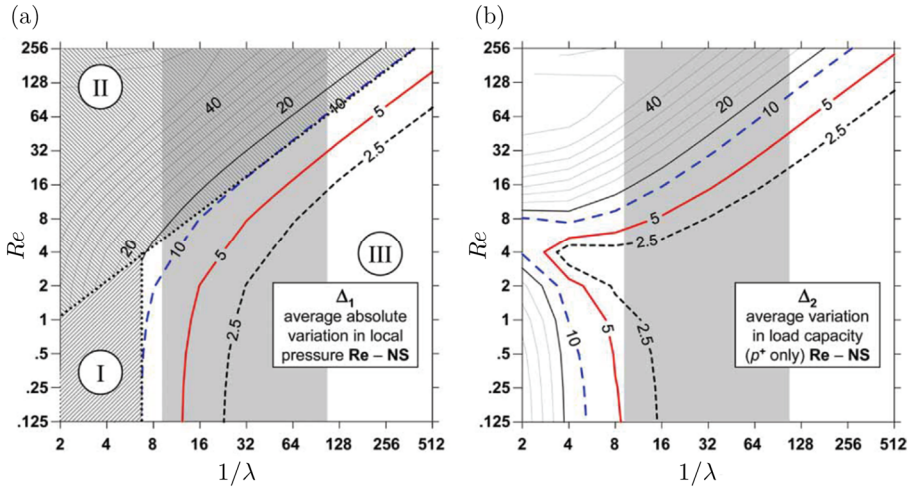

Figure 3.5 Relative differences Δ_1 and Δ_2 between the results obtained with the Reynolds equation and Navier-Stokes equations (adapted from [75]).

Three areas were identified:

(I) For this case inertia effects are negligible, however, the variations in film thickness are high and the assumptions made during the derivation of the Reynolds equation are violated. Therefore, a Stokes model should be used.

(II) For this case both inertia effects are important and the variations in film thickness are high with respect to the texture length. The full Navier-Stokes system of equations should be applied.

(III) For this case the variations of film thickness are low and inertia effects are unimportant. Hence, the Reynolds equation is applicable.

In this study, the Reynolds number is defined as $Re = \rho u h_{min}/\eta$ and the texture aspect ratio as $\lambda = h_{texture}/l$, where l is the arc length of the texture at the mid radius. To ensure satisfying accuracies, the validity of the Reynolds equation is evaluated for all simulations presented.

3.2.2 Cavitation

Cavitation does not usually occur in textured tilting pad thrust bearings, as the overall convergence builds up enough pressure to prevent pressures from falling below the cavitation pressure. However, under extreme operating conditions that result in particularly low convergence ratios or whenever very deep textures are analysed, cavitation may occur inside individual textures close to the pad inlet and the outer pad radius.

As discussed in detail in chapter 2.3.2, a mass conserving treatment of cavitation is required when simulating textured surfaces. In order to ensure mass-conservation, Jakobsson and Floberg [153] together with Olsson [154] developed a theory known as JFO cavitation boundary condition, named after its three inventors. However, the direct solution of the JFO boundary conditions has proven to be very difficult. A first efficient numerical algorithm that implicitly satisfies this boundary conditions was developed by Elrod and Adams [156] and Elrod [155] in 1974 and 1981 respectively. Since then, many different algorithms have been proposed to solve the cavitation problem in a mass-conserving way. The cavitation model used in this work was adapted from [227] and is similar to the algorithm proposed by Ausas *et al.* [16, 173]. This method requires an iterative solution of the Reynolds equation. Similar to the concept of Elrod, the solution domain ($\boldsymbol{\mathcal{F}}$) is divided in two subdomains: A pressurized region $\boldsymbol{\mathcal{D}}^+$, where the pressure is superior to the cavitation pressure and a cavitated region $\boldsymbol{\mathcal{D}}^0$, where the pressure is constant and equal to the cavitation pressure (Figure 3.6).

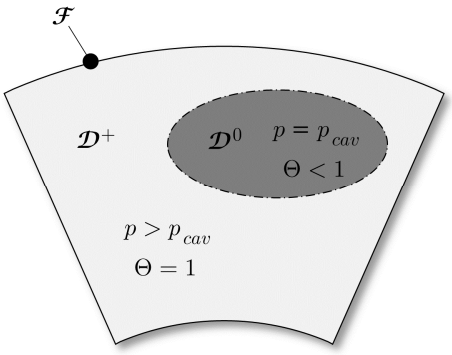

Figure 3.6 Computational domain with pressurized and cavitated subdomains.

Furthermore, a fractional film content is defined as follows [155]:

$$\Theta = \frac{V_{liq}}{V} = \frac{V_{liq}}{V_{liq} + V_{gas}} \tag{3.8}$$

This parameter describes relatively how much liquid lubricant is present and allows to correct the lubricant density. The Reynolds equation (3.7) can now be rewritten to incorporate mass-conserving cavitation:

$$\frac{\partial}{\partial r}\left(r\frac{\rho h^3}{\eta}\frac{\partial p}{\partial r}\right) + \frac{1}{r}\frac{\partial}{\partial \theta}\left(\frac{\rho h^3}{\eta}\frac{\partial p}{\partial \theta}\right) = 6\omega r\frac{\partial(\Theta\rho h)}{\partial \theta} \tag{3.9}$$

with

$$\Theta = 1 \quad \text{and} \quad p > p_{cav} \quad \text{in pressurized regions } (\boldsymbol{\mathcal{D}}^+) \tag{3.10}$$

$$\Theta < 1 \quad \text{and} \quad p = p_{cav} \quad \text{in cavitated regions } (\boldsymbol{\mathcal{D}}^0) \tag{3.11}$$

where p_{cav} is the cavitation pressure. Although both pressure and fractional film content are unknown, equation (3.9) remains solvable, as in $\boldsymbol{\mathcal{D}}^+$ the fractional film content is known ($\Theta = 1$) and in $\boldsymbol{\mathcal{D}}^0$ the pressure is known ($p = p_{cav}$). The modified Reynolds equation remains of elliptic character in $\boldsymbol{\mathcal{D}}^+$, however, becomes hyperbolic in $\boldsymbol{\mathcal{D}}^0$.The utilized mass-conserving treatment of cavitation requires an iterative and simultaneous solution for p and Θ. The implemented numerical procedure is described in chapter 4.1.

3.2.3 Lubricant rheology

For the relatively low pressures encountered in hydrodynamic lubrication, the pressure dependency of the lubricant density and viscosity are negligible [228]. Moreover, the lubricant's heat capacity is assumed to be constant in the present model. The most impactful effect in hydrodynamic bearings is the dependency of viscosity on the lubricant temperature. As the temperature rises, the viscosity drops significantly and the load carrying capacity diminishes. This variation is modelled using the expression proposed by Mac Coull and Walther [229]:

$$log_{10}[log_{10}(\nu_{cSt} + a)] = n - m\, log_{10}(T_{\circ K}) \tag{3.12}$$

where ν_{cSt} is the lubricant kinematic viscosity in centistokes, $T_{\circ K}$ the lubricant temperature in degrees Kelvin and a, n and m are lubricant dependent parameters. If centistokes is used as the unit of viscosity, a takes values between 0.6 and 0.75. In the present study, $a = const. = 0.6$. The parameters n and m can easily be determined by solving the system of equations that arises for two given temperatures and corresponding viscosities. Figure 3.7 shows the predicted viscosity for a range of standard ISO mineral oils.

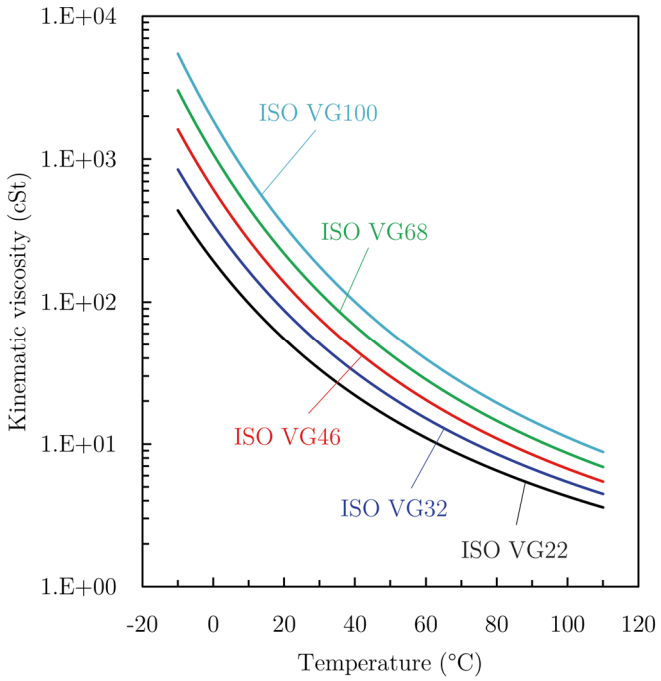

Figure 3.7 Variation of lubricant viscosity with temperature for standard ISO mineral oils as predicted by equation (3.12).

3.3 Bearing equilibrium

The bearing equilibrium is reached, if the integral of the pressure distribution over the pad area, i.e. the load carrying capacity, balances the applied load per pad. Furthermore, the centre of pressure, i.e. line of action through which the resultant force acts, must be directly above the pivot in order to cause no resultant moments around the pivot. As shown in Figure 3.8, the forces acting on a thrust pad are: the applied load (W_0), the reaction force from the pressure field acting in the direction normal to the pad surface (W_{res}) and the load carrying capacity (W), which is the vertical component of the reaction force.

If the pad is not in equilibrium, the load carrying capacity does not equal the applied load and the centre of pressure is acting at a location away from the pivot. This allows to define three error terms:

$$\delta W = W - W_0 \tag{3.13}$$

$$\delta\theta = \theta_{cop} - \theta_p \tag{3.14}$$

$$\delta r = r_{cop} - r_p \tag{3.15}$$

where (θ_{cop}, r_{cop}) and (θ_p, r_p) are the coordinates of the centre of pressure and the pivot respectively. The load carrying capacity is easily evaluated by integrating the

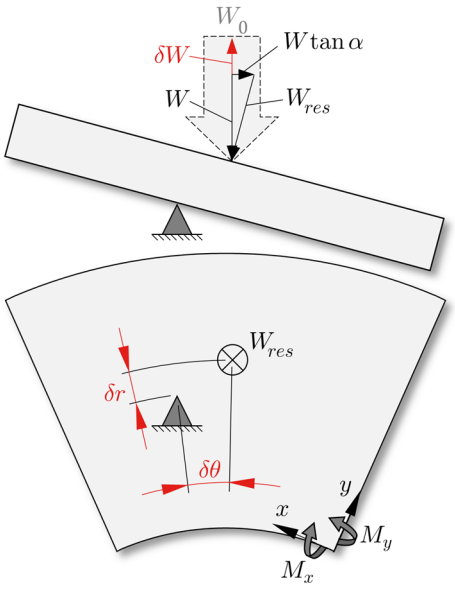

Figure 3.8 Load components acting on a thrust pad.

pressure distribution over the pad area:

$$W = \int_{\theta=0}^{\theta=\theta_{pad}} \int_{r=r_i}^{r=r_o} pr \, d\theta dr \tag{3.16}$$

To evaluate the centre of pressure, a local Cartesian coordinate system (x, y) with origin at the pad inlet and the inner radius is defined. The moments of force about this point are then computed according to

$$M_x = \int_{\theta=0}^{\theta=\theta_{pad}} \int_{r=r_i}^{r=r_o} pr \left(r\cos\theta - r_i\right) d\theta dr \tag{3.17}$$

$$M_y = \int_{\theta=0}^{\theta=\theta_{pad}} \int_{r=r_i}^{r=r_o} pr^2 \sin\theta \, d\theta dr \tag{3.18}$$

This allows to calculate the centre of pressure:

$$\theta_{cop} = \tan^{-1}\left(\frac{M_y}{M_x + W r_i}\right) \tag{3.19}$$

$$r_{cop} = \sqrt{\left(\frac{M_y}{W_{res}}\right)^2 + \left(\frac{M_x}{W_{res}} + r_i\right)^2} \tag{3.20}$$

For given operating conditions, the error parameters δW, $\delta\theta$ and δr only depend on the film thickness distribution, i.e. the pitch and roll angle as well as the film thickness at the pivot. The task is now to find a vector $\boldsymbol{x} = (\alpha_r, \alpha_\theta, h_p)^t$ that satisfies the equilibrium condition:

$$\boldsymbol{F}(\boldsymbol{x}) = \begin{bmatrix} \delta W(\boldsymbol{x}) \\ \delta\theta(\boldsymbol{x}) \\ \delta r(\boldsymbol{x}) \end{bmatrix} = \mathbf{0} \tag{3.21}$$

This assembles a nonlinear system in three dimensions, which is solved numerically as explained in chapter 4.2. For bearings with line pivot $\alpha_\theta = 0$ and equation (3.21) is reduced to a two-dimensional system.

3.4 Thermal effects

3.4.1 Effective temperature method

During operation, viscous shearing of the lubricant generates heat and consequently the temperatures of the lubricant and surrounding bodies rise. As the lubricant viscosity significantly depends on the temperature, thermal effects should be considered in the numerical simulation of hydrodynamic bearings. A complete description of thermal effects can be achieved by solving the generalized Reynolds equation, the three-dimensional energy equation and the heat conduction equation. However, for the purpose of this study, thermal effects are considered through an effective temperature method [17, 229], where isothermal and isoviscous conditions are assumed, using an effective temperature and effective viscosity. This simplified approach was chosen to keep computation times low and allow for parametric and optimization studies in reasonable time. However, as shown in chapters 5.2.3 and 7.4 the applied methodology provides good accuracy with respect to CFD simulations and experiments.

At thermal equilibrium the energy dissipated by viscous shearing balances the heat carried away by the lubricant (convection) and surrounding bodies (conduction). Assuming that a constant percentage of energy is carried away through convection, one can write:

$$\Pi k_{con} = \Delta T Q_{in} \rho c_p \tag{3.22}$$

where Π is the dissipated energy, k_{con} the percentage of energy removed by convection, typically between 50 and 100% [229] (in the present study $k_{con} = 75\%$), ΔT the temperature rise of the lubricant, Q_{in} lubricant flow entering the contact, ρ the lubricant density and c_p the lubricant's specific heat. The effective lubricant temperature can then be evaluated:

$$T_{eff} = T_{in} + k_{con} \frac{\Pi}{Q_{in} \rho c_p} \tag{3.23}$$

where T_{in} is the lubricant temperature at the pad inlet. The dissipated energy is

equal to the frictional power loss:

$$\Pi = T_f \omega \tag{3.24}$$

where the friction torque is found by integrating the shear stress over the pad area:

$$T_f = \int_{\theta=0}^{\theta=\theta_{pad}} \int_{r=r_i}^{r=r_o} \tau r^2 \, d\theta dr \tag{3.25}$$

Note that churning losses are not accounted for in the present model. As many thrust pad coatings have a limited operating temperature, the maximum pad temperature is an important performance parameter. Here, T_{max} is approximated by the empirical relation [229]:

$$T_{max} = 2T_{eff} - T_{in} \tag{3.26}$$

3.4.2 Hot-oil-carry-over effect

The lubricant entering the pad is not pure supply oil, but a mixture of cold supply oil and already hot oil carried over from the preceding pad (Figure 3.9).

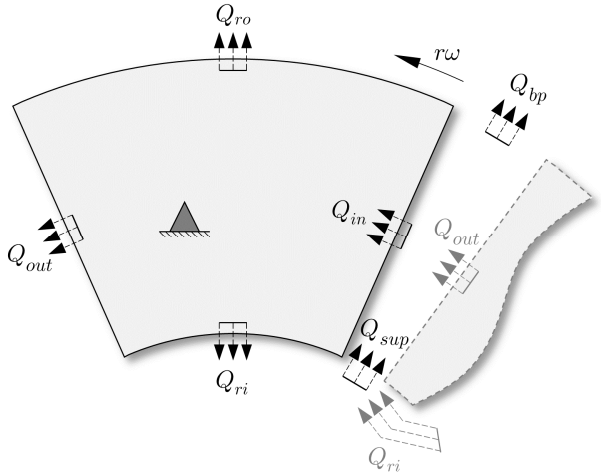

Figure 3.9 Thrust pad with lubricant flow rates.

This causes an increased oil temperature at the pad inlet and is commonly known as hot-oil-carry-over-effect. Due to the considerable influence of temperature on viscosity, this effect should be considered for accurate results. In the present work, this effect is modelled by assuming that the oil entering a pad (T_{in}, Q_{in}) is a homogeneous mixture of supply oil (T_{sup}, Q_{sup}) and oil transported over from the preceding pad [18, 230]. The oil transported over is comprised of the oil leaving the preceding pad's outlet (T_{out}, Q_{out}) and inner radius (T_{ir}, Q_{ir}):

$$T_{in} = \frac{T_{out}Q_{out} + T_{sup}Q_{sup} + T_{ir}Q_{ir}}{Q_{out} + Q_{sup} + Q_{ir}} \tag{3.27}$$

Due to the interdependency of T_{eff} and T_{in} an iterative temperature solver is utilized until thermal equilibrium is reached. Details of the numerical procedure is given in chapter 4.3.

3.5 Texture design optimization

The optimization of a texture design involves finding the geometrical texture design parameters that minimize or maximize a certain bearing performance parameter. This assembles a multidimensional constrained optimization problem:

$$\min_{\boldsymbol{x}} f(\boldsymbol{x}) \text{ subject to } \boldsymbol{x}_{lb} \leq \boldsymbol{x} \leq \boldsymbol{x}_{ub} \tag{3.28}$$

where $f(\boldsymbol{x})$ is the objective function, e.g. the frictional moment T_f, and $\boldsymbol{x} = (h_{texture}, \alpha, \beta)^t$ is a vector containing the geometrical texture design parameters subject to the lower and upper bounds $\boldsymbol{x}_{lb}$ and $\boldsymbol{x}_{ub}$. A maximization is made possible by simply multiplying the objective function with -1. Optimum texture density, shape and bottom profile are already known from literature and therefore not considered during the optimization (see chapter 2), i.e. $\boldsymbol{x}$ only contains the texture depth and relative texture extents in circumferential and radial direction. Texture patterns with $0\ \mu\text{m} \leq h_{texture} \leq 75\ \mu\text{m}$, $10\% \leq \alpha \leq 95\%$ and $10\% \leq \beta \leq 95\%$ are considered. As a value of zero is allowed for the texture depth, the conventional untextured design is automatically considered during the optimization. The optimization is performed by utilizing an interior-point algorithm. Solution details are given in chapter 4.4.

3.6 Summary

A mathematical model to analyse and optimize textured tilting pad thrust bearings was presented in this chapter. A polar coordinate system is utilized to describe the geometry of tilting pad thrust bearings. Texture patterns are defined by the following parameters:

- The number of textures in circumferential and radial direction (n_θ, n_r)
- The relative texture extent in circumferential and radial direction (α, β)
- The texture density in circumferential and radial direction (ρ_θ, ρ_r)
- The texture depth ($h_{texture}$)

This methodology allows to easily generate a variety of textured, grooved or pocketed pads. The Reynolds equation is used to describe the hydrodynamic pressure development. For accurate results, cavitation is taken into account in a mass-conserving way by respecting the JFO boundary conditions. Thermal effects are considered by applying an effective temperature method that takes into account the hot-oil-carry-over effect and considers the dependence of viscosity on the lubricant temperature.

Chapter 4

Numerical Solution

This chapter presents all implemented numerical procedures to solve the developed mathematical model. As the main focus of the present work is to facilitate the design of surface textures, the computational speed and robustness of the model are of vital importance. Therefore, a variety of advanced solution procedures find application and novel numerical methods were developed. In particular, the model is capable of efficiently treating film discontinuities, taking advantage of multicore processing and strategically combining three different root-finding techniques to find the bearing equilibrium most effectively.

4.1 Fluid solver

4.1.1 Discretization

The modified Reynolds equation (3.9) is a mixed-type partial differential equation for which no analytical solution exists, hence, a numerical solution is required. The numerical solution generally consists of a discretization of the governing equations and a subsequent solution of the resulting algebraic system with appropriate boundary conditions. For textured bearings, the finite volume method [231] (also known as control volume method) has been shown to be a good compromise between accuracy and implementation complexity [209, 210]. Therefore, this method is applied in this work to discretize the modified Reynolds equation. For conventional untextured pads, simple uniform meshes are used, i.e. all control volumes have the same size. For the textured pads on the other hand, non-uniform meshes are applied instead for the following reasons:

- A fine mesh can be used for textured pad areas, where the complex texture geometry requires a fine mesh, and a coarse mesh for untextured areas, where a coarse mesh is sufficient to describe the simple, smooth geometry resulting in a more efficient solution of the Reynolds equation.
- Control volume (CV) faces can be aligned with film thickness discontinuities to minimize discretization errors [215].
- Additional nodes can easily be placed around discontinuities to decrease discretization errors as discussed in chapter 5.1.2.

Three variations of the finite volume method are considered for the purpose of this work: A conventional non-uniform finite volume discretization (NUFVD), a version of this method where additional CVs are placed around film discontinuities (NUFVD+A) and a version of this method where discontinuities are directly incorporated during the derivation of the discrete system (MNUFVD). Details of these methods are given in the following.

4.1.1.1 Non-uniform finite volume discretization (NUFVD)

The solution domain ($\mathcal{F}$) is first divided into discrete CVs and nodes are placed at the centre of each volume (Figure 4.1).

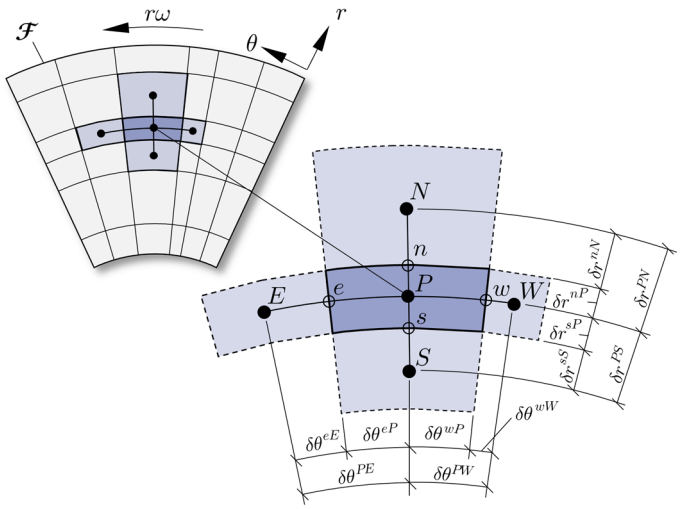

Figure 4.1 Non-uniform finite volume discretization (NUFVD) of the thrust pad with details of a control volume.

As flows normal to the pad surface are neglected, control volumes are actually areas, however, the same terminology is usually used. The general nodal point is defined as P and surrounding nodes are identified by their relative location, i.e. E for east, W for west, S for south and N for north. The faces or boundaries of the CVs are referred to accordingly by small letters. It is convenient to define the downstream direction

as east. Therefore, east is against expectation set to be on the left hand side when looking at the thrust pads from the runner's side.

The finite volume formulation of the Reynolds equation is based on the conservation of mass (continuity equation), which makes this method naturally mass-conserving. Consequently, it is possible to simply balance the flows into and out of a CV (Figure 4.2):

$$q^w - q^e + q^s - q^n = 0 \tag{4.1}$$

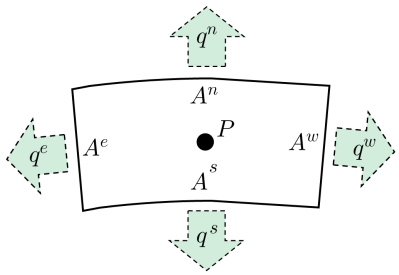

Figure 4.2 Control volume with mass inflows and outflows.

The flows over the cell faces can be expressed as:

$$q^w = -\frac{A^w}{r^w}\frac{\rho^w (h^w)^3}{\eta^w}\left(\frac{\partial p}{\partial \theta}\right)^w + 6\omega A^w r^w \Theta^w \rho^w h^w \tag{4.2}$$

$$q^e = -\frac{A^e}{r^e}\frac{\rho^e (h^e)^3}{\eta^e}\left(\frac{\partial p}{\partial \theta}\right)^e + 6\omega A^e r^e \Theta^e \rho^e h^e \tag{4.3}$$

$$q^s = -A^s r^s \frac{\rho^s (h^s)^3}{\eta^s}\left(\frac{\partial p}{\partial r}\right)^s \tag{4.4}$$

$$q^n = -A^n r^n \frac{\rho^n (h^n)^3}{\eta^n}\left(\frac{\partial p}{\partial r}\right)^n \tag{4.5}$$

where A^w, A^e, A^s and A^n are the CV's face dimensions. The pressure gradients at the CV faces are approximated by central finite difference formulae, given here only for the west cell boundary:

$$\left(\frac{\partial p}{\partial \theta}\right)^w = \frac{p^P - p^W}{\delta\theta^{PW}} \tag{4.6}$$

The other pressure gradients are approximated accordingly. The second terms of equations (4.2) and (4.3) are the Couette components of the flow that contain the fractional film content as a dependable variable. As the problem is of hyperbolic type in $\mathcal{D}^0$, the utilization of central finite difference schemes is not possible as one may get an ill solution. Upwind schemes on the other hand account for the direction of flow and are capable of correctly passing along the information about cavitation downstream. Therefore, upwind schemes are used in the present work, i.e. values of

the fractional film content are simply passed along downstream, i.e. $\Theta^w = \Theta^W$ and $\Theta^e = \Theta^P$. Although the accuracy may be improved by using type-dependent discretization schemes as proposed by Vijayaraghavan and Keith [160, 161], where different schemes are used for $\boldsymbol{\mathcal{D}}^+$ and $\boldsymbol{\mathcal{D}}^0$, upwind schemes are used for the entire solution domain.

With the introduction of interfacial diffusion coefficients for the Poiseuille terms as

$$\Gamma = \frac{\rho h^3}{\eta} \tag{4.7}$$

the flows at the CV faces can be expressed as

$$q^w \approx -\frac{A^w}{r^w}\Gamma^w \frac{p^P - p^W}{\delta\theta^{PW}} + 6\omega A^w r^w \Theta^W \rho^w h^w \tag{4.8}$$

$$q^e \approx -\frac{A^e}{r^e}\Gamma^e \frac{p^E - p^P}{\delta\theta^{PE}} + 6\omega A^e r^e \Theta^P \rho^e h^e \tag{4.9}$$

$$q^s \approx -A^s r^s \Gamma^s \frac{p^P - p^S}{\delta r^{PS}} \tag{4.10}$$

$$q^n \approx -A^n r^n \Gamma^n \frac{p^N - p^P}{\delta r^{PN}} \tag{4.11}$$

Unlike interfacial values of the pressure gradients, which remain constant between two nodes, interface values of the diffusion coefficients require special attention [171, 231]. Here, interfacial diffusion coefficients are evaluated by using linearly interpolated values for ρ, h^3 and η. Using the west face as an example:

$$\Gamma^w = \frac{\rho^w (h^w)^3}{\eta^w} \tag{4.12}$$

with

$$\rho^w = (1 - f^W)\rho^W + f^W \rho^P \tag{4.13}$$

$$h^w = (1 - f^W)h^W + f^W h^P \tag{4.14}$$

$$\eta^w = (1 - f^W)\eta^W + f^W \eta^P \tag{4.15}$$

where f^W is the interpolation factor given by:

$$f^W = \frac{\delta\theta^{wW}}{\delta\theta^{wW} + \delta\theta^{wP}} \tag{4.16}$$

Interfacial diffusion coefficients at the other cell faces are calculated accordingly. Finally, identifying the coefficients a^W, a^E, a^S, a^N, a^P, $a^{\Theta W}$ and $a^{\Theta P}$ and

rearranging, the equations for the nodal values of pressure and fractional film content are obtained:

$$p^P = \frac{1}{a^P}\left(a^W p^W + a^E p^E + a^S p^S + a^N p^N + a^{\Theta W}\Theta^W + a^{\Theta P}\Theta^P\right) \tag{4.17}$$

$$\Theta^P = -\frac{1}{a^{\Theta P}}\left(a^W p^W + a^E p^E + a^S p^S + a^N p^N - a^P p^P + a^{\Theta W}\Theta^W\right) \tag{4.18}$$

Formulating these equations for every internal node results in a linear algebraic system, which can be solved with appropriate boundary conditions. A full list of the used coefficients is given in Appendix A.1.

4.1.1.2 Non-uniform finite volume discretization (NUFVD+A)

Unlike methods based on the weak solution of the Reynolds equation, e.g. finite element methods, the FVM is based on boundary flux approximations, i.e. derivatives at film discontinuities directly depend on the mesh size. Particularly for textured surfaces this may cause major discretization errors as textures naturally introduce numerous discontinuities into the film thickness equation. Consequently, discontinuities should be treated in order to avoid large discretization errors or high computation times caused by fine meshes.

A first way of handling discontinuities is to place additional nodes around all discontinuities, i.e. around texture edges [14, 171, 217]. For the purpose of this work, an original methodology is utilized. The method is outlined in the following only for the east side of a certain CV, as the procedure is equivalent for the other sides. During the numerical mesh generation coordinates of all discontinuities CV boundaries are stored. Subsequently, the circumferential size of both adjacent CVs is evaluated. Additional CVs are then added on both sides of the discontinuity, having a circumferential size of

$$\widetilde{\delta\theta} = d_f \cdot \mathrm{MIN}[\delta\theta_{i,j}, \delta\theta_{i,j+1}] \tag{4.19}$$

where i and j are the positions of the CV in radial and circumferential direction respectively, and d_f is the *discontinuity coefficient* (Figure 4.3).

Using a very small value for the discontinuity coefficient can result in instability whereas a large value will not result in notable discretization error improvements. Good results are generally achieved for $d_f = 10^{-1}$ and therefore this value is used. The discrete system is assembled the same way as for the standard NUFVD method, although it is larger in size due to the additionally placed CVs.

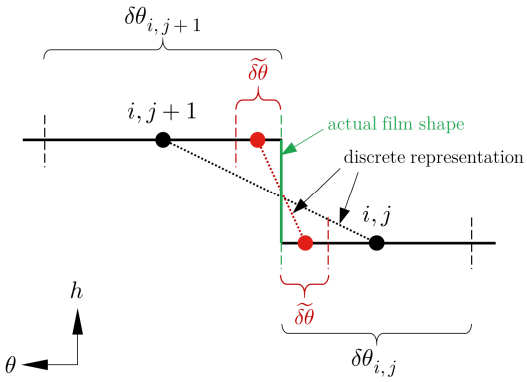

Figure 4.3 Schematic showing the placement of additional control volumes around a discontinuity.

4.1.1.3 Modified non-uniform finite volume discretization (MNUFVD)

Another way of treating discontinuities is to directly consider jumps in the film thickness during the derivation of the discrete system. This is based on the idea that the sudden variation in film thickness at discontinuities results in a sudden variation in pressure and consequently the pressure distribution itself becomes discontinuous. This effect is often referred to as *concentrated inertia* and can be considered by setting up a generalized Bernoulli equation just before and just after the jump in film thickness as follows:

$$p^- + \frac{\rho(U^-)^2}{2} = p^+ + \frac{\rho(U^+)^2}{2} + \xi\frac{\rho \cdot \mathrm{MAX}[U^-, U^+]^2}{2} \tag{4.20}$$

where "$-$" denotes the location just before the jump (upstream) and "$+$" the location just after the jump (downstream). p and U denote the local pressure and average fluid velocity at these locations and ξ is an additional correction factor or *pressure drop coefficient*. Values for ξ are not available in literature and need to be determined numerically or experimentally.

A way to incorporate this effect in a general finite volume discretization was proposed by Arghir *et al.* [215] and subsequently applied for textured slider bearings by Dobrica and Fillon [75]. In reference [75] it was also shown that the application of this method extents the validity of the Reynolds equation to flows with higher Reynolds numbers or deeper textures. Thus, implementing this method allows the application of Reynolds-based models for most textured bearings, avoiding the more time-consuming solution of the full Navier-Stokes system of equations. For the purpose of this work, this method is adapted in the following for the present non-uniform polar system in two dimensions. Note that the MNUFVD method is limited to the pressurized regions of the solution domain ($\boldsymbol{\mathcal{D}}^+$) where the Reynolds equation is elliptic, i.e. not in cavitation regions. The approach is only presented for a west cell boundary as the procedure is equivalent for the other CV faces.

Without the presence of a discontinuity, values for film thickness and pressure at the west boundary of a certain CV are identical to the values at the east boundary of the CV just upstream, i.e. $h^w_{i,j} = h^e_{i,j+1}$ and $p^w_{i,j} = p^e_{i,j+1}$ (Figure 4.4).

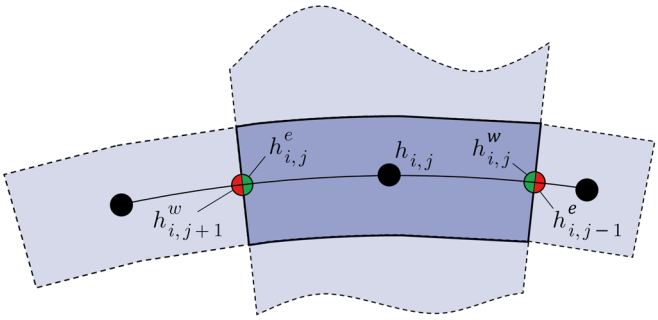

Figure 4.4 MNUFVD method: Additional boundary values for film thickness and pressure.

As described in reference [215], this no longer holds true if the west cell boundary is discontinuous, hence $h^w_{i,j} \neq h^e_{i,j+1}$ and $p^w_{i,j} \neq p^e_{i,j+1}$. However, the interface flux continuity must still be respected, i.e. $q^w_{i,j}$ must equal $q^w_{i,j+1}$. Using these additional interface values for film thickness and pressure, the aforementioned flow rate expression can be written as:

$$\begin{aligned} &-\frac{A^w_{i,j}}{r^w_{i,j}}\Gamma^w_{i,j}\frac{p^P_{i,j}-p^w_{i,j}}{\delta\theta^{wP}_{i,j}} + 6\omega A^w_{i,j} r^w_{i,j}\rho^w_{i,j}h^w_{i,j} \\ &\quad = -\frac{A^e_{i,j-1}}{r^e_{i,j-1}}\Gamma^e_{i,j-1}\frac{p^e_{i,j-1}-p^P_{i,j-1}}{\delta\theta^{eP}_{i,j-1}} + 6\omega A^e_{i,j-1} r^e_{i,j-1}\rho^e_{i,j-1}h^e_{i,j-1} \end{aligned} \tag{4.21}$$

Rearranging this, one obtains:

$$\begin{aligned} &\frac{A^w_{i,j}\Gamma^w_{i,j}}{r^w_{i,j}\delta\theta^{wP}_{i,j}}p^w_{i,j} + \frac{A^e_{i,j-1}\Gamma^e_{i,j-1}}{r^e_{i,j-1}\delta\theta^{eP}_{i,j-1}}p^e_{i,j-1} \\ &\quad = \frac{A^w_{i,j}\Gamma^w_{i,j}}{r^w_{i,j}\delta\theta^{wP}_{i,j}}p^P_{i,j} + \frac{A^e_{i,j-1}\Gamma^e_{i,j-1}}{r^e_{i,j-1}\delta\theta^{eP}_{i,j-1}}p^P_{i,j-1} + 6\omega A^e_{i,j-1} r^e_{i,j-1}\rho^e_{i,j-1}h^e_{i,j-1} \\ &\quad - 6\omega A^w_{i,j} r^w_{i,j}\rho^w_{i,j}h^w_{i,j} \end{aligned} \tag{4.22}$$

Introducing the coefficients $b^w_{i,j}$ and $b^e_{i,j-1}$, one can further simplify the expression above to:

$$\begin{aligned} &b^w_{i,j}p^w_{i,j} + b^e_{i,j-1}p^e_{i,j-1} \\ &\quad = b^w_{i,j}p^P_{i,j} + b^e_{i,j-1}p^P_{i,j-1} + 6\omega A^e_{i,j-1} r^e_{i,j-1}\rho^e_{i,j-1}h^e_{i,j-1} \\ &\quad - 6\omega A^w_{i,j} r^w_{i,j}\rho^w_{i,j}h^w_{i,j} \end{aligned} \tag{4.23}$$

The required expressions for the interface pressures $p^w_{i,j}$ and $p^e_{i,j-1}$ are now obtained from the generalized Bernoulli equation (4.20):

$$p^w_{i,j} = p^e_{i,j-1} + B^w \tag{4.24}$$

where the *interface Bernoulli coefficient* for the west cell boundary is defined as follows, where the density is considered to be constant:

$$B^w = -\frac{\rho(u^w_{i,j})^2}{2} + \frac{\rho(u^e_{i,j-1})^2}{2} - \xi\frac{\rho \cdot \mathrm{MAX}[u^w_{i,j}, u^e_{i,j-1}]^2}{2} \tag{4.25}$$

The required average velocities are calculated from the corresponding flow rates:

$$U^w_{i,j} = \frac{q^w_{i,j}}{h^w_{i,j}} \qquad \text{and} \qquad U^e_{i,j-1} = \frac{q^e_{i,j-1}}{h^e_{i,j-1}} \tag{4.26}$$

Equations (4.23) and (4.24) now allow the evaluation of the interface pressure values as:

$$\begin{aligned} p^w_{i,j} = \frac{1}{b^w_{i,j} + b^e_{i,j-1}} (&b^w_{i,j} p^P_{i,j} + b^e_{i,j-1} p^P_{i,j-1} + b^e_{i,j-1} B^w \\ &+ 6\omega A^e_{i,j-1} r^e_{i,j-1} \rho^e_{i,j-1} h^e_{i,j-1} - 6\omega A^w_{i,j} r^w_{i,j} \rho^w_{i,j} h^w_{i,j}) \end{aligned} \tag{4.27}$$

and

$$\begin{aligned} p^e_{i,j} = \frac{1}{b^w_{i,j} + b^e_{i,j-1}} (&b^w_{i,j} p^P_{i,j} + b^e_{i,j-1} p^P_{i,j-1} - b^w_{i,j} B^w \\ &+ 6\omega A^e_{i,j-1} r^e_{i,j-1} \rho^e_{i,j-1} h^e_{i,j-1} - 6\omega A^w_{i,j} r^w_{i,j} \rho^w_{i,j} h^w_{i,j}) \end{aligned} \tag{4.28}$$

Repeating this procedure for the interface pressures at the east, south and north CV faces and substituting the obtained expressions in the general continuity equation (4.1) allows to set up equations for the nodal values of pressure and frictional film content:

$$\begin{aligned} p^P = \frac{1}{a^P} (&a^W p^W + a^E p^E + a^S p^S + a^N p^N + a^{\Theta W} \Theta^W + a^{\Theta P} \Theta^P + B^P \\ &+ J^P) \end{aligned} \tag{4.29}$$

$$\begin{aligned} \Theta^P = -\frac{1}{a^{\Theta P}} (&a^W p^W + a^E p^E + a^S p^S + a^N p^N - a^P p^P + a^{\Theta W} \Theta^W + B^P \\ &+ J^P) \end{aligned} \tag{4.30}$$

with the *jump coefficient*

$$J^P = \frac{6\omega A^e_{i,j-1} r^e_{i,j-1} \rho^e_{i,j-1} h^e_{i,j-1} b^w_{i,j}}{b^w_{i,j} + b^e_{i,j-1}} - \frac{6\omega A^w_{i,j+1} r^w_{i,j+1} \rho^w_{i,j+1} h^w_{i,j+1} b^e_{i,j}}{b^e_{i,j} + b^w_{i,j+1}} \tag{4.31}$$

and the *Bernoulli coefficient*

$$B^P = a^W B^w + a^E B^e + a^S B^s + a^N B^n \tag{4.32}$$

Remaining coefficients are given in Appendix A.2. Expressions (4.29) and (4.30) are similar to the expressions used for the NUFVD and NUFVD+A methods, however, two new parameters are now present: J^P, which directly incorporates the jump in the film thickness distribution caused by introducing discontinuities through

texturing and B^P, which describes the effects of concentrated inertia at discontinuities through the generalized Bernoulli equation.

Whenever the jumps in film thickness and pressure are neglected, the equations reduce to the ones found for the NUFVD and NUFVD+A method. If the jump term is included, film thickness discontinuities are incorporated and the first order pressure derivatives become discontinuous. In this case the problem remains linear, as the interface film thicknesses are already known. If both the jump in film thickness and pressure are considered, i.e. $J^P \neq 0$ and $B^P \neq 0$, both effects are incorporated in the solution and the pressure and its first order derivatives become discontinuous. In this case, an additional preceding loop is required to deal with the nonlinearity of the discrete system by updating the velocities based on the flow rates found in previous iterations. Formulating this set of equations for all internal nodes of the solution domain enables an iterative solution of the system.

4.1.2 Adaptive mesh generation

The mesh is generated in a sub-function that divides the solution domain into discrete control volumes. If conventional, untextured pads are investigated, a uniform mesh is used, i.e. CVs have a uniform size and are evenly distributed over the entire pad area (Figure 4.5). For textured pads, a non-uniform mesh is used for enhanced computational performance and reduced discretization errors.

In this case, the method ensures an alignment of CV boundaries with texture edges (discontinuities). For best computational performance, the developed numerical procedure allows to define different mesh densities for different pad areas:

- The number of CVs inside each individual texture.
- The number of CVs in-between adjacent textures.
- The number of CVs for the untextured portions of the pad in circumferential and radial direction.

Nodes are placed at the centre of each CV and denoted by j and i in circumferential and radial direction respectively. The total number of nodes in circumferential and radial direction are defined by jj and ii respectively.

4.1.3 Gauss-Seidel method with successive relaxation

The discrete systems given in equations (4.17) and (4.18) for the NUFVD and NUFVD+A methods and equations (4.29) and (4.30) for the MNUFVD method are solved iteratively, as required by the applied mass-conserving cavitation algorithm.

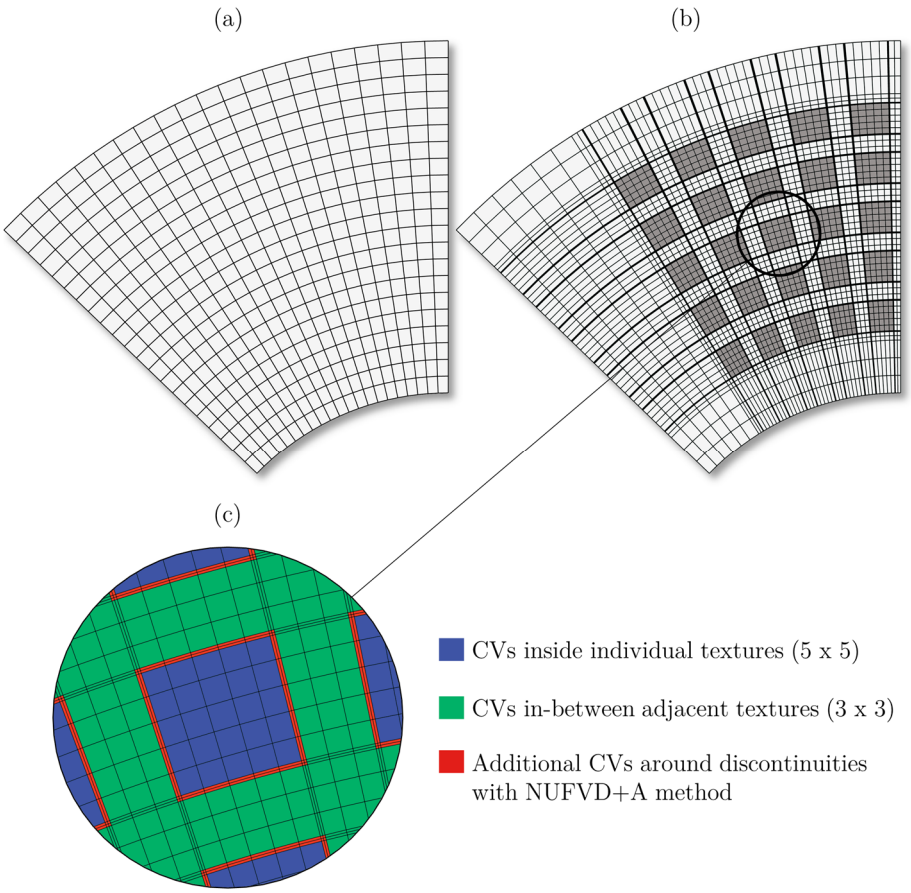

Figure 4.5 (a) Mesh for an untextured pad, (b) mesh for a textured pad and (c) mesh details around a single texture.

In the present work, a Gauss-Seidel method is utilized to update nodal values for p and Θ, i.e. new approximations are computed iteratively based on previously calculated approximations. To improve stability and computational speed, a relaxation technique finds application, where at each iteration k, nodal values for pressure and film content are approximated by:

$$p_{i,j}^{k} = p_{i,j}^{k-1} + \omega_p(\tilde{p}_{i,j}^{k} - p_{i,j}^{k-1}) \tag{4.33}$$

$$\Theta_{i,j}^{k} = \Theta_{i,j}^{k-1} + \omega_\Theta\left(\widetilde{\Theta}_{i,j}^{k} - \Theta_{i,j}^{k-1}\right) \tag{4.34}$$

where $\tilde{p}_{i,j}^{k}$ and $\widetilde{\Theta}_{i,j}^{k}$ are the nodal values found with the standard Gauss-Seidel method. ω_p and ω_Θ are the relaxation parameters for pressure and film content respectively. For relaxation parameters $0 < \omega < 1$ the procedure improves the numerical stability of the system and is called successive under-relaxation. For values of $\omega > 1$ the convergence speed is increased and the technique is called successive over-relaxation (SOR). The optimum relaxation parameter resulting in the fastest solution of the system depends on the size and stiffness of the discrete system itself and cannot easily be determined. In the present work, over-relaxation is used for pressure values and under-relaxation for fractional film content values.

4.1.4 Flow chart of the fluid solver

The fluid solver is responsible for obtaining the distributions of pressure and fractional film content over the thrust pad for given mesh details, film thickness distribution and lubricant temperature. This key step within the overall solution procedure is illustrated in Figure 4.6 and explained in detail in the following paragraphs.

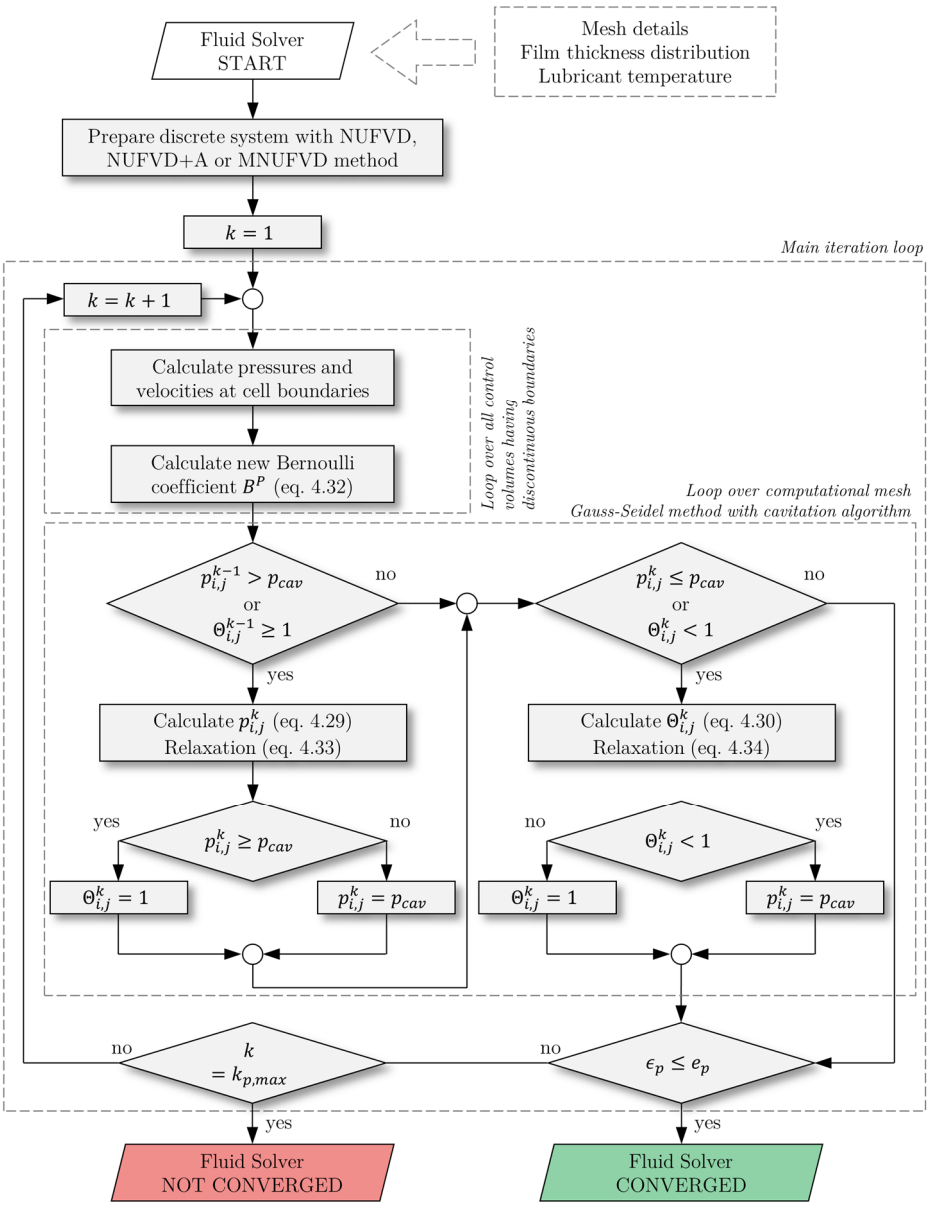

Figure 4.6 Flow chart of the fluid solver.

Once all mesh details, film thickness distribution and lubricant temperature are available, the fluid solver starts by preparing the discrete system with the NUFVD, NUFVD+A or MNUFVD method and calculating all coefficients required to solve equations (4.29) and (4.30) as given in Appendix A. As these factors remain constant during the solution procedure, they can be evaluated outside of the main iteration

loop. k denotes the current iteration and is set to 1 before the main iteration loop starts. If any of the control volumes contains discontinuities and the MNUFVD method is applied, the Bernoulli coefficient (B^P) is required and the interface pressures and average velocities need to be calculated based on the results of the previous iteration, adding a nonlinearity to the system. This is done in a preceding loop that only runs over the control volumes actually having discontinuities to safe computation time. For the first iteration these calculations are based on the initial guesses for p and Θ. For consecutive iterations values from the previous iteration are used.

After that, the loop over all internal nodes starts. This loop contains the mass-conserving cavitation algorithm and solves for pressure and fractional film content simultaneously based on the method described in chapter 3.2.2. It is first checked, whether cavitation took place at the current node during the last iteration (for the first loop this refers to the initial guess). If cavitation took place, only $\Theta^k_{i,j}$ is calculated using equation (4.30) and again, cavitation is checked. If cavitation occurs now, the pressure is set to p_{cav}, if not, $\Theta^k_{i,j}$ is set to 1. If cavitation did not take place during the previous iteration, $p^k_{i,j}$ is calculated using equation (4.29) and again cavitation is checked. If cavitation occurs now, the pressure is set to p_{cav} and $\Theta^k_{i,j}$ is evaluated, if not, $\Theta^k_{i,j}$ is set equal 1. This procedure is repeated for every internal node in the computational domain. This algorithm correctly divides the solution domain in active ($\boldsymbol{\mathcal{D}}^+$) and cavitated areas ($\boldsymbol{\mathcal{D}}^0$), i.e. ensures a correct prediction of film rupture and reformation.

Once all nodal values have been updated, the convergence of the solution is checked using the following criteria:

$$\varepsilon_p = \sum_{j=2}^{jj-1}\sum_{i=2}^{ii-1}\frac{\left|p^k_{i,j}-p^{k-1}_{i,j}\right|}{\left|p^k_{i,j}\right|} + \sum_{j=2}^{jj-1}\sum_{i=2}^{ii-1}\frac{\left|\Theta^k_{i,j}-\Theta^{k-1}_{i,j}\right|}{\left|\Theta^k_{i,j}\right|} \leq e_p \tag{4.35}$$

where ε_p is the sum of all nodal relative fractional residuals of both, pressure and film content and e_p is a predefined tolerance value. In the current study, $e_p = 10^{-6}$ unless otherwise stated. If convergence is reached, all results are stored and the fluid solver is terminated. If not, nodal values are updated as described above until convergence is reached or the maximum number of iterations is reached. If the maximum number of pressure iterations ($k_{p,max}$) is reached before $\varepsilon_p \leq e_p$, the fluid solver returns an error and stops.

The solution procedure for pressure and film content is computationally expensive. Also, the fluid solver is required numerous times during the overall solution procedure. Therefore, the solution of the Reynolds equation is performed directly in MATLAB only whenever the discrete system is linear. If the system is nonlinear, the computation is performed in a sub-routine that runs in C by using a C/MEX code as this was found to result in better performance.

4.2 Equilibrium solver

As described in chapter 3.3, the problem of finding the pad's equilibrium position can be formulated as a nonlinear system in three dimensions for point-pivoted pads and two dimensions for line-pivoted pads, in general:

$$\boldsymbol{F}(\boldsymbol{x}) = \boldsymbol{0} \tag{4.36}$$

The solution of this kind of problem is a key step in the simulation of tilting pad thrust bearings and other hydrodynamic bearings. In particular for textured bearings, a fast and robust solver for the equilibrium is crucial. Therefore, three nonlinear root-finding methods are introduced in the following and compared in chapter 5.1.4 to find the most suitable one for the purpose of this study (detailed descriptions of the applied methods can be found in literature, e.g. references [232, 233]):

- Newton-Raphson method
- Broyden's method with Sherman-Morrison Formula
- Continuation method with fourth-order Runge-Kutta technique

4.2.1 Newton-Raphson method

The Newton-Raphson method (or short Newton's method) is one of the most popular techniques to solve nonlinear root-finding problems and has been used extensively for the study of textured bearings (e.g. [16, 18, 220]). An initial approximation of the solution vector $\boldsymbol{x}^{k=0} = ({\alpha_r}^0, {\alpha_\theta}^0, {h_p}^0)^t$ is updated iteratively by the following expression:

$$\boldsymbol{x}^{k+1} = \boldsymbol{x}^k - \boldsymbol{\mathcal{J}}(\boldsymbol{x}^k)^{-1}\boldsymbol{F}(\boldsymbol{x}^k) \tag{4.37}$$

where $\boldsymbol{\mathcal{J}}(\boldsymbol{x}^k)^{-1}$ is the inverse of the Jacobian matrix at $\boldsymbol{x}^k$. To avoid the explicit evaluation of the inverse of the Jacobian, the linear system $\boldsymbol{\mathcal{J}}(\boldsymbol{x}^k)\boldsymbol{y}^k = -\boldsymbol{F}(\boldsymbol{x}^k)$ is first solved for $\boldsymbol{y}^k$. $\boldsymbol{x}^{k+1}$ is then calculated as $\boldsymbol{x}^{k+1} = \boldsymbol{x}^k + \boldsymbol{y}^k$. The required solution of the linear system $\boldsymbol{\mathcal{J}}(\boldsymbol{x}^k)\boldsymbol{y}^k = -\boldsymbol{F}(\boldsymbol{x}^k)$ at each iteration is obtained through the MATLAB function *mldivide*.

The initial guess ($\boldsymbol{x}^0$) consists either of user-defined values or already improved values from other algorithms or results from previous simulations. The iterative procedure stops when either convergence is reached or a user-defined maximum number of Newton iterations $k_{n,max}$ is reached.

4.2.2 Broyden's method with Sherman-Morrison formula

The major drawback of Newton's method is the necessity to evaluate the Jacobian matrix at each iteration. Although the method has a quadratic convergence, the determination of the Jacobian at each iteration can result in high computation times. Broyden's method is a Quasi-Newton method that only requires the computation of the Jacobian once. Although the convergence of this method is only superlinear, the computational effort during each iteration can be reduced significantly.

The first improvement of an initial guess is obtained with Newton's method, i.e. equation (4.37), requiring the determination of the Jacobian. For subsequent iterations, however, new solutions are found with the following expression:

$$\boldsymbol{x}^{k+1} = \boldsymbol{x}^k - (A^k)^{-1}\boldsymbol{F}(\boldsymbol{x}^k) \tag{4.38}$$

Note that the only difference to Newton's method is the use of the inverse of A^k instead of the inverse of the Jacobian. $(A^k)^{-1}$ is calculated based on a Secant method as follows:

$$A^k = A^{k-1} + \frac{\boldsymbol{y}^k - A^{k-1}\boldsymbol{s}^k}{\|\boldsymbol{s}^k\|_2^2}(\boldsymbol{s}^k)^t \tag{4.39}$$

with

$$\boldsymbol{y}^k = \boldsymbol{F}(\boldsymbol{x}^k) - \boldsymbol{F}(\boldsymbol{x}^{k-1}) \tag{4.40}$$

$$\boldsymbol{s}^k = \boldsymbol{x}^k - \boldsymbol{x}^{k-1} \tag{4.41}$$

The matrix inversion formula of Sherman and Morrison allows to efficiently calculate the inverse of A^k directly from $(A^{k-1})^{-1}$, while also avoiding the time-consuming solution of the linear system $A^k\boldsymbol{s}^{k+1} = -\boldsymbol{F}(\boldsymbol{x}^k)$:

$$A^k = A^{k-1}\frac{(\boldsymbol{s}^k - (A^{k-1})^{-1}\boldsymbol{y}^k)(\boldsymbol{s}^k)^t(A^{k-1})^{-1}}{(\boldsymbol{s}^k)^t(A^{k-1})^{-1}\boldsymbol{y}^k} \tag{4.42}$$

The inverse of the Jacobian matrix during the first iteration (Newton's method) is evaluated through the MATLAB function *inv*, where a LU decomposition is performed to obtain the inverse.

4.2.3 Continuation method with fourth-order Runge-Kutta technique

Another powerful tool for finding the equilibrium position, especially whenever a good first approximation is unavailable, is called continuation or homotopy method. The idea behind this method is to transform the problem $\boldsymbol{F}(\boldsymbol{x}) = \boldsymbol{0}$ into a collection

of problems by using a parameter $\Lambda = [0,1]$. This can be achieved by defining a convex homotopy $\boldsymbol{G}(\Lambda, \boldsymbol{x})$, which allows the connection of the functions $\boldsymbol{G}(0, \boldsymbol{x})$ and $\boldsymbol{G}(1, \boldsymbol{x})$ as follwos:

$$\boldsymbol{G}(\Lambda, \boldsymbol{x}) = \boldsymbol{F}(\boldsymbol{x}) + (\Lambda - 1)\boldsymbol{F}\big(\boldsymbol{x}(0)\big) \tag{4.43}$$

Here, $\boldsymbol{G}(0, \boldsymbol{x})$ is a problem with known solution, corresponding to an initial film thickness guess $\boldsymbol{x}(0)$ and $\boldsymbol{G}(1, \boldsymbol{x})$ is the original problem with unknown solution, corresponding to film thickness at equilibrium $\boldsymbol{x}(1)$, where the set $\{\boldsymbol{x}(\Lambda)|0 \leq \Lambda \leq 1\}$ can be interpreted as an arc or curve parameterized by Λ. It is now possible to proceed from $\Lambda = 0$ to $\Lambda = 1$ in a finite number of steps (N). If the involved functions are differentiable, the Implicit Function Theorem allows to set up the following expression for $\boldsymbol{x}'(\Lambda)$:

$$\boldsymbol{x}'(\Lambda) = -\boldsymbol{\mathcal{J}}\big(\boldsymbol{x}(\Lambda)\big)^{-1}\boldsymbol{F}\big(\boldsymbol{x}(0)\big) \tag{4.44}$$

This system of ordinary differential equations can now be solved using standard methods to find the solution $\boldsymbol{x}(1)$ of the original problem $\boldsymbol{F}(\boldsymbol{x}) = \boldsymbol{0}$, i.e. the equilibrium position of the pad. The method used in this work to solve the set of differential equations is the classic fourth-order Runge-Kutta method. Each step N requires the solution of four linear systems, which are solved by the MATLAB function *mldivide*.

4.2.4 Computation of the Jacobian matrix

Solving the nonlinear system given in equation (4.36) always involves the evaluation of all first-order partial derivatives of $\boldsymbol{F}$ for a certain $\boldsymbol{x}^k$. The matrix containing these derivatives is called Jacobian matrix and for point-pivoted pads takes the form:

$$\boldsymbol{\mathcal{J}}(\boldsymbol{x}^k) = \begin{bmatrix} \dfrac{\partial \delta W}{\partial \alpha_r}(\boldsymbol{x}^k) & \dfrac{\partial \delta W}{\partial \alpha_\theta}(\boldsymbol{x}^k) & \dfrac{\partial \delta W}{\partial h_p}(\boldsymbol{x}^k) \\ \dfrac{\partial \delta \theta}{\partial \alpha_r}(\boldsymbol{x}^k) & \dfrac{\partial \delta \theta}{\partial \alpha_\theta}(\boldsymbol{x}^k) & \dfrac{\partial \delta \theta}{\partial h_p}(\boldsymbol{x}^k) \\ \dfrac{\partial \delta r}{\partial \alpha_r}(\boldsymbol{x}^k) & \dfrac{\partial \delta r}{\partial \alpha_\theta}(\boldsymbol{x}^k) & \dfrac{\partial \delta r}{\partial h_p}(\boldsymbol{x}^k) \end{bmatrix} \tag{4.45}$$

As no analytical expressions are available to calculate the partial derivatives, finite difference formulae are utilized to determine the Jacobian matrix. For example, the first element of the matrix is approximated by the following perturbation:

$$\frac{\partial \delta W}{\partial \alpha_r}(\boldsymbol{x}^k) \approx \frac{\delta W(\boldsymbol{x}^k + \boldsymbol{x}^k \boldsymbol{e}_1 f_t) - \delta W(\boldsymbol{x}^k)}{\alpha_r f_t} \tag{4.46}$$

where $\boldsymbol{e}_1$ is a vector whose only nonzero entry is 1 in the α_r direction and f_t is a

used-defined offset factor (in the present work $f_t = 0.01$). All other elements of the Jacobian matrix are approximated accordingly. A single determination of the Jacobian matrix requires the complete evaluation of pressure and film content distributions for four different film thickness distributions and a subsequent computation of load carrying capacity and centre of pressure. As the elements of the Jacobian are independent from each other, a simultaneous evaluation on multiple processor cores is possible and utilized in the present model whenever free cores are available.

Although good convergence behaviour is usually encountered, a particularly poor initial guess for the film thickness distribution may at times lead to numerical instability. Therefore, an original empirical damping procedure is used for the Newton-Raphson method and Broyden's method, where the Jacobian is replaced by a *damped Jacobian*:

$$\boldsymbol{\mathcal{J}}_{damped} = c_d \boldsymbol{\mathcal{J}} \tag{4.47}$$

where c_d is a damping coefficient, which reduces the step size by artificially increasing the elements of the Jacobian and is defined as:

$$c_d = \frac{D}{k^2} + 1 \tag{4.48}$$

D is a factor that allows to control the damping intensity (Figure 4.7).

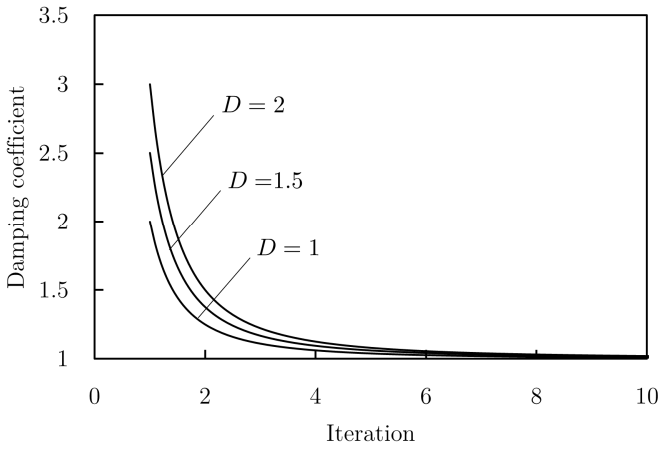

Figure 4.7 Damping coefficient for different values of D.

Several test simulations have shown that a damping intensity of $D = 1.5$ results in improved stability and computation time for most cases, therefore this value is used whenever damping is required, otherwise $D = 0$ and equation (4.47) reduces to the normal Jacobian matrix.

4.2.5 Flow chart of the equilibrium solver

The proposed numerical procedure to find the pads equilibrium position is based on the idea of using Broyden's method. Broyden's method does not usually work as a standalone method, as the initial guess needs to be sufficiently close to the actual solution. Three ways to address this issue are proposed and implemented in the present model:

- Newton's method or the Continuation algorithm are performed for a limited number of iterations first. This is usually enough to obtain a sufficiently good solution to start Broyden's method.
- The equilibrium position is first found for an equivalent untextured pad. Due to the much coarser meshes required, this only takes a fraction of the time as compared to finding the equilibrium position for a textured pad. Although the introduction of surface textures obviously changes the equilibrium position, both solutions are usually close enough to use the *untextured solution* as first approximation for the *textured solution*.
- The effective temperature is found iteratively, i.e. the equilibrium position needs to be updated a number of times (requiring a multiple execution of the equilibrium solver). Once the equilibrium position is found for the first temperature iteration, the results are usually good enough to be used as a first approximation for Broyden's method for the next temperature iteration.

The implemented procedure to find the pad's equilibrium position is shown in Figure 4.8.

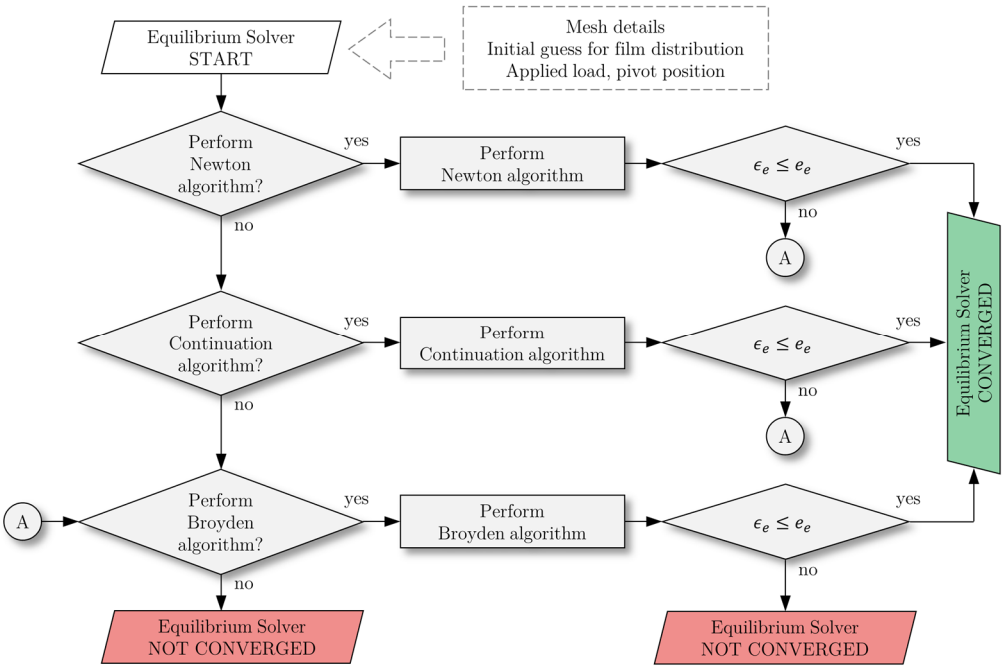

Figure 4.8 Flow chart of the equilibrium solver.

The procedure starts with a first guess for the solution (a user-defined initial guess for the film thickness distribution). This first guess is then updated by one of the pre-algorithms (Newton's method or Continuation method), if necessary. If the solution already converges during the execution of the pre-algorithm, the results are stored and the procedure is terminated. If not, Broyden's method is performed to further update the solution until convergence is reached. The following convergence criteria is used for the equilibrium solver:

$$\varepsilon_e = \frac{|\delta W^k|}{W_0} + \frac{|\delta \theta^k|}{\theta_p} + \frac{|\delta r^k|}{r_p} \leq e_e \tag{4.49}$$

where e_e is the tolerance value for the pad's equilibrium position. A value of 10^{-4} is used in this work if not otherwise specified. For line-pivoted pads, the third term of equation (4.49) is omitted.

Intermediate results are continuously stored and used as first approximations. Also, obtained pressure and film thickness distributions are stored and used as first guesses for the fluid solver if the film thickness distribution is similar. The proposed method is very robust and results in a very efficient solution of the problem. A comparative analysis of different solution strategies is performed in chapter 5.1.4.

4.3 Temperature solver

The thermal model is based on an iterative effective temperature or effective viscosity method, while additionally considering changes in the inlet temperature caused by the hot-oil-carry-over effect as discussed in chapter 3.4. Both these methods are iterative procedures and require a multiple determination of the bearing equilibrium.

4.3.1 Flow chart of the temperature solver

The implemented procedure is shown in Figure 4.9 and explained in the following. For the first iteration both effective temperature and inlet temperature are set equal to the supply oil temperature. Based on this information, an initial effective viscosity is determined according to equation (3.12) and the equilibrium solver is called to evaluate the frictional power loss as well as the lubricant flow rates into and out of the thrust pad. Following this, new values for effective temperature are computed as follows:

$$T_{eff}{}^{k+1} = T_{in}{}^{k} + k_{con} \frac{\Pi^k}{Q_{in}{}^{k} \rho c_p} \tag{4.50}$$

The new inlet temperature is then calculated as:

$$T_{in}{}^{k+1} = \frac{T_{out}{}^{k} Q_{out}{}^{k} + T_{sup} Q_{sup} + T_{ir}{}^{k} Q_{ir}{}^{k}}{Q_{out}{}^{k} + Q_{sup} + Q_{ir}{}^{k}} \tag{4.51}$$

where it is assumed that $T_{out}{}^{k} = 2T_{eff}{}^{k+1} - T_{in}{}^{k}$ and $T_{ir}{}^{k} = T_{eff}{}^{k+1}$. Subsequently, the effective viscosity is updated and the procedure is repeated until thermal equilibrium or the maximum number of temperature iterations ($k_{t,max}$) is reached.

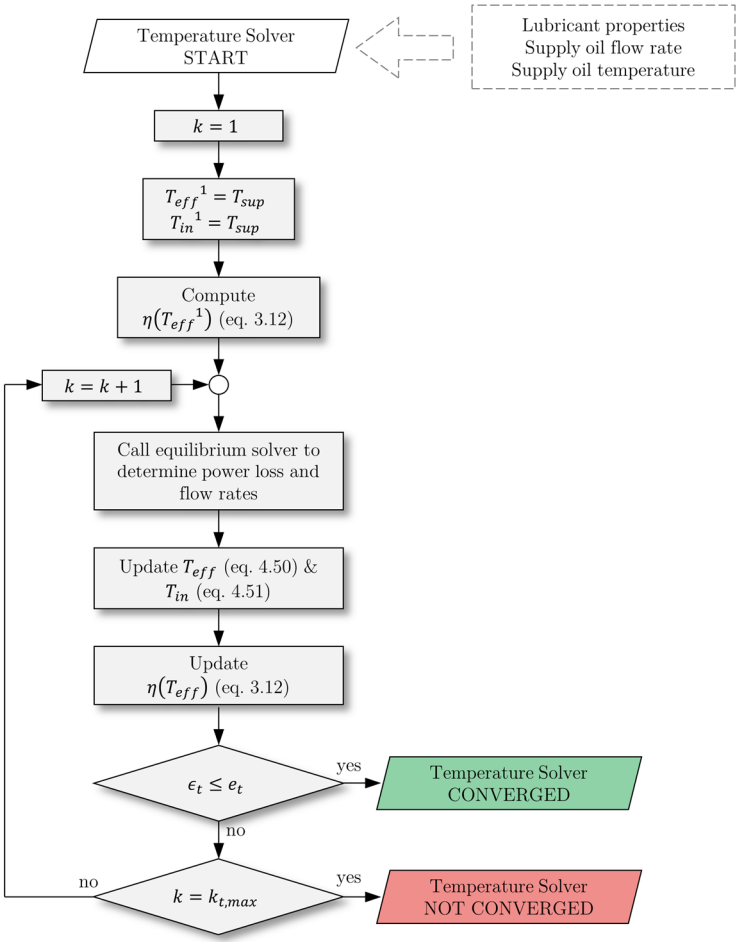

Figure 4.9 Flow chart of the temperature solver.

The temperature convergence criteria used in this work is

$$\varepsilon_t = \frac{\left| T_{eff}^{k} - T_{eff}^{k-1} \right|}{T_{eff}^{k}} \leq e_t \tag{4.52}$$

where a value of 10^{-5} is normally used for e_t. All intermediate results obtained during one temperature iteration (results of the equilibrium solver, different pressure and film thickness distributions) are stored and used as first approximations for the next temperature iteration to decrease computation time.

4.4 Optimization solver

4.4.1 Interior-point method

Finding optimum geometrical texture design parameters requires the solution of the constrained minimization problem given in equation (3.28). In the present work an interior-point algorithm (also called barrier method) is utilized to obtain this solution. The basic strategy is to transform the inequality constraints of the original problem by a logarithmic barrier function. The arising approximate problem is a sequence of equality constrained problems, which are easier to solve than the original problem.

The optimization is performed in MATLAB with the function *fmincon* [234], using forward finite difference formulae to evaluate the gradients of the objective functions, where multiple processor cores are utilized if available. Start values of $\boldsymbol{x} = (10\ \mu\text{m}, 50\%, 50\%)^t$ and a step tolerance of 10^{-8} are used. For more details on interior-point algorithms, the reader is referred to [235-237].

4.4.2 Flow chart of the optimization solver

The optimization procedure is shown in Figure 4.10 and starts by evaluating the objective function $f(\boldsymbol{x})$ as well as its gradient $\nabla f(\boldsymbol{x})$ by utilizing the fluid, equilibrium and temperature solvers.

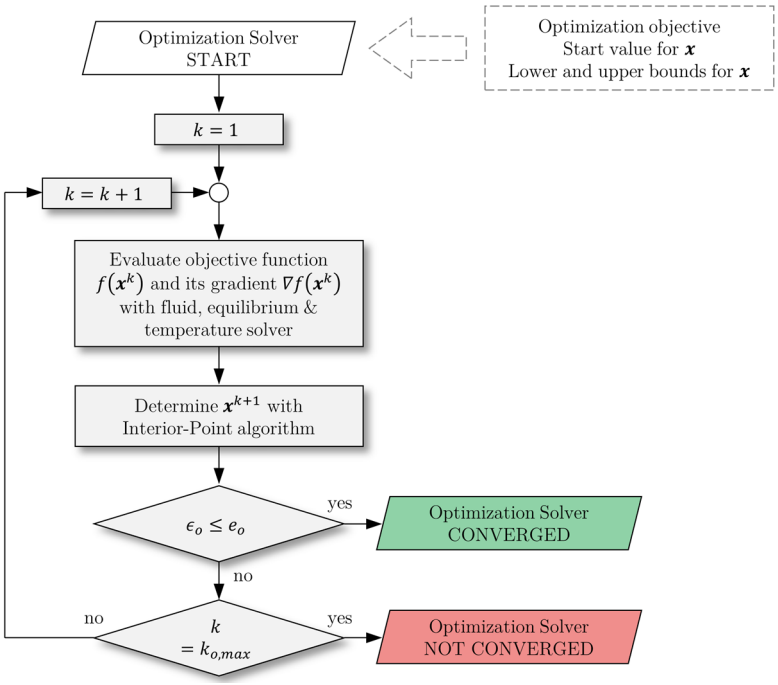

Figure 4.10 Flow chart of the optimization solver.

Note that a total of four complete bearing simulations is required to determine the gradient of the objective function as the texture design vector has three elements ($\boldsymbol{x} = (h_{texture}, \alpha, \beta)^t$). These four evaluation are performed on multiple threads if available to save computation time. The procedure stops when the first order optimality is equal to or smaller than the specified optimality tolerance ($\epsilon_o \leq e_0$) or the computed step is smaller than the predefined step tolerance of 10^{-8}. For all simulations, an optimality tolerance of $e_0 = 10^{-5}$ is used.

4.5 Assembled model (TPT5)

The present model *TPT5* (*Tilting Pad Texturing version 5*) was developed in MATLAB and is capable of efficiently evaluating the performance of untextured and textured thrust bearings having tilting pads or fixed pads (friction torque, minimum film thickness, maximum temperature etc.). The model also allows to perform arbitrary parametric studies as well as texture optimization studies. The numerical details and implemented solution strategies are easily adaptable to study other textured or untextured hydrodynamic bearings, as the basic principles are the same. The model requires one input **.txt* file, that contains a total of 89 parameters, including the bearing and texture geometry, lubricant properties, operating conditions as well as parameters to control the computation such as the mesh details, tolerance values for the different solvers and output preferences. An exemplary input file is given in Appendix B1 for reference. To facilitate post-processing, all results are saved in a single **.csv* file. A typical output file for a parametric simulation can be found in Appendix B2. Appendix C contains an overview of all developed MATLAB scrips, functions and apps.

4.5.1 Flow chart of the assembled model

A simplified flow chart of the model is illustrated in Figure 4.11 and explained in detail in the following paragraphs. First, all input variables are imported from the input file into MATLAB. The names of the MATLAB workspace variables are created dynamically based on the names specified in the input file. Following this, the mesh is generated and the discrete system is prepared using the NUFVD, NUFVD+A or MNUFVD method. After this, the Reynolds equation is solved using the iterative Gauss-Seidel method with successive relaxation in combination with the mass-conserving cavitation algorithm until pressure convergence is reached ($\varepsilon_p \leq e_p$). The film thickness distribution, i.e. pitch, tilt and roll angles, are then updated using a combination of the Newton, Broyden and Continuation algorithms until the pads are in equilibrium ($\varepsilon_e \leq e_e$). The effective temperature method is subsequently

applied to update effective temperature, inlet temperature and effective lubricant viscosity until thermal equilibrium is reached ($\varepsilon_t \leq e_t$).

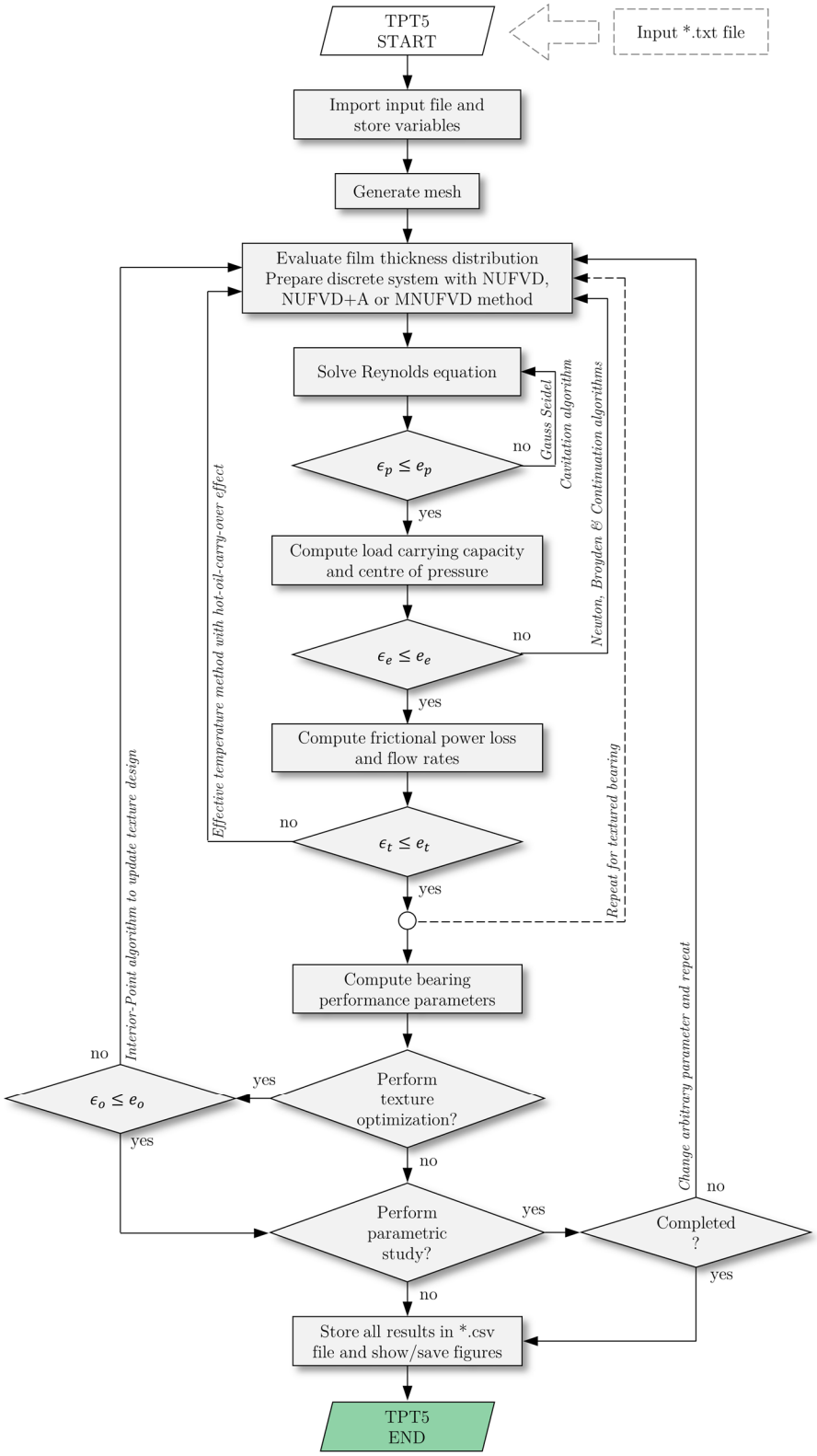

Figure 4.11 Flow chart of the assembled model (TPT5).

This series of steps is initially executed for the equivalent untextured bearing, where a coarse and uniform mesh is used, and then repeated for the textured bearing using

all results from the untextured bearing. As discussed in chapter 5.1.4, this leads to a significant reduction in computation time. What follows is the computation of all bearing performance parameters, such as power loss, flow rates, coefficient of friction etc. If an optimization study is run, this procedure is performed multiple times to evaluate the specified objective function and its gradient to update the texture design until the optimality reaches a satisfactory value. This entire simulation – including the optimization – can be performed as a parametric study, e.g. for varying load and speed conditions, by simple specifying a parameter and corresponding range in the input file. Once all simulations are completed, all results are stored in a single **.csv* file for easy post-processing. Export files containing detailed information about the pressure and film thickness distribution are stored optionally.

4.6 Summary

This chapter was concerned with the utilized numerical procedures to solve the mathematical model presented in chapter 3.

The fluid solver is based on a non-uniform finite volume discretization (NUFVD) of the modified Reynolds equation (3.9). Two ways of improving this method in terms of accuracy and computational speed were developed for the purpose of this work:

- A non-uniform finite volume discretization, where additional control volumes are placed closely around film discontinuities (NUFVD+A).
- A modified non-uniform finite volume discretization, where film discontinuities are directly incorporated in the direct system (MNUFVD).

To maximize the efficiency of the equilibrium solver, three root finding techniques are implemented:

- A conventional Newton-Raphson method.
- Broyden's method with Sherman-Morrison formula.
- A continuation method with fourth-order Runge-Kutta technique.

The solver also allows the utilization of a combination of these methods. The discretization methods and root-finding methods are compared and selected in chapter 5. The thermal equilibrium is solved by applying an iterative effective temperature method, where the hot-oil-carry-over effect is incorporated. Furthermore, the developed model allows the optimization of texture patterns by using an interior-point algorithm and the simulation of arbitrary parametric studies.

Chapter 5

Model Improvement and Validation

This chapter is concerned with the improvement of the developed numerical framework described in the previous chapters in terms of computational speed and robustness. For this purpose, the three previously introduced discretization methods are compared:

- A non-uniform finite volume discretization (NUFVD).
- A version of this method, where additional nodes are placed around discontinuities (NUFVD+A).
- A modification to this method, where discontinuities are directly incorporated in the discrete system (MNUFVD).

Also, possible improvements by taking advantage of multiple processor cores are analysed and three equilibrium solvers (Newton-Raphson method, Broyden's method and a continuation approach) as well as combinations of these methods are compared. To ensure a correct implementation and judge the accuracy of the computational results, three validation cases are presented at the end of this chapter: a spherical cap dimple, a journal bearing and a tilting pad thrust bearing.

All simulations are performed on a desktop workstation with INTEL CORE i7-3770 @ 3.40 GHz CPU and 16 GB of RAM.

5.1 Model improvement

5.1.1 Considered bearing and operating conditions

The bearing considered for the purpose of this chapter is a partially textured point-pivoted tilting pad thrust bearing (Figure 5.1).

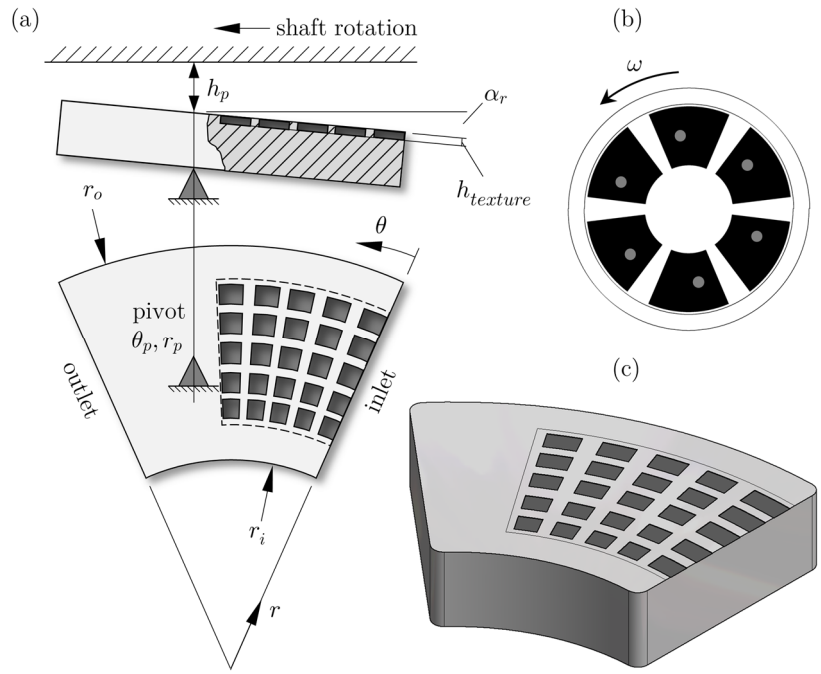

Figure 5.1 (a) Pad details with coordinate system, (b) tilting pad thrust bearing geometry and (c) texture pattern with $\alpha = \beta = 70\%$ and $\rho_{texture} = 40\%$.

A relatively simple texture design with 5 x 5 textures is used to introduce discontinuities in the film thickness distribution in order to keep the computation times low and facilitate comparing the different numerical methods. However, conclusions will still hold true for more complex texture designs as higher numbers of textures only scale the size of the encountered discrete system. The complete list of input parameters is given in Table 5.1. For thrust pad bearings it is common to use a specific applied load rather than an absolute applied load, which is defined as load per active thrust area and usually given in MPa.

5.1.2 Comparison of discretization methods

To compare the three discretization methods described in chapter 4.1.1 in terms of computational speed and accuracy, a mesh study is conducted. The model is run for

a given film thickness and effective temperature, i.e. only the fluid solver is utilized. The pre-defined film thickness and effective temperature are chosen to be approximately corresponding to a bearing operation at 1.0 MPa specific load. All input parameters are given in Table 5.2.

Table 5.1 Bearing geometry and operating conditions.

Description	Symbol	Quantity
Bearing geometry		
Number of pads	n_{pad}	6
Inner pad radius (mm)	r_i	57.15
Outer pad radius (mm)	r_o	114.3
Pad angle (°)	θ_{pad}	50
Circumferential coordinate of pivot (°)	θ_p	30
Radial coordinate of pivot (mm)	r_p	85.725
Operating conditions		
Applied specific load (MPa)	w_0	0.5 – 2.0
Rotational speed (rpm)	ω	1500 and 3000
Lubricant		ISO VG 46
Density (kg/m^3)	ρ	855
Viscosity at 40°C (cSt)	ν_{40}	42.646
Viscosity at 100°C (cSt)	ν_{100}	6.499
Supply oil flow rate (l/min)	Q_{sup}	15
Supply oil temperature (°C)	T_{sup}	50
Lubricant specific heat (J/kg/K)	c_p	2035

Table 5.2 Input parameters for the mesh study.

Description	**Symbol**	**Quantity**
Film thickness at pivot position (µm)	h_p	50
Pitch angle (µrad)	α_r	400
Roll angle (µrad)	α_θ	-185
Rotational speed (rpm)	ω	3000
Effective temperature (°C)	T_{eff}	70
Texture depth (µm)	$h_{texture}$	15
Texture extent in circumferential direction (%)	α	70
Texture extent in radial direction (%)	β	70
Texture density in circumferential direction (%)	ρ_θ	63.25
Texture density in radial direction (%)	ρ_r	63.25
Inlet textured?		yes

After running numerous simulations, it was found that the predicted load carrying capacity is the parameter most influenced by the mesh size. Therefore, this parameter

is used for the mesh study. The procedure used to compare the discretization methods is similar to the one used by Woloszynski *et al.* [210] and is briefly explained in the following. The Reynolds equation is solved for an initial coarse mesh and subsequently the corresponding load carrying capacity is evaluated. This is done for the NUFVD, NUFVD+A and MNUFVD method successively. The MNUFVD method is used without the consideration of concentrated inertia effects at discontinuities, i.e. $B^P = 0$. The initial mesh consists of 2 CVs inside each texture, 1 CV in-between adjacent textures, 4 CVs for the untextured pad area in circumferential direction and 2 CVs each for the untextured pad areas in radial direction; or in short notation: 2 / 1 / 4 / 2. This corresponds to a mesh with a total of 20 x 20 CVs, hence 400 degrees of freedom (DOF). The mesh is then iteratively refined using a global refinement factor of 1.25 and the calculations are repeated. This is done for a total of 17 meshes, resulting in a finest mesh with 458329 DOF (71 / 36 / 142 / 71). For every refinement, the consecutive error, i.e. the difference in predicted load carrying capacity between the current and previous mesh iteration, is evaluated. After all consecutive errors are known for all discretization methods and meshes, the predicted load carrying capacity of the method and mesh resulting in the smallest consecutive error is used as a reference value. This allows to evaluate the required DOF to reach a certain error with respect to the reference value for all three discretization methods and meshes.

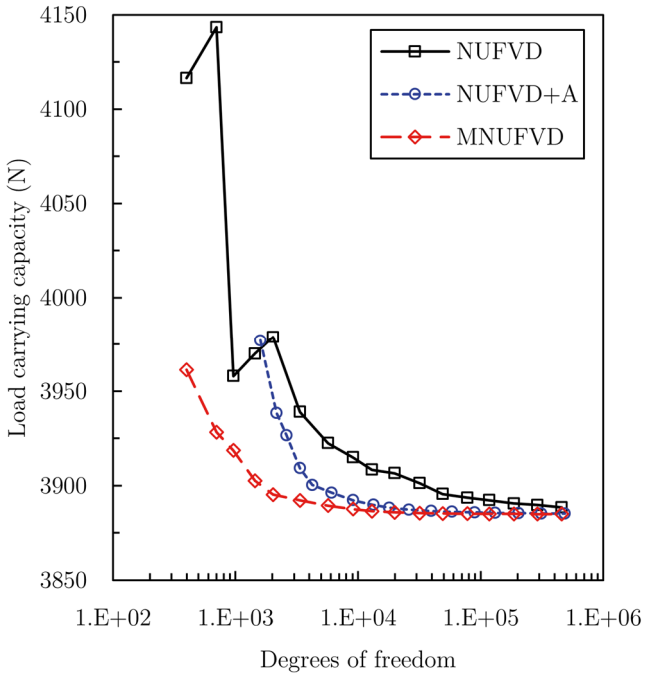

Figure 5.2 Load carrying capacity as predicted by the different discretization methods for different meshes.

Figure 5.2 shows the predicted load carrying capacity for the different meshes and discretization methods. Results are plotted over DOF rather than a mesh index as additional CVs are added when using the NUFVD+A method.

A clear trend towards a common load carrying capacity of approximately 3885 N can be observed for all methods. For all meshes studied, the MNUFVD method showed the smallest consecutive errors, followed by the NUFVD+A method. Largest errors were obtained with the NUFVD method. Therefore, the reference value is determined by the MNUFVD method at the finest mesh ($W_{ref} = 3884.95$ N). The relative differences to the reference value can now be evaluated for all methods and meshes (Figure 5.3).

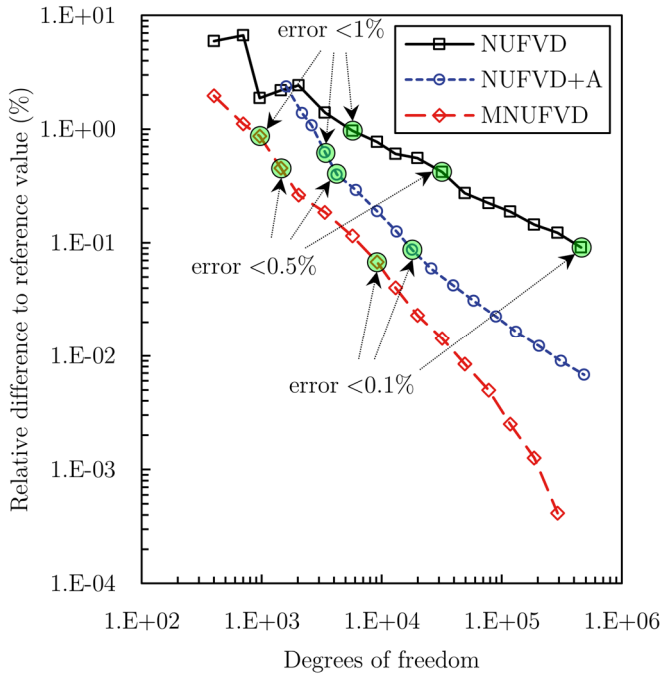

Figure 5.3 Relative differences to the reference value for different discretization methods and meshes.

It is evident that the MNUFVD exhibits superior performance, followed by the NUFVD+A method. Highest errors are obtained when using the NUFVD method. As the expected influence of surface texturing on the load carrying capacity usually lies in a single figure percent range, the DOF required to achieve errors of 1%, 0.5% and 0.1% are compared. Note however that the evaluated required DOF are approximations as the meshes are refined incrementally. The conventional NUFVD method requires 5700, 31862 and 458329 DOF to achieve errors of 1%, 0.5% and 0.1% respectively. If additional nodes are placed around discontinuities (NUFVD+A), these errors can be achieved with much coarser meshes. Only 3364, 4225 and 17956 DOF are required to achieve errors of 1%, 0.5% and 0.1% respectively, resulting in a considerably more efficient solution of the Reynolds equation. The lowest number of DOF is required by the MNUFVD method, where errors of 1%, 0.5% and 0.1% are achieved with 961, 1444 and 9120 DOF respectively.

The pressure distribution obtained with the NUFVD+A method for 17956 DOF is shown in Figure 5.4 for example.

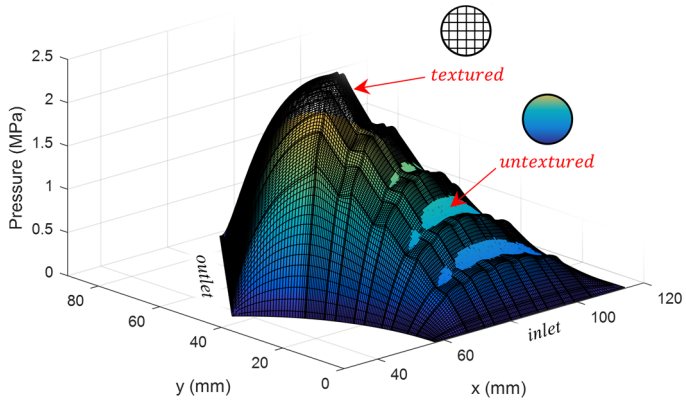

Figure 5.4 Predicted pressure distribution for the textured pad with the NUFVD+A method and 17956 DOF and predicted pressure distribution for the equivalent untextured pad as obtained with a uniform mesh of 51 x 51 CVs.

For reference, the pressure distribution for the equivalent untextured pad is also plotted. It is evident that the texture pattern has a significant influence on the pressure development and is clearly reflected in the pressure distribution. Although closer to the pad inlet pressures are partially below the equivalent untextured pad, the maximum pressure is considerably increased from 1.88 MPa to about 2.39 MPa at the last texture row's edge, resulting in a higher load carrying capacity and potentially superior bearing performance. Figure 5.5 shows the pressure distribution at the pad's mean radius for the three discretization methods investigated.

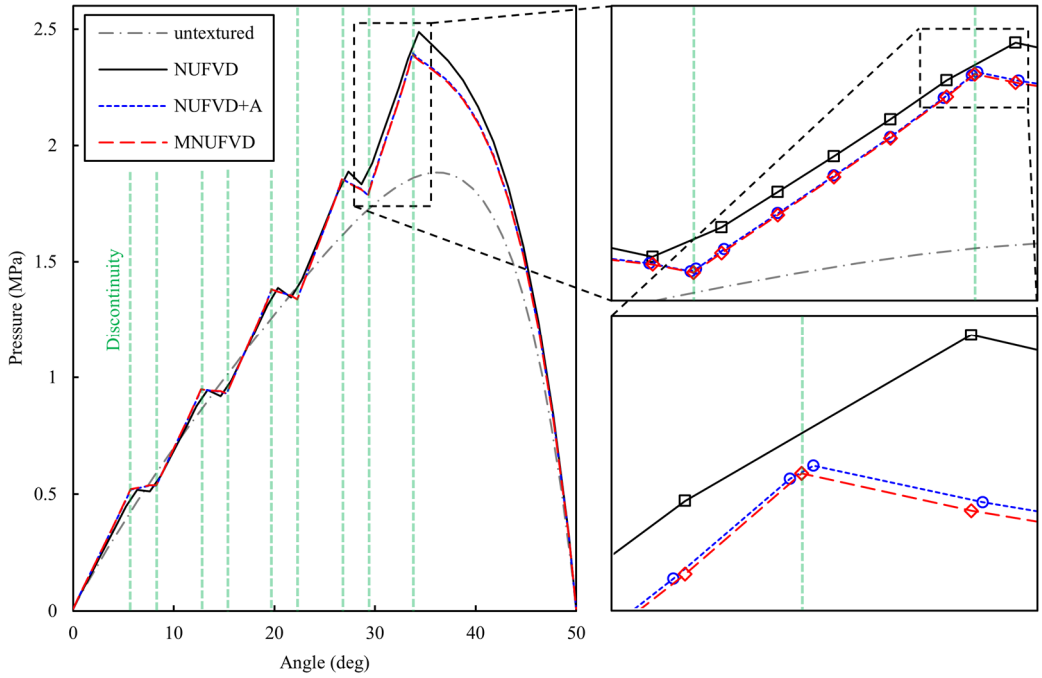

Figure 5.5 Pressure distribution at the mean radius as predicted by different discretization methods for mesh 5: 5 / 2 / 10 / 5.

It can be seen that the NUFVD method highly overestimates the maximum pressure

and load carrying capacity due to the inaccurate approximation of the film at discontinuities. Placing additional nodes around the discontinuity lines results in a better representation of the real geometry and provides pressure values very close to the ones obtained with the MNUFVD method where additional pressure and film thickness values are considered directly on discontinuity lines without increasing the required DOF.

To compare the discretization methods in terms of computational speed, the CPU time required to solve the Reynolds equation is also evaluated. Although the mesh preparation takes slightly longer for both the NUFVD+A and MNUFVD method, the influence is very small and therefore not considered. Hence, times required for the sole solution of the Reynolds equation are compared. Note that encountered computation times are relatively low for all methods due to the simplicity of the analysed texture pattern. Therefore, the more complex implementation of the NUFVD+A and MNUFVD methods may not be justified for the present example. However, when simulating more complex texture patterns or conducting parametric/optimization studies the application of these methods becomes necessary. As the computation time significantly depends on the relaxation parameter (ω_p) and the optimum relaxation parameter ($\omega_{p,opt}$) depends on the mesh details and discretization method used, simulations are performed with a fixed relaxation parameter of 1.98 as well as with the individually optimized relaxation parameter. The respective optimum relaxation parameters are iteratively found and optimized to three decimal places. Given computation times are arithmetic means of five consecutively run simulations.

As shown in Figure 5.6, the conventional NUFVD method results in the highest computation times for all cases considered. Considerable improvements can be achieved by using the NUFVD+A method. For the case of non-optimized relaxation parameters, the computation is 1.7, 7.8 and 399 times faster as compared to the conventional NUFVD method to achieve errors of 1%, 0.5% and 0.1% respectively. When using optimized relaxation parameters, a speedup by a factor of 1.6, 12.3 and 137 is possible for errors of 1%, 0.5% and 0.1% respectively. Notably lowest computation times are encountered when the MNUFVD method is used. The CPU time needed to solve the Reynolds equation is 5.6, 22.6 and 767 times lower as compared to the NUFVD method when a fixed relaxation parameter is used. For optimized relaxation parameters speedup values change to 10, 63 and 431. For all cases considered realizable improvements increase with an increase in DOF.

For comparison, if concentrated inertia effects are considered in the MNUFVD method with $\xi = 0$ for the case of $\omega_p = \omega_{p,opt}$, computation times increase from 0.014, 0.024 and 0.264 to 0.388, 0.641 and 4.495 seconds to reach errors of 1%, 0.5% and 0.1% respectively. These CPU times are required if the nonlinear discrete system is solved directly in MATLAB. Solving the same problem in C reduces those

computation times to 0.031, 0.055 and 0.625 seconds, being about 1 order of magnitude faster. However, this is only the case whenever the discrete system is nonlinear.

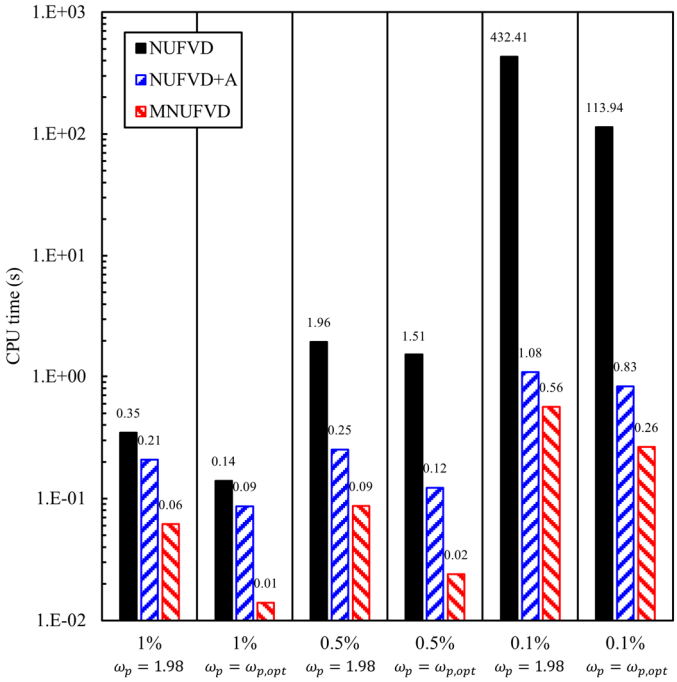

Figure 5.6 CPU time required to solve the Reynolds equation for different discretization methods, desired errors and relaxation parameters.

In conclusion, significant improvements in discretization error and computational speed can be achieved by treating discontinuities with the NUFVD+A or MNUFVD method. If a non-uniform discretization is already available, a modification to allow a placement of additional nodes as required by the NUFVD+A method is rather simple. Although superior, the MNUFVD method is more complex to implement and is limited to problems without cavitation. However, as mentioned above, cavitation does not usually occur for textured tilting pad thrust bearings. In fact, cavitation did not occur for any of the simulations presented in this chapter. If cavitation occurs for the majority of operating conditions (e.g. journal bearings or parallel slider bearings), the reader may be interested in the FBNS algorithm [179].

5.1.3 Parallel computation of the Jacobian matrix

As most modern computers are equipped with multiple processor cores, the following section is devoted to evaluating the achievable advantages in terms of computational speed by parallelizing the computation of the Jacobian matrix. The elements of the Jacobian are independent from each other, hence a simultaneous evaluation is feasible. To study the impact of parallelization, simulations are run for the same bearing and texture design used previously, however, this time the film thickness is

not pre-determined. A conventional Newton-Raphson method is utilized to find the equilibrium. The model is run for an applied specific load of 1.0 MPa at 3000 rpm using only the MNUFVD method. A film with $\alpha_r = 593$ µrad, $\alpha_\theta = -272$ µrad and $h_p = 72$ µm is used as first approximation, which is a guess of average quality, being about 50% away from the actual solution. For these simulations no damping is applied for the Jacobian matrix. Furthermore, a constant relaxation parameter of 1.98 is used and simulations are run for a given effective temperature of 70°C, hence only the fluid solver and equilibrium solver are utilized.

For the aforementioned problem, a total of six Newton iterations are required to reach convergence. Hence, the Jacobian is evaluated six times, resulting in a total of 24 solutions of the Reynolds equation. The time needed to evaluate the Jacobian is stored each time and averaged once all six Newton iterations are completed. This simulation is repeated 15 times and calculation times to determine the Jacobian are averaged once again, using only the ultimate ten simulations to exclude computational start-up effects. This procedure is conducted for 13 different meshes, ranging from 400 to 77841 DOF and repeated utilizing one thread, two threads, four threads and eight threads. In the latter case hyper-threading is enabled as only four physical cores are available on the present workstation. Speedup values are defined as the ratio of the execution time for the non-parallelized algorithm over the execution time for the parallelized algorithm and are shown in Figure 5.7.

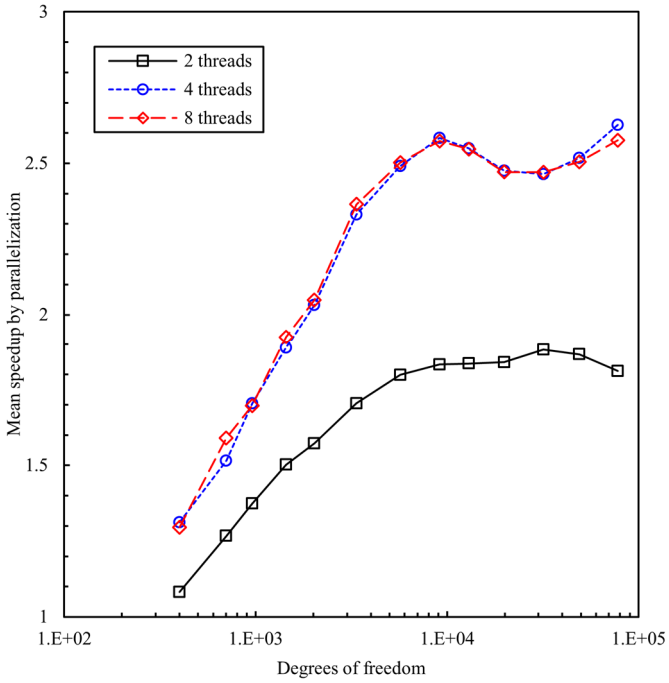

Figure 5.7 Mean speedup by parallelizing the computation of the Jacobian matrix.

For all simulations performed, the achievable speedup increases with an increase in DOF up to approximately 10^4 DOF and then stabilizes to a relatively constant value. This is due to the CPU time required to divide the workload onto multiple threads,

which becomes less impactful for higher numbers of DOF as the evaluation of the Reynolds equation takes longer. A maximum speedup factor of about 1.9 is possible when two threads are utilized. When the workload is shared by four threads, a speedup by a factor of around 2.6 is realizable. Utilizing eight threads does not lead to further improvements, as only four solutions of the Reynolds equation are feasible to be parallelized.

Total computation times required to run the whole simulation (i.e. all six Newton iterations and a consecutive calculation of bearing performance characteristics) are shown in Figure 5.8 for the three meshes required by the MNUFVD method to achieve discretization errors of 1%, 0.5% and 0.1%.

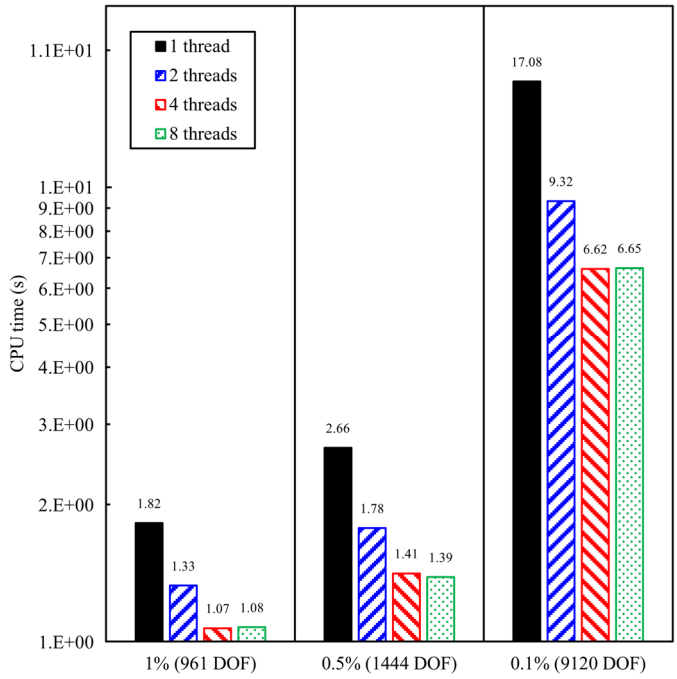

Figure 5.8 Total CPU time to perform all 6 Newton iterations for different desired errors and numbers of threads using the MNUFVD method.

The simulation takes longest when no parallelization is utilized. Evaluating the Jacobian on two cores simultaneously results in an overall speedup by a factor of 1.37, 1.5 and 1.83 from coarsest mesh to finest respectively. The application of four threads further decreases computation times. In this case the computation runs 1.70, 1.89 and 2.58 times faster. As explained above, using hyper-threading, i.e. using eight logical cores, does not result in further performance improvements. Although not discussed in detail, the parallel computation of the Jacobian will also be beneficial when using Broyden's method. However, as this method only requires the evaluation of the Jacobian once, the overall speedup will not be as significant. The continuation method with fourth-order Runge-Kutta requires the determination of the Jacobian four times during each step, hence a parallelization is highly beneficial.

5.1.4 Comparison of solution strategies for the equilibrium solver

The three root-finding methods for nonlinear systems introduced in chapter 4 for solving the equilibrium problem are compared in terms of computational speed and numerical stability. For simplicity, the following abbreviations are used from here on forth: N: Newton-Raphson method/ B: Broyden's method with Sherman-Morrison formula/ C: continuation method with fourth-order Runge-Kutta technique. Also, combination of these methods are compared: C2(+B): continuation method with two steps and consecutive solution with Broyden's method in case convergence is not reached by the continuation method alone/ N3+B: Newton's method performed for three iterations and consecutive solution with Broyden's method. As the numerical analysis of hydrodynamic bearings always involves the solution of a nonlinear problem similar to the one given in equation (3.21) or (4.36), the investigations below are also applicable to other types of textured or conventional bearings.

Simulations are performed for the same bearing and texture design as above, operating at 3000 rpm and 1.0 MPa specific load. Discretization is performed using the MNUFVD method without considering concentrated inertia for 9120 DOF and the temperature is pre-defined and constant at $T_{eff} = 70°C$.

5.1.4.1 Quality of initial guess unknown

Firstly, cases are considered where the quality of the film thickness guess is unknown, which corresponds to an initial user-defined guess. Hence, no previous knowledge of the film thickness is available. Simulations are run with the available root-finding methods for three different qualities of the initial guess: A good initial guess 10% away from the actual solution, an average guess 50% away from the solution and a poor guess 100% away from the solution. For comparison, all simulations are repeated for the case of one computational thread and four threads with and without damping. Total computation times to find the equilibrium are shown in Figure 5.9 and more detailed in Table 5.3 and Table 5.4.

As seen in Figure 5.9 (a), a particularly poorly chosen initial guess will not be sufficient for most methods to converge. The only method converging for this case is the C2(+B) method, requiring three additional Broyden iterations to converge, resulting in a total CPU time of 11.8 seconds. Note that this requires a total of 38 solutions of the Reynolds equation: 32 times for the four required computations of the Jacobian matrix for each step of the continuation method, four times for the Jacobian matrix required for the first Broyden iteration and two more times for iterations two and three of Broyden's method. For the guess of average quality, all but the N1+B method converge. In this case the fastest methods are the N, C1(+B) and N4+B method with computation times ranging from 6.4 seconds for the C1(+B)

Table 5.3 Total CPU time, required iterations and required solutions of the Reynolds equation (RE) for different equilibrium solver strategies for 4 threads.

Method		4 threads								
		Poor guess (+100%)			Average guess (+50%)			Good guess (+10%)		
		CPU time	Iterations[a]	RE solved	CPU time	Iterations[a]	RE solved	CPU time	Iterations[a]	RE solved
Without damping	N	NC	NC	NC	6.9	6	24	3.11	3	12
	C1(+B)	NC	NC	NC	6.38	2	21	6.6	2	21
	C2(+B)	11.78	3	38	11.42	2	37	8.79	0	32
	B	NC	NC	NC	10.22	14	17	3.81	5	8
	N1+B	NC	NC	NC	NC	NC	NC	3.25	2	9
	N2+B	NC	NC	NC	10.47	11	22	4.16	2	13
	N3+B	NC	NC	NC	8.08	6	21			
	N4+B	NC	NC	NC	6.5	2	21			
	N5+B	NC	NC	NC	7.62	2	25			
With damping ($D = 1.5$)	N	6.75	6	24	5.71	5	20	5.05	5	20
	C1(+B)	NC	NC	NC	NC	NC	NC	6.77	2	21
	C2(+B)	18.98	14	49	17.09	11	46	8.76	0	32
	B	14.33	20	23	10.8	15	18	9.92	14	17
	N1+B	13.89	19	26	NC	NC	NC	5.88	6	13
	N2+B	13.33	16	27	11.55	13	24	5.99	5	16
	N3+B	8.77	7	22	6.58	4	19	6.04	3	18
	N4+B	7.18	3	22	6.31	2	21	6.11	2	21
	N5+B	7.81	2	25						

[a] For method N Newton iterations and for all other methods Broyden iterations.

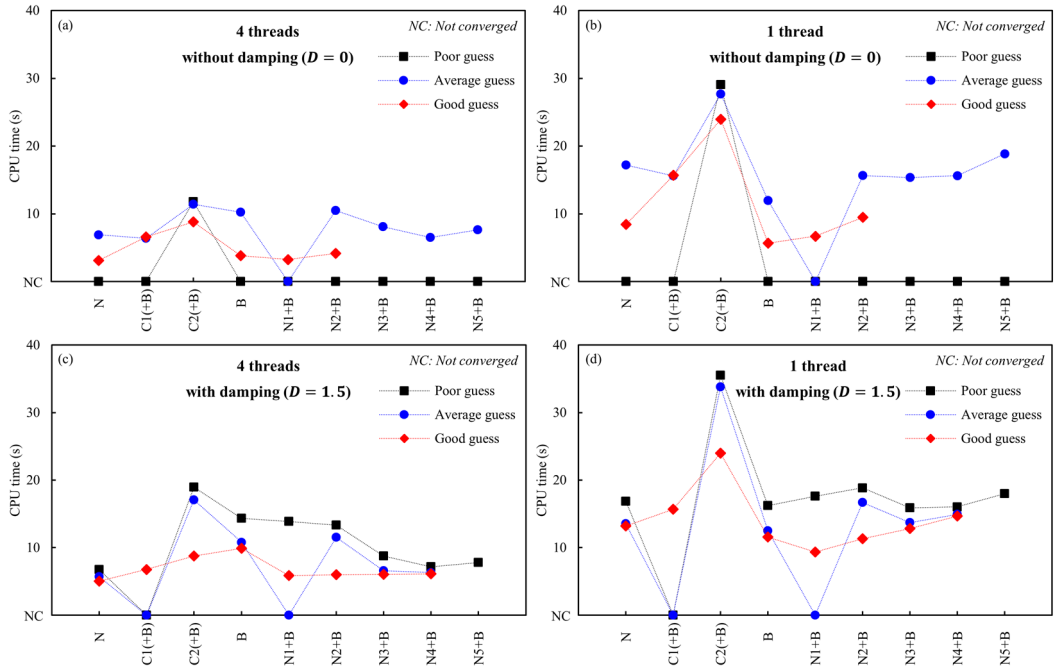

Figure 5.9 Total simulation times for different equilibrium solver strategies: (a) 4 threads without damping, (b) 1 thread without damping, (c) 4 threads with damping and (d) 1 thread with damping.

Table 5.4 Total CPU time, required iterations and required solutions of the Reynolds equation (RE) for different equilibrium solver strategies for 1 thread.

Method		1 thread								
		Poor guess (+100%)			Average guess (+50%)			Good guess (+10%)		
		CPU time	Iterations[a]	RE solved	CPU time	Iterations[a]	RE solved	CPU time	Iterations[a]	RE solved
Without damping	N	NC	NC	NC	17.18	6	24	8.44	3	12
	C1(+B)	NC	NC	NC	15.61	2	21	15.68	2	21
	C2(+B)	29.06	3	38	27.69	2	37	23.95	0	32
	B	NC	NC	NC	11.94	14	17	5.68	5	8
	N1+B	NC	NC	NC	NC	NC	NC	6.69	2	9
	N2+B	NC	NC	NC	15.66	11	22	9.49	2	13
	N3+B	NC	NC	NC	15.34	6	21			
	N4+B	NC	NC	NC	15.62	2	21			
	N5+B	NC	NC	NC	18.85	2	25			
With damping ($D = 1.5$)	N	16.88	6	24	13.55	5	20	13.22	5	20
	C1(+B)		NC	NC		NC	NC	15.7	2	21
	C2(+B)	35.53	14	49	33.8	11	46	24	0	32
	B	16.22	20	23	12.52	15	18	11.59	14	17
	N1+B	17.62	19	26		NC	NC	9.35	6	13
	N2+B	18.85	16	27	16.69	13	24	11.34	5	16
	N3+B	15.89	7	22	13.7	4	19	12.85	3	18
	N4+B	16.04	3	22	14.93	2	21	14.68	2	21
	N5+B	18	2	25						

[a] For method N Newton iterations and for all other methods Broyden iterations.

method to 6.9 seconds for the N method. If the guess is close enough to the actual solution, all methods run stable and provide converged solutions. This time the conventional Newton method is fastest, requiring only three iterations, i.e. a total of 12 solutions of the Reynolds equation and resulting in a CPU time of 3.1 seconds. It is evident that the parallelization of the determination of the Jacobian matrix improves Newton's method enough to overshadow the advantage of Broyden's method. Broyden's method converges on its own, requiring 5 iterations, i.e. only 8 solutions of the Reynolds equation as compared to the 12 solutions Newton's method requires. The fact that Newton's method is faster anyway can be explained by the speedup achieved by multithreading the evaluation of the Jacobian. For the MNUFVD method with 9120 DOF, the speedup factor by parallelization is approximately 2.7. This means that four solutions of the Reynolds equation take effectively only just about as long as 1.5 serial solutions of the Reynolds equation. Although the first iteration of Broyden's method also benefits from parallelization, Newton's method is slightly faster than Broyden's method nevertheless.

This is not the case when no multithreading is utilized (Figure 5.9 (b)). Here, the advantage of Broyden's method to only have to calculate the Jacobian once is more influential. This, for the case of a good quality guess, results in Broyden's method being the fastest with 5.7 seconds CPU time, being about 1.5 times as fast as the

conventional Newton method. For the average guess, Broyden's method is fastest again, being approximately 1.4 times as fast as Newton's method. The slowest method is the C2(+B) method, which is 2.3 and 4.2 times slower than Broyden's method for the average and good guess respectively. For the poor guess, no comparison is possible as none of the methods except C2(+B) converge.

Results are different when the proposed damping procedure is applied (Figure 5.9 (c)). Now, for the case of a poor initial guess, all methods but C1(+B) converge. Fastest method is the conventional Newton-Raphson method, requiring six iterations and resulting in 6.75 seconds total computation time. Although Broyden's method usually demands a guess relatively close to the actual solution, the damping procedure results in a stable solution even for the poor initial guess. The computation time for this case is about twice as high as compared to the damped Newton method. For the average and good quality cases, the damped Newton method is fastest again. Longest computation times are generally encountered for the C2(+B) method and interestingly C1(+B) only converges for the good quality guess.

When damping is applied and the Jacobian is evaluated in series, Broyden's method is fastest for an average guess, being about 8% faster than Newton's method (Figure 5.9 (d)). For a good initial guess, N1+B is fastest with 9.4 seconds and for a poor initial guess N3+B with 15.9 seconds. Again, highest computation times are required by the C2(+B) method, being as high as 33.8 seconds for the case of a poor quality guess. A point that is not discussed in detail is the fact that required iterations to solve the Reynolds equation depend on the film geometry as well. However, the influence is insignificant and is therefore not considered in the present comparison. For example, the required iterations to solve the Reynolds equation are 918, 918, 921 and 905 for the film geometry corresponding to the actual solution, the good quality guess, the average quality guess and the poor quality guess respectively.

In conclusion, the advantages of Broyden's method are generally overshadowed by the speedup achieved by parallelizing the evaluation of the Jacobian matrix. Therefore, a conventional Newton method is recommended whenever the quality of the first guess is unknown. If only one thread is available, the implementation of Broyden's can result in considerable improvements in terms of computation times, although damping may be required for poor quality guesses to improve stability. As an alternative to damping, a continuation method with at least two steps seems to provide improved numerical stability although CPU times are increased and the implementation is more complex.

5.1.4.2 Quality of initial guess known

As discussed above, Broyden's method performs best for initial guesses of good

quality. One way to be capable of assessing the quality of the initial approximation of the film thickness distribution and therefore efficiently applying Broyden's method, is the use of results from a previous simulation of the equivalent untextured bearing. The idea behind this is to first run a complete bearing simulation for the equivalent untextured bearing and then use all obtained results as first approximations for the textured bearing. Although surface texturing alters the bearing equilibrium, changes are usually subtle. Hence, it can be assumed that results from the untextured bearing are good quality approximations for the textured bearing. The simulation of an untextured bearing is straightforward and can be done with relatively coarse and uniform meshes. Hence, only requiring a fraction of the time required to simulate a complexly textured bearing.

To analyse possible improvements by this methodology, simulations are run for the same conditions as above, using an average quality guess for the textured bearing as well as the untextured bearing. For the untextured bearing, a coarse uniform mesh with 11 x 11 CVs is used. Three methods are compared: Running only the simulation for the textured bearing with Newton's method (N), running the simulation first for the untextured bearing with Newton's method and subsequently for the textured bearing with Newton's method while using the results of the untextured bearing (UT+N) and running the simulation first for the untextured bearing with Newton's method and subsequently for the textured bearing with Broyden's method while using the results of the untextured bearing (UT+B). Computation times are given in Figure 5.10 (a) and in more detail in Table 5.5.

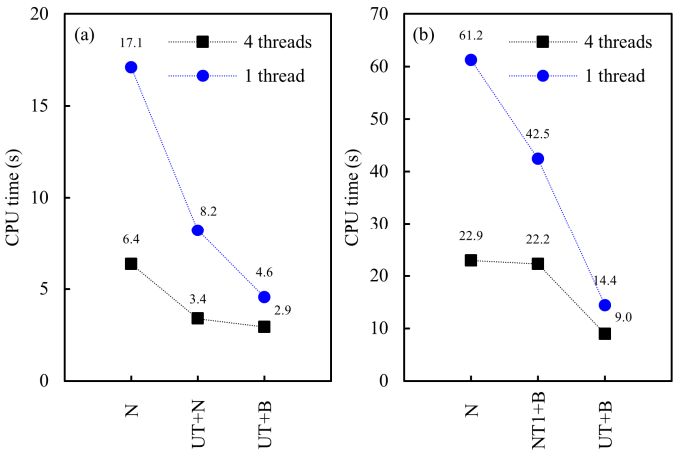

Figure 5.10 Total CPU time for different equilibrium solver strategies for two cases: (a) temperature is pre-defined and (b) temperature is found with the iterative temperature solver.

When four threads are utilized, the simulation with Newton's method takes 6.4 seconds. By using the UT+N method, the total computation time can be reduced to 3.4 seconds if Newton's method is used for both the untextured bearing and the textured one. Six iterations and 0.5 seconds are needed for the untextured bearing and 2.9 seconds and three iterations for the textured one. The initial guess for the textured bearing in this case is the solution of the untextured bearing, here: $\alpha_r =$

380 µrad, $\alpha_\theta = -173$ µrad µrad and $h_p = 46$ µm. For the textured bearing this corresponds to a guess of very good quality, being on average about 4% away from the actual solution. If the textured bearing is solved with Broyden's method only, the execution time further decreases to 2.9 seconds. In this case only three Broyden iterations are necessary. Hence, computation times can be decreased by factors of approximately 1.9 and 2.2 by the UT+N and UT+B methods respectively. If the simulations are run on one thread only, these factors increase to about 2.1 and 3.7. The non-parallelized simulation of the untextured bearing takes 0.25 seconds, being faster than the parallelized computation due to the communication overhead, which is notable for the small scale problem having just 11 x 11 CVs. Once again, achievable improvements are higher for the non-parallelized simulations.

Table 5.5 Total CPU time and required iterations for different equilibrium solver strategies for a predefined temperature.

Method	4 threads			1 thread		
	CPU time	Iterations[a]	RE solved	CPU time	Iterations[a]	RE solved
N	6.36	6	24	17.09	6	24
UT+N	3.39	3	12	8.21	3	12
UT+B	2.93	3	6	4.56	3	6

[a] For method N and UT+N Newton iterations, for method UT+B Broyden iterations.

The quality of the film thickness guess can also be approximated during consecutive temperature iterations. New effective and inlet temperatures will change the equilibrium film thickness less and less with increasing temperature iterations. Hence, it can be assumed that the film thickness from a previous temperature iteration is a good quality guess for the next temperature iteration. To assess possible improvements, the complete model is now run including the temperature solver. An initial guess of 50°C is used for both inlet temperature and effective temperature. Used initial guesses for the film thickness are 50% away from the corresponding actual solution. Results are presented in Figure 5.10 (b) and Table 5.6.

Table 5.6 Total CPU time and required iterations for different equilibrium solver strategies when applying the iterative temperature solver.

Method	4 threads			1 thread		
	CPU time	Iterations[a]	RE solved	CPU time	Iterations[a]	RE solved
N	22.9	6/4/4/3/2/2/2	92	61.2	6/4/4/3/2/2/2	92
NT1+B	22.2	-/6/6/3/2/2/2	63	42.5	-/6/6/3/2/2/2	63
UT+B	9.0	3/2/2/2	21	14.4	3/2/2/2	21

[a] For method N Newton iterations, for methods NT1+B and UT+B Broyden iterations.

If only Newton's method is applied, seven temperature iterations are required to

reach thermal equilibrium. A total of 92 solutions of the Reynolds equation are necessary for this case and execution times are 22.9 and 61.2 seconds for four threads and one thread respectively. For the first temperature iteration, six Newton iterations are necessary to find the bearing equilibrium and for the remaining six temperature iterations 4, 4, 3, 2, 2 and 2 iterations. If Newton's method is only applied for the first temperature iteration and for all remaining iterations Broyden's method (NT1+B), computation times are reduced by factors of 1.03 and 1.4 to 22.2 and 42.5 seconds for four threads and one thread respectively. For these cases, the equilibrium position corresponding to the first temperature iteration is solved with six Newton iterations, the following six temperature iterations with 6, 6, 3, 2, 2 and 2 Broyden iterations, resulting in a total of 63 solutions of the Reynolds equation. If effective temperature, inlet temperature and equilibrium position are first found for the equivalent untextured bearing, then used as first approximations for the textured bearing and all equilibrium positions of the textured bearing are found with Broyden's method only (UT+B), computation times reduce further to 9 and 14.4 seconds for four threads and one thread respectively, resulting in a speedup by factors of 2.6 and 4.3 as compared to the conventional approach. The simulation of the equivalent untextured bearing with 11 x 11 CVs requires seven temperature iterations to find thermal equilibrium, where only Newton's method is applied. Computation times for the untextured bearing are 0.8 and 1.7 seconds for one thread and four respectively. Again, due to the communication time required, the computation is faster if only one thread is utilized. The improved guesses for inlet and effective temperature lower the required temperature iterations for the textured bearing from seven to four. 3, 2, 2 and 2 Broyden iterations are required for the UT+B method, resulting in a total of 21 solutions of the Reynolds equation.

Using results from the equivalent untextured bearing may be interpreted as a special kind of multigrid method with the difference that textures are ignored and a coarse uniform mesh is used for the initial simulation. These results are then used as initial approximations for the textured case, where a fine, non-uniform mesh is used. The method is capable of reducing computation times for textured bearings significantly, especially when strategically combined with Broyden's method. Although introduced here for tilting pad bearings, this method is readily adaptable for other kinds of textured contacts under hydrodynamic conditions.

5.2 Validation cases

To evaluate the correctness of the implemented code and accuracy of the developed model, results are compared to numerical data available in literature. Initially, the fluid solver is analysed by comparing predicted pressure values to numerical data from Qiu and Khonsari [67] for a simple single dimple geometry in the form of a

spherical cap. Subsequently, the correct implementation of the mass-conserving cavitation algorithm is investigated by running a simulation for a typical journal bearing and comparing the obtained pressure distribution with published data from Bartel [228].

Once the fluid solver is validated, simulations are performed for tilting pad thrust bearings to validate the equilibrium and temperature solvers. Results are compared to numerical data from Zouzoulas and Papadopoulos [18, 238].

5.2.1 Spherical cap

The correctness of the numerical solution of the Reynolds equation is analysed. For this purpose, the developed model is run for a given film thickness and viscosity, while neglecting cavitation. The single dimple geometry in form of a spherical cap studied by Qiu and Khonsari [67] is chosen for comparison. An illustration of the considered geometry and input parameters are given in Figure 5.11 and Table 5.7.

Table 5.7 Input parameters for the validation study on a spherical cap dimple.

Description	Symbol	Quantity
Viscosity (mPa.s)	η	3.5
Contact dimensions (µm)	X_c, Y_c	600 x 600
Sliding speed (m/s)	u	10
Film thickness around texture (µm)	h_0	4
Dimple depth (µm)	$h_{texture}$	10
Dimple radius (µm)	l	150
Mesh size		101 x 101

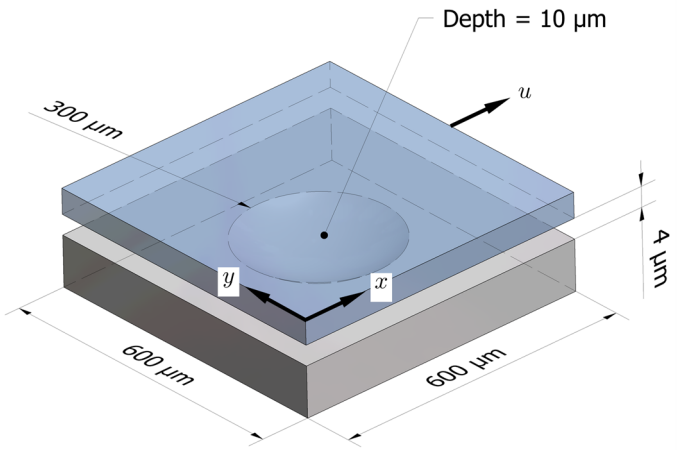

Figure 5.11 Geometrical details of the spherical cap dimple.

The film thickness distribution can be defined by the following expression:

$$h(x,y) = \begin{cases} h_0 & \text{for } r \geq l \\ \sqrt{\left(\frac{l^2 + h_{texture}^2}{2h_{texture}}\right)^2 - r^2} - \frac{l^2 + h_{texture}^2}{2h_{texture}} + h_{texture} + h_0 & \text{for } r < l \end{cases} \tag{5.1}$$

with

$$r(x,y) = \sqrt{(x - X_c)^2 - (y - Y_c)^2} \tag{5.2}$$

where X_c and Y_c are the contact dimensions in x and y direction respectively. l is the dimple radius, $h_{texture}$ the maximum texture depth and h_0 the film thickness around the texture. The pressure at the sides is fixed at 0.9 MPa. A uniform mesh with 101 x 101 nodes and the NUFVD method are used for this simulation. The predicted pressure distribution of the present model as well as reference [67] are shown in Figure 5.12.

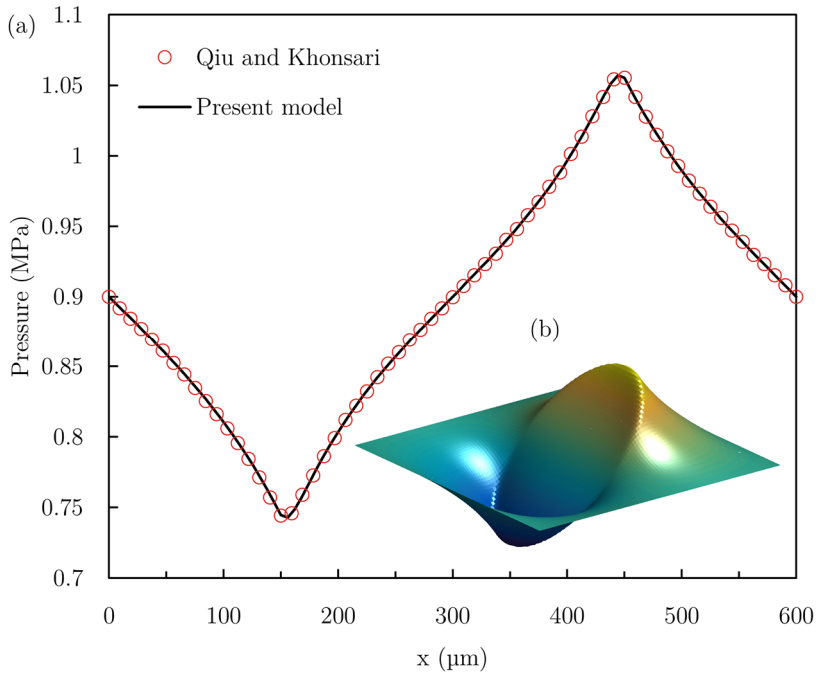

Figure 5.12 (a) Pressure distribution at y=300 µm as predicted by the present model and Qiu and Khonsari [67], (b) surface plot of the pressure distribution as predicted by the present model.

The pressure distribution is point symmetric and has its maximum and minimum at the dimple's edges. It is evident that the computed pressure distribution of the two models is nearly identical, confirming the correct implementation of the fluid solver.

5.2.2 Journal bearing

To validate the fluid solver including the mass-conserving cavitation algorithm, a

study is conducted for a journal bearing for a given eccentricity, i.e. only the fluid solver is run. The simulation is run for the journal bearing studied by Bartel [228]. The oil is predominantly supplied through an oil supply hole situated at the top of the bush. Only some oil is supplied through the bearing sides. A full list of the input parameters is given in Table 5.8. The film thickness is given by:

$$h(\theta) = c[1 + \varepsilon \cos(\theta)] \tag{5.3}$$

where c is the radial clearance, ε the eccentricity ratio and θ the circumferential coordinate. A relatively fine mesh of 360 nodes in circumferential direction and 71 nodes in radial direction is used to accurately capture the oil supply hole. The results for the pressure and fractional film content distribution at the bearing mid-section are given in Figure 5.13 and show an excellent agreement.

Table 5.8 Input parameters for the validation study on a journal bearing.

Description	Symbol	Quantity
Bearing diameter (mm)	D	80
Bearing width (mm)	Y_c	40
Rotational speed (rpm)	ω	2960
Diameter of the oil supply hole (mm)		5
Position of the oil supply hole (deg)		0
Supply pressure (MPa)	p_{sup}	0.5
Viscosity (mPa.s)	η	24.8
Pressure at the bearing sides (MPa)	p_{side}	0.01
Cavitation pressure (Pa)	p_{cav}	0
Clearance (µm)	c	59.2
Eccentricity ratio	ε	0.685
Attitude angle (deg)	φ	39.5
Mesh size		360 x 71

As the correct prediction of the pressure values demands a correct prediction of the fractional film content values, the implemented mass-conserving cavitation algorithm works correctly as well. Detailed results of pressure and film content distributions are presented in Figure 5.14. It can clearly be seen that the increase in film thickness after the minimum film thickness results in a drop in pressure, causing the formation of cavitation. The cavitated area is then disturbed by the oil supply hole, where the fresh oil results in a film reformation.

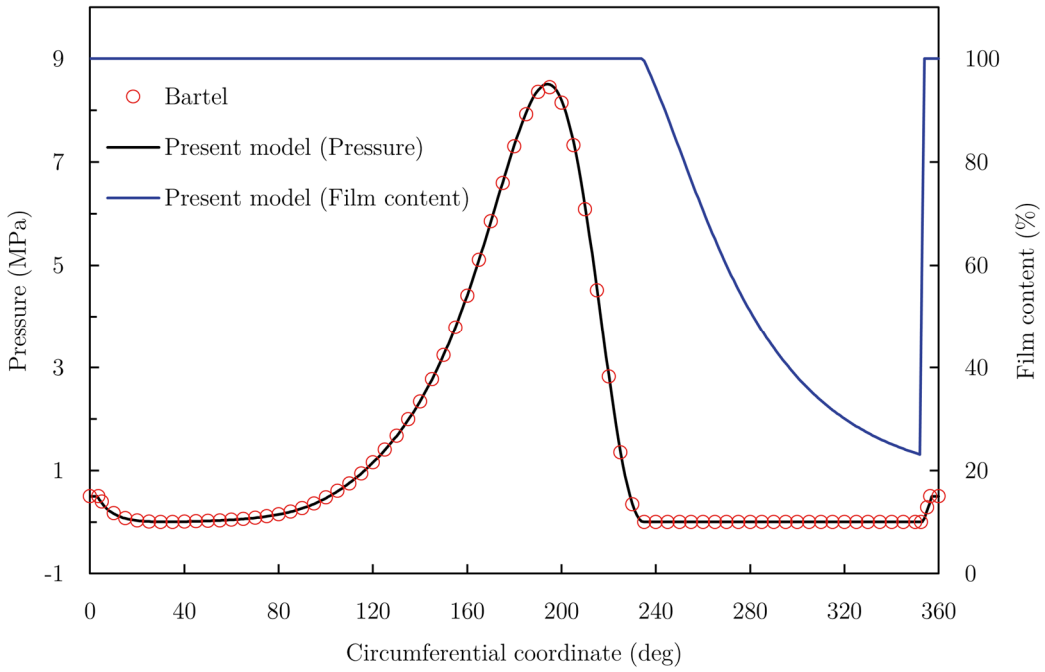

Figure 5.13 Pressure distribution at the bearing mid-section as predicted by the present model and Bartel [228].

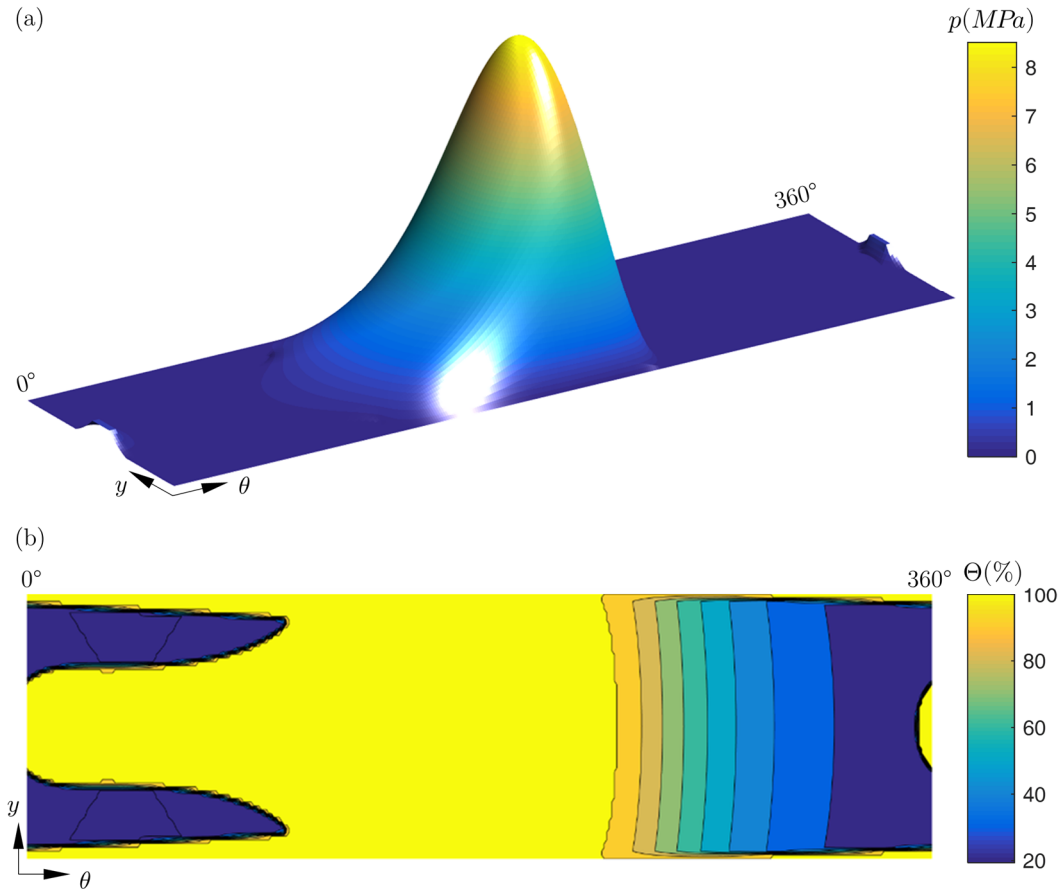

Figure 5.14 (a) Pressure distribution, (b) fractional film content distribution.

5.2.3 Tilting pad thrust bearing

Simulations are performed for the tilting pad thrust bearing investigated through CFD by Zouzoulas and Papadopoulos [18]. Results are compared for the bearing performance characteristics considered most important, namely minimum film thickness, friction torque per pad, maximum temperature and maximum pressure. To evaluate the accuracy over a wide range of conditions, results are compared for eight different operating conditions (0.5, 1, 1.5 and 2.0 MPa at 1500 and 3000 rpm) and three different pad designs (untextured, pocket and circumferential grooves).

All simulations are run with a universal initial film thickness guess of $\alpha_r = 300$ μrad, $\alpha_\theta = -150$ μrad and $h_p = 35$ μm to also assess the robustness of the present model. The initial guess for effective and inlet temperature is 50°C, and tolerance values of $e_p = 10^{-5}$, $e_e = 10^{-2}$ and $e_t = 10^{-4}$ are used. Note that the quality of these guesses significantly depends on the operating conditions. A total of three simulations are run, i.e. one simulation per pad design, where the eight operating conditions are evaluated simultaneously on eight computational threads. For the untextured pad, a uniform mesh with 101 x 101 CVs is used and exclusively Newton's method is applied for the first temperature iteration followed by Broyden's method for the remaining temperature iterations. For the pocketed pad, the simulation is first run for the equivalent untextured pad with 11 x 11 CVs and then Newton's method is applied for the first temperature iteration and Broyden's method for the remaining temperature iterations. The mesh for the pocketed pad consists of a total of 109 x 89 CVs. To simulate the grooved pad, again the equivalent untextured solution as obtained with 11 x 11 CVs is used, however, the textured pad is then simulated by applying a continuation method with two steps for the first temperature iteration, followed by Broyden's method for the remaining temperature iterations. This is done because numerical instability is encountered when using Newton's method only, due to the fluctuations in the quality of the initial guess. The mesh for the grooved pad consists of 109 x 98 CVs. The MNUFVD method is used for the both the pocketed and grooved pad. The relaxation parameter for pressure is set to 1.93 and 1.98 for the untextured pad and textured pads respectively. Results of the validation study are shown in Figure 5.15 in terms of the relative differences.

Despite the use of a uniform initial guess, all performed simulations converged, demonstrating the robustness of the present model. The computation times were 55.2, 115.5 and 193.8 seconds for the untextured, pocketed and grooved pad respectively. It is evident that the obtained results for maximum pressure and friction torque by both models are remarkably similar, showing a maximum difference of just 3.3%. Generally, maximum pressure values are slightly overestimated by the present model, whereas predicted friction torque values are underestimated for the pocket design and evenly spread between -1.7% and 2.4% for the other two designs. Hence,

obtained differences for p_{max} and T_f are relatively independent of the operating conditions. Larger differences are encountered for the predicted minimum film thickness and maximum temperature. Minimum film thickness values are underestimated for most cases, being slightly overestimated only for the untextured and grooved pad operating at 0.5 MPa and 3000 rpm. The largest difference for h_{min} is encountered for the untextured pad, being about -8.9% for an operation at 2.0 MPa and 1500 rpm. The differences in T_{max} show the most significant dependence on the operating conditions, ranging from -10.5% to 10.9% for the untextured pad. For the pocketed and grooved pad differences in T_{max} range from -5.7% to 3.5%.

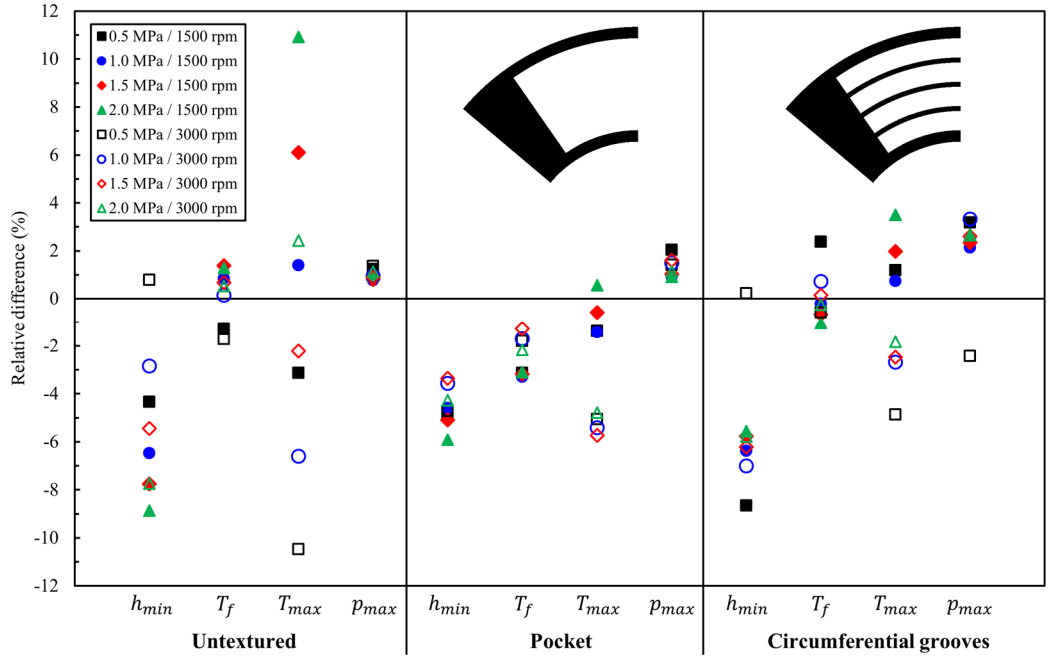

Figure 5.15 Comparison of the results as predicted by the present model and CFD data from reference [18] for different pad designs and operating conditions.

It is noteworthy that temperatures are generally overestimated for an operation at 1500 rpm and underestimated for an operation at 3000 rpm. This is mainly due to the application of a constant convection parameter ($k_{con} = 75\%$), which overestimates convection at 1500 rpm and underestimates convection at 3000 rpm. It is evident that differences are more scattered for the untextured pad. This is related to the effective temperature method where a constant temperature is assumed over the entire pad area. This causes an underestimation of the tilt angles as local temperatures closer to the pad outlet are underestimated and local temperatures closer to the pad inlet overestimated. The higher the difference between inlet and outlet temperature, the higher the error in the predicted tilt angles. As these temperature differences are considerably smaller and less dependent on the operating condition for the pocketed and grooved pad, encountered differences between the present model and CFD are smaller and less scattered. In fact, it is likely that most differences are caused by the application of a simplified effective temperature method

rather than solving the energy and heat conduction equations. However, in particular the results for friction torque and maximum pressure are remarkably close to the much more time consuming CFD simulation. In fact, the CFD simulation took approximately 64 hours for each pad design according to the authors [18]. Hence, the present model is roughly three orders of magnitude faster than a comparable CFD study. Averaging the absolute values of all obtained differences into a single value yields 3%, which the authors deem sufficient for the purpose of texture design, especially considering the significant improvement in computational speed, which allows the numerical optimization of texture designs.

5.3 Summary

This chapter was concerned with the improvement of the developed model in terms of accuracy and computational speed as well as the validation of the developed codes.

Three discretization methods are compared: a non-uniform finite volume discretization (NUFVD), a version of this method where additional nodes are placed around discontinuities (NUFVD+A) and a modification to this method where discontinuities are directly incorporated in the discrete Reynolds equation (MNUFVD). Also, possible performance improvements by taking advantage of multiple processor cores are analysed and three equilibrium solvers (Newton-Raphson, Broyden's method and continuation with fourth-order Runge-Kutta) and combinations of those are compared. The performance of the numerical tool is enhanced by using results from the equivalent untextured bearing and the accuracy of the model is validated by comparison with data available literature. The main conclusions from this chapter are:

- A special treatment of discontinuities can substantially decrease the computation time required to solve the Reynolds equation by restricting discretization errors, where the MNUFVD method results in higher performance improvements than the NUFVD+A method. In general, the lower the desired discretization error and hence, the finer the mesh, the higher the achievable speedup by the NUFVD+A and MNUFVD methods.
- Parallelizing the evaluation of the Jacobian matrix leads to considerable performance improvements, particularly for fine meshes.
- Utilizing Broyden's method instead of Newton's method can be highly beneficial whenever the initial guess for the bearing equilibrium is sufficiently close to the actual solution. However, a parallel evaluation of the Jacobian matrix overshows this advantage in most cases. The algorithm with the best convergence behaviour is the continuation method with two steps. Newton's

algorithm converges for most scenarios and is comparably fast. The proposed damping procedure highly improves Newton's and Broyden's method in terms of numerical stability.

- Improving the initial film thickness guess by using results from the equivalent untextured bearing significantly reduces required CPU times, regardless of the equilibrium solvers utilized. In fact, the simulation of the untextured bearing and subsequent simulation of the textured bearing is much faster than the sole simulation of the textured bearing.

The model is successfully validated by comparison with data available in literature for a simple, single texture geometry and a journal bearing. Also, the model is compared to a sophisticated CFD simulation of a tilting pad thrust bearing, where differences are smallest for predicted friction torque and maximum pressure values and highest for minimum film thickness and maximum temperature values. For the three texture configurations analysed, average errors are 5.3, 1.4, 3.6 and 1.7% for h_{min}, T_f, T_{max} and p_{max} respectively, while the present model is approximately three orders of magnitude faster than the CFD simulation.

Chapter 6

Texture Design Optimization

This chapter is concerned with the mathematical optimization of texture patterns for a tilting pad thrust bearing with offset line pivot. Using the developed numerical model, texture depth ($h_{texture}$), circumferential extent (α) and radial extent (β) are optimized to improve three bearing performance parameters: minimum film thickness (h_{min}), friction torque (T_f) and maximum temperature (T_{max}). Simulations are run for various operating conditions and texture densities for the same bearing used for the experimental part of this work presented in chapter 7. An in-depth analysis regarding the dependency of optimum texturing parameters on the operating conditions and optimization objective as well as achievable performance improvements under hydrodynamic conditions are presented. Furthermore, texture design recommendations are given for a wide range of conditions.

All simulations are performed on a desktop workstation with INTEL CORE i7-3770 @ 3.40 GHz CPU and 16 GB of RAM.

6.1 Considered bearing and operating conditions

The bearing considered is a partially textured tilting pad thrust bearing with offset line pivots (Figure 6.1).

Only partial texturing is considered as it is well known from literature that partial texturing outperforms full texturing for the case of parallel pad bearings. The pads have an inner radius of 30.25 mm, an outer radius of 70.25 mm and span an angle of 46.05° with the pivot being located at 60% from the inlet. Although it is known from literature that a pocketed or grooved design may provide better performance for parallel and convergent contacts under hydrodynamic conditions, the chosen surface

pattern consists of 529 individual angular sector shaped textures with flat bottom profile arranged in a 23 x 23 grid. This design was chosen as individual textures may act as lubricant reservoirs or trap wear debris and therefore outperform pocketed pads under critical mixed lubrication conditions while still providing reasonable performance under hydrodynamic conditions, although these effects still lack experimental evidence. The first row of textures is elongated towards the inlet to promote lubricant supply [14] and only angular sector shaped textures are considered to most closely approximate a pocketed configuration as recommended in literature. The same pattern is also investigated in the experimental part of this work described in chapter 7. A complete list of input parameters is given in Table 6.1.

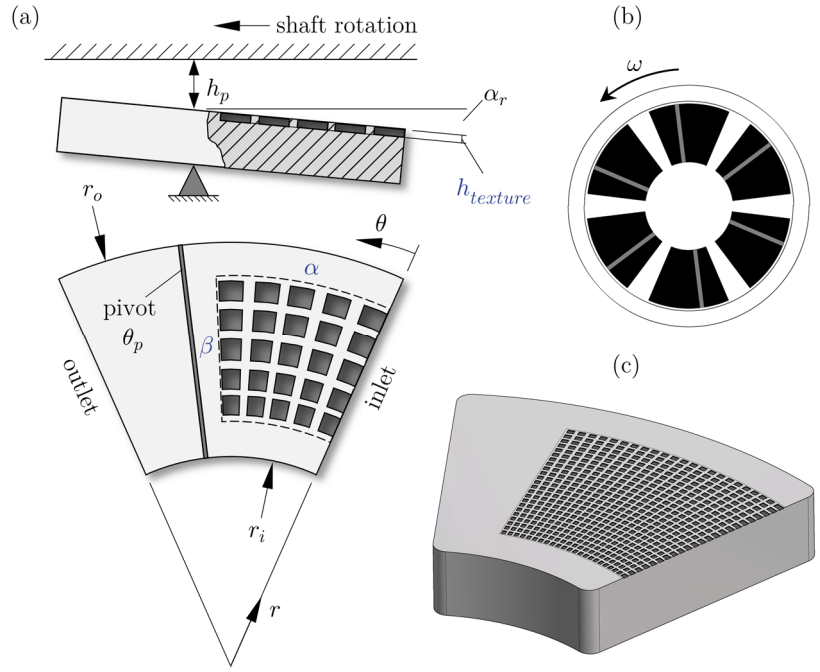

Figure 6.1 (a) Pad details with coordinate system, (b) tilting pad thrust bearing geometry and (c) exemplary 23 x 23 texture pattern with $\alpha = 70\%$, $\beta = 70\%$, $h_{texture} = 10$ µm and $\rho_{texture} = 40\%$.

Tolerance values of $e_p = 10^{-6}$, $e_e = 10^{-4}$, $e_t = 10^{-5}$ and $e_o = 10^{-5}$ are used. For discretization, the MNUFVD method is applied without considering concentrated inertia effects ($B^P = 0$). This is justified by the low Reynolds numbers and high texture aspect ratios encountered. The Reynolds number is defined as $Re = \rho u h_{min}/\eta$ and the texture aspect ratio as $\lambda = l/h_{texture}$, where l is the arc length at the mid radius of the texture. Re varies over the pad area due to local changes in viscosity (caused by the local changes in temperature) and runner velocity. λ varies with the radius, as the textures are defined by a constant angular span. Hence, multiple combinations of Reynolds numbers and texture aspect ratios are encountered for each simulation. For all performed simulations in this chapter, Re ranges from 1 to 36 and λ from 8 to 104. Encountered combinations result in good agreement between the Reynolds and Navier-Stokes models with respect to the

predicted load carrying capacity.

Table 6.1 Bearing geometry and operating conditions.

Description	Symbol	Quantity
Bearing geometry		
Number of pads	n_{pad}	3
Inner pad radius (mm)	r_i	30.25
Outer pad radius (mm)	r_o	70.25
Pad angle (°)	θ_{pad}	46.05
Circumferential coordinate of pivot (°)	θ_p	27.63
Operating conditions		
Applied specific load (MPa)	w_0	0.5 – 2.0
Rotational speed (rpm)	ω	1000 – 3000
Lubricant		ISO VG 32
Density (kg/m^3)	ρ	875
Viscosity at 40°C (cSt)	ν_{40}	32
Viscosity at 100°C (cSt)	ν_{100}	5.4
Supply oil flow rate (l/min)	Q_{sup}	5.55
Supply oil temperature (°C)	T_{sup}	30
Lubricant specific heat (J/kg/K)	c_p	2035

6.2 Mesh study

To ensure accurate results, a number of mesh studies are conducted for a reference case, where the bearing runs at 1000 rpm and a film thickness similar to the one encountered at an operation at a specific load of 1.0 MPa. A texture design with $\alpha = 70\%$, $\beta = 70\%$ and $h_{texture} = 15$ µm is considered for this purpose. The mesh studies are based on the predicted load carrying capacity, as this was found to be the parameter most influenced by the mesh size based on numerous test simulations. Computations are performed for 10 meshes, ranging from 5476 to 288369 degrees of freedom for texture densities of 40%, 50% and 60%. The results are plotted in Figure 6.2 in terms of the difference in predicted load carrying capacity with respect to the load carrying capacity computed with the finest mesh.

It can be seen that, independent of the texture density, the mesh with 21316 degrees of freedom results in a deviation of less than 0.5%. Therefore, all simulations presented in this chapter are conducted with this mesh, consisting of 4 CVs inside individual textures, 2 CVs in-between adjacent textures and 8 CVs for the untextured pad area in circumferential direction and 4 CVs for the untextured pad areas in radial direction (Figure 6.3).

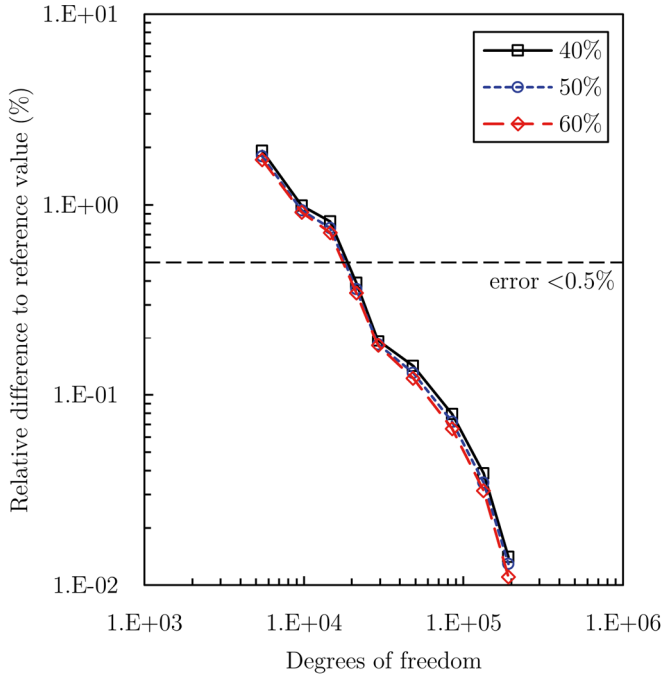

Figure 6.2 Results of the mesh study for texture densities of 40%, 50% and 60%.

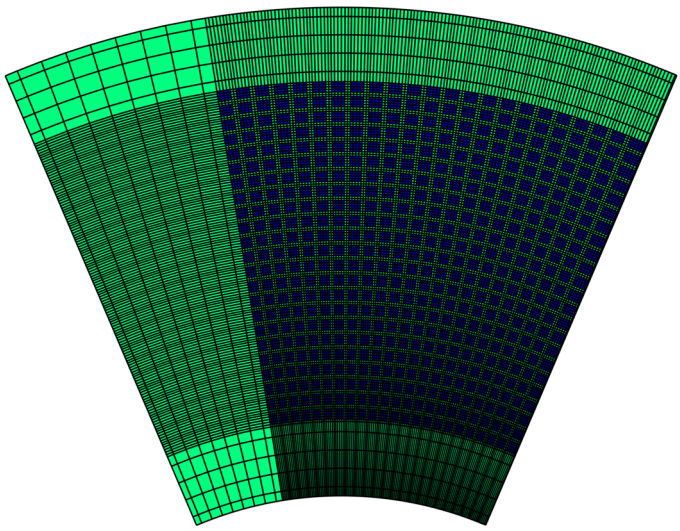

Figure 6.3 Computational mesh with 4 x 4 CVs inside individual textures, 2 x 2 CVs in-between adjacent textures, 8 CVs for the untextured pad area in circumferential direction and 4 CVs each for the untextured pad areas in radial direction.

6.3 Validation of the optimization procedure

The accuracy of the applied numerical model in terms of h_{min}, T_f and T_{max} is investigated in detail in chapter 5.2.3 by comparison with CFD results. It was shown that average deviations to CFD were 5.3, 1.4 and 3.6% with respect to minimum film thickness, friction toque and maximum temperature respectively. Therefore, only

the numerical implementation and convergence of the optimization procedure based on the interior-point algorithm is analysed here. For this purpose, an exhaustive parametric study is performed for a thrust pad with $\rho_{texture} = 50\%$ operating at 1000 rpm and 1.0 MPa specific load. The objective functions are evaluated for a total of 1573 texture designs parameterized as follows: $30\% \leq \alpha \leq 80\%$ (step 5%), $30\% \leq \beta \leq 90\%$ (step 5%) and 5 µm $\leq h_{texture} \leq$ 30 µm (step 2.5 µm). The optimization is then performed for four different start values at the corners of the parameter space (Table 6.2).

Table 6.2 Start values for the texture design.

	$h_{texture}$	α	β
$\boldsymbol{x}_{start,1}$	10	30	30
$\boldsymbol{x}_{start,2}$	10	80	90
$\boldsymbol{x}_{start,3}$	30	30	90
$\boldsymbol{x}_{start,4}$	30	80	30

Figure 6.4 shows the parametric results in terms of the relative difference to the optimum value as well as the paths of the optimization algorithm, where iterations of the interior-point algorithm are indicated by black "x" markers and start and end values by black and yellow circles respectively.

Based on the optimality tolerance, the interior-point algorithm converges for all cases, needing between 26 and 43 iterations. Furthermore, the prediction of the optimum texturing parameters is independent of the start value. Within the parameter space investigated, local minima (maxima) are also global minima (maxima), indicating a successful optimization.

It is noticeable that the optimum texture design does, however, depend on the optimization objective. Whereas the optimum texture depth is fairly independent of the optimization objective (15.2 µm $\leq h_{texture,opt} \leq$ 17.5 µm), the optimum extents of the textured area show a significant dependence on the optimization objective; for the presented case: $41\% \leq \alpha_{opt} \leq 72\%$ and $68\% \leq \beta_{opt} \leq 86\%$. It is further observable that the area around the optimum texture design where the objective function value is only a few percent away from its optimum is different for the three optimization objectives. Whereas the minimum film thickness is very sensitive to a change in texturing parameters around the optimum, reasonably good friction and temperature characteristics can be achieved with a texture design that is a bit further away from the optimum. This means that, for the considered cases, the chosen texture design would most likely be based on the design resulting in the highest minimum film thickness.

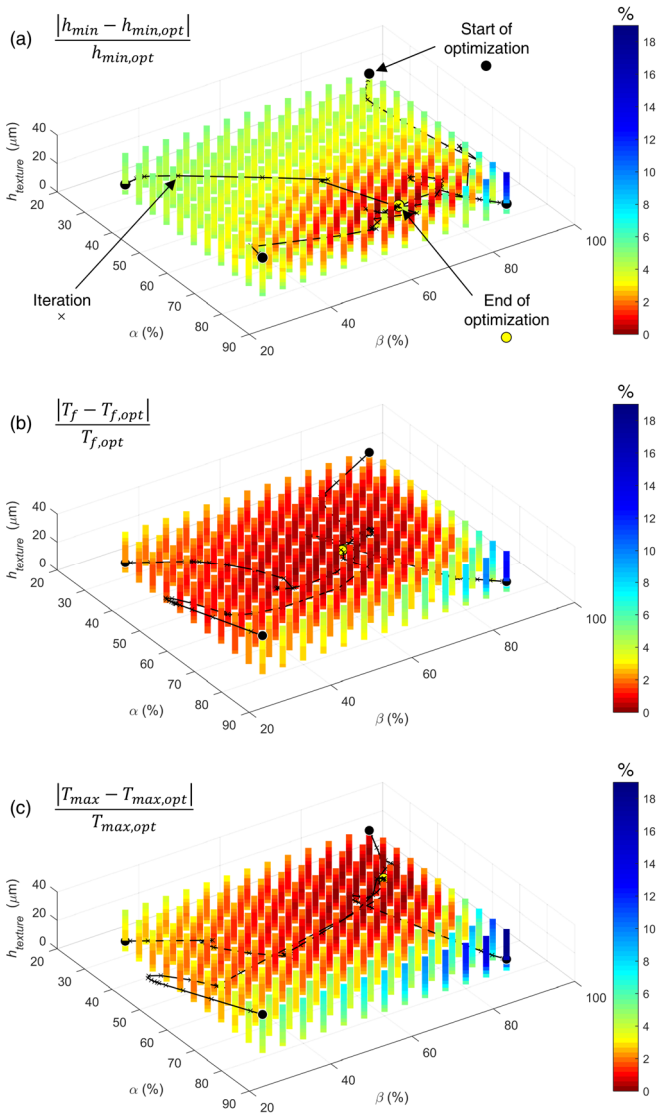

Figure 6.4 Validation of the optimization algorithm for three optimization objectives: (a) minimum film thickness, (b) friction torque and (c) maximum temperature.

6.4 Optimization results

The texture design optimization is performed for a total of 12 operating conditions (1000, 2000, 3000 rpm at 0.5, 1.0, 1.5, 2.0 MPa), three optimization objectives (h_{min}, T_f, T_{max}) and three texture densities (40, 50, 60%), resulting in a total of 108 simulations. The lower and upper bounds of the optimization were set to $\boldsymbol{x}_{lb} = (0\ \mu\text{m}, 10\ \%, 10\ \%)^t$ and $\boldsymbol{x}_{ub} = (75\ \mu\text{m}, 95\ \%, 95\ \%)^t$ and start values of $\boldsymbol{x} = (10\ \mu\text{m}, 50\ \%, 50\ \%)^t$ were used. The step tolerance was set to 10^{-8} and the optimality tolerance to $e_0 = 10^{-5}$. The required computation time for each optimization was around 40 minutes. Note that a cubic spline interpolation is used to smoothen the graphs presented in the following.

6.4.1 Optimum texture depth

Results of the optimization in terms of the optimum texture depth are shown in Figure 6.5.

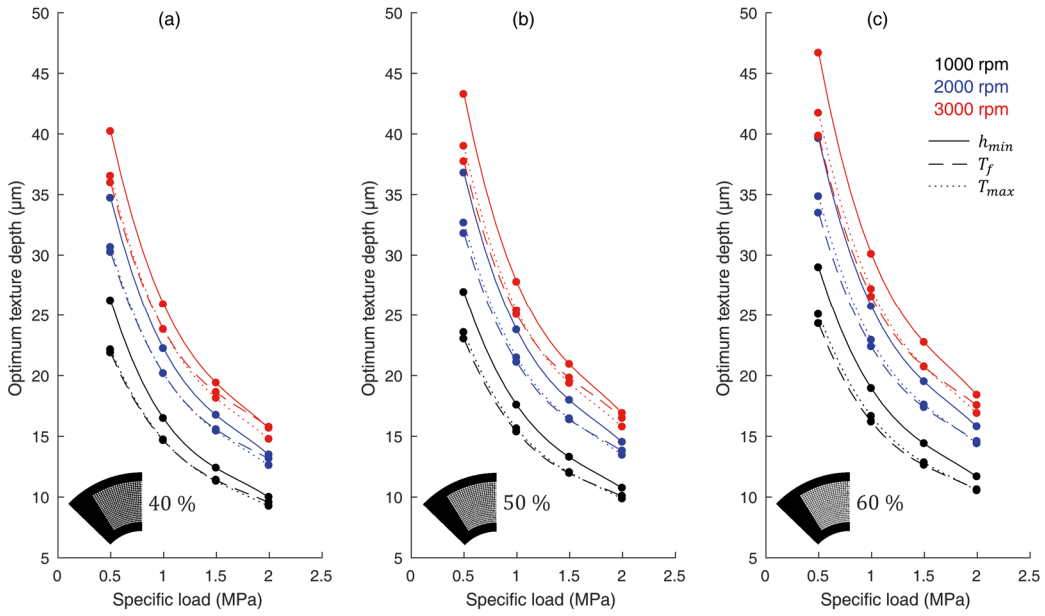

Figure 6.5 Optimum texture depth for different operating conditions and optimization objectives for a texture density of (a) 40%, (b) 50% and (c) 60%.

The results show that the optimum texture depth depends on the applied load and speed, the optimization objective as well as the texture density, ranging from 9 to 47 µm. A clear relation between the optimum texture depth and the operating condition is present for all 12 cases considered, where $h_{texture,opt}$ increases with an increase in speed and decreases with an increase in load, indicating a dependency of $h_{texture,opt}$ on the minimum film thickness. The results further demonstrate that the optimum texture depth depends on the texture density, where a higher density entails deeper textures. The optimization objective does have an impact on the optimum texture depth as well. Whereas predicted values for $h_{texture,opt}$ are almost identical for the optimization of T_f and T_{max}, values are considerably higher when the bearing is optimized in terms of h_{min} (on average about 11%).

To further analyse the relation between the optimum texture depth and the minimum film thickness, results are plotted again in terms of the relative texture depth defined as $S = h_{texture}/h_{min}$, where h_{min} is taken from the equivalent untextured bearing rather than the texture bearing to allow a selection of the texture depth based on easily available data from the conventional bearing (Figure 6.6).

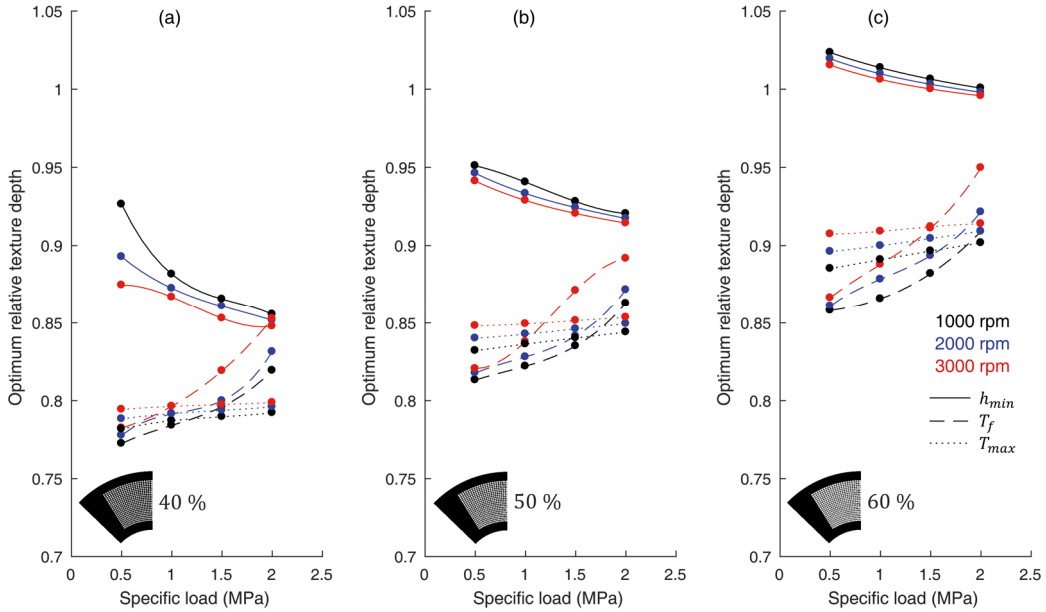

Figure 6.6 Relative optimum texture depth for different operating conditions and optimization objectives for a texture density of (a) 40%, (b) 50% and (c) 60%.

The optimum relative texture depth is almost independent of the rotational speed and only varies slightly with a change in applied specific load, where the optimum relative texture depth decreases with an increase in load when the pattern is optimized for h_{min} and increases with an increase in load for the other objectives. However, as the changes are marginal and a texture depth deviating only slightly from the optimum will still result in almost optimal performance as presented in Figure 6.4, justify the simplification of the data by averaging over the 12 investigated operating conditions. This results in a recommended relative texture depth of 0.87, 0.93 and 1.01 for densities of 40, 50 and 60% respectively if a high minimum film thickness is desired. To optimize the bearing in terms of friction and maximum temperature, the relative texture depth should be slightly lower at 0.8, 0.84 and 0.9 for the three investigated densities. As a rule of thumb, a relative texture depth of just under 1 seems to be preferable. In fact, it is well known that a relative texture depth of approximately 1 results in best performance for partially textured fixed geometry parallel and near-parallel hydrodynamic contacts (see chapter 2). The found values for the relative texture depth confirm that this is also true for the case of pivoted pad bearings. Furthermore, slightly deeper textures seem be the better for increasing the minimum film thickness whereas lower texture depths are preferred for a reduction of friction and temperature. This was also concluded in the parametric CFD study for point-pivoted pads by Zouzoulas and Papadopoulos [18]. The high dependency of the optimum texture depth on bearing speed and specific load makes it clear that the texture depth has to be selected for the expected operating condition or will be a compromise for the expected range of conditions.

6.4.2 Optimum circumferential extend

Results for the optimum extent of the textured region in circumferential direction are given in Figure 6.7.

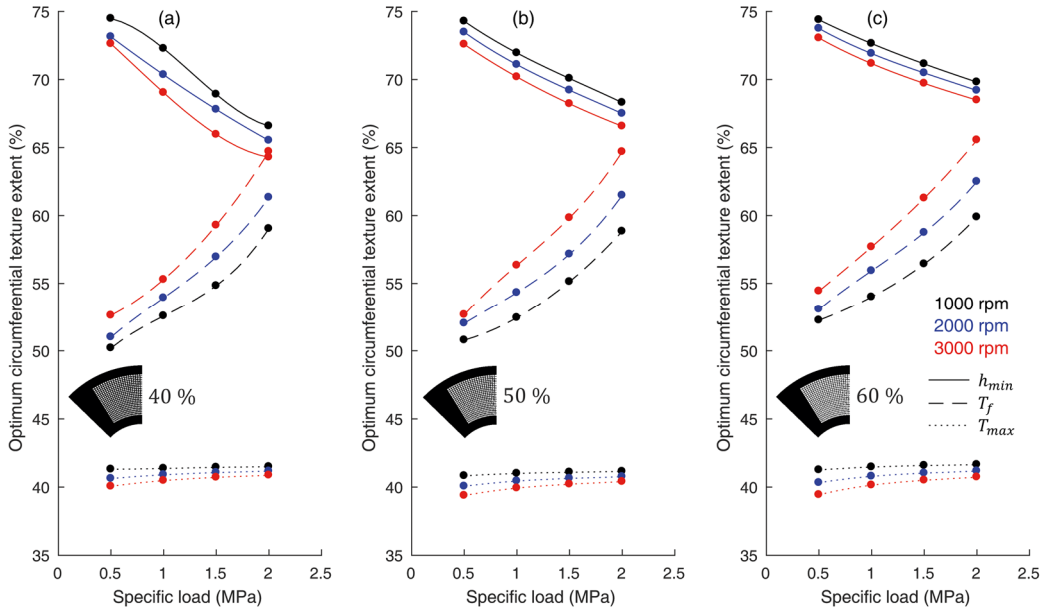

Figure 6.7 Optimum circumferential texture extent for different operating conditions and optimization objectives for a texture density of (a) 40%, (b) 50% and (c) 60%.

It is notable that α_{opt} is almost independent of the rotational speed as well as the texture density. However, values significantly depend on the optimization objective and specific load, ranging from 39 to 74%. α_{opt} decreases with an increase in specific load when optimized for h_{min}, starting at about 73% and ending at about 64%. The opposite is the case when α is optimized for T_f, where values range from 50% to 65%. Interestingly, α_{opt} is independent of the specific load when optimized for minimizing the maximum temperature, allowing to recommend a single value of 41%. This can be explained by the high influence of the texture extent in circumferential direction on the centre of pressure and therefore the equilibrium of the pad in terms of the tilt angle. To minimize the maximum temperature, a high lubricant inflow is desired, which is achieved by increasing the film thickness at the pad inlet by increasing the convergence ratio or tilt angle. For the investigated bearing and pivot position, this is achieved by texturing about 41% of the pad. The presented results show that as a rule of thumb about 3/4 of the pad should be textured in circumferential direction for maximizing the minimum film thickness, just over half of the pad for minimizing friction and about 2/5 of the pad for minimizing the maximum temperature.

6.4.3 Optimum radial extend

Regarding the optimum extent of the textured region in radial extent, values range from 56 to 91% (Figure 6.8).

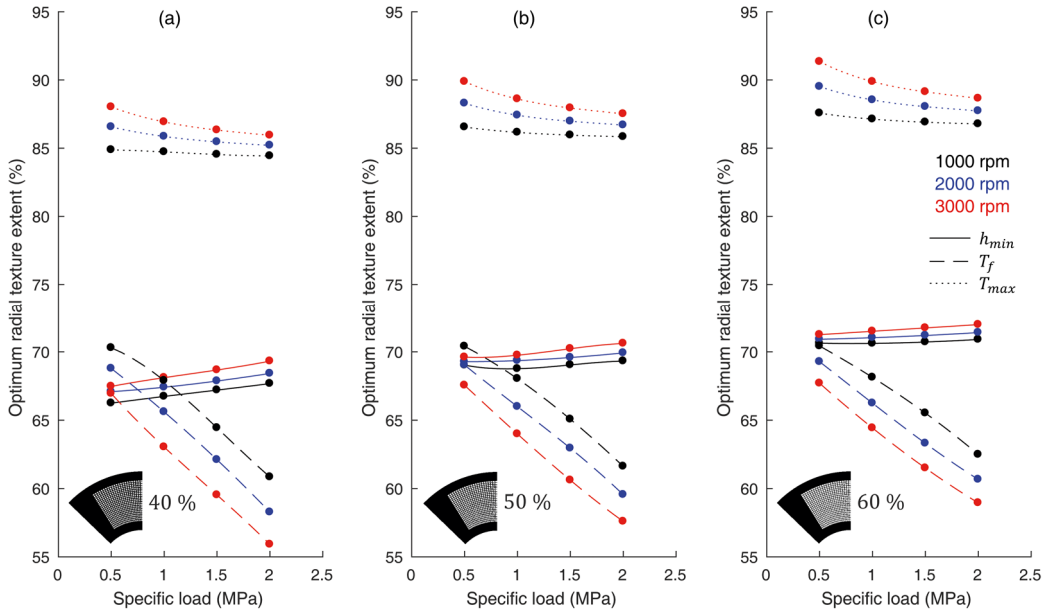

Figure 6.8 Optimum radial texture extent for different operating conditions and optimization objectives for a texture density of (a) 40%, (b) 50% and (c) 60%.

β_{opt} is mostly independent of the rotational speed and only shows a relevant dependency on the specific load when optimized in terms of the friction torque, where β_{opt} gets smaller with an increase in load, ranging from 70 to 56%. It is also evident that a higher texture extent is required for higher texture densities, although differences are small. Similarly to the optimum extent in circumferential direction, the most influential parameter is the optimization objective. If optimized in terms of minimum film thickness, the radial extent should be between 66 and 72%. Much higher values are predicted when the bearing is optimized for minimizing the maximum temperature. In this case, β_{opt} should be between 84 and 91%. The reason behind this is that the higher the texture extent in radial direction, the higher the lubricant inflow, which promotes cooling and results in lower temperatures. In fact, the lubricant inflow is increased by 9% on average with respect to the untextured bearing. The results show that as a rule of thumb, it can be concluded that a relatively high extent in radial direction of approximately 87% is recommended when the objective is a minimization of the maximum temperature. About 2/3 of the pad should be textured for optimum performance regarding the minimum film thickness and good frictional behaviour.

6.5 Discussion

6.5.1 Performance of the untextured bearing

To evaluate the influence of texturing on the bearing performance, the key characteristics of the conventional untextured bearing are evaluated. For these computations, a uniform mesh with 101 x 101 CVs is used. Results are presented in Figure 6.9.

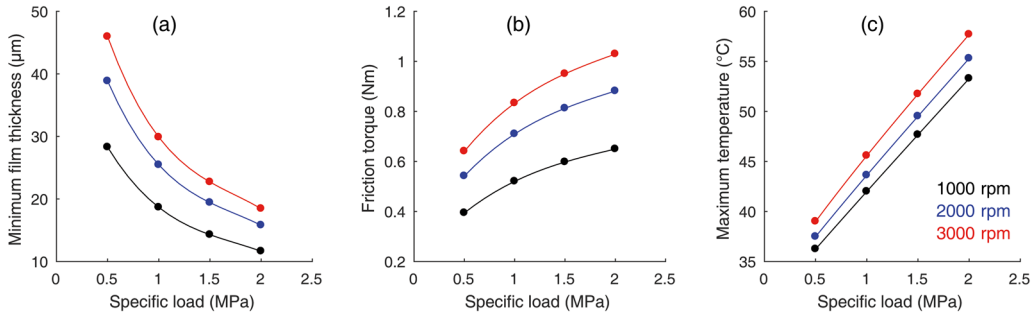

Figure 6.9 Performance of the untextured bearing: (a) minimum film thickness, (b) friction torque and (c) maximum temperature.

As expected, the minimum film thickness increases with an increase in speed and decreases with an increase in applied load. Operating at a specific load of 2.0 MPa and a rotational speed of 1000 rpm, a minimum film of just under 12 µm is predicted. The highest value is predicted for an operation at 0.5 MPa and 3000 rpm (46 µm). Both friction torque and maximum temperature increase with an increase in applied load as well as rotational speed. For the considered bearing, values range from 0.39 to 1.03 Nm and from 36 to 58°C for T_f and T_{max} respectively.

6.5.2 Performance of the textured bearing

The relative performance of the textured bearing with respect to the untextured bearing is evaluated for all 108 optimized texture patterns (Figure 6.10).

It should be remembered that all considered texture patterns in this graph are optimized for either h_{min}, T_f or T_{max}. Therefore, given results can be interpreted as highest achievable improvements through surface texturing. Note however that a significant degradation in bearing performance may occur if a particular surface design is used under operating conditions it was not designed for. For example, consider the design with 50% texture density optimized for maximizing h_{min} at 0.5 MPa and 3000 rpm ($h_{texture,opt} = 43$ µm, $\alpha_{opt} = 73\%$, $\beta_{opt} = 70\%$). As shown in Figure 6.10, this particular design increases h_{min} by about 9% while not having a

noteworthy influence on friction torque nor temperature. If this pattern was used at 2.0 MPa specific load and 1000 rpm, the minimum film thickness would be decreased drastically by about 14%. Although the friction torque is not influenced much, the maximum temperature would also be increased by 18% with respect to the untextured bearing. This highlights the importance of a thorough texture design for a specific application.

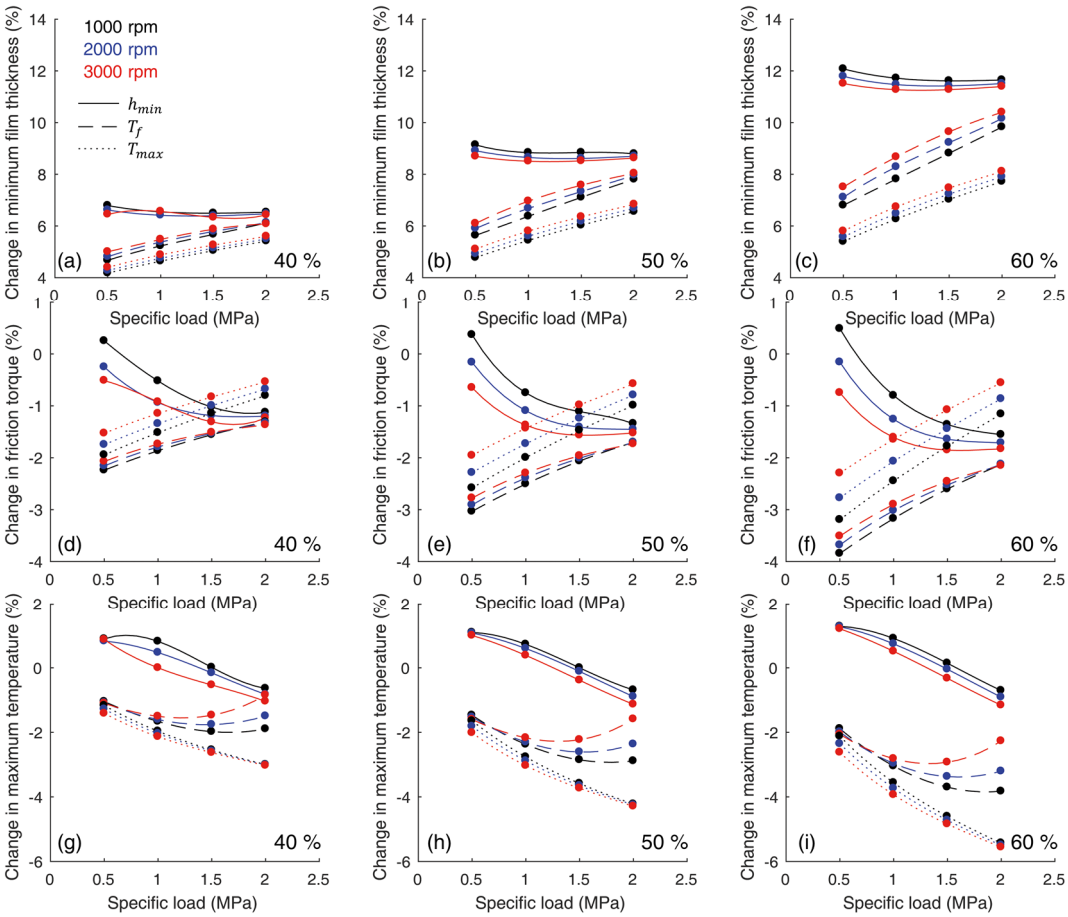

Figure 6.10 Performance change caused by texturing: (a) – (c) change in minimum film thickness, (d) – (f) change in friction torque and (g) – (i) change in maximum temperature.

The results also show that the beneficial influence of texturing increases with an increase in texture density for all considered cases. However, this is expected, as it is known for other partially textured contacts that the density cannot be optimized as a higher density will always improve bearing performance (see chapter 2). Therefore, the beneficial impact of the considered texture designs could most likely be further enhanced by using higher texture densities. However, this was not done as the density is limited by stress concentration and mixed lubrication considerations.

Interestingly, by far most of the investigated texture patterns improve all three of the considered performance characteristics, independent of the optimization objective, although highest improvements of a particular performance parameter are obviously always achieved by the pattern that was optimized for this parameter.

Exceptions to this are the patterns optimized to improve the minimum film thickness, which increase maximum temperature and friction for cases where the bearing operates at low specific loads. Whereas the achievable improvement of the minimum film thickness reaches values of up to 12%, possible enhancements in terms of friction torque and temperature are rather small, being only about 4 and 6% respectively, likely not justifying the application of surface textures under hydrodynamic conditions.

It is also noteworthy that the convergence ratio of the pads in equilibrium is no longer determined solely by the pivot position, which is the case for conventional tilting pad thrust bearings. The high influence of the texture extent in circumferential direction on the centre of pressure also entails a dependency of the convergence ratio on the circumferential texture extent, as investigated also by Yagi and Sugimura [239]. Interestingly, the studied texture patterns always decrease the convergence ratio (Figure 6.11).

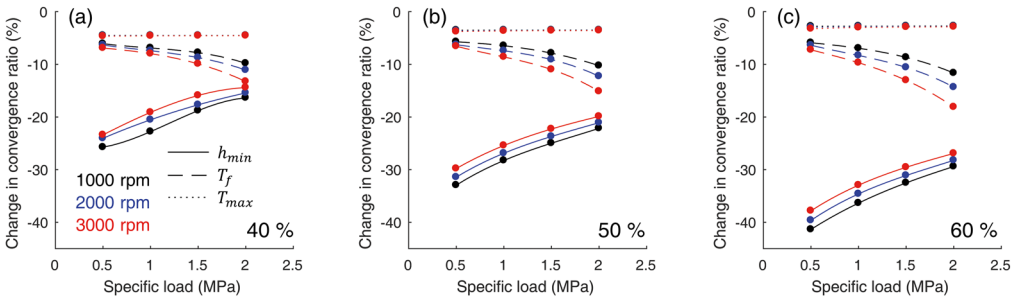

Figure 6.11 Change in convergence ratio caused by texturing for different texture densities: (a) 40%, (b) 50% and (c) 60%.

It can be seen that regarding the patterns optimized for T_{max}, the convergence ratio is slightly decreased by approximately 4% independently from texture density and operating conditions. Slightly higher changes are encountered for the patterns optimized for T_f, being decreased by about 6% for low load and speed and up to 18% for high load and speed. The most significant changes in convergence ratio are encountered when the texture pattern is optimized for h_{min}. For a texture density of 40%, texturing causes the convergence ratio to drop by 14 to 26%, depending on the operating conditions. For texture densities of 50 and 60% the convergence ratio is decreased by 20 to 33% and 27 to 41% respectively. In summary, all optimized texture patterns cause the bearing to operate at lower convergence ratios, reaching values of up to 41%.

The impact of texturing on the amount of lubricant entering the pads at the leading edge is also analysed (Figure 6.12). For nearly all configurations, more lubricant is entering the textured pads than the untextured pads, reaching differences of up to about 14%. Again, exceptions are the patterns optimized for h_{min} operating at low loads, where less lubricant is entering the pads. It can also be noted that the higher

the texture density, the higher the amount of lubricant entering the pads. Understandably, the patterns optimized for minimizing T_{max} require the highest amount of lubricant.

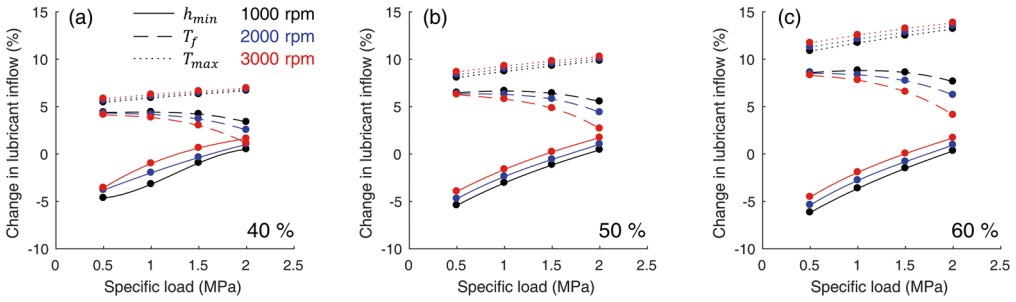

Figure 6.12 Change in lubricant inflow caused by texturing for different texture densities: (a) 40%, (b) 50% and (c) 60%.

With an exception to the designs optimized for T_{max} and the designs optimized for T_f at low loads, the maximum film thickness is decreased for all configurations (Figure 6.13). The highest decrease in maximum film thickness (up to 20%) is encountered for the patterns optimized to maximize h_{min}. This is understandable, as the increase in minimum film thickness is primarily achieved by altering the bearing equilibrium in order to decrease the pitch angle and convergence ratio. Therefore, when h_{min} is increased, h_{max} is decreased as a result.

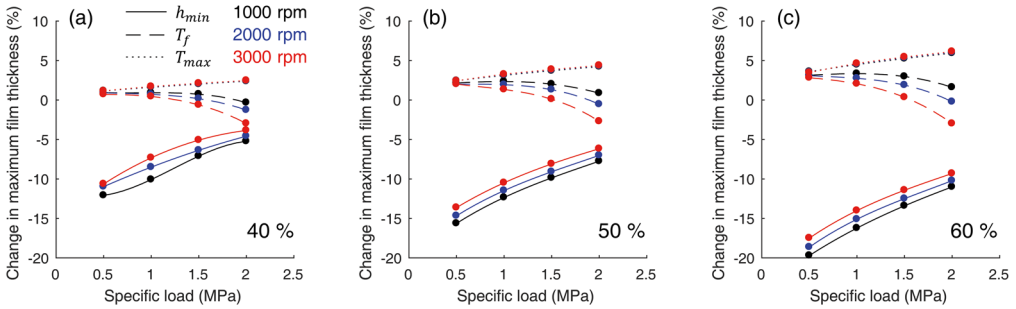

Figure 6.13 Change in maximum film thickness caused by texturing for different texture densities: (a) 40%, (b) 50% and (c) 60%.

To analyse the influence of texturing on the temperature distribution over the pads, Figure 6.14 shows the change in the maximum temperature increase, which is defined as $T_{max} - T_{in}$, as well as the change in the effective lubricant temperature (the change in the inlet temperature T_{in} is insignificant and is therefore omitted).

Analog to all previous result, the higher the texture density, the higher the impact of texturing. As compared to the untexterd pads, the textured pads that were optimized for h_{min} result in higher temperature increases for most operating conditions, reaching values of up to 7%. All other configurations cause the temperature increase to be lower than the one encountered for the equivalent untextured pad. With regards to the effective temperature, results are similar. The designs optimized for h_{min} cause an increase of up to 1% of the effective temperature,

while the all other configurations cause a decrease in the effective lubricant temperature. Unsurprisingly, the patterns optimized for T_{max} have the highest impact on the effective temperature, decreasing it by up to 4%.

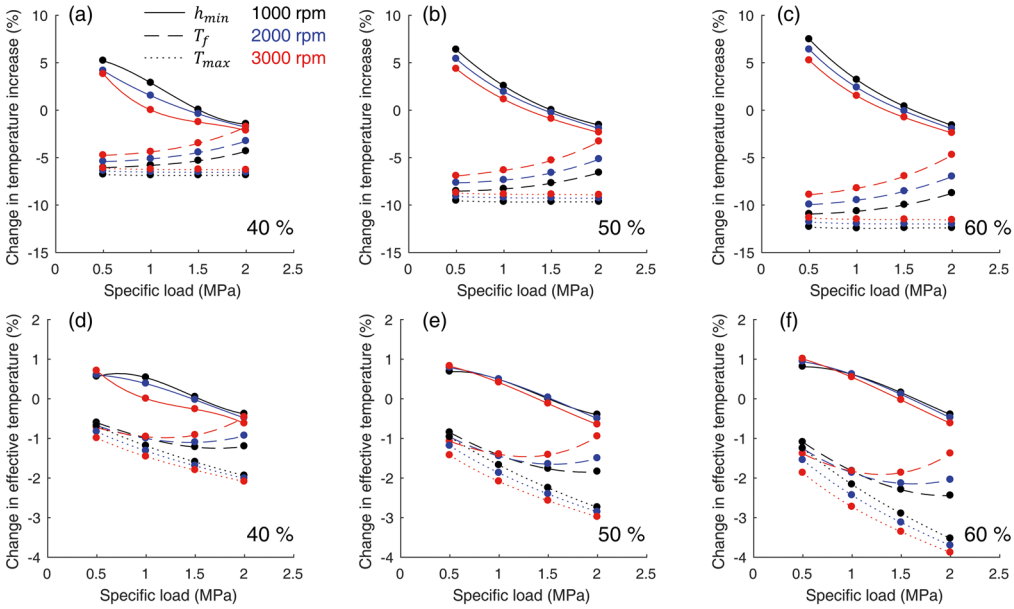

Figure 6.14 Change in temperature increase (a) – (c) and effective temperature (d) – (f) caused by texturing for different texture densities.

6.6 Summary

This chapter presented the numerical optimization of surface textures for tilting pad thrust bearings in terms of texture depth, circumferential extent and radial extent for various operating conditions and optimization objectives (minimum film thickness, friction torque and maximum temperature). The developed numerical model was utilized in combination with an interior-point algorithm to perform a texture design optimization on a normal desktop computer within 40 minutes.

The results show that the optimum texture depth depends significantly on the operating conditions and texture density but is mostly independent of the optimization goal. It is also found that the optimum texture depth should be just slightly smaller than the encountered minimum film thickness of the untextured bearing. The optimum texture extent in circumferential direction is largely independent of rotational speed and texture density but does depend on the specific bearing load and the optimization objective. Around 3/4 of the pad should be textured for high minimum film thickness values, just over half of the pad for low friction values and about 2/5 of the pad for low maximum temperatures. The optimum texture extent in radial direction only depends on the applied specific load and the optimization objective. A radial extent of 87% is recommended for low

maximum temperatures and approximately 2/3 of the pad should be textured for both high minimum film thickness and good friction characteristics. Three densities are investigated, where the highest density of 60% results in most significant performance improvements. Whereas minimum film thickness values can be improved by up to 12%, friction and temperature characteristics can only be improved marginally.

Overall, the results highlight the importance of a proper texture design, which is only possible if the bearing application and predominant operating conditions are known. The developed numerical model allows a fast optimization and initial selection of texture designs. A final texture design may then be chosen based on additional CFD simulations or experimental studies.

Chapter 7

Experimental Work

In order to further assess the accuracy of the developed model and also study the potential benefit of surface texturing under conditions close to the ones found in an industrial setting, experiments are carried out on a purposely developed bearing test rig. The test rig was designed by the industrial sponsor of this project, John Crane UK Ltd, and experiments were carried out by Dr Fabio Ricchiuto in their laboratories in Slough, UK. All other work (development of the test methodology, data preparation and analysis) was conducted by the author of this thesis.

In this chapter, the utilized test rig and its instrumentation are introduced. Details of the testing procedures and the investigated tilting pad thrust bearing are given. Results are presented for various operating conditions, while comparing the conventional plain pads with the textured ones in terms of friction torque and pad temperature. The end of the chapter contains a detailed comparison of obtained experimental results with the developed mathematical model.

7.1 Experimental setup

7.1.1 Test rig

All experimental data is obtained using the developed load controlled test rig for tilting pad thrust bearings shown in Figure 7.1.

An electric motor with 45 kW provides enough energy to run the system with up to 4500 rpm, using a flat belt for transmission. A pneumatic loading system is used to load the stationary test bearing against the runner with a maximum of 18 kN. The oil supply system is capable of controlling oil flow rate, pressure and temperature

and is used to supply the tilting pad bearing as well as the supporting rolling element bearings with lubricant. The test bearing is mounted in a test chamber, as shown in Figure 7.2.

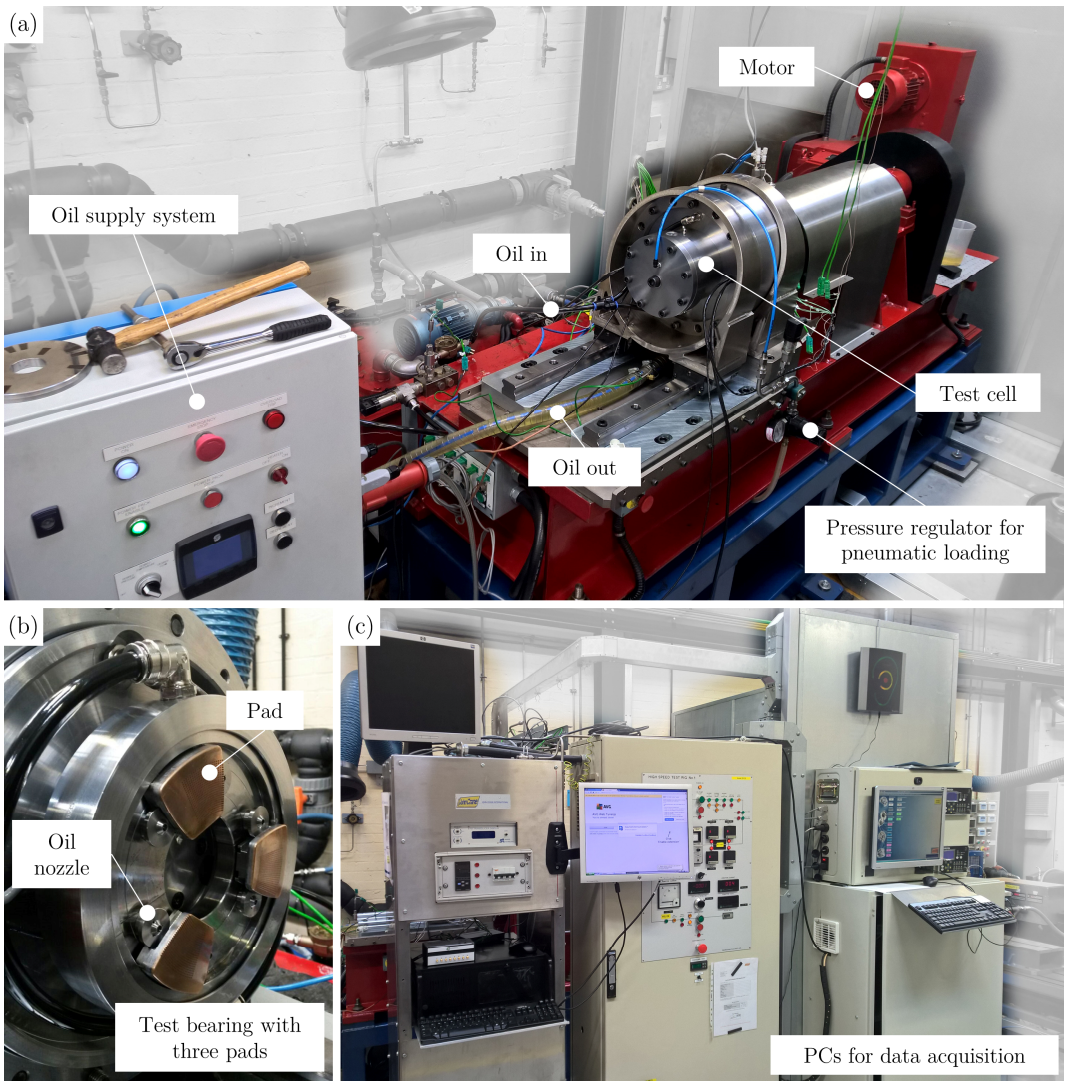

Figure 7.1 (a) Test rig with test cell, motor and oil supply system, (b) Test bearing mounted in the test cell, (c) data acquisition system.

The tilting pad thrust bearing (9) is the same as the one analysed in the previous chapter, geometrical details can be found in Table 6.1. The bearing is equipped with three thrust pads (8) (material number: 1.0401), coated with a 1.5 mm bronze layer (material number: 2.1182) rather than the more commonly used white metal to avoid increased wear of the texture pattern. The bearing is run against the runner (7), which is mounted on the main shaft (1) by a clamping device (6). Two tapered roller bearings in back-to-back arrangement are used to bear the axial loads. A 33213 on the tilting pad bearing side (4) and a 33212 on the motor side (3). Two oil drop nozzles (5) supply the roller bearings with fresh oil, which is drained through two outlets outside the bearing pair and one drain in-between them (17) to avoid entrapment of lubricant. The roller bearings are sealed by two labyrinth seals (2).

The test bearing (9) sits in the bearing cage (10) and is directly lubricated through oil supply nozzles (16) situated at each pad's inlet. The nozzles (16) are supplied with lubricant through the circumferential groove in the bearing housing, which is supplied through two tubes from the main oil inlet (11). The main oil outlet (15) drains the cell from lubricant. Compressed air is supplied at (13) to move the piston (12) and load the test bearing (9) against the runner (7). The left hand side of the test cell sits on linear bearings (14) to allow fast and easy access to the test bearing.

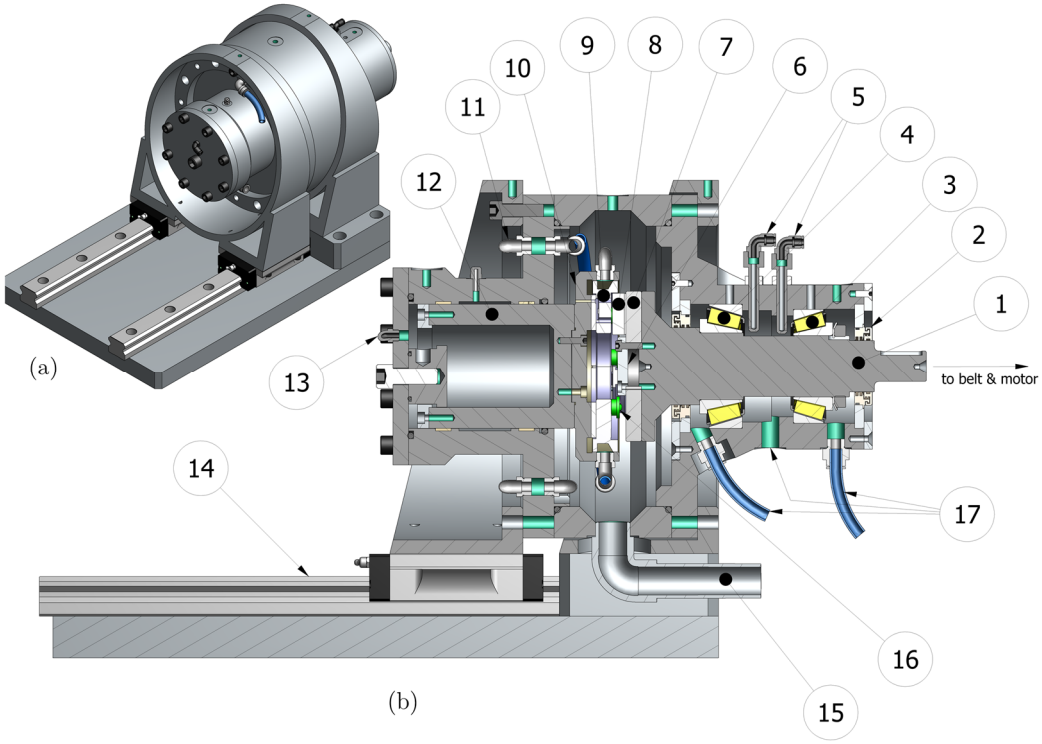

Figure 7.2 Details of the test cell: (a) 3D view and (b) sectional view.

7.1.2 Instrumentation

To monitor the operating conditions and bearing performance characteristics, the test rig and particularly the test bearing are equipped with a variety of sensors. The shaft is equipped with a tachometer and a Rayleigh wave torque transducer to measure the rotational speed and frictional torque respectively. The pneumatic loading system includes a pressure sensor that provides the current air pressure. The main oil inlet is equipped with a flow meter to measure the oil supply flow rate. Also, type-K thermocouples are used to monitor oil inlet and outlet temperature as well as the temperature of the two roller bearings, where the temperature of the outer bearing rings are monitored.

The bearing housing is equipped with an integral thrust measuring ring, where each pad is supported by a beam (Figure 7.3). Each of these beams is equipped with temperature compensated strain gauges at the back, which allow monitoring the load

each individual pad carries with an accuracy of 2% (patent pending "Constant Strain Beam CSB": EP2475900B1 [240]). Specific loads of up to 5 MPa can be measured.

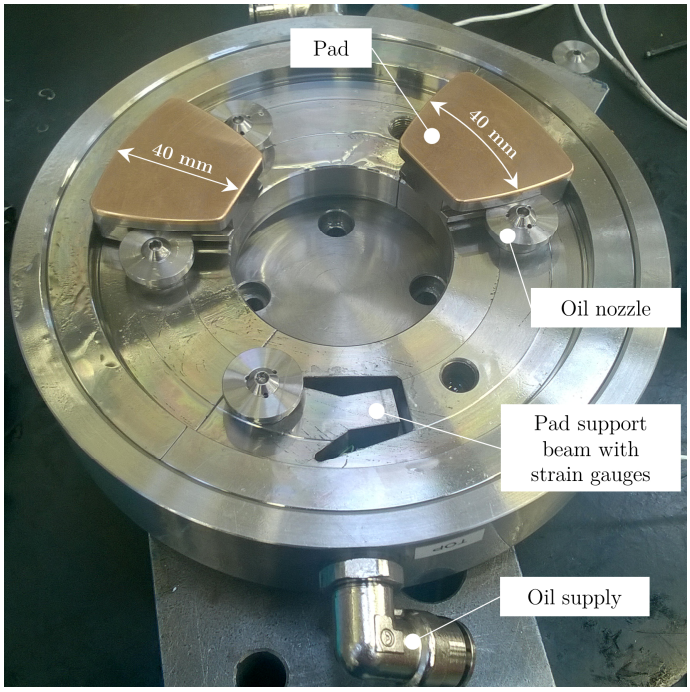

Figure 7.3 Photograph of the test bearing with one pad removed.

One of the pads is equipped with 10 type-K thermocouples as well as two ultrasonic sensors to approximate the temperature distribution and film thickness respectively (Figure 7.4).

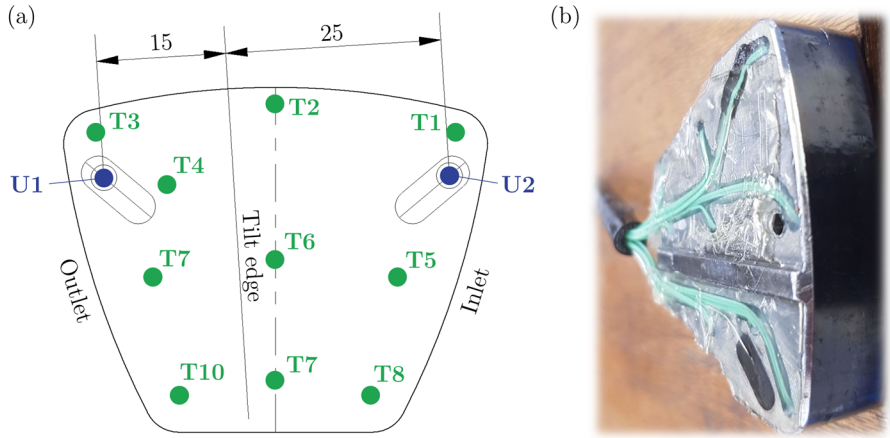

Figure 7.4 (a) Thrust pad with thermocouple and ultrasonic sensor positions, (b) photograph of a fully equipped pad.

The thermocouples are inserted through 2 mm holes machined in the back of the pad and measure the temperature approximately 2.5 mm below the active pad surface. The relative positions of the thermocouples in circumferential direction and radial directions are given in Table 7.1.

Table 7.1 Relative thermocouple positions.

Thermocouple	Circumferential position (%)	Radial position (%)
T1	13	95
T2	50	95
T3	87	95
T4	75	75
T5	17	50
T6	50	50
T7	83	50
T8	12	15
T9	50	15
T10	88	15

One thermocouple (T4) is placed at the traditional 75/75 position to measure the maximum pad temperature. The CAD drawing of the modified thrust pads can be found in Appendix D.1. To measure the film thickness, two ultrasonic sensors are placed in machined pockets close to the pad inlet and outlet. Channels are machined in the back pad surface to guide all cables and avoid any disturbance of the pad's tilt motions. The acoustic properties of the pad materials and the lubricant (ISO VG 32) used for the acquisition software of the ultrasonic measuring system are given in Table 7.2.

Table 7.2 Acoustic properties of the pad and lubricant used for the acquisition software of the ultrasonic measurement system.

Description	Symbol	Quantity
Specific acoustic impedance of the pad, C15 (Mrayl)	z_{pad}	46
Specific acoustic impedance of the bronze coating, CuPb15Sn (Mrayl)	$z_{coating}$	32.12
Lubricant density (kg/m^3)	ρ	871
Speed of sound in oil at 20°C (m/s)	c	1461
Temperature compensation (m/s/K)		-3.5

As only the static bearing performance is investigated, a data acquisition rate of 1 Hz was used for all measurements.

7.1.3 Bearing and texture geometry

The test bearing is a standard-size tilting pad thrust bearing with offset line pivots

and is the same as the one investigated in chapter 6. Therefore, geometrical details and lubricant properties can be found in Table 6.1. The texture pattern for the experiments was designed before the optimization results presented in chapter 6 were available. For this reason, the texture design was based on the findings of the literature review only. The texture pattern used for the experiments is shown in Figure 7.5.

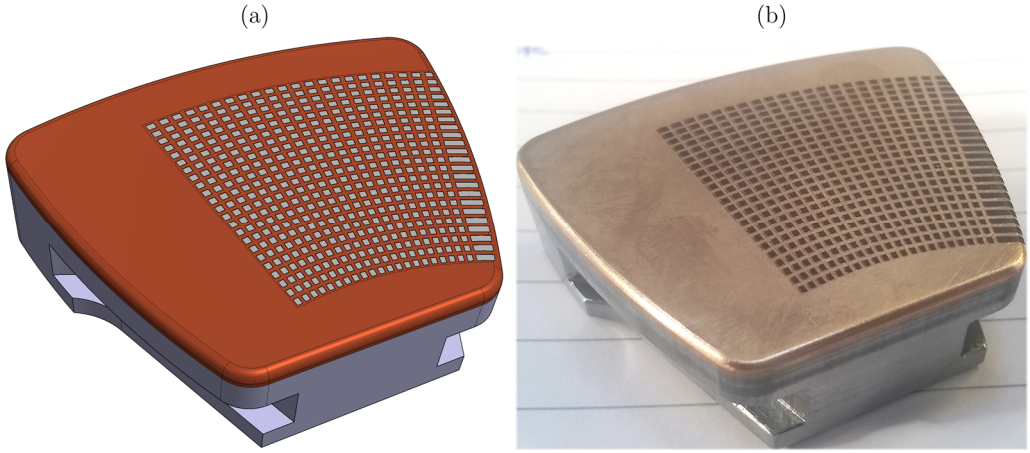

Figure 7.5 (a) CAD model of the texture pattern and (b) photograph of the laser textured thrust pad.

As only partial texturing is capable of reasonably improving the bearing performance, 70% of the pad is textured in circumferential direction. The same extent was used for the radial direction. The first row of textures is elongated towards the inlet to increase the lubricant inflow as recommended in literature. The chosen texture pattern consists of 23 x 23 angular sector shaped textures at a density of 40%, resulting in an average texture size of approximately 770 x 770 µm. This texture density results in reasonably sized areas in-between textures, thus, limiting increased wear while still being capable of providing hydrodynamic lift. A texture density of 100%, i.e. a pocket, would most likely result in better performance during hydrodynamic operation. However, although no clear experimental evidence is available, individual textures may be capable of trapping wear debris or acting as lubricant reservoirs and therefore increase bearing lifetime and decrease friction during critical mixed lubrication conditions.

The most problematic parameter to choose is the texture depth, as its optimum value depends significantly on the encountered minimum film thickness. Therefore, calculations were carried out to approximate the expected minimum film thickness values for the load and speed range chosen for the experiments (0.5 – 1.5 MPa and 1000 – 3000 rpm). Those values were then averaged and multiplied with the average recommended relative texture depth found in literature of 0.87. This results in a texture depth of approximately 15 µm. This value was chosen for the experiments. A CAD drawing of the texture design can be found in Appendix D.2, texturing parameters are given in Table 7.3.

The textures were manufactured by laser surface texturing (LST), where a pulsed high energy laser is used to remove material through ablation. An optical microscope (*Alicona Infinite-Focus by Alicona Imaging GmbH Austria*) was used to assess the quality of the produced textures. For this purpose, the topography of the four textures at the edges of the textured area was measured. A magnification of 10x was used and the vertical and lateral resolution was set to 100 nm and 2 µm respectively. The obtained topographies were averaged over the circumferential and radial direction, resulting in two two-dimensional height distributions. Figure 7.6 presents images of a texture and the derived 2-D height distributions for example. These distributions were then averaged again to get the average texture depth. All measurements were performed for two textured pads. As shown in Table 7.4, the depth of the manufactured textures lies within the specified tolerance of 15 ± 3 µm.

Table 7.3 Texturing parameters for the experimental study.

Description	Symbol	Quantity
Texture depth (µm)	$h_{texture}$	15
Relative texture extent in circumferential direction (%)	α	70
Relative texture extent in radial direction (%)	β	70
Inlet textured?		yes
Texture density (%)	$\rho_{texture}$	40
Number of textured in circumferential direction	n_θ	23
Number of textured in radial direction	n_r	23

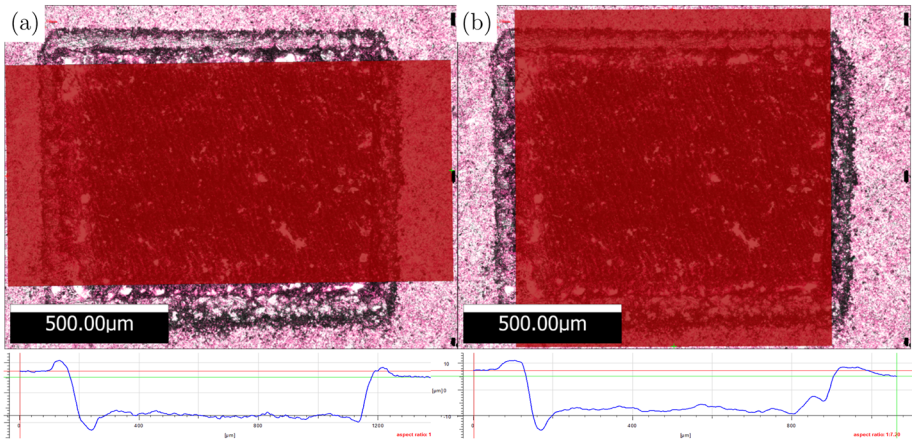

Figure 7.6 Images of a texture and red shaded areas used to average the height data in (a) circumferential and (b) radial direction.

Table 7.4 Measurement results for the texture depth.

Pad number	Texture	Average depth (µm)	Pad average (µm)
S10189760	upper left	16	15.3
	upper right	16	
	lower left	14	
	lower right	15	
S10189765	upper left	14	13.9
	upper right	14.5	
	lower left	13	
	lower right	14	

7.2 Test methodology

The experiments are aimed at comparing the performance of conventional plain pads with textured pads under steady-state operating conditions as well as validating the developed mathematical model. For this purpose, experiments are conducted for various combinations of speed and load, where all tests are carried out for the conventional bearing and then repeated for the bearing equipped with the textured pads.

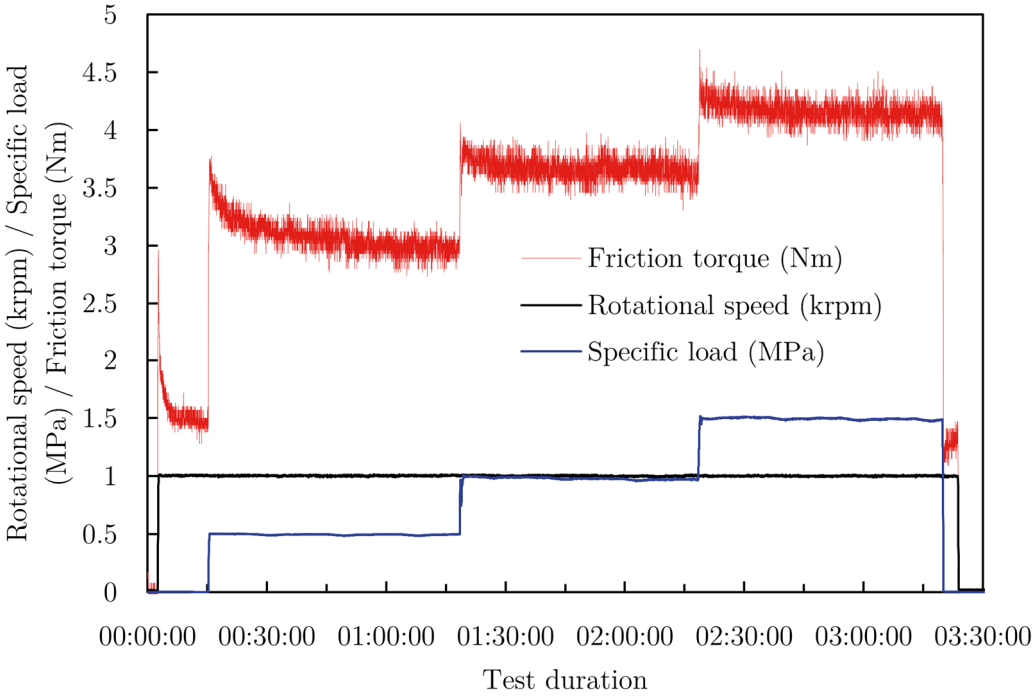

Figure 7.7 Friction torque measurements for the textured pad at 1000 rpm.

Each test is carried out for a constant rotational speed of either 1000, 2000 or 3000 rpm, while the specific bearing load is increased incrementally from 0.5 to 1.0 MPa

and then from 1.0 to 1.5 MPa, i.e. 807.8 – 2423.4 N of load per pad. To ensure thermal equilibrium, each load is applied for a duration of 1 hour, i.e. each test lasts approximately 3 hours. Results of a typical test are shown in Figure 7.7 for the bearing with textured pads at 1000 rpm. The bearing is supplied with 5.55 l/min of ISO VG 32 mineral oil at a constant temperature of 30°C. The oil supply system is started and run for at least 10 minutes before the test to ensure identical conditions for each test. After increasing the rotational speed to the desired value, the bearing is run without any load for about 10 minutes before applying the first load step of 0.5 MPa through the pneumatic loading system. To achieve the desired loading, the air pressure is increased until the sum of the strain gauge measurements of each pad is equal to the desired load. The alignment of the system is adjusted if necessary through screws at the test cell until each pad carries the same load with a tolerance of ±50 N. A clear reduction in torque is visible during the first hour, caused by the increase in temperature and corresponding decrease in viscosity. Subsequently, the load is increased to 1.0 MPa and again held constant for 1 hour. After an initial spike, the torque slowly decreases again during this hour due to the increasing temperature, although this effect is less pronounced as compared to 0.5 MPa. Thereafter, the load is set to the final value of 1.5 MPa and held constant for another hour. The load is then taken away completely and the motor is stopped. Each of the 3 hour tests were conducted three times for each rotational speed to ensure a good repeatability of the results.

Note that the oil supply temperature is regulated by the heater and cooler of the oil supply system. This causes a fluctuation of the oil supply temperature by approximately ±1°C (Figure 7.8).

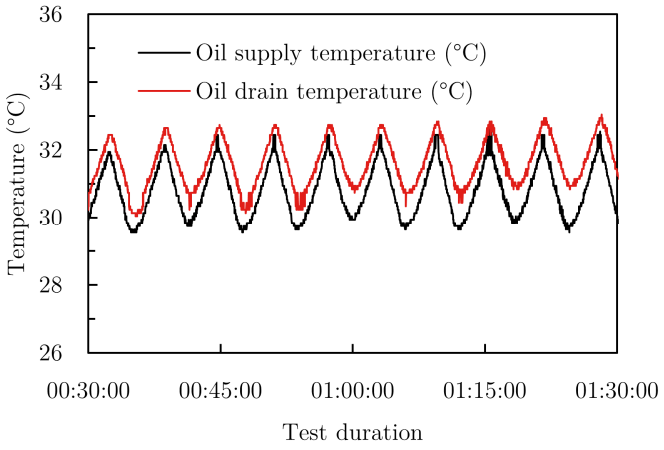

Figure 7.8 Fluctuations of the oil supply and oil drain temperature.

This fluctuation is also visible in the measured drain temperature. In fact, as all bearing performance parameters depend significantly on the oil temperature, the encountered fluctuation is slightly visible in all measurements. For this reason, results presented in this chapter are all averaged over one oil cooling cycle, which is usually about 6 minutes long.

7.3 Experimental results

Film thickness measurements are omitted from the following sections, as the utilized ultrasonic measurement system was a prototype and did not provide reliable film thickness measurements. The main issues were the temperature compensation of the readings as well as the repeatability of the measurements. Future work includes the optimization of the test rig by installing eddy current proximity probes at the centre of the test bearing, although no tilt angle measurements are possible this way.

7.3.1 Friction torque

Figure 7.9 presents the averaged values of the measured friction torque as a function of the applied load for different rotational speeds for the plain and textured bearing.

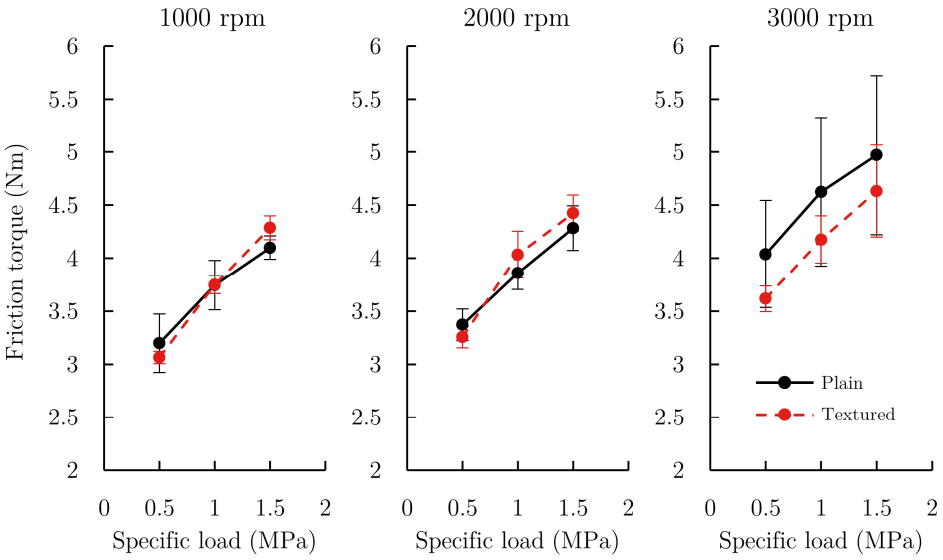

Figure 7.9 Average values of the measured friction torque for the plain and textured bearing.

Note that, due to the location of the torque transducer, the measured friction torque consists of the frictional torque caused by the tilting pad bearing as well as the friction torque caused by the two support bearings. Unfortunately, the test rig did not allow to measure the friction torque caused by the tilting pad bearing only. As expected, the higher the applied load and the higher the rotational speed, the higher the friction torque. The lowest measured friction torque is 3.01 Nm and encountered for the textured pads at 0.5 MPa and 1000 rpm. The highest torque is measured at 1.5 MPa and 3000 rpm for the plain pads. For this case, a torque value of 4.97 Nm is measured on average.

Although small differences in torque between the plain and textured pads are noticeable, the standard deviation of the results does not allow to draw conclusions

regarding the influence of texturing on the performance of the bearing in terms of friction torque. Numerical simulations predict a small reduction in friction torque, however, not reaching values above 1%. Even if the texture design was optimized for a friction reduction, possible performance improvements would be marginal for a texture density of 40% (Figure 6.10 (d)). Hence, no clear influence of texturing is observable in the measured friction torque values.

7.3.2 Pad temperature

To see whether texturing has an influence on the maximum pad temperature, the measured temperatures at the pad's 75/75 position (T4) are plotted in Figure 7.10.

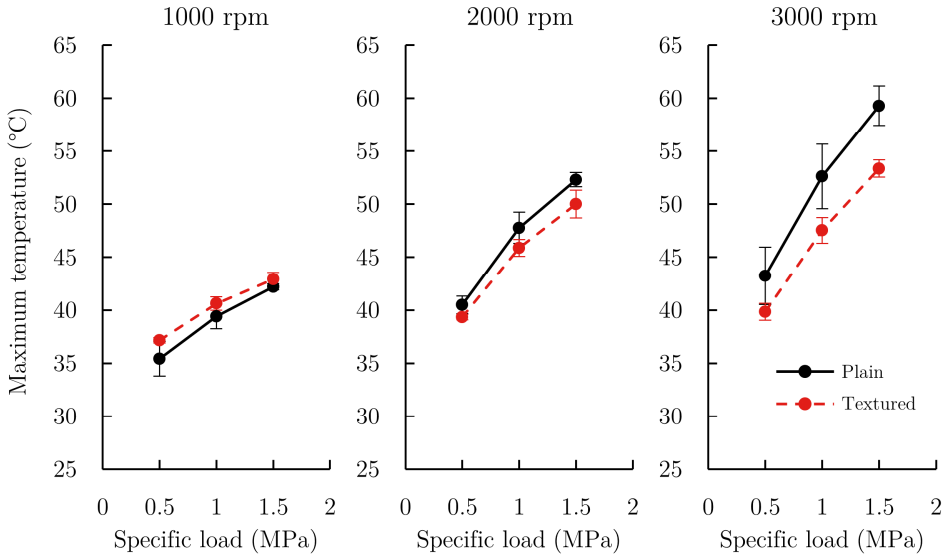

Figure 7.10 Average values of the measured maximum temperature (T4) for the plain and textured bearing.

Similarly to the friction torque values, the standard deviation is relatively high with regards to the changes in temperature caused by texturing. However, for rotational speeds of 2000 and 3000 rpm, it is observable that the textured pad exhibits lower temperatures at the 75/75 position, in particular at higher loads. To investigate this further, measured temperatures from the other 9 thermocouples are plotted in Figure 7.11. The plots show the thermocouple measurements at different pad locations after 1 hour of steady state operation for the investigated loads and speeds. The shown temperatures are averages of three experiments. As expected, temperatures are lower close to the pad's inlet and higher close to the pad's outlet. The higher the load and the speed, the higher the encountered temperatures. The temperature change along the radial direction is far less pronounced than the change in circumferential direction. For the experiments at 1000 rpm, the textured pad exhibits higher temperatures than the plain pad, although differences are insignificant. For rotational speeds of 2000 and 3000 rpm, the temperatures of the textured pad are slightly lower

than the temperatures of the plain pad, on average about 2°C at 2000 rpm and 4°C at 3000 rpm. This indicates that texturing is capable of decreasing the maximum pad temperature, although differences are small.

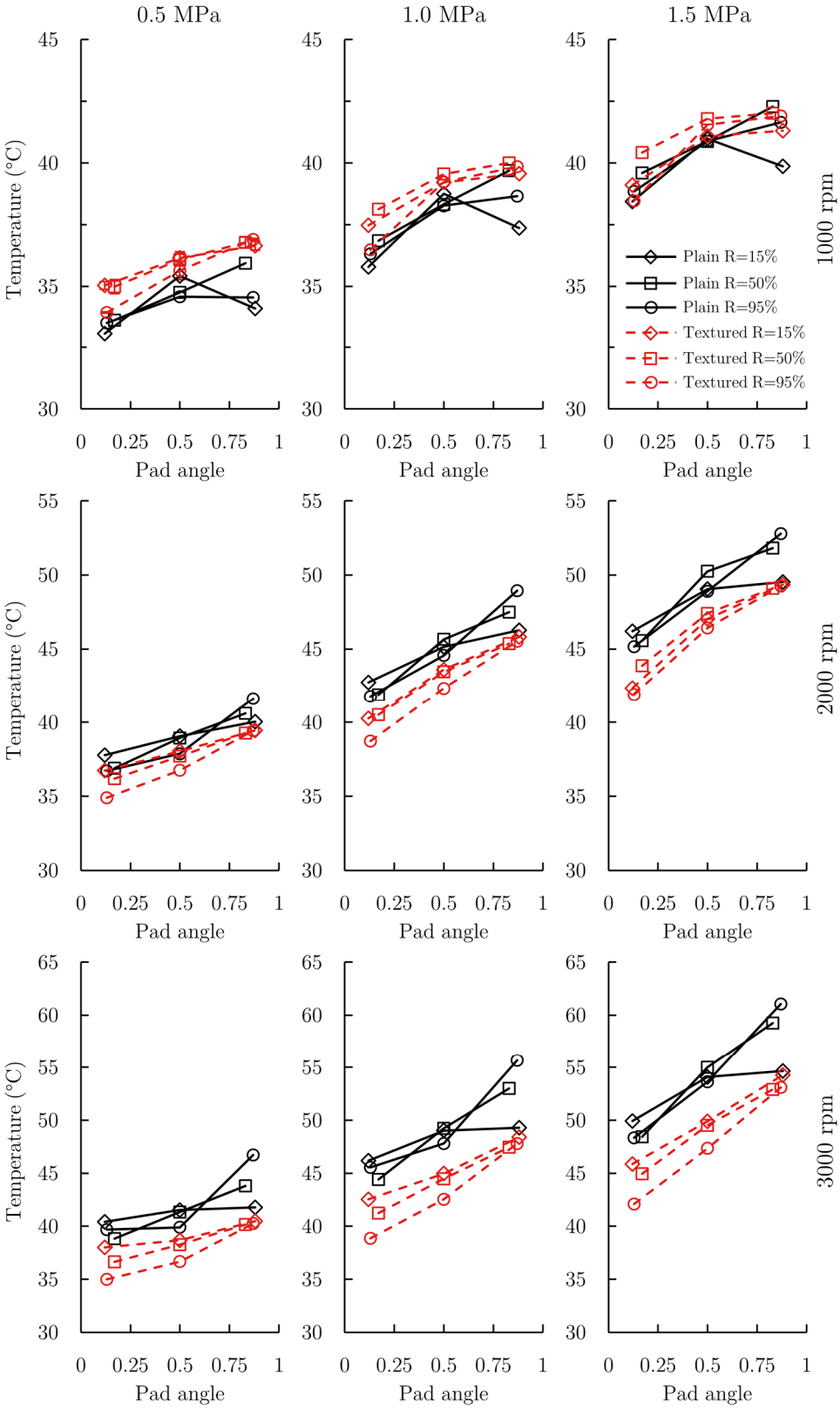

Figure 7.11 Average values of the measured temperatures for the plain and textured bearing.

7.4 Comparison with numerical data

7.4.1 Numerical simulation

To compare the experimental data with predictions of the developed numerical model, a parametric simulation is run for the 9 load and speed combinations. A mesh with 101 x 101 control volumes is used for the plain pad and a mesh with 144 x 144 control volumes for the textured pad (as shown in Figure 6.3), where the MNUFVD method is used for discretization. Tolerance values of $e_p = 10^{-6}$, $e_e = 10^{-4}$ and $e_t = 10^{-5}$ are used. Newton's algorithm is performed for the first temperature iteration, followed by Broyden's method for the remaining temperature iterations. The total computation time for all 9 operating conditions including the plain and textured bearing was just under 6 minutes.

7.4.2 Friction torque

The numerically predicted friction torque is the friction torque caused solely by the tilting pad thrust bearing. The measured friction torque on the other hand includes the torque caused by the two tapered roller bearings. Therefore, further computations need to be carried out to estimate the friction torque caused by the two support roller bearings. These values are then added to the numerically predicted friction torque of the tilting pad bearing. The frictional torque of the support bearings is estimated by the *SKF Bearing Calculator*, which is available online [241]. In order to predict the friction torque of the support bearings, the temperature at the outer ring is required. These temperatures were therefore measured in each experiment through two additional thermocouples (Figure 7.12).

As expected, the support bearing temperatures are higher for higher applied loads as well as higher rotational speeds. Due to the back-to-back arrangement, the 33213 bearing (bearing side) carries all of the applied thrust load. Therefore, considerably higher temperatures are measured for this bearing. Also, most of the friction torque is caused by this bearing, due to the higher loading. Depending on the operating conditions, the friction torque caused by this bearing ranges from 1.45 to 1.98 Nm. As the 33212 bearing (motor side) only carries the radial load, which essentially is only the weight of the shaft assembly, measured temperatures are much lower. The calculated friction torque ranges from 0.15 to 0.21 Nm.

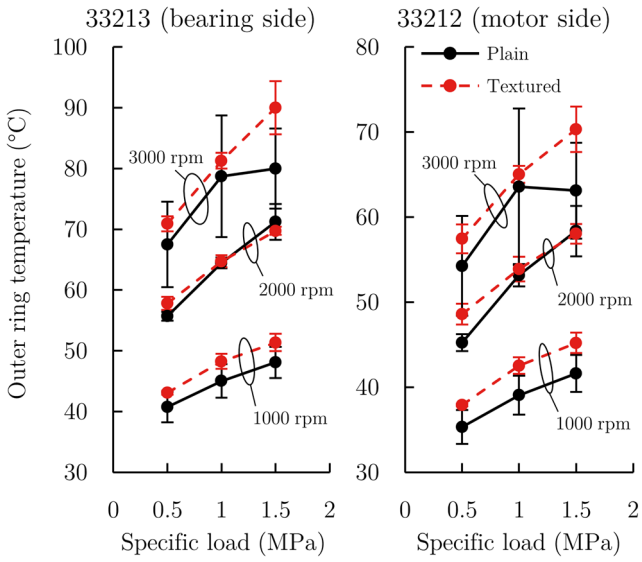

Figure 7.12 Average values of the measured outer ring temperatures of the support bearings for the plain and textured bearing.

The total friction torque is calculated by adding the numerically obtained friction torque of the tilting pad bearing to the friction torque of the two roller bearings. For example, the composition of the total friction torque is shown in Figure 7.13 for the bearing equipped with the plain pads at an operation at 2000 rpm.

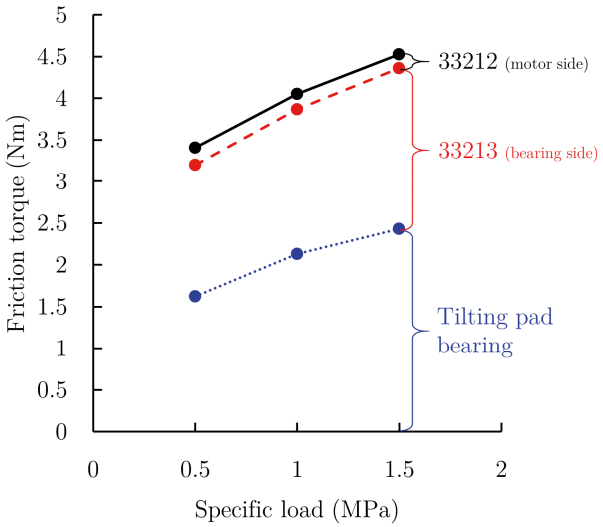

Figure 7.13 Composition of the theoretically predicted friction torque for the plain pad at 2000 rpm.

Due to the light loading, only about 5% of the total friction torque is caused by the 33212 roller bearing. The remaining torque is caused by the 33213 bearing and the tilting pad thrust bearing, where both bearings are responsible for an equal amount of friction.

For comparison, the theoretically predicted total friction torque as well as the measured friction torque are plotted in Figure 7.14.

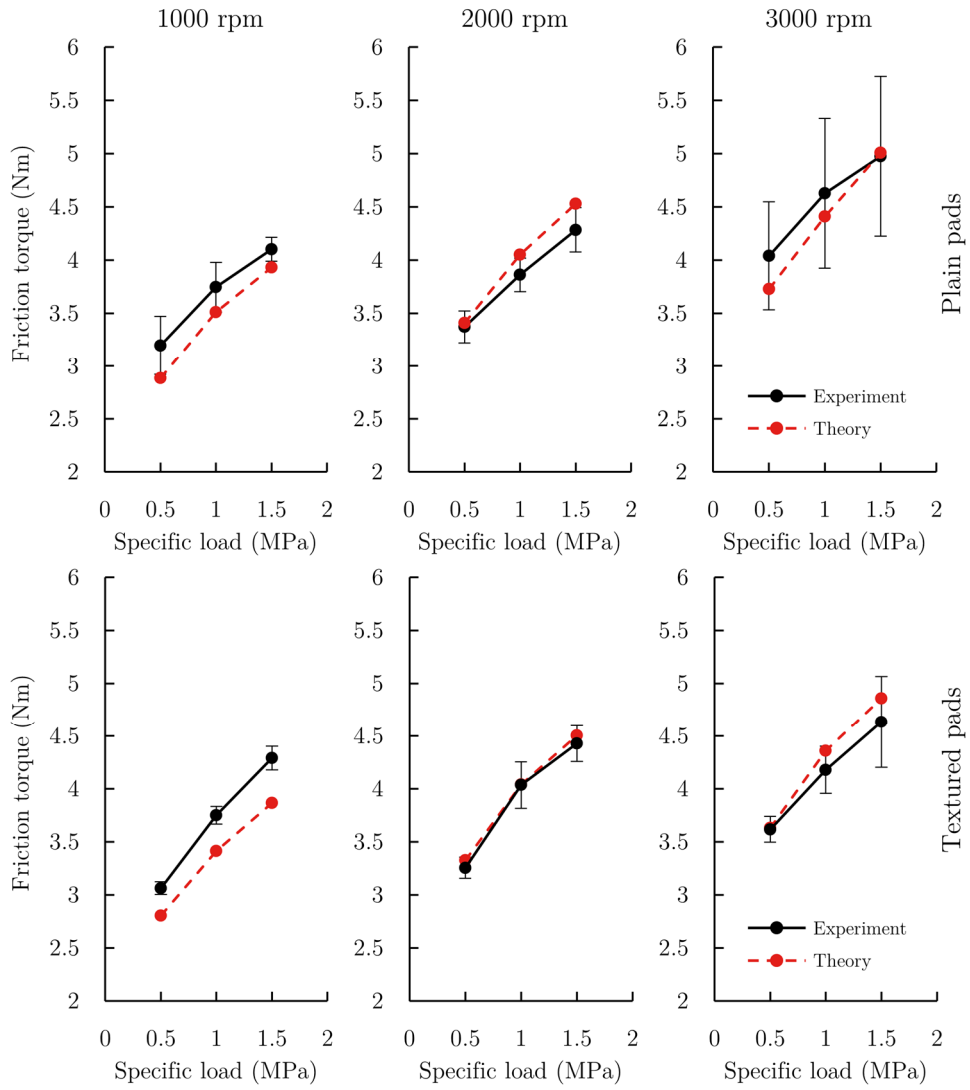

Figure 7.14 Friction torque as predicted by the theoretical model and the experiments.

A good agreement is found between the theoretical and experimental values. The overall mean difference between the model and the experiments is 4.8% with a standard deviation of $\sigma = 3.2\%$. For an operation at 1000 rpm, the theoretically predicted torque is slightly lower than the measured torque for both the plain and the textured pads, on average about 8%. For the textured pads at 2000 rpm, the theoretical value is almost identical to the measured one, with an average deviation of just 1%. For the plain pads at 2000 rpm, higher deviations are encountered, where the theoretical value is between 1 and 6% higher than the measured one. For an operation at 3000 rpm, the standard deviation of the experimental values makes the comparison to theoretical values difficult, in particular for the plain pads. However, average values of the measured friction torque suggest a very good agreement with the theory. For the plain pads, differences are between -8% and 1%. For the textured pads, better agreement if found. The encountered differences for this case are between 0 and 5%.

7.4.3 Pad temperature

To investigate the accuracy of the numerical temperature model, predicted maximum temperatures are compared to the ones measured at the pad's 75/75 position, i.e. T4. The maximum pad temperature is calculated by the empirical relation $T_{max} = 2T_{eff} - T_{in}$ and compared to the temperatures measured at the pad's 75/75 position (T4), where the maximum temperature is expected. Results are shown in Figure 7.15 for the plain and textured pads for the investigated operating conditions.

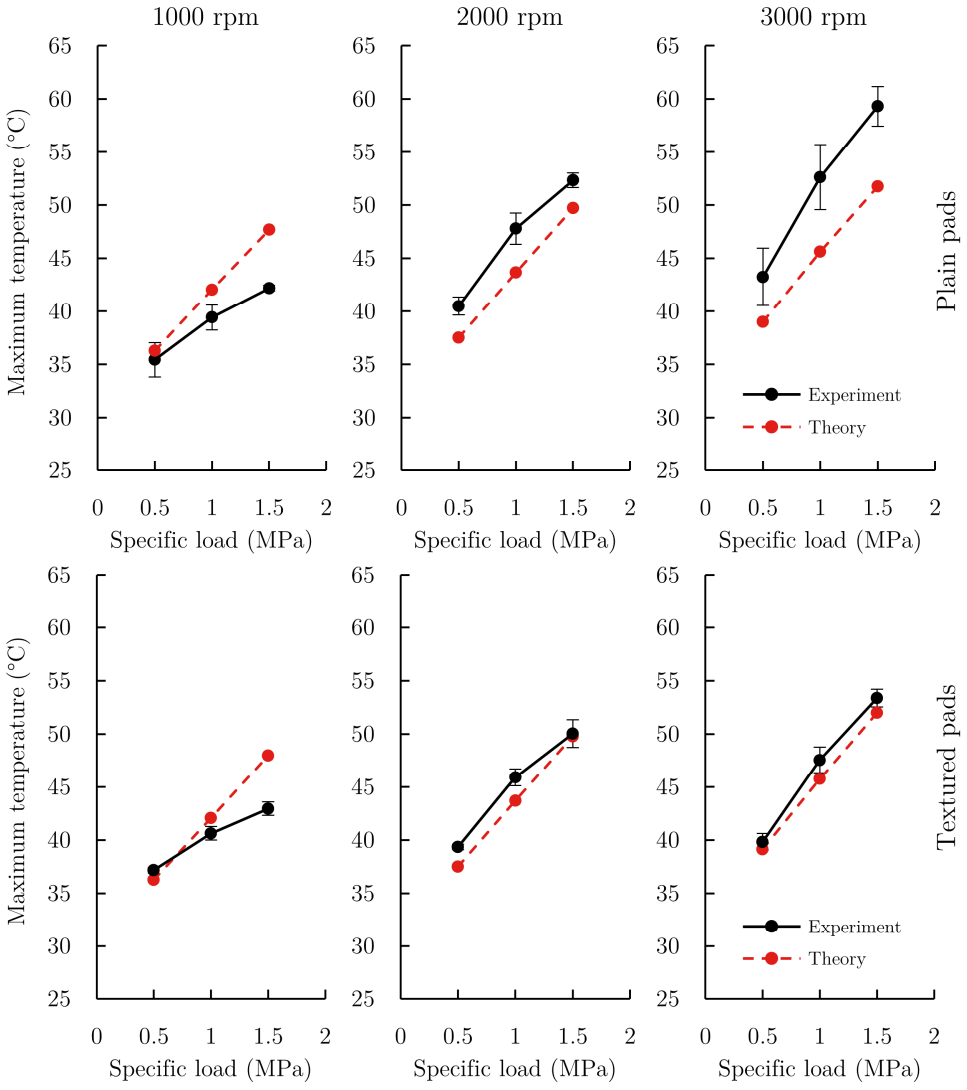

Figure 7.15 Maximum pad temperature as predicted by the theoretical model and the experiments.

A mean difference of 6% ($\sigma = 4.1\%$.) between theory and experiment is encountered, with a maximum difference of below 13%. Whereas temperatures are mostly overestimated for an operation at 1000 rpm, temperatures at higher speeds are generally underestimated for both the plain and the textured pads. It is likely that most differences are caused by the application of a simplified temperature model based on a constant convection parameter. Similarly to the comparison with CFD

results presented in chapter 5.2.3.2, convection is overestimated at low speeds and underestimated at high speeds. To investigate this further, all thermocouple measurements as well as the corresponding theoretical values are shown in Figure 7.16 and Figure 7.17 for the plain and textured pads respectively. It should be noted that the theoretical values are lubricant temperatures whereas the experimental values are the pad temperatures at about 2.5 mm below the pad surface. The theoretical temperatures are computed based on a linear temperature increase, where at the inlet temperatures are equal to T_{in} (equation (3.27)) and at the outlet temperatures are equal to $T_{out} = T_{max}$ (equation (3.26)).

It is evident that the temperatures close to the pad inlet are underestimated for the plain and textured pads for all 9 operating conditions. The most likely cause for this is the assumption that the temperature of the oil entering the contact through the oil supply nozzles remains at a constant 30°C. Although the oil supply temperature is controlled and kept constant at 30°C during the experiments, the oil temperature is measured close to the oil supply system. On the way through the pipes and the oil supply groove to the nozzles of the tilting pad bearing, the oil temperature rises due to conduction. This effect is not considered in the numerical calculation and most likely is responsible for the underestimation of the temperatures close the pad inlet. The temperature of surrounding bodies is higher for higher loads and rotational speeds, hence, this effect is more pronounced for high loads and speeds.

If the oil supply temperature is artificially increased to consider this effect, the estimated temperatures are much closer to the measure ones (Figure 7.18 (a)). As mentioned above, another error is caused by the assumption of a constant convection parameter. At lower speeds and higher loads the amount of heat removed through convection is higher than the amount of heat removed through convection at higher speeds and lower loads. Better temperature estimates can thus be achieved by choosing a more appropriate convection parameter (Figure 7.18 (b)).

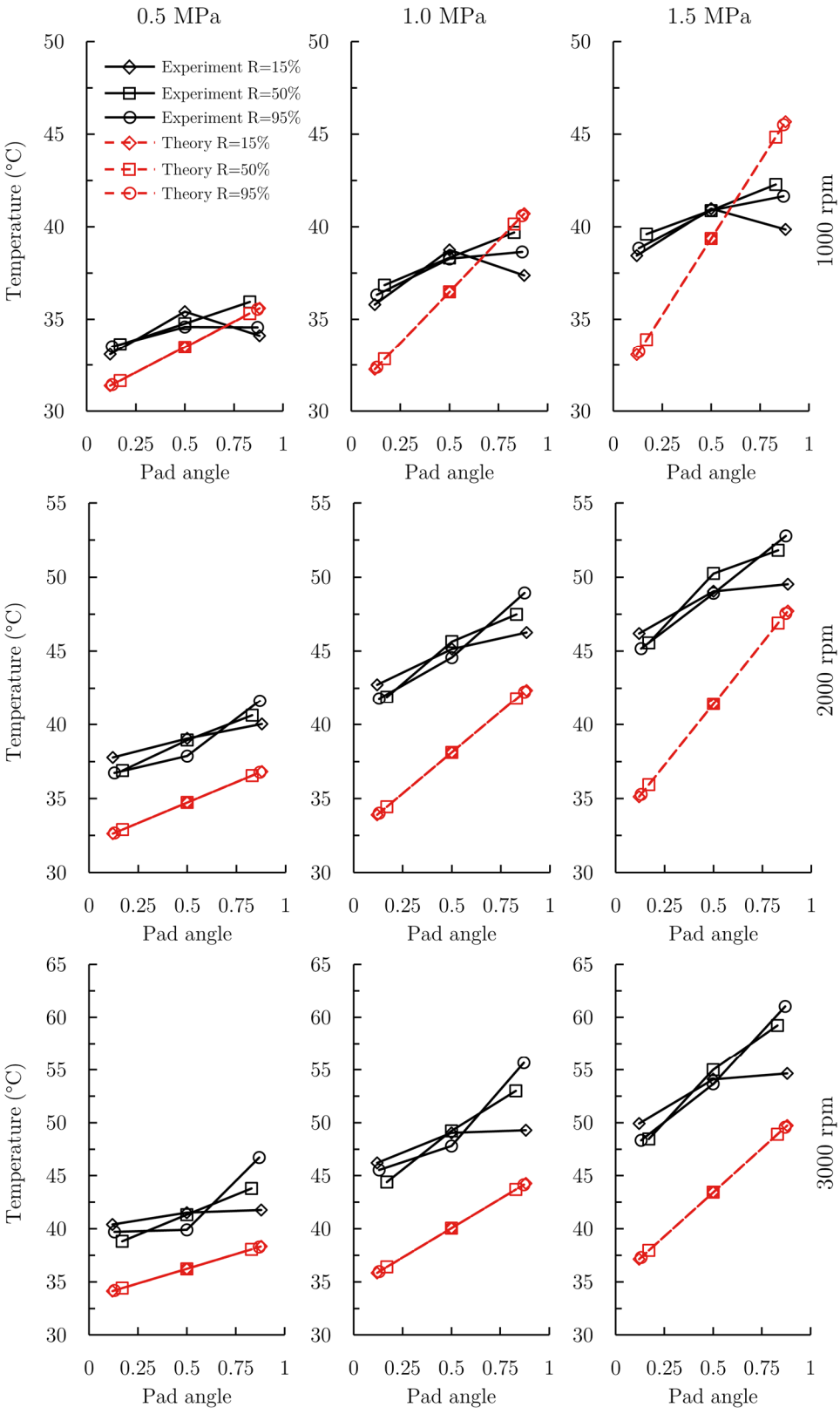

Figure 7.16 Temperatures of the plain pads as predicted by the theoretical model and the experiments.

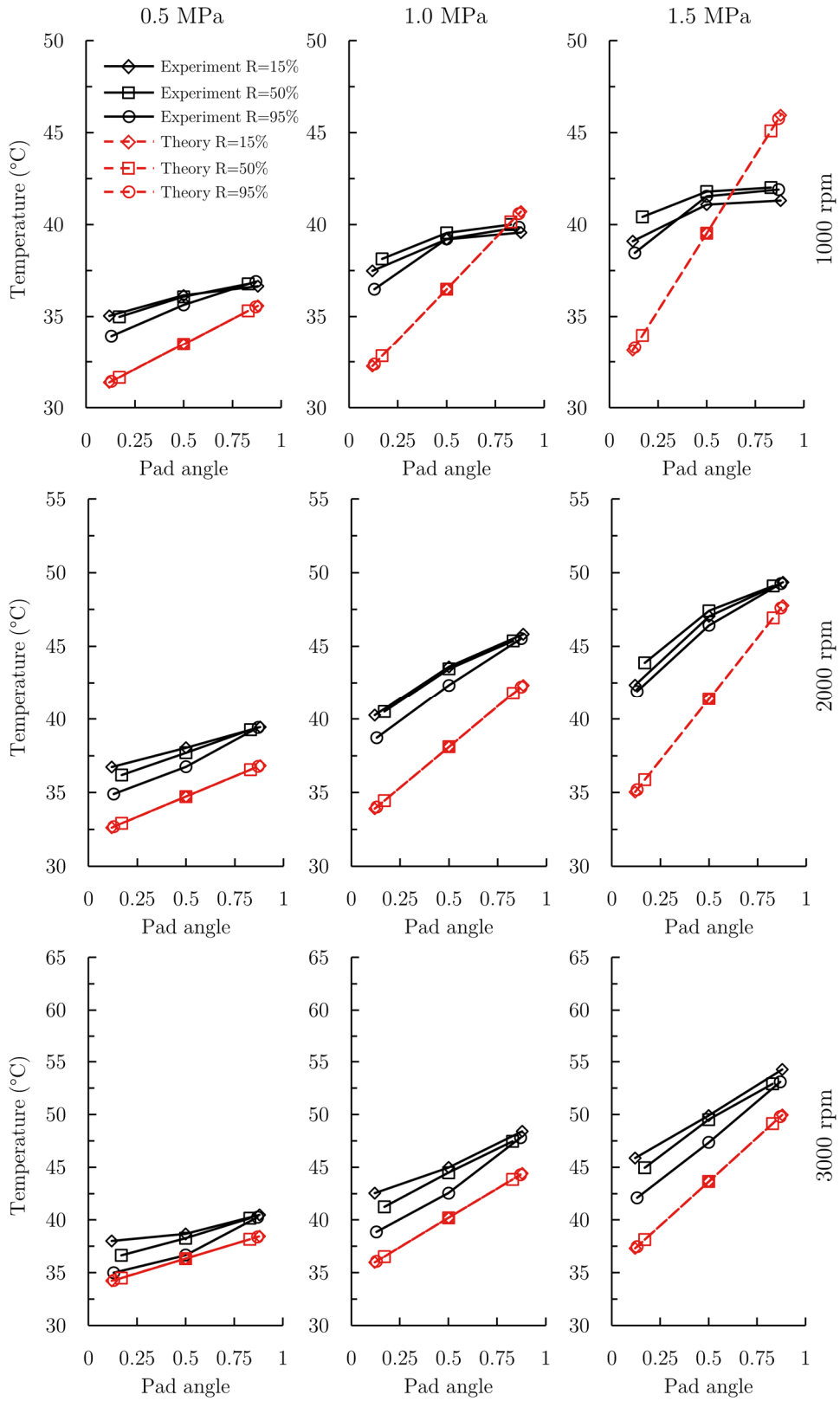

Figure 7.17 Temperatures of the textured pads as predicted by the theoretical model and the experiments.

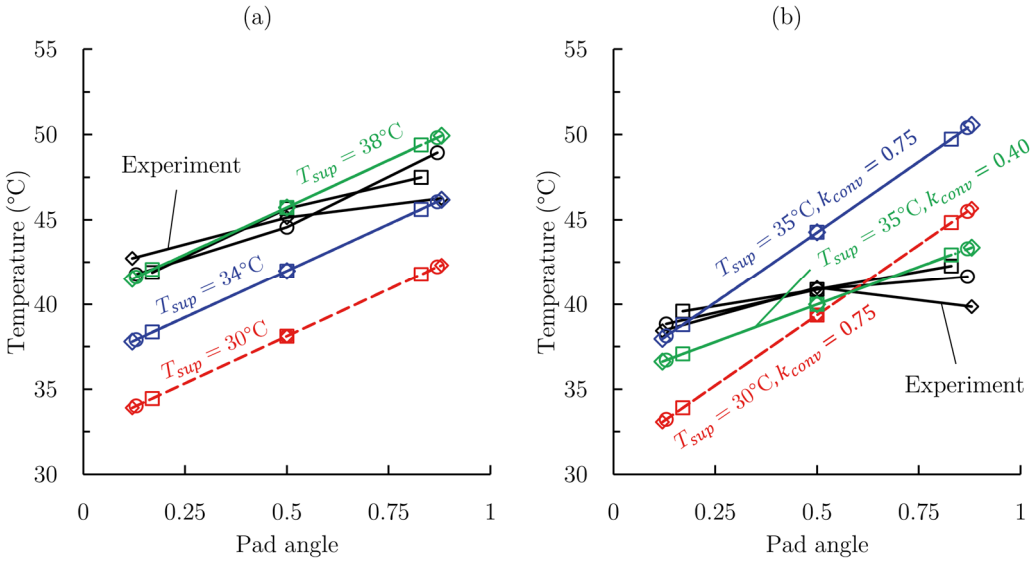

Figure 7.18 Influence of the actual supply temperature and the convection parameter on the predicted temperature distribution for (a) 1.0 MPa at 2000 rpm and (b) 1.5 MPa at 1000 rpm.

7.5 Summary

The utilized thrust bearing test rig and its instrumentation were presented in this chapter. Experiments were conducted to study the influence of surface texturing on the performance of tilting pad thrust bearings in terms of friction torque and pad temperature distribution. Experiments were conducted for 9 operating points with loads between 0.5 and 1.5 MPa and speeds from 1000 to 3000 rpm for both a bearing equipped with conventional plain pads and a bearing equipped with textured pads. A texture design with a 23 x 23 individual pockets and a texture density of 40% was manufactured through laser surface texturing and used for the experiments. Obtained experimental results are compared to predictions of the numerical model.

With regards to friction torque and temperature, no significant influence of surface texturing was found in the experiments. The numerically predicted change in these parameters does not exceed 1%, which was too small to be detectable experimentally due to the accuracy of the measurements. The theoretically predicted increase in the minimum film thickness by up to 7% could not be confirmed in the experiments due to issues with the ultrasonic measurement system. Good agreement is found between the experimental results and the numerical predictions. Averaging the absolute value of the relative difference between theory and experiment yields 4.8% with a standard deviation of $\sigma = 3.2\%$ for the friction torque and 6.4% with $\sigma = 4.1\%$ for the maximum pad temperature. To also validate the numerical predictions of the minimum film thickness and tilt angle of the pads, further experiments should be carried out in future work.

Chapter 8

Conclusions and Future Work

8.1 Conclusions

The aim of this work was to facilitate the design of surface textures for hydrodynamic bearings. For this purpose, an in-depth literature review was conducted, analysing the current understandings on how textures can enhance the bearing performance, discussing recommended texture geometries and providing a comparative summary of currently available modelling techniques. An advanced numerical model was developed that utilizes special discretization schemes, adaptive meshes, multicore processing and a strategic combination of root-finding techniques to find the bearing equilibrium for improved computational speed and numerical stability. The model allows the investigation and optimization of surface patterns under various conditions within minutes. The model is successfully validated through comparison with data from literature. The model is applied to assess possible benefits of surface texturing for a typical tilting pad thrust bearing. Experiments are conducted to validate the numerical model and gain further insights into the influence of texturing on the performance of tilting pad thrust bearings.

From the comprehensive literature review presented in this work, it can be concluded that:

- Although surface texturing is capable of enhancing the performance of hydrodynamic bearings in terms of film thickness, friction, temperature and wear, it has become clear that, in most cases, textures need to be designed for a specific type of contact and operating conditions due to the large dependency of optimum texture geometries on the application and operating conditions.
- Therefore, a successful application of surface texturing relies to a great degree

on fast and robust numerical models that allow an effective design of surface patterns for a given application and expected operating conditions.

- Although crucial, the numerical simulation of textured contacts involves three major challenges: (i) the requirement of complex mass-conserving cavitation algorithms due to the possible occurrence of multiple cavitation zones, (ii) the large discretization errors caused by numerous discontinuities in the film thickness distribution and (iii) the large computation times caused by complex geometry and corresponding fine meshes.

An advanced numerical model was developed specifically for the design of surface textures. To optimize the model in terms of accuracy and computational speed, numerical experiments were conducted. The following conclusions can be drawn from these analyses:

- An explicit treatment of discontinuities through local mesh refinements or special discretization schemes can significantly decrease the computation time required to solve the Reynolds equation. The lower the desired discretization error and hence, the finer the mesh, the higher the achievable speedup.
- Parallelizing the evaluation of the Jacobian matrix leads to considerable performance improvements, particularly for fine meshes.
- Utilizing Broyden's method instead of Newton's method can be highly beneficial whenever the initial guess for the bearing equilibrium is sufficiently close to the actual solution.
- Improving the initial film thickness guess by using results from the equivalent untextured bearing significantly reduces required computation times. In fact, the simulation of the untextured bearing and subsequent simulation of the textured bearing is much faster than the sole simulation of the textured bearing.
- The interior-point algorithm can be used for the purpose of single-objective texture optimization studies.

The model was applied to analyse and optimize texture patterns for a typical tilting pad thrust bearing. From these investigations, it can be concluded that:

- Whereas minimum film thickness values can be improved by up to 12%, friction and temperature characteristics can only be improved marginally.
- The optimum texture depth should be slightly smaller than the minimum film thickness encountered for the untextured bearing.
- With respect to the optimum circumferential extent, around 3/4 of the pad should be textured for high minimum film thickness values, just over half of

the pad for low friction values and about 2/5 of the pad for low maximum temperatures

- A radial extent of 87% is recommended for low maximum temperatures and approximately 2/3 of the pad should be textured for both high minimum film thickness and good friction characteristics.
- The higher the density, the higher the impact of texturing on the performance of tilting pad bearings.

Experiments were conducted on a bearing test rig to validate the predictions of the theoretical model and analyse the influence of texturing on the performance of tilting pad thrust bearings under hydrodynamic conditions. From these studies, it can be concluded that:

- The developed model allows an accurate prediction of friction torque (mean deviation: 4.8%) and maximum temperature (mean deviation: 6%).
- With regards to friction torque and temperature, the investigated texture pattern with a texture density of 40% does not result in considerable performance improvements, agreeing with the predictions of the numerical model.
- The numerically predicted improvement of the minimum film thickness by up to 7% could not be confirmed experimentally due to issues with the ultrasonic measurement system.

8.2 Future work

Possible future work to further advance the knowledge in the field of surface texturing for hydrodynamic bearings and particularly tilting pad thrust bearings is summarized in the following.

- **Model improvement** Although the model shows good agreement with data from literature and experimental results, the accuracy can be further improved, although at the cost of computational speed. E.g. by considering three-dimensional heat convection through solving the energy equation, utilizing the heat transfer equation to more accurately describe heat conduction in the pads and runner, considering thermal and elastic pad deformations or incorporating the effect of surface roughness.
- **Mixed lubrication conditions** So far, the numerical and experimental studies were limited to purely hydrodynamic lubrication conditions. Surface texturing may provide enhanced performance during critical mixed lubrication conditions encountered during start-up and shut-down by storing

lubricant and reducing the contact area.

- **Film thickness measurements** The utilized ultrasonic measurement system did not provide reliable film thickness measurements. For the purpose of validating the predictions of the mathematical model as well as experimentally studying the influence of texturing on the film thickness and tilt angle, other types of sensors might be viable.
- **Dynamic bearing characteristics** Only static characteristics were investigated within the scope of this work. However, the dynamic properties, i.e. stiffness and damping, of tilting pad bearing are important. The influence of texturing on these characteristics should be investigated as well.

Appendix A: List of Coefficients for Reynolds Equation

A.1 Coefficients for NUFVD and NUFVD+A methods

$$a^W = \frac{A^w \Gamma^w}{r^w \delta\theta^{PW}} \tag{A.1}$$

$$a^E = \frac{A^e \Gamma^e}{r^e \delta\theta^{PE}} \tag{A.2}$$

$$a^S = \frac{A^s \Gamma^s r^s}{\delta r^{PS}} \tag{A.3}$$

$$a^N = \frac{A^n \Gamma^n r^n}{\delta r^{PN}} \tag{A.4}$$

$$a^P = a^W + a^E + a^S + a^N \tag{A.5}$$

$$a^{\Theta W} = 6\omega A^w h^w \rho^w r^w \tag{A.6}$$

$$a^{\Theta P} = 6\omega A^e h^e \rho^e r^e \tag{A.7}$$

A.2 Coefficients for MNUFVD method

$$a^{\mathrm{W}} = \frac{b^w_{i,j} b^e_{i,j-1}}{b^w_{i,j} + b^e_{i,j-1}} \tag{A.8}$$

$$b^w_{i,j} = \frac{A^w_{i,j} \Gamma^w_{i,j}}{r^w_{i,j} \delta\theta^{wP}_{i,j}} \tag{A.9}$$

$$b^e_{i,j-1} = \frac{A^e_{i,j-1}\Gamma^e_{i,j-1}}{r^e_{i,j-1}\delta\theta^{eP}_{i,j-1}} \tag{A.10}$$

$$a^{\mathrm{E}} = -\frac{b^e_{i,j}b^w_{i,j+1}}{b^e_{i,j} + b^w_{i,j+1}} \tag{A.11}$$

$$b^e_{i,j} = -\frac{A^e_{i,j}\Gamma^e_{i,j}}{r^e_{i,j}\delta\theta^{eP}_{i,j}} \tag{A.12}$$

$$b^w_{i,j+1} = -\frac{A^w_{i,j+1}\Gamma^w_{i,j+1}}{r^w_{i,j+1}\delta\theta^{wP}_{i,j+1}} \tag{A.13}$$

$$a^{\mathrm{S}} = \frac{b^s_{i,j}b^n_{i-1,j}}{b^s_{i,j} + b^n_{i-1,j}} \tag{A.14}$$

$$b^s_{i,j} = \frac{A^s_{i,j}\Gamma^s_{i,j}r^s_{i,j}}{\delta r^{sP}_{i,j}} \tag{A.15}$$

$$b^n_{i-1,j} = \frac{A^n_{i-1,j}\Gamma^n_{i-1,j}r^n_{i-1,j}}{\delta r^{nP}_{i-1,j}} \tag{A.16}$$

$$a^{\mathrm{N}} = -\frac{b^n_{i,j}b^s_{i+1,j}}{b^n_{i,j} + b^s_{i+1,j}} \tag{A.17}$$

$$b^n_{i,j} = -\frac{A^n_{i,j}\Gamma^n_{i,j}r^n_{i,j}}{\delta r^{nP}_{i,j}} \tag{A.18}$$

$$b^s_{i+1,j} = -\frac{A^s_{i+1,j}\Gamma^s_{i+1,j}r^s_{i+1,j}}{\delta r^{sP}_{i+1,j}} \tag{A.19}$$

$$a^P = a^W + a^E + a^S + a^N \tag{A.20}$$

$$a^{\Theta W} = \frac{6\omega A^w_{i,j}h^w_{i,j}\rho^w_{i,j}r^w_{i,j}b^e_{i,j-1}}{b^e_{i,j-1} + b^w_{i,j}} \tag{A.21}$$

$$a^{\Theta P} = -\frac{6\omega A^e_{i,j}h^e_{i,j}\rho^e_{i,j}r^e_{i,j}b^w_{i,j+1}}{b^w_{i,j+1} + b^e_{i,j}} \tag{A.22}$$

$$J^P = \frac{6\omega A^e_{i,j-1}r^e_{i,j-1}\rho^e_{i,j-1}h^e_{i,j-1}b^w_{i,j}}{b^w_{i,j} + b^e_{i,j-1}} - \frac{6\omega A^w_{i,j+1}r^w_{i,j+1}\rho^w_{i,j+1}h^w_{i,j+1}b^e_{i,j}}{b^e_{i,j} + b^w_{i,j+1}} \tag{A.23}$$

$$B^P = a^W B^w + a^E B^e + a^S B^s + a^N B^n \tag{A.24}$$

Appendix B: INPUT and OUTPUT Files of TPT5

B.1 INPUT file

#	Value	Name	Unit	Description
1	30	hpg	µm	Film thickness at pivot guess
2	400	arg	µrad	Pitch angle guess
3	0	athg	µrad	Roll angle guess
4	0	ma	1	Michell approximation?(0=no,1=yes)-default:0
5	3	npad	1	Number of pads
6	30.25	ripad	mm	Pad inner radius
7	70.25	ropad	mm	Pad outer radius
8	1615.6	Apad	mm^2	Pad area
9	0	pivottype	1	Type of pivot (0=line pivot,1=point pivot,2=no pivot)
10	0.6	pivot	1	Relative pivot position circumferentially
11	0.5	rpivot	1	Relative pivot position radially
12	1615.6	W0	N	Load per pad
13	1000	rpm	1/min	Rotational speed
14	1.85	Qsup	l/min	Supply oil flow rate per pad
15	32	eta40	cSt	Viscosity at 40C in cSt
16	5.4	eta100	cSt	Viscosity at 100C in cSt
17	875	rho	kg/m^3	Lubricant density
18	0.00001	pinlet	Pa	Inlet pressure-default:0.0001
19	0.00001	patm	Pa	Atmospheric pressure-default:0.0001
20	0.00001	pcav	Pa	Cavitation pressure-default:0.0001

21	1	thermal	1	Consider thermal effects?(0=no,1=yes)-default:1
22	0	tlin	1	Effective or linear temperature?(0=effective,1=linear)-default:0
23	1	hoco	1	Consider hot-oil-carry-over effect?(0=no,1=yes)-default:1
24	30	Tsup	degC	Oil supply Temperature
25	30	Teff	degC	Effective Temperature first guess or fixed value
26	2035	cp	J/(kgK)	Specific heat capacity of lubricant
27	0.75	k	1	Amount of heat removed through convection-default:0.75
28	1	texturing	1	Calculate textured pad (0=no,1=yes,2=only textured pad)?
29	15	htexture	µm	Texture depth
30	0.7	alpha	1	Relative texture extend in circumferential direction
31	0.7	beta	1	Relative texture extend in radial direction
32	1	inlet	1	Is inlet textured?-default:1
33	0.632455532	rhotextureth	1	Texture density in circumferential direction
34	0.632455532	rhotexturer	1	Texture density in radial direction (rhotexture=rhotextureth*rhotexturer)
35	23	nth	1	Number of textures in circumferential direction
36	23	nr	1	Number of textures in radial direction
37	0	tshape	1	Texture bottom profile (0=flat,1=diverging,2=converging)-default:0
38	0	htc	1	Texture depth at last texture row (0=same as htexture)-default:0
39	100000	iterMAXp	1	Maximum number of iterations pressure iteration-default:100000
40	50	iterMAXb	1	Maximum number of iterations Broyden s Method-default:50
41	10	iterMAXt	1	Maximum number of iterations temperature iteration-default:10
42	10	iterMAXn	1	Maximum number of iterations Newton s Method-default:10
43	1	newtons	1	Perform Newton s Method instead of Continuation Algorithm (smooth)?(0=no,1=yes)-default:1
44	0	contis	1	Continuation Algorithm (smooth)? (0=no,1=yes=N,2=yes=N etc.)-default:0
45	1	newtont	1	Perform Newton s Method instead of Continuation Algorithm (textured)?(0=no,1=yes)-default:1
46	0	contit	1	Continuation Algorithm (textured)? (0=no,1=yes=N,2=yes=N etc.)-default:0
47	1	obafs	1	Only broyden after first temperature iteration (smooth)?(0=no,1=yes)-default:1

48	1	obaft	1	Only broyden after first temperature iteration (textured)?(0=no,1=yes)-default:1
49	0	damping	1	Damping coefficient for Newton and Broyden Method-default:0
50	0.001	ft	1	Offset factor for Jacobian Matrix-default:0.001
51	1.5	wps	1	Relaxation parameter for pressure for smooth solution-default:1.5
52	1.95	wpt	1	Relaxation parameter for pressure for textured solution-default:1.95
53	0.8	wo	1	Relaxation parameter for fractional film content-default:0.8
54	0.00001	ep	1	Permissible relative error pressure iteration-default:.00001
55	0.001	ee	1	Permissible relative error equilibrium iteration-default:.001
56	0.0001	et	1	Permissible relative error temperature iteration-default:.0001
57	2	cavalg	1	Cavitation algorithm (0=None,1=Reynolds,2=MassConserving)
58	1	scheme	1	Normal discretization scheme or Arghir?(0=normal,1=Arghir)-default:1
59	0	bernoulli	1	Consider bernulli equation at discontinuities?-default:0
60	0	xi	1	Pressure drop coefficient at discontinuities-default:0
61	0	fscmex	1	Run fluid solver for textured solution in MATLAB or C?(0=MATLAB,1=C)-default:0
---	---	---	---	---
62	101	cvths	1	Number of control volumes in circumferential direction for nontextured pad
63	101	cvrs	1	Number of control volumes in radial direction for nontextured pad
64	4	cvtht	1	Number of control volumes inside textures in circumferential direction
65	4	cvrt	1	Number of control volumes inside textures in radial direction
66	2	cvthbt	1	Number of control volumes between textures in circumferential direction
67	2	cvrbt	1	Number of control volumes between textures in radial direction
68	8	cvthut	1	Number of control volumes in untextured pad area in circumferential direction
69	4	cvrut	1	Number of control volumes in untextured pad area in radial direction
70	0	disc	1	Add additional points around all discontinuities?-default:0
71	0.1	discf	1	Discontinuity factor -default:0.1
---	---	---	---	---
72	0	post	1	Save results? (0=no,1=Save main results,2=Save all results)
73	1	figshow	1	Show Figures? (0=no,1=Show main figures,2=Show all figures)
74	0	email	1	Send email with results?(0=no,1=yes)

75	0	shutdown	1	Shut down computer after calculation?(0=no,1=yes)
76	1	cmbo	1	Command box output?(0=no,1=yes)
77	0	fixed	1	Fixed simulation (0=find equilibrium,1=dont find equilibrium)-default:0
78	0	complete	1	Run complete evaluation over range of operating conditions?-default:0
79	807.8	W0start	N	Start for W0
80	3231.2	W0end	N	End for W0
81	403.9	W0step	N	Step for W0
82	1000	rpmstart	1/min	Start for rpm
83	3000	rpmend	1/min	End for rpm
84	500	rpmstep	1/min	Step for rpm
85	1	parametric	1	Run parametric study?-default:0
86	29	vpar	1	Which parameter?
87	0.00001	vparstart	1	Start value
88	0.00002	vparend	1	End value
89	0.000005	vparstep	1	Step

B.2 OUTPUT file

Given below is the output *.csv file for a parametric study with a total of three simulations corresponding to the input file above.

Description	**Unit**	**Simulation 1**	**Simulation 2**	**Simulation 3**
Start of Simulation		15/5/2018 16.06	15/5/2018 16.06	15/5/2018 16.06
Number of simulations		3	3	3
### Input				
# Bearing Geometry				
Inner Radius	mm	30.25	30.25	30.25
Outer Radius	mm	70.25	70.25	70.25
Pad Angle	°	46.05326437	46.05326437	46.05326437
Pad Angle	rad	0.803781095	0.803781095	0.803781095
Pad Length	mm	40.39	40.39	40.39
Pad Width	mm	40	40	40
Pad Area	mm^2	1615.6	1615.6	1615.6
Number of Pads		3	3	3
Total Thrust Area	mm^2	4846.8	4846.8	4846.8

Type of pivot (0=line, 1=spherical, 2=no pivot)		0	0	0
Relative Pivot Position from Inlet		0.6	0.6	0.6
Relative Pivot Position from Inner Radius		0.5	0.5	0.5
# Operating Conditions				
Load per Pad	N	1615.6	1615.6	1615.6
Shaft Speed	rpm	1000	1000	1000
Supply flow rate	l/min	1.85	1.85	1.85
Total Load	N	4846.8	4846.8	4846.8
Specific Load	MPa	1	1	1
Equivalent air pressure test rig Slough	bar	4.917460189	4.917460189	4.917460189
Mean Sliding Speed	m/s	5.262167695	5.262167695	5.262167695
Pressure at Pad Inlet	Pa	1.00E-05	1.00E-05	1.00E-05
Pressure at Pad Edges	Pa	1.00E-05	1.00E-05	1.00E-05
# Lubricant Properties				
Density	kg/m^3	875	875	875
Kinematic Viscosity at 40°C	cSt	32	32	32
Kinematic Viscosity at 100°C	cSt	5.4	5.4	5.4
Dynamic Viscosity at 40°C	Pas	0.028	0.028	0.028
Dynamic Viscosity at 100°C	Pas	0.004725	0.004725	0.004725
Supply Temperature	°C	30	30	30
Effective Temperature	°C	30	30	30
Percentage of heat evacuated by oil	%	75	75	75
Specific Heat Capacity	J/kg/K	2035	2035	2035
Cavitation Pressure	Pa	1.00E-05	1.00E-05	1.00E-05
# Texturing Parameters				
Texture Depth	µm	10	15	20
Relative Extend in circumferential direction	%	70	70	70
Relative Extend in radial direction	%	70	70	70
Is the pad Inlet textured?		1	1	1

Texture Density in circumferential direction		0.632455532	0.632455532	0.632455532
Texture Density in radial direction		0.632455532	0.632455532	0.632455532
Texture Density		0.4	0.4	0.4
Texture Density (numeric)		0.405053381	0.405053381	0.405053381
Number of Textures in circumferential direction		23	23	23
Number of Textures in radial direction		23	23	23
Texture bottom profile (0=flat 1=converging 2=diverging)		0	0	0
Texture depth at last row (0=same as first row)		0	0	0
Total number of Textures		529	529	529
Texture size in radial direction	mm	0.769945865	0.769945865	0.769945865
Maximum Texture size in circumferential direction	mm	0.984639057	0.984639057	0.984639057
Minimum Texture size in circumferential direction	mm	0.570266617	0.570266617	0.570266617
Mean Texture size in circumferential direction	mm	0.777452837	0.777452837	0.777452837
Maximum Texture size	mm^2	0.758118771	0.758118771	0.758118771
Minimum Texture size	mm^2	0.439074424	0.439074424	0.439074424
Mean Texture size	mm^2	0.598596597	0.598596597	0.598596597
Maximum aspect ratio		0.017535657	0.026303486	0.035071315
Minimum aspect ratio		0.010156006	0.015234009	0.020312012
Mean aspect ratio		0.012862517	0.019293775	0.025725033
Relative Texture depth htex/hmin (hmin of textured bearing)		0.505995359	0.753926982	1.00763754
Relative Texture depth htex/hp (hp of textured bearing)		0.321500249	0.484750691	0.651201757
# Program Control Parameters				
Calculate Textured Bearing?		1	1	1
Find Equilibrium Position?		1	1	1

Damping coefficient for Newton and Broyden Method		0	0	0
Perform Newton Algorithm for smooth solution?		1	1	1
Perform Continuation Algorithm for smooth solution?		0	0	0
Only broyden for temp iter for smooth solution?		1	1	1
Perform Newton Algorithm for textured solution?		1	1	1
Perform Continuation Algorithm for textured solution?		0	0	0
Only Broyden for temp iter for textured solution?		1	1	1
Find Effective Temperature?		1	1	1
Consider hot-oil-carry-over effect?		1	1	1
Effective or linear temperature? (0=eff/1=linear)		0	0	0
Save Results?		1	1	1
Show Figures?		1	1	1
Send Email with Results?		0	0	0
Shutdown Computer after calculation?		0	0	0
Perform complete Bearing evaluation?		0	0	0
Load per Pad start	N	807.8	807.8	807.8
Load per Pad end	N	3231.2	3231.2	3231.2
Load per Pad increment	N	403.9	403.9	403.9
Shaft Speed start	rpm	1000	1000	1000
Shaft Speed end	rpm	3000	3000	3000
Shaft Speed increment	rpm	500	500	500
Perform parametric study?		1	1	1
Parameter to change		29	29	29
Start		1.00E-05	1.00E-05	1.00E-05
End		2.00E-05	2.00E-05	2.00E-05
Step		5.00E-06	5.00E-06	5.00E-06
# Calculation Control Parameters				

Michell film shape approximation?		0	0	0
Maximum Iterations for Pressure Calculation		100000	100000	100000
Maximum Iterations for Bryoden's Algorithm		50	50	50
Maximum Iterations for Temperature Calculation		10	10	10
Maximum Iterations for Newton's Algorithm		10	10	10
Convergence criterion for Pressure Calculation		1.00E-05	1.00E-05	1.00E-05
Convergence criterion for Equilibrium Calculation		0.001	0.001	0.001
Convergence criterion for Temperature Calculation		0.0001	0.0001	0.0001
Relaxation parameter for Pressure (smooth)		1.5	1.5	1.5
Relaxation parameter for Pressure (textured)		1.95	1.95	1.95
Relaxation parameter for Fractional Film Content		0.8	0.8	0.8
Offset factor for Jacobian Matrices		0.001	0.001	0.001
Cavitation algorithm (0=None/ 1=Reynolds/ 2=Mass-conserving)		2	2	2
Discretization scheme used (0=Standard/ 1=Arghir)		1	1	1
Consider Bernoulli equation at discontinuities?		0	0	0
Pressure drop coefficient at discontinuities		0	0	0
Run fluid solver in C or MATLAB (0=MATLAB/1=C)		0	0	0
Guess for Film Thickness at pivot location	µm	30	30	30
Guess for Pitch Angle	µrad	400	400	400
Guess for Roll Angle	µrad	0	0	0

# Mesh Control Parameters			
CVs smooth Pad in circumferential direction	101	101	101
CVs for smooth Pad in radial direction	101	101	101
CVs inside textures in circumferential direction	4	4	4
CVs inside textures in radial direction	4	4	4
CVs between textures in circumferential direction	2	2	2
CVs between textures in radial direction	2	2	2
CVs for untextured pad area in circumferential direction	8	8	8
CVs for untextured pad area in radial direction	4	4	4
Additional numbers of CVs at all discontinuities?	0	0	0
Discontinuity factor	0.1	0.1	0.1
---	---	---	---
### Results			
End of Simulation	15/5/2018 16.8	15/5/2018 16.8	15/5/2018 16.8
Total Calculation Time (For all Simulations)	109.21sec/ 1.82min/ 0.03h/ 0d	109.21sec/ 1.82min/ 0.03h/ 0d	109.21sec/ 1.82min/ 0.03h/ 0d
Everything converged (For all Simulations)	1	1	1
Number of Warnings (For all Simulations)	0	0	0
## Results current calculation			
Total Calculation Time	86.26sec/ 1.44min/ 0.02h/ 0d	88.63sec/ 1.48min/ 0.02h/ 0d	102.36sec/ 1.71min/ 0.03h/ 0d
Everything converged	1	1	1
Number of Warnings	0	0	0
---	---	---	---
# Smooth Solution			
Calculation Time	58.67sec/ 0.98min/ 0.02h/ 0d	58.1sec/ 0.97min/ 0.02h/ 0d	58.56sec/ 0.98min/ 0.02h/ 0d
Mesh Details	103 x 103 = 10609	103 x 103 = 10609	103 x 103 = 10609
Temperature iterations	4	4	4

Temperatures	°C	[30 35.5 36.5 36.5]	[30 35.5 36.5 36.5]	[30 35.5 36.5 36.5]
Iterations Newton's Algorithm		3	3	3
Iterations Broyden's Algorithm		0/3/2/1	0/3/2/1	0/3/2/1
Times Reynolds Equation solved		24	24	24
---	---	---	---	---
Pitch Angle	µrad	597.3253922	597.3253922	597.3253922
Roll Angle	µrad	0	0	0
Combined Angle	µrad	597.3253922	597.3253922	597.3253922
Film Thickness at Pivot location	µm	31.90993512	31.90993512	31.90993512
Maximum Reynolds number		4.674746532	4.674746532	4.674746532
Effective Lubricant Temperature	°C	36.49130241	36.49130241	36.49130241
Effective Lubricant Viscosity	cSt	37.35852381	37.35852381	37.35852381
Effective Lubricant Viscosity	Pas	0.032688708	0.032688708	0.032688708
Inlet Temperature	°C	30.94184167	30.94184167	30.94184167
Outlet Temperature	°C	42.04076316	42.04076316	42.04076316
Maximum Pad Temperature	°C	42.04076316	42.04076316	42.04076316
Minimum Film Thickness	µm	18.64983149	18.64983149	18.64983149
Mean Outlet Film Thickness	µm	22.42494996	22.42494996	22.42494996
Outlet Film Thickness at mean Radius	µm	22.42494996	22.42494996	22.42494996
Mean Inlet Film Thickness	µm	45.83087804	45.83087804	45.83087804
Inlet Film Thickness at mean Radius	µm	45.83087804	45.83087804	45.83087804
Maximum Film Thickness	µm	51.37155184	51.37155184	51.37155184
Film Thickness at ultrasonic sensor 1	µm	46.77690522	46.77690522	46.77690522
Film Thickness at ultrasonic sensor 2	µm	23.05054732	23.05054732	23.05054732
Mean Convergence Ratio		1.078821815	1.078821815	1.078821815
Convergence Ratio at mean Radius		1.043744941	1.043744941	1.043744941
Load Carrying Capacity	N	1615.593812	1615.593812	1615.593812
Relative Centre of Pressure (circumferential)		0.599999937	0.599999937	0.599999937
Relative Centre of Pressure (radial)		0.552224422	0.552224422	0.552224422

Maximum Pressure	MPa	2.378182526	2.378182526	2.378182526
Minimum Pressure	MPa	1.00E-11	1.00E-11	1.00E-11
Mean Pressure	MPa	0.99999617	0.99999617	0.99999617
Coefficient of Friction		0.005830493	0.005830493	0.005830493
Friction Torque Pad	Nm	0.520215435	0.520215435	0.520215435
Friction Torque Bearing	Nm	1.560646305	1.560646305	1.560646305
Power loss Pad	kW	0.054476833	0.054476833	0.054476833
Power loss Bearing	kW	0.163430499	0.163430499	0.163430499
Lubricant Flow Pad (required)	l/min	0.249089764	0.249089764	0.249089764
Lubricant Flow Bearing (required)	l/min	0.747269292	0.747269292	0.747269292
Heat carried away by Lubricant	kW	0.041023044	0.041023044	0.041023044

# Textured Solution				
Calculation Time		27.58sec/ 0.46min/ 0.01h/ 0d	30.53sec/ 0.51min/ 0.01h/ 0d	43.79sec/ 0.73min/ 0.01h/ 0d
Mesh Details		148 x 148 = 21904	148 x 148 = 21904	148 x 148 = 21904
Temperature iterations		1	1	2
Temperatures	°C	36.5	36.5	[36.5 36.6]
Iterations Newton's Algorithm		3	3	3
Iterations Broyden's Algorithm		0	0	0/1
Times Reynolds Equation solved		9	9	13

Pitch Angle	µrad	510.8825448	497.6733561	489.3903929
Roll Angle	µrad	0	0	0
Combined Angle	µrad	510.8825448	497.6733561	489.3903929
Film Thickness at Pivot location	µm	31.10417499	30.94374133	30.71244784
Maximum Reynolds number		4.953778941	4.987066147	4.997975263
Effective Lubricant Temperature	°C	36.49130241	36.49130241	36.56138126
Effective Lubricant Viscosity	cSt	37.35852381	37.35852381	37.24024719
Effective Lubricant Viscosity	Pas	0.032688708	0.032688708	0.032585216
Inlet Temperature	°C	30.94184167	30.94184167	30.97243734
Outlet Temperature	°C	42.04076316	42.04076316	42.15032518
Maximum Pad Temperature	°C	42.04076316	42.04076316	42.15032518
Minimum Film Thickness	µm	19.76302712	19.89582593	19.848407

Mean Outlet Film Thickness	µm	22.99182367	23.04113992	22.94137237
Outlet Film Thickness at mean Radius	µm	23.00736116	23.05627568	22.95625622
Mean Inlet Film Thickness	µm	49.22674401	51.86657226	54.55034863
Inlet Film Thickness at mean Radius	µm	52.98772369	57.52003345	62.09607143
Maximum Film Thickness	µm	56.25190713	60.69981938	65.22293501
Film Thickness at ultrasonic sensor 1	µm	43.86336192	43.3730315	42.93487272
Film Thickness at ultrasonic sensor 2	µm	23.24321766	23.28603397	23.18219055
Mean Convergence Ratio		0.884314852	0.859136538	0.848313757
Convergence Ratio at mean Radius		0.868433472	0.844184813	0.833751594
Load Carrying Capacity	N	1615.633015	1615.650717	1615.625711
Relative Centre of Pressure (circumferential)		0.600000152	0.600000162	0.600000144
Relative Centre of Pressure (radial)		0.550374109	0.550310936	0.550587037
Maximum Pressure	MPa	2.517289058	2.534387155	2.527453827
Minimum Pressure	MPa	1.00E-11	1.00E-11	1.00E-11
Mean Pressure	MPa	1.000020435	1.000031392	1.000015914
Coefficient of Friction		0.005794518	0.005790646	0.005797014
Friction Torque Pad	Nm	0.517278561	0.51696875	0.517539755
Friction Torque Bearing	Nm	1.551835684	1.550906249	1.552619265
Power loss Pad	kW	0.054169284	0.054136841	0.054196636
Power loss Bearing	kW	0.162507853	0.162410523	0.162589909
Lubricant Flow Pad (required)	l/min	0.245609293	0.245273336	0.243721168
Lubricant Flow Bearing (required)	l/min	0.736827879	0.735820007	0.731163504
Heat carried away by Lubricant	kW	0.040449839	0.040394509	0.040424459
Did cavitation occur?		no	no	no

# Smooth vs Textured				
Relative change in Pitch Angle	%	-14.47165122	-16.68304033	-18.06971555
Relative change in Roll Angle	%	NaN	NaN	NaN
Relative change in Film Thickness at Pivot Location	%	-2.525107407	-3.027877656	-3.752709859

Relative change in Effective Lubricant Temperature	%	0	0	0.192042611
Relative change in Effective Lubricant Viscosity	%	0	0	-0.316598739
Relative change in Max Pad Temperature	%	0	0	0.260609033
Relative change in Minimum Film Thickness	%	5.968931317	6.680995707	6.426736433
Relative change in Mean Outlet Film Thickness	%	2.527870548	2.747787451	2.302892121
Relative change in Mean Inlet Film Thickness	%	7.409559038	13.16949288	19.02531865
Relative change in Maximum Film Thickness	%	9.50011264	18.15843051	26.96313947
Relative change in Mean Convergence Ratio	%	-18.02957267	-20.36344407	-21.36664779
Relative change in Maximum Pressure	%	5.849279021	6.568235479	6.27669654
Relative change in Mean Pressure	%	0.002426538	0.003522204	0.001974427
Relative change in Coefficient of Friction	%	-0.617012022	-0.683432577	-0.574209754
Relative change in Friction Torque	%	-0.564549505	-0.624103988	-0.514340773
Relative change in Power loss	%	-0.564549505	-0.624103988	-0.514340773
Relative change in required Lubricant Flow	%	-1.397275815	-1.532149712	-2.155285696

Appendix C: List of MATLAB Files

C.1 MATLAB scripts

TPT5_RUN.m	Main script to run all simulations except optimization studies.
TPT5_Optimization.m	Script to run optimization studies for one or more operating conditions using the interior-point algorithm. Optimization specific input parameters are specified directly in this script (e.g. optimization objective, $\boldsymbol{x}_{lb}$, $\boldsymbol{x}_{ub}$, $\boldsymbol{x}_{start}$).
TPT5_meshstudy.m	Shows the specified meshes for the untextured and the textured pad before running the simulation to facilitate choosing the meshing parameters.

C.2 MATLAB functions

TPT5_input.m	Opens the input **.txt* file and stores all input variables in a structure *I*. Variable names are automatically generated based on the specifications in the input file.
TPT5_fixed.m	Runs the fluid solver for a given film thickness distribution and effective temperature (only fluid solver is executed).
TPT5_main.m	Runs a complete simulation (fluid solver, equilibrium solver and temperature solver) for a given operating condition. For parametric studies specified in *TPT5_RUN.m* this function is called multiple times.
TPT5_mesh.m	Generates the mesh for the untextured or textured pad.
TPT5_reynolds.m	Prepares all coefficients necessary to solve the discrete Reynolds equation.
TPT5_visc.m	Computes the dynamic viscosity at a given temperature.

TPT5_solver.m	Solves the discrete Reynolds equation using the Gauss-Seidel method with successive relaxation and the mass-conserving cavitation algorithm.
TPT5_solver_mex.mexw64	Same as *TPT5_solver.m* but in C rather than MATLAB directly.
TPT5_wcop.m	Integrates the pressure distribution to obtain load carrying capacity, centre of pressure, friction torque, power loss etc.
TPT5_newton.m	Equilibrium solver using the Newton-Raphson method.
TPT5_conti.m	Equilibrium solver using the Continuation method with fourth-order Runge-Kutta technique.
TPT5_broyden.m	Equilibrium solver using Broyden's method with Sherman-Morrison formula.
TPT5_jacobian.m	Evaluates the Jacobian matrix through a perturbation approach by calling the fluid solver multiple times.
TPT5_post.m	Performs all post-processing, i.e. generating and saving figures, preparing and saving output files on the hard drive.
TPT5_sendolmail.m	Sends an Email with the results of a simulation to a specified address.

C.3 MATLAB apps

TPT5_Realtime.mlapp	Application with user interface to run simulations based on *TPT5_fixed.m* (Figure C.1).

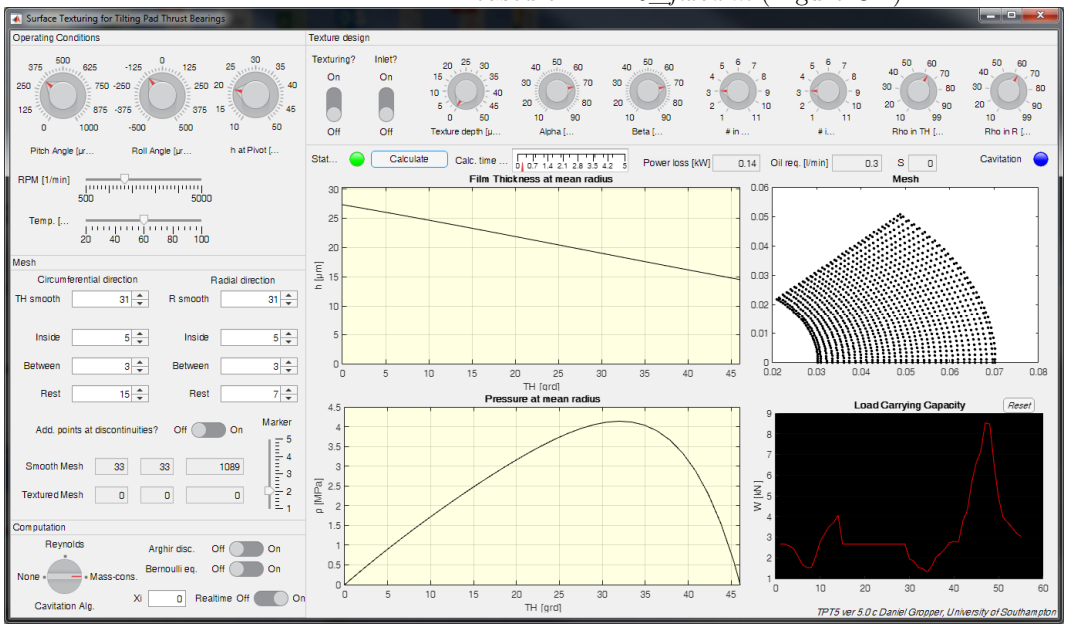

Figure C.1 Screenshot of TPT5_Realtime.mlapp.

Appendix D: CAD Drawings

D.1 Modified pad

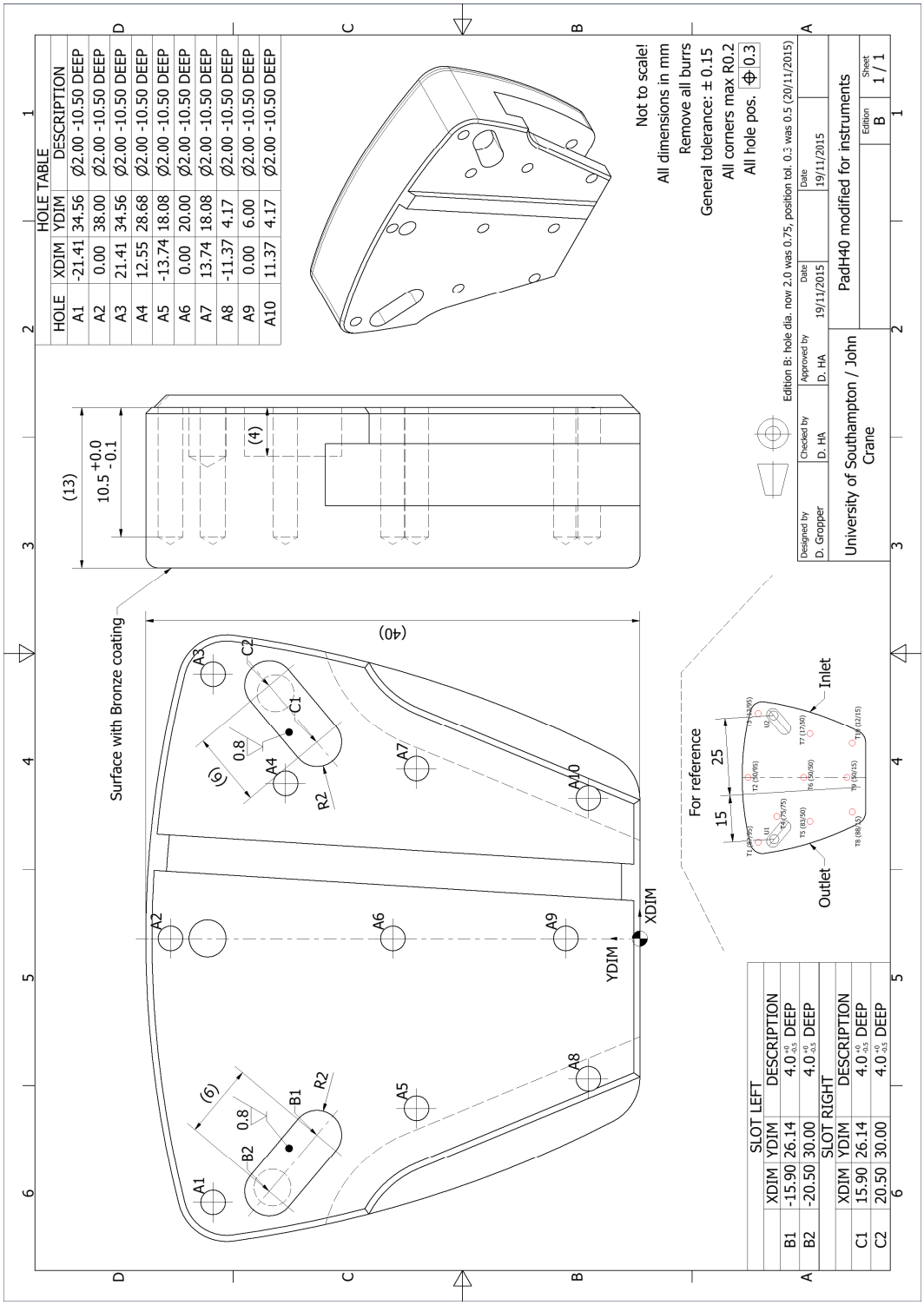

D.2 Texture design for experiments

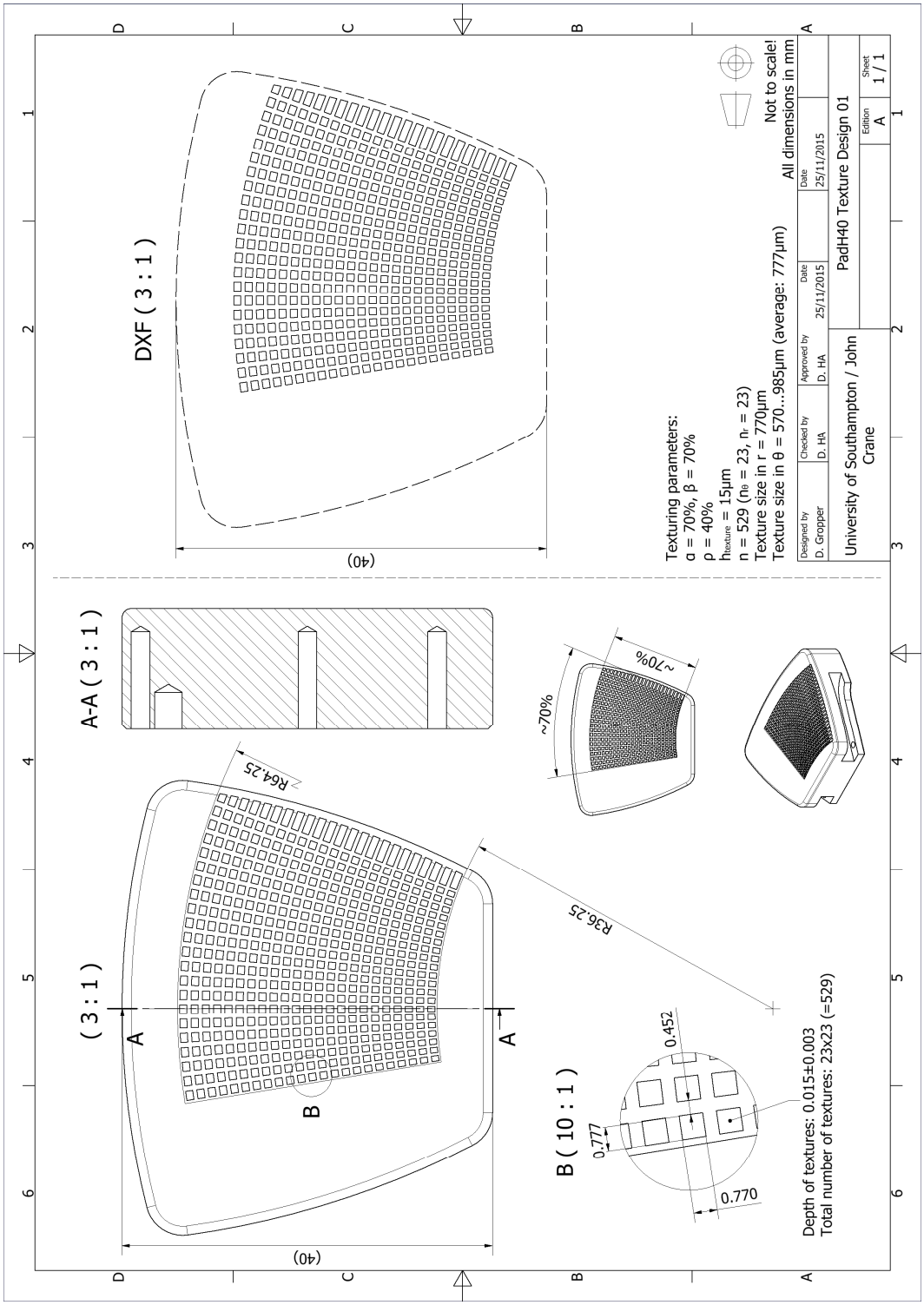

References

[1] Bhushan B. Biomimetics: lessons from nature–an overview. Philosophical Transactions of the Royal Society of London A: Mathematical, Physical and Engineering Sciences. 2009;367:1445-86.
[2] Dean B, Bhushan B. Shark-skin surfaces for fluid-drag reduction in turbulent flow: a review. Philosophical Transactions of the Royal Society A: Mathematical, Physical and Engineering Sciences. 2010;368:4775-806.
[3] Jearl W. More on boomerangs, including their connection with the dimpled golf ball. Scientific American. 1979:180.
[4] Hamilton DB, Walowit JA, Allen CM. A Theory of Lubrication by Microirregularities. Journal of Fluids Engineering. 1966;88:177-85.
[5] https://theblissprojectblog.wordpress.com/2012/06/07/frog-feet/. accessed 05.08.2018.
[6] Scholz I, Barnes WJP, Smith JM, Baumgartner W. Ultrastructure and physical properties of an adhesive surface, the toe pad epithelium of the tree frog, Litoria caerulea White. Journal of Experimental Biology. 2009;212:155-62.
[7] https://www.youtube.com/watch?v=0BQzsNatQOY. accessed 05.08.2018.
[8] Oeffner J, Lauder GV. The hydrodynamic function of shark skin and two biomimetic applications. The Journal of Experimental Biology. 2012;215:785-95.
[9] Anno JN, Walowit JA, Allen CM. Microasperity Lubrication. Journal of Tribology. 1968;90:351-5.
[10] Anno JN, Walowit JA, Allen CM. Load Support and Leakage from Microasperity-Lubricated Face Seals. Journal of Tribology. 1969;91:726-31.
[11] Willis E. Surface finish in relation to cylinder liners. Wear. 1986;109:351-66.
[12] Etsion I, Burstein L. A Model for Mechanical Seals with Regular Microsurface Structure. Tribology Transactions. 1996;39:677-83.
[13] Etsion I. State of the Art in Laser Surface Texturing. Journal of Tribology. 2005;127:248-53.
[14] Dobrica MB, Fillon M, Pascovici MD, Cicone T. Optimizing surface texture for hydrodynamic lubricated contacts using a mass-conserving numerical approach. Journal of Engineering Tribology. 2010;224:737-50.
[15] Fowell MT, Medina S, Olver AV, Spikes HA, Pegg IG. Parametric study of texturing in convergent bearings. Tribology International. 2012;52:7-16.
[16] Ausas RF, Ragot P, Leiva J, Jai M, Bayada G, Buscaglia GC. The Impact of

the Cavitation Model in the Analysis of Microtextured Lubricated Journal Bearings. Journal of Tribology. 2007;129:868-75.
[17] Stachowiak GW, Batchelor AW. Engineering Tribology. 4th ed. Amsterdam; London: Elsevier/Butterworth-Heinemann; 2014.
[18] Zouzoulas V, Papadopoulos CI. 3-D thermohydrodynamic analysis of textured, grooved, pocketed and hydrophobic pivoted-pad thrust bearings. Tribology International. 2017;110:426-40.
[19] Tala-Ighil N, Maspeyrot P, Fillon M, Bounif A. Effects of surface texture on journal-bearing characteristics under steady-state operating conditions. Proceedings of the Institution of Mechanical Engineers, Part J: Journal of Engineering Tribology. 2007;221:623-33.
[20] Tala-Ighil N, Fillon M, Maspeyrot P. Effect of textured area on the performances of a hydrodynamic journal bearing. Tribology International. 2011;44:211-9.
[21] Kango S, Singh D, Sharma RK. Numerical investigation on the influence of surface texture on the performance of hydrodynamic journal bearing. Meccanica. 2012;47:469-82.
[22] Brizmer V, Kligerman Y. A laser surface textured journal bearing. Journal of Tribology. 2012;134:031702.
[23] Kango S, Sharma RK. Studies on the Influence of positive Roughness on the Performance of Journal Bearing. Journal of Tribology and Surface Engineering. 2010;1:243-62.
[24] Etsion I, Kligerman Y, Halperin G. Analytical and Experimental Investigation of Laser-Textured Mechanical Seal Faces. Tribology Transactions. 1999;42:511-6.
[25] Razzaque MM, Faisal MTR. Performance of Mechanical Face Seals with Surface Micropores. Journal of Mechanical Engineering. 2007;37.
[26] Brizmer V, Kligerman Y, Etsion I. A Laser Surface Textured Parallel Thrust Bearing. Tribology Transactions. 2003;46:397-403.
[27] Fesanghary M, Khonsari MM. On the optimum groove shapes for load-carrying capacity enhancement in parallel flat surface bearings: Theory and experiment. Tribology International. 2013;67:254-62.
[28] Mezghani S, Demirci I, Zahouani H, Mansori ME. The effect of groove texture patterns on piston-ring pack friction. Precision Engineering. 2012;36:210-7.
[29] Zhou Y, Zhu H, Tang W, Ma C, Zhang W. Development of the theoretical model for the optimal design of surface texturing on cylinder liner. Tribology International. 2012;52:1-6.
[30] Papadopoulos CI, Kaiktsis L, Fillon M. Computational fluid dynamics thermohydrodynamic analysis of three-dimensional sector-pad thrust bearings with rectangular dimples. Journal of Tribology. 2014;136:011702-1-10.
[31] Kango S, Sharma RK, Pandey RK. Thermal analysis of microtextured journal bearing using non-Newtonian rheology of lubricant and JFO boundary conditions. Tribology International. 2014;69:19-29.
[32] Han Y-F, Chan C-W, Wang Z, Shi F, Wang J, Wang N, et al. Effects of Shaft Axial Motion and Misalignment on the Lubrication Performance of Journal Bearings Via a Fast Mixed EHL Computing Technology. Tribology Transactions. 2015;58:247-59.

[33] Kovalchenko A, Ajayi O, Erdemir A, Fenske G, Etsion I. The Effect of Laser Texturing of Steel Surfaces and Speed-Load Parameters on the Transition of Lubrication Regime from Boundary to Hydrodynamic. Tribology Transactions. 2004;47:299-307.
[34] Podgornik B, Vilhena LM, Sedlacek M, Rek Z, Žun I. Effectiveness and design of surface texturing for different lubrication regimes. Meccanica. 2012;47:1613-22.
[35] Scaraggi M, Mezzapesa FP, Carbone G, Ancona A, Tricarico L. Friction Properties of Lubricated Laser-MicroTextured-Surfaces: An Experimental Study from Boundary- to Hydrodynamic-Lubrication. Tribology Letters. 2013;49:117-25.
[36] Braun D, Greiner C, Schneider J, Gumbsch P. Efficiency of laser surface texturing in the reduction of friction under mixed lubrication. Tribology International. 2014;77:142-7.
[37] Scaraggi M, Mezzapesa FP, Carbone G, Ancona A, Sorgente D, Lugarà PM. Minimize friction of lubricated laser-microtextured-surfaces by tuning microholes depth. Tribology International. 2014;75:123-7.
[38] Zhang H, Zhang DY, Hua M, Dong GN, Chin KS. A Study on the Tribological Behavior of Surface Texturing on Babbitt Alloy under Mixed or Starved Lubrication. Tribology Letters. 2014;56:305-15.
[39] Wang W, Huang Z, Shen D, Kong L, Li S. The Effect of Triangle-Shaped Surface Textures on the Performance of the Lubricated Point-Contacts. Journal of Tribology. 2013;135:021503-.
[40] Costa HL, Hutchings IM. Hydrodynamic lubrication of textured steel surfaces under reciprocating sliding conditions. Tribology International. 2007;40:1227-38.
[41] Dadouche A, Conlon M, Dmochowski W, Koszela W, Galda L, Pawlus P. Experimental Evaluation of Steady-State and Dynamic Performance of Hydrodynamic Journal Bearings: Plain Versus Textured Surface. 10th EDF/Pprime Workshop. Poitiers, France2011.
[42] Lu X, Khonsari MM. An Experimental Investigation of Dimple Effect on the Stribeck Curve of Journal Bearings. Tribology Letters. 2007;27:169-76.
[43] Etsion I, Halperin G, Brizmer V, Kligerman Y. Experimental Investigation of Laser Surface Textured Parallel Thrust Bearings. Tribology Letters. 2004;17:295-300.
[44] Henry Y, Bouyer J, Fillon M. An experimental analysis of the hydrodynamic contribution of textured thrust bearings during steady-state operation: A comparison with the untextured parallel surface configuration. Proceedings of the Institution of Mechanical Engineers, Part J: Journal of Engineering Tribology. 2014;229:362-75.
[45] Qiu Y, Khonsari MM. Experimental investigation of tribological performance of laser textured stainless steel rings. Tribology International. 2011;44:635-44.
[46] Bai LQ, Bai S. Frictional Performance of a Textured Surface with Elliptical Dimples: Geometric and Distribution Effects. Tribology Transactions. 2014;57:1122-8.
[47] Etsion I. Improving tribological performance of mechanical seals by laser surface texturing. Proc 17th Int Pump Users Symposium2000. p. 17.
[48] Yu XQ, He S, Cai RL. Frictional characteristics of mechanical seals with a laser-textured seal face. Journal of Materials Processing Technology. 2002;129:463-6.
[49] Erdemir A. Review of engineered tribological interfaces for improved boundary

lubrication. Tribology International. 2005;38:249-56.
[50] Wang L. Use of structured surfaces for friction and wear control on bearing surfaces. Surface Topography: Metrology and Properties. 2014;2.
[51] Bruzzone AAG, Costa HL, Lonardo PM, Lucca DA. Advances in engineered surfaces for functional performance. CIRP Annals - Manufacturing Technology. 2008;57:750-69.
[52] Sudeep U, Tandon N, Pandey RK. Performance of Lubricated Rolling/Sliding Concentrated Contacts With Surface Textures: A Review. J Tribol-T Asme. 2015;137.
[53] Yu H, Huang W, Wang X. Dimple patterns design for different circumstances. Lubrication Science. 2013;25:67-78.
[54] Zhu D, Wang QJ. Elastohydrodynamic Lubrication: A Gateway to Interfacial Mechanics—Review and Prospect. Journal of Tribology. 2011;133:041001-.
[55] Coblas DG, Fatu A, Hajjam M. Manufacturing textured surfaces: State of art and recent developments. Proceedings of the Institution of Mechanical Engineers, Part J: Journal of Engineering Tribology. 2015;229:3-29.
[56] Venkatesan S. Surface Textures for enhanced lubrication: Fabrication and characterization techniques [Uniersity of Ketucky Master's Thesis]: University of Ketucky; 2005.
[57] Costa HL, Hutchings IM. Some innovative surface texturing techniques for tribological purposes. Proceedings of the Institution of Mechanical Engineers Part J-Journal of Engineering Tribology. 2015;229:429-48.
[58] Stachowiak GW, Podsiadlo P. 3-D characterization, optimization, and classification of textured surfaces. Tribology Letters. 2008;32:13-21.
[59] Henry Y. Experimental analysis of the effect of pads texturing on fixed geometry hydrodynamic thrust bearings behavior [PhD Thesis]: Université de Poitiers; 2013.
[60] Wakuda M, Yamauchi Y, Kanzaki S, Yasuda Y. Effect of surface texturing on friction reduction between ceramic and steel materials under lubricated sliding contact. Wear. 2003;254:356-63.
[61] Varenberg M, Halperin G, Etsion I. Different aspects of the role of wear debris in fretting wear. Wear. 2002;252:902-10.
[62] Yamakiri H, Sasaki S, Kurita T, Kasashima N. Effects of laser surface texturing on friction behavior of silicon nitride under lubrication with water. Tribology International. 2011;44:579-84.
[63] Dadouche A, Conlon MJ. Operational performance of textured journal bearings lubricated with a contaminated fluid. Tribology International. 2016;93:377-89.
[64] Wan Y, Xiong D. The effect of laser surface texturing on frictional performance of face seal. Journal of Materials Processing Technology. 2008;197:96-100.
[65] Kovalchenko A, Ajayi O, Erdemir A, Fenske G, Etsion I. The effect of laser surface texturing on transitions in lubrication regimes during unidirectional sliding contact. Tribology International. 2005;38:219-25.
[66] Ronen A, Etsion I, Kligerman Y. Friction-Reducing Surface-Texturing in Reciprocating Automotive Components. Tribology Transactions. 2001;44:359-66.
[67] Qiu Y, Khonsari MM. On the Prediction of Cavitation in Dimples Using a Mass-Conservative Algorithm. Journal of Tribology. 2009;131:11.

[68] Zhang J, Meng Y. Direct Observation of Cavitation Phenomenon and Hydrodynamic Lubrication Analysis of Textured Surfaces. Tribology Letters. 2012;46:147-58.
[69] Olver AV, Fowell MT, Spikes HA, Pegg IG. 'Inlet suction', a load support mechanism in non-convergent, pocketed, hydrodynamic bearings. Proceedings of the Institution of Mechanical Engineers, Part J: Journal of Engineering Tribology. 2006;220:105-8.
[70] Fowell MT, Olver AV, Gosman AD, Spikes HA, Pegg IG. Entrainment and inlet suction: Two mechanisms of hydrodynamic lubrication in textured bearings. Journal of Tribology. 2007;129:336-47.
[71] Tønder K. Dynamics of rough slider bearings: effects of one-sided roughness/waviness. Tribology International. 1996;29:117-22.
[72] Tønder K. Hydrodynamic effects of tailored inlet roughnesses: extended theory. Tribology International. 2004;37:137-42.
[73] Arghir M, Roucou N, Helene M, Frene J. Theoretical Analysis of the Incompressible Laminar Flow in a Macro-Roughness Cell. Journal of Tribology. 2003;125:309-18.
[74] Sahlin F, Glavatskih S, Almqvist Tr, Larsson R. Two-Dimensional CFD-Analysis of Micro-Patterned Surfaces in Hydrodynamic Lubrication. Journal of Tribology. 2005;127:96-102.
[75] Dobrica MB, Fillon M. About the validity of Reynolds equation and inertia effects in textured sliders of infinite width. Proceedings of the Institution of Mechanical Engineers, Part J: Journal of Engineering Tribology. 2009;223:69-78.
[76] de Kraker A, van Ostayen RAJ, Rixen DJ. Development of a texture averaged Reynolds equation. Tribology International. 2010;43:2100-9.
[77] Cupillard S, Glavatskih S, Cervantes MJ. 3D thermohydrodynamic analysis of a textured slider. Tribology International. 2009;42:1487-95.
[78] Cupillard S, Cervantes MJ, Glavatskih S. Pressure Buildup Mechanism in a Textured Inlet of a Hydrodynamic Contact. Journal of Tribology. 2008;130:021701-.
[79] Cupillard S, Glavatskih S, Cervantes MJ. Inertia effects in textured hydrodynamic contacts. Proceedings of the Institution of Mechanical Engineers, Part J: Journal of Engineering Tribology. 2010;224:751-6.
[80] Cupillard S, Glavatskih S, Cervantes MJ. Computational fluid dynamics analysis of a journal bearing with surface texturing. Journal of Engineering Tribology. 2008;222:97-108.
[81] Cupillard S, Cervantes MJ, Glavatskih S. A CFD study of a finite textured journal bearing. IAHR Symposium on Hydraulic Machinery and Systems Foz do Iguassu, Brazil2008.
[82] Yagi K, Sugimura J. Balancing Wedge Action: A Contribution of Textured Surface to Hydrodynamic Pressure Generation. Tribology Letters. 2013;50:349-64.
[83] Etsion I, Halperin G. A Laser Surface Textured Hydrostatic Mechanical Seal. Tribology Transactions. 2002;45:430-4.
[84] Kligerman Y, Etsion I, Shinkarenko A. Improving Tribological Performance of Piston Rings by Partial Surface Texturing. Journal of Tribology. 2005;127:632-8.
[85] Ryk G, Kligerman Y, Etsion I, Shinkarenko A. Experimental Investigation of

Partial Laser Surface Texturing for Piston-Ring Friction Reduction. Tribology Transactions. 2005;48:583-8.
[86] Ryk G, Etsion I. Testing piston rings with partial laser surface texturing for friction reduction. Wear. 2006;261:792-6.
[87] Bai S, Peng X, Li Y, Sheng S. A Hydrodynamic Laser Surface-Textured Gas Mechanical Face Seal. Tribology Letters. 2010;38:187-94.
[88] Meng X, Bai S, Peng X. Lubrication film flow control by oriented dimples for liquid lubricated mechanical seals. Tribology International. 2014;77:132-41.
[89] Ma C, Li D, Sun J. Integrated Influence of Sliding Velocity, Outlet Pressure, and Seal Clearance on Optimum Dimple Area Density for Mechanical Seal. IEEE Access. 2018;6:14030-7.
[90] Wang X, Shi L, Dai Q, Huang W, Wang X. Multi-objective optimization on dimple shapes for gas face seals. Tribology International.
[91] Brunetiere N, Tournerie B. Numerical analysis of a surface-textured mechanical seal operating in mixed lubrication regime. Tribology International. 2012;49:80-9.
[92] Braun MJ, Hannon WM. Cavitation formation and modelling for fluid film bearings: a review. Proc Inst Mech Eng. 2014;224:839-63.
[93] Qiu Y, Khonsari MM. Performance Analysis of Full-Film Textured Surfaces With Consideration of Roughness Effects. Journal of Tribology. 2011;133:021704-1-10.
[94] Wang X, Kato K, Adachi K, Aizawa K. Loads carrying capacity map for the surface texture design of SiC thrust bearing sliding in water. Tribology International. 2003;36:189-97.
[95] Wang X, Adachi K, Otsuka K, Kato K. Optimization of the surface texture for silicon carbide sliding in water. Applied Surface Science. 2006;253:1282-6.
[96] Wang X, Wang J, Zhang B, Huang W. Design principles for the area density of dimple patterns. Proceedings of the Institution of Mechanical Engineers Part J-Journal of Engineering Tribology. 2015;229:538-46.
[97] Sharma SC, Yadav SK. A comparative study of full and partial textured hybrid orifice compensated circular thrust pad bearing system. Tribology International. 2016;95:170-80.
[98] Shi LP, Wang XY, Su X, Huang W, Wang XL. Comparison of the Load-Carrying Performance of Mechanical Gas Seals Textured With Microgrooves and Microdimples. J Tribol-T Asme. 2016;138:7.
[99] Rahmani R, Shirvani A, Shirvani H. Optimization of Partially Textured Parallel Thrust Bearings with Square-Shaped Micro-Dimples. Tribology Transactions. 2007;50:401-6.
[100] Rahmani R, Mirzaee I, Shirvani A, Shirvani H. An analytical approach for analysis and optimisation of slider bearings with infinite width parallel textures. Tribology International. 2010;43:1551-65.
[101] Rahmani R, Rahnejat H. Enhanced performance of optimised partially textured load bearing surfaces. Tribology International. 2017.
[102] Pascovici MD, Cicone T, Fillon M, Dobrica MB. Analytical investigation of a partially textured parallel slider. Proceedings of the Institution of Mechanical Engineers, Part J: Journal of Engineering Tribology. 2009;223:151-8.

[103] Guzek A, Podsiadlo P, Stachowiak GW. A Unified Computational Approach to the Optimization of Surface Textures:One Dimensional Hydrodynamic Bearings. Tribology Online. 2010;5:150-60.
[104] Guzek A, Podsiadlo P, Stachowiak GW. Optimization of textured surface in 2D parallel bearings governed by the Reynolds equation including cavitation and temperature. Tribology Online. 2013;8:7-21.
[105] Gherca A, Fatu A, Hajjam M, Maspeyrot P. Effects of surface texturing in steady-state and transient flow conditions: Two-dimensional numerical simulation using a mass-conserving cavitation model. Proceedings of the Institution of Mechanical Engineers, Part J: Journal of Engineering Tribology. 2014;229:505-22.
[106] Malik S, Kakoty SK. Analysis of dimple textured parallel and inclined slider bearing. Proceedings of the Institution of Mechanical Engineers, Part J: Journal of Engineering Tribology. 2014;228:1343-57.
[107] Marian VG, Kilian M, Scholz W. Theoretical and experimental analysis of a partially textured thrust bearing with square dimples. Proceedings of the Institution of Mechanical Engineers, Part J: Journal of Engineering Tribology. 2007;221:771-8.
[108] Charitopoulos AG, Fouflias DG, Papadopoulos CI, Kaiktsis L, Fillon M. Thermohydrodynamic Analysis of a Textured Sector-Pad Thrust Bearing: Effects on Mechanical Deformations. Mechanics & Industry. 2014;15:403-11.
[109] Charitopoulos A, Visser R, Eling R, Papadopoulos C. Optimization of an Automotive Turbocharger Thrust Bearing Using a CFD-Based THD Computational Approach. Lubricants. 2018;6:21.
[110] Henry Y, Bouyer J, Fillon M. Experimental analysis of the hydrodynamic effect during start-up of fixed geometry thrust bearings. Tribology International. 2018;120:299-308.
[111] Fouflias DG, Charitopoulos AG, Papadopoulos CI, Kaiktsis L, Fillon M. Performance comparison between textured, pocket, and tapered-land sector-pad thrust bearings using computational fluid dynamics thermohydrodynamic analysis. Proceedings of the Institution of Mechanical Engineers, Part J: Journal of Engineering Tribology. 2014;229:376-97.
[112] Fouflias DG, Charitopoulos AG, Papadopoulos CI, Kaiktsis L. Thermohydrodynamic Analysis and Tribological Optimization of a Curved Pocket Thrust Bearing. Tribology International. 2017;110:291-306.
[113] Cameron A. Basic Lubrication Theory. 3rd ed. London: Longman Group Ltd.; 1971.
[114] Wang L, Wang W, Wang H, Ma T, Hu Y. Numerical analysis on the factors affecting the hydrodynamic performance for the parallel surfaces with microtextures. Journal of Tribology. 2014;136.
[115] Cupillard S, Glavatskih S, Cervantes MJ. Thermal analysis of lubricant flow in a textured inlet contact. In: Kim JH, editor. Proceedings of the 19th International Symposium on Transport Phenomena (ISTP-19): University of Iceland, Faculty of Industrial Engineering, Mechanical Engineering and Computer Science; 2008.
[116] Tønder K. Dimpled pivoted plane bearings: Modified coefficients. Tribology International. 2010;43:2303-7.
[117] Tønder K. Micro- and macro-modifications of pivoted slider bearings:

Performance comparison and texturing versus width reduction. Tribology International. 2011;44:463-7.
[118] Patir N, Cheng HS. An Average Flow Model for Determining Effects of Three-Dimensional Roughness on Partial Hydrodynamic Lubrication. Journal of Tribology. 1978;100:12-7.
[119] Papadopoulos CI, Efstathiou EE, Nikolakopoulos PG, Kaiktsis L. Geometry Optimization of Textured Three-Dimensional Micro- Thrust Bearings. Journal of Tribology. 2011;133:041702-.
[120] Papadopoulos CI, Nikolakopoulos PG, Kaiktsis L. Characterization of Stiffness and Damping in Textured Sector Pad Micro Thrust Bearings Using Computational Fluid Dynamics. Journal of Engineering for Gas Turbines and Power. 2012;134:112502.
[121] Aggarwal S, Pandey RK. Frictional and load-carrying behaviours of micro-textured sector shape pad thrust bearing incorporating the cavitation and thermal effects. Lubrication Science. 2016:n/a-n/a.
[122] Brajdic-Mitidieri P, Gosman AD, Ioannides E, Spikes HA. CFD Analysis of a Low Friction Pocketed Pad Bearing. Journal of Tribology. 2005;127:803-12.
[123] Kango S, Sharma RK, Pandey RK. Comparative analysis of textured and grooved hydrodynamic journal bearing. Proceedings of the Institution of Mechanical Engineers, Part J: Journal of Engineering Tribology. 2014;228:82-95.
[124] Lin Q, Bao Q, Li K, Khonsari MM, Zhao H. An investigation into the transient behavior of journal bearing with surface texture based on fluid-structure interaction approach. Tribology International. 2017.
[125] Matele S, Pandey K. Effect of surface texturing on the dynamic characteristics of hydrodynamic journal bearing comprising concepts of green tribology. Proceedings of the Institution of Mechanical Engineers, Part J: Journal of Engineering Tribology.0:1350650117752611.
[126] Gu C, Meng X, Zhang D, Xie Y. Transient analysis of the textured journal bearing operating with the piezoviscous and shear-thinning fluids. Journal of Tribology. 2017.
[127] Gui C, Meng F. Comparative study of spherical dimple and bump effects on the tribological performances of journal bearing. Proceedings of the Institution of Mechanical Engineers, Part J: Journal of Engineering Tribology.0:1350650118770355.
[128] Meng F, Zhang L, Liu Y, Li TT. Effect of compound dimple on tribological performances of journal bearing. Tribology International. 2015;91:99-110.
[129] Yamada H, Taura H, Kaneko S. Static Characteristics of Journal Bearings with Square Dimples. Journal of Tribology. 2017.
[130] Yamada H, Taura H, Kaneko S. Numerical and Experimntal Analyses of the Dynamic Characteristics of Journal Bearings with Square Dimples. Journal of Tribology. 2017.
[131] Zhang H, Hafezi M, Dong G, Liu Y. A design of coverage area for textured surface of sliding journal bearing based on Genetic Algorithm. Journal of Tribology. 2018.
[132] Nanbu T, Ren N, Yasuda Y, Zhu D, Wang QJ. Micro-Textures in Concentrated Conformal-Contact Lubrication: Effects of Texture Bottom Shape and Surface

Relative Motion. Tribology Letters. 2008;29:241-52.
[133] Yu H, Wang X, Zhou F. Geometric Shape Effects of Surface Texture on the Generation of Hydrodynamic Pressure Between Conformal Contacting Surfaces. Tribology Letters. 2010;37:123-30.
[134] Etsion I. Modeling of surface texturing in hydrodynamic lubrication. Friction. 2013;1:195-209.
[135] Yu H, Deng H, Huang W, Wang X. The effect of dimple shapes on friction of parallel surfaces. Proceedings of the Institution of Mechanical Engineers, Part J: Journal of Engineering Tribology. 2011;225:693-703.
[136] Qiu M, Delic A, Raeymaekers B. The effect of texture shape on the load-carrying capacity of gas-lubricated parallel slider bearings. Tribology Letters. 2012;48:315-27.
[137] Qiu M, Minson BR, Raeymaekers B. The effect of texture shape on the friction coefficient and stiffness of gas-lubricated parallel slider bearings. Tribology International. 2013;67:278-88.
[138] Shen C, Khonsari MM. Numerical optimization of texture shape for parallel surfaces under unidirectional and bidirectional sliding. Tribology International. 2015;82:1-11.
[139] Shen C, Khonsari MM. Effect of Dimple's Internal Structure on Hydrodynamic Lubrication. Tribology Letters. 2013;52:415-30.
[140] Uddin MS, Liu YW. Design and optimization of a new geometric texture shape for the enhancement of hydrodynamic lubrication performance of parallel slider surfaces. Biosurface and Biotribology. 2016;2:59-69.
[141] Zhang H, Hua M, Dong G-z, Zhang D-y, Chen W-j, Dong G-n. Optimization of texture shape based on Genetic Algorithm under unidirectional sliding. Tribology International.
[142] Shen C, Khonsari MM. Texture Shape Optimization for Seal-Like Parallel Surfaces: Theory and Experiment. Tribology Transactions. 2016;59:698-706.
[143] Wang W, He Y, Zhao J, Li Y, Luo J. Numerical Optimization of the Groove Texture Bottom Profile for Thrust Bearings. Tribology International. 2016.
[144] Qiu M, Raeymaekers B. The load-carrying capacity and friction coefficient of incompressible textured parallel slider bearings with surface roughness inside the texture features. Proceedings of the Institution of Mechanical Engineers, Part J: Journal of Engineering Tribology. 2014;229:547-56.
[145] Charitopoulos AG, Efstathiou EE, Papadopoulos CI, Nikolakopoulos PG, Kaiktsis L. Effects of manufacturing errors on tribological characteristics of 3-D textured micro- thrust bearings. CIRP Journal of Manufacturing Science and Technology. 2013;6:128-42.
[146] Reynolds O. On the Theory of Lubrication and Its Application to Mr. Beauchamp Tower's Experiments, Including an Experimental Determination of the Viscosity of Olive Oil. Philosophical Transactions of the Royal Society of London. 1886;177:157-234.
[147] Caramia G, Carbone G, De Palma P. Hydrodynamic lubrication of micro-textured surfaces: Two dimensional CFD-analysis. Tribology International. 2015;88:162-9.

[148] Han J, Fang L, Sun J, Ge S. Hydrodynamic Lubrication of Microdimple Textured Surface Using Three-Dimensional CFD. Tribology Transactions. 2010;53:860-70.
[149] Papadopoulos CI, Nikolakopoulos PG, Kaiktsis L. Evolutionary Optimization of Micro-Thrust Bearings With Periodic Partial Trapezoidal Surface Texturing. Journal of Engineering for Gas Turbines and Power. 2010;133:012301-.
[150] Feldman Y, Kligerman Y, Etsion I, Haber S. The Validity of the Reynolds Equation in Modeling Hydrostatic Effects in Gas Lubricated Textured Parallel Surfaces. Journal of Tribology. 2005;128:345-50.
[151] Qiu M, Bailey BN, Stoll R, Raeymaekers B. The accuracy of the compressible Reynolds equation for predicting the local pressure in gas-lubricated textured parallel slider bearings. Tribology International. 2014;72:83-9.
[152] Marian VG, Predescu A, Pascovici MD. Theoretical analysis of an infinitely wide rigid cylinder rotating over a grooved surface in hydrodynamic conditions. Proceedings of the Institution of Mechanical Engineers, Part J: Journal of Engineering Tribology. 2009;224:757-63.
[153] Jakobsson B, Floberg L. The finite journal bearing, considering vaporization. Tran Chalmers University of Tech Gothenburg. 1957;190:1-116.
[154] Olsson KO. Cavitation in Dynamically Loaded Bearings. Tran Chalmers University of Tech Gothenburg. 1965;308.
[155] Elrod HG. A Cavitation Algorithm. Journal of Tribology. 1981;103:350-4.
[156] Elrod HG, Adams ML. A Computer Program for Cavitation and Starvation Problems. Cavitation and Related Phenomena in Lubrication, Mechanical Engineering Publication. 1974:37-41.
[157] Fesanghary M, Khonsari MM. A Modification of the Switch Function in the Elrod Cavitation Algorithm. Journal of Tribology. 2011;133:4.
[158] Brewe DE. Theoretical Modeling of the Vapor Cavitation in Dynamically Loaded Journal Bearings. Journal of Tribology. 1986;108:628-37.
[159] Woods CM, Brewe DE. The Solution of the Elrod Algorithm for a Dynamically Loaded Journal Bearing Using Multigrid Techniques. Tribology Conference. Baltimore, Maryland1988.
[160] Vijayaraghavan D, Keith TG. Development and Evaluation of a Cavitation Algorithm. Tribology Transactions. 1989;32:225-33.
[161] Vijayaraghavan D, Keith TG. An Efficient, Robust, and Time Accurate Numerical Scheme Applied to a Cavitation Algorithm. Journal of Tribology. 1990;112:44-51.
[162] Kumar A, Booker JF. A Finite Element Cavitation Algorithm. Journal of Tribology. 1991;113:276-84.
[163] Kumar A, Booker JF. A Finite Element Cavitation Algorithm: Application/Validation. Journal of Tribology. 1991;113:255-60.
[164] XIE Yi LY, SUO ShuangFu, LIU XiangFeng, LI JingHao, WANG YuMing. A mass-conservative average flow model based on finite element method for complex textured surfaces. SCIENCE CHINA Physics, Mechanics & Astronomy. 2013;56:1909-19.
[165] Shi F, Paranjpe R. An Implicit Finite Element Cavitation Algorithm. Comput

Model Eng Sci. 2002;3:507-15.
[166] Hajjam M, Bonneau D. A transient finite element cavitation algorithm with application to radial lip seals. Tribology International. 2007;40:1258-69.
[167] Payvar P, Salant RF. A Computational Method for Cavitation in a Wavy Mechanical Seal. Journal of Tribology. 1992;114:199-204.
[168] Wang Y, Wang QJ, Lin C. Mixed Lubrication of Coupled Journal-Thrust-Bearing Systems Including Mass Conserving Cavitation. Journal of Tribology. 2003;125:747-55.
[169] Harp SR, Salant RF. An Average Flow Model of Rough Surface Lubrication With Inter-Asperity Cavitation. Journal of Tribology. 2000;123:134-43.
[170] Shi F, Salant RF. A Mixed Soft Elastohydrodynamic Lubrication Model With Interasperity Cavitation and Surface Shear Deformation. Journal of Tribology. 1999;122:308-16.
[171] Xiong S, Wang QJ. Steady-State Hydrodynamic Lubrication Modeled With the Payvar-Salant Mass Conservation Model. Journal of Tribology. 2012;134:031703-.
[172] Sahlin F, Almqvist A, Larsson R, Glavatskih S. A cavitation algorithm for arbitrary lubricant compressibility. Tribology International. 2007;40:1294-300.
[173] Ausas RF, Jai M, Buscaglia GC. A Mass-Conserving Algorithm for Dynamical Lubrication Problems With Cavitation. Journal of Tribology. 2009;131:031702-1.
[174] Spencer A, Almqvist A, Larsson R. A semi-deterministic texture-roughness model of the piston ring–cylinder liner contact. Proceedings of the Institution of Mechanical Engineers, Part J: Journal of Engineering Tribology. 2011;225:325-33.
[175] Giacopini M, Fowell MT, Dini D, Strozzi A. A Mass-Conserving Complementarity Formulation to Study Lubricant Films in the Presence of Cavitation. Journal of Tribology. 2010;132:041702-.
[176] Bertocchi L, Dini D, Giacopini M, Fowell MT, Baldini A. Fluid film lubrication in the presence of cavitation: a mass-conserving two-dimensional formulation for compressible, piezoviscous and non-Newtonian fluids. Tribology International. 2013;67:61-71.
[177] Medina S, Fowell MT, Vladescu SC, Reddyhoff T, Pegg I, Olver AV, et al. Transient effects in lubricated textured bearings. Proceedings of the Institution of Mechanical Engineers Part J-Journal of Engineering Tribology. 2015;229:523-37.
[178] Miraskari M, Hemmati F, Jalali A, Alqaradawi MY, Gadala MS. A Robust Modification to the Universal Cavitation Algorithm in Journal Bearings. Journal of Tribology. 2016;139:031703-.
[179] Woloszynski T, Podsiadlo P, Stachowiak GW. Efficient Solution to the Cavitation Problem in Hydrodynamic Lubrication. Tribology Letters. 2015;58:1-11.
[180] Hu Y, Zhu D. A Full Numerical Solution to the Mixed Lubrication in Point Contacts. Journal of Tribology. 1999;122:1-9.
[181] Zhu D, Hu Y. A Computer Program Package for the Prediction of EHL and Mixed Lubrication Characteristics, Friction, Subsurface Stresses and Flash Temperatures Based on Measured 3-D Surface Roughness. Tribology Transactions. 2001;44:383-90.
[182] Epstein D, Keer LM, Wang QJ, Cheng HS, Zhu D. Effect of Surface Topography on Contact Fatigue in Mixed Lubrication. Tribology Transactions.

2003;46:506-13.
[183] Wang QJ, Zhu D. Virtual Texturing: Modeling the Performance of Lubricated Contacts of Engineered Surfaces. Journal of Tribology. 2005;127:722-8.
[184] Wang QJ, Zhu D, Zhou R, Hashimoto F. Investigating the Effect of Surface Finish on Mixed EHL in Rolling and Rolling-Sliding Contacts. Tribology Transactions. 2008;51:748-61.
[185] Jiang X, Hua DY, Cheng HS, Ai X, Lee SC. A Mixed Elastohydrodynamic Lubrication Model With Asperity Contact. Journal of Tribology. 1999;121:481-91.
[186] Patir N, Cheng HS. Application of Average Flow Model to Lubrication Between Rough Sliding Surfaces. Journal of Tribology. 1979;101:220-9.
[187] Elrod HG. A General Theory for Laminar Lubrication With Reynolds Roughness. Journal of Tribology. 1979;101:8-14.
[188] Tripp JH. Surface Roughness Effects in Hydrodynamic Lubrication: The Flow Factor Method. Journal of Tribology. 1983;105:458-63.
[189] Wu C, Zheng L. An Average Reynolds Equation for Partial Film Lubrication With a Contact Factor. Journal of Tribology. 1989;111:188-91.
[190] Rocke AH, Salant RF. Elastohydrodynamic Analysis of a Rotary Lip Seal Using Flow Factors. Tribology Transactions. 2005;48:308-16.
[191] Wilson WRD, Marsault N. Partial Hydrodynamic Lubrication With Large Fractional Contact Areas. Journal of Tribology. 1998;120:16-20.
[192] Chan C-W, Han Y-F, Wang Z, Wang J, Shi F, Wang N, et al. Exploration on a Fast EHL Computing Technology for Analyzing Journal Bearings with Engineered Surface Textures. Tribology Transactions. 2013;57:206-15.
[193] de Kraker A, van Ostayen RAJ, van Beek A, Rixen DJ. A Multiscale Method Modeling Surface Texture Effects. Journal of Tribology. 2006;129:221-30.
[194] Dobrica MB, Fillon M, Maspeyrot P. Mixed Elastohydrodynamic Lubrication in a Partial Journal Bearing—Comparison Between Deterministic and Stochastic Models. Journal of Tribology. 2006;128:778-88.
[195] Elrod HG. Thin-Film Lubrication Theory for Newtonian Fluids With Surfaces Possessing Striated Roughness or Grooving. Journal of Tribology. 1973;95:484-9.
[196] Bayada G, Faure JB. A Double Scale Analysis Approach of the Reynolds Roughness Comments and Application to the Journal Bearing. Journal of Tribology. 1989;111:323-30.
[197] Jai M, Bou-Saïd B. A Comparison of Homogenization and Averaging Techniques for the Treatment of Roughness in Slip-Flow-Modified Reynolds Equation. Journal of Tribology. 2001;124:327-35.
[198] Kane M, Bou-Said B. Comparison of Homogenization and Direct Techniques for the Treatment of Roughness in Incompressible Lubrication. Journal of Tribology. 2004;126:733-7.
[199] Bayada G, Martin S, Vázquez C. An Average Flow Model of the Reynolds Roughness Including a Mass-Flow Preserving Cavitation Model. Journal of Tribology. 2005;127:793-802.
[200] Almqvist A, Dasht J. The homogenization process of the Reynolds equation describing compressible liquid flow. Tribology International. 2006;39:994-1002.
[201] Almqvist A, Essel EK, Persson LE, Wall P. Homogenization of the unstationary

incompressible Reynolds equation. Tribology International. 2007;40:1344-50.
[202] Almqvist A, Lukkassen D, Meidell A, Wall P. New concepts of homogenization applied in rough surface hydrodynamic lubrication. International Journal of Engineering Science. 2007;45:139-54.
[203] Sahlin F, Almqvist A, Larsson R, Glavatskih S. Rough surface flow factors in full film lubrication based on a homogenization technique. Tribology International. 2007;40:1025-34.
[204] Almqvist A, Essel EK, Fabricius J, Wall P. Reiterated homogenization applied in hydrodynamic lubrication. Proceedings of the Institution of Mechanical Engineers, Part J: Journal of Engineering Tribology. 2008;222:827-41.
[205] Sahlin F, Larsson R, Almqvist A, Lugt PM, Marklund P. A mixed lubrication model incorporating measured surface topography. Part 1: Theory of flow factors. Proceedings of the Institution of Mechanical Engineers, Part J: Journal of Engineering Tribology. 2010;224:335-51.
[206] Sahlin F, Larsson R, Marklund P, Almqvist A, Lugt PM. A mixed lubrication model incorporating measured surface topography. Part 2: Roughness treatment, model validation, and simulation. Proceedings of the Institution of Mechanical Engineers, Part J: Journal of Engineering Tribology. 2010;224:353-65.
[207] Almqvist A, Fabricius J, Spencer A, Wall P. Similarities and Differences Between the Flow Factor Method by Patir and Cheng and Homogenization. Journal of Tribology. 2011;133:031702-.
[208] Rom M, Mueller S. A Reduced Basis Method for the Homogenized Reynolds Equation Applied to Textured Surfaces. Commun Comput Phys. 2018.
[209] Woloszynski T, Podsiadlo P, Stachowiak GW. Evaluation of discretisation and integration methods for the analysis of hydrodynamic bearings with and without surface texturing. Tribology Letters. 2013;51:25-47.
[210] Woloszynski T, Podsiadlo P, Stachowiak GW. Evaluation of discretization and integration methods for the analysis of finite hydrodynamic bearings with surface texturing. Proceedings of the Institution of Mechanical Engineers Part J-Journal of Engineering Tribology. 2015;229:465-77.
[211] Minet C, Brunetiere N, Tournerie B. A Deterministic Mixed Lubrication Model for Mechanical Seals. Journal of Tribology. 2011;133:042203-.
[212] Pei S, Ma S, Xu H, Wang F, Zhang Y. A multiscale method of modeling surface texture in hydrodynamic regime. Tribology International. 2011;44:1810-8.
[213] Pei S, Xu H, Shi F. A deterministic multiscale computation method for rough surface lubrication. Tribology International. 2016;94:502-8.
[214] Profito F, Giacopini M, Zachariadis D, Dini D. A General Finite Volume Method for the Solution of the Reynolds Lubrication Equation with a Mass-Conserving Cavitation Model. Tribology Letters. 2015;60:1-21.
[215] Arghir M, Alsayed A, Nicolas D. The finite volume solution of the Reynolds equation of lubrication with film discontinuities. International Journal of Mechanical Sciences. 2002;44:2119-32.
[216] Bonneau D, Fatu A, Souchet D. Hydrodynamic Bearings. London, New York: ISTE, Wiley & Sons; 2014.
[217] Dobrica MB, Fillon M. Reynolds' Model Suitability in Simulating Rayleigh Step

Bearing Thermohydrodynamic Problems. Tribology Transactions. 2005;48:522-30.
[218] Arghir M, Lez SL, Frene J. Finite-volume solution of the compressible Reynolds equation: Linear and non-linear analysis of gas bearings. Proceedings of the Institution of Mechanical Engineers, Part J: Journal of Engineering Tribology. 2006;220:617-27.
[219] Buscaglia GC, Jai M. Homogenization of the Generalized Reynolds Equation for Ultra-Thin Gas Films and Its Resolution by FEM. Journal of Tribology. 2004;126:547-52.
[220] Sharma SC, Yadav SK. Performance analysis of a fully textured hybrid circular thrust pad bearing system operating with non-Newtonian lubricant. Tribology International. 2014;77:50-64.
[221] Almqvist A, Fabricius J, Larsson R, Wall P. A New Approach for Studying Cavitation in Lubrication. Journal of Tribology. 2013;136:011706-.
[222] Cottle RW, Pang JS, Stone RE. The Linear Complementarity Problem: Society for Industrial and Applied Mathematics; 2009.
[223] Zhu D. On some aspects of numerical solutions of thin-film and mixed elastohydrodynamic lubrication. Proceedings of the Institution of Mechanical Engineers, Part J: Journal of Engineering Tribology. 2007;221:561-79.
[224] Wang W, Wang H, Liu Y, Hu Y, Zhu D. A comparative study of the methods for calculation of surface elastic deformation. Proceedings of the Institution of Mechanical Engineers, Part J: Journal of Engineering Tribology. 2003;217:145-54.
[225] Lugt PM, Morales-Espejel GE. A Review of Elasto-Hydrodynamic Lubrication Theory. Tribology Transactions. 2011;54:470-96.
[226] Etsion I. Design Charts for Arbitrarily Pivoted, Liquid-Lubricated, Flat-Sector-Pad Thrust Bearing. Journal of Lubrication Technology. 1978;100:279-84.
[227] Bobach L. Simulation dynamisch belasteter Radialgleitlager unter Mischreibungsbedingungen [Dissertation]. Aachen: Otto-von-Guericke-Universät; 2008.
[228] Bartel D. Simulation von Tribosystemen. Wiesbaden: Vieweg+Teubner; 2010.
[229] Frene J, Nicolas D, Degueurce B, Berthe D, Godet M. Hydrodynamic Lubrication: Bearings and Thrust Bearings: Elsevier Science; 1997.
[230] Glavatskih SB, Fillon M, Larsson R. The Significance of Oil Thermal Properties on the Performance of a Tilting-Pad Thrust Bearing. Journal of Tribology. 2001;124:377-85.
[231] Versteeg HK, Malalasekera W. An Introduction to Computational Fluid Dynamics: The Finite Volume Method: Pearson Education Limited; 2007.
[232] Burden RL, Faires JD. Numerical Analysis: Brooks/Cole, Cengage Learning; 2011.
[233] Kincaid DR, Cheney EW. Numerical Analysis: Mathematics of Scientific Computing: American Mathematical Society; 2002.
[234] Mathworks. Documentation: fmincon, https://uk.mathworks.com/help/optim/ug/fmincon.html. accessed 08.05.2018.
[235] Byrd RH, Gilbert JC, Nocedal J. A trust region method based on interior point techniques for nonlinear programming. Mathematical Programming. 2000;89:149-85.
[236] Byrd RH, Hribar ME, Nocedal J. An Interior Point Algorithm for Large-Scale

Nonlinear Programming. SIAM Journal on Optimization. 1999;9:877-900.
[237] Waltz RA, Morales JL, Nocedal J, Orban D. An interior algorithm for nonlinear optimization that combines line search and trust region steps. Mathematical Programming. 2006;107:391-408.
[238] Zouzoulas V. Thermohydrodynamic analysis of tilting pad thrust bearings with artificial surface texturing [Diploma Thesis]: National Technical University of Athens; 2014.
[239] Yagi K, Sugimura J. Performance of Balancing Wedge Action in Textured Hydrodynamic Pad Bearings. Journal of Tribology. 2016;139:011704-.
[240] Klein U, Beneke R. Support ring. European Patent EP2475900B1. 2013
[241] SKFBearingCalculator. http://www.skf.com/uk/knowledge-centre/engineering-tools/skfbearingcalculator.html. accessed 25.05.2018.